Fission Gas Release Measurements in relation to ANS Standard Modelling of Radiological Releases

by

J. A. Turnbull[2], E. Kolstad [1], W. Wiesenack [1]

[1] OECD Halden Reactor Project

[2] Consultant

Summary

Early data on fission gas release (FGR) were obtained solely from Post Irradiation Examination (PIE), when discharged fuel rods were punctured and the internal gas extracted and analysed by techniques such as mass spectrometry. PIE is extremely useful when applied to commercially irradiated fuel, as it provides data for a prototypic irradiation and fuel loading strategy. However, it is of only limited use when required for developing an understanding of the mechanisms and factors involved in the FGR process. This gap was filled by the development of in-pile instrumentation to provide on-line information from which the kinetics of release can be determined.

Two types of experiments have been used in the Halden reactor to investigate the release of fission gases from LWR fuel. The first employs internal pressure sensors from which the kinetics and quantity of stable gases can be measured during irradiation. The second is the use of sweep gases to carry released fission gases from the fuel rod to a detector situated outside the reactor. With this equipment, it is possible to measure, using gamma spectroscopy, both radioactive and stable fission product release. In conjunction with fuel centreline thermocouples to measure fuel temperatures, these techniques have been successful in improving our understanding of the release process and the factors affecting it. The data generated have been used in many member countries to develop models and validate fuel performance codes used in reactor safety assessments.

In the sweep gas experiments, gas lines are attached to both ends of the fuel rod. This allows the introduction of a gas to pass through the free volume and carry entrained gases released from the fuel to a gamma detector situated outside but adjacent to the reactor. In this way, stable fission gas release can be inferred from measurements on the long lived isotope ^{85}Kr with a half life of ~10 years as well as the release of radioactive fission products, e.g. the radiologically important isotope ^{131}I from measurements of short lived krypton and xenon with half lives spanning ~90 secs to around 5 days. The release of ^{131}I is of greatest importance primarily due to its long half-life. Iodine release data are obtained by measuring the decay product ^{131m}Xe. Estimates of ^{131}I inventories are also obtained by measurements on ^{85m}Kr. Experiments to measure the release of short lived rare gases have made a significant contribution to our understanding of stable gas release, in particular in the determination of the in-pile diffusion coefficient and the processes occurring at grain boundaries.

The American Nuclear Society has recently formed a work group to review the current ANS-5.4 model with a view to improving it. The Halden Project will take active part in this committee and supply experimental data.

This paper will discuss some of the more important measurements made with in-pile instrumentation and sweep gas experiments performed in the Halden reactor with particular reference to the release of radioactive fission gases.

INTRODUCTION

This paper will discuss some of the more important measurements made with in-pile instrumentation and sweep gas experiments performed in the Halden reactor with particular reference to the release of radioactive fission gases and iodine. The present authors have not been involved with all the experiments described and acknowledgement is made to other secondees and Halden staff who carried out the measurements and interpretations, in particular, Dr R. J. White.

STABLE FISSION GAS RELEASE: THE CONCEPT OF A RELEASE THRESHOLD

PIE of commercially irradiated fuel rods showed that there was a strong correlation between linear heat rate and the amount of fission gases released. Whereas low powered rods maintained very low levels of release even up to high burn-up, substantial fractional release was observed in high rated rods even at low burn-up. Such observations suggested that fuel temperature was a major parameter in controlling FGR. This lead the Halden Project to embark on a campaign of experiments using rods equipped with both fuel centreline thermocouples and pressure sensors to determine the conditions necessary to distinguish between 'high' and 'low' fission gas release. The chosen criterion separating these two regimes was a threshold value of 1% fractional release. The experiments encompassed different levels of linear power and burn-up which eventually lead to an empirical relation between fuel centreline temperature TF(°C) and burn-up BU(MWd/kgUO_2) for this threshold [1]:

$$BU = 0.005 \times \exp(9800/TF) \qquad /1/$$

This relationship, shown in Figure 1, is purely empirically based on experimental data, and although derived from Halden experimental fuel rods, it is remarkably successful in predicting behaviour for a variety of fuel manufactures and designs including MOX. The empirical threshold can be described in terms of the interlinkage of porosity along grain boundaries. With this interpretation, it is possible to reproduce the threshold by including, within a code for calculating temperature as a function of burn-up, a model for stable fission gas release based on single atom diffusion and re-solution at grain boundaries, [2]. Values of the disposable parameters describing re-solution and grain boundary saturation can be obtained by benchmarking the code predictions to 1% release at the level of the empirical threshold.

The original empirical threshold was derived on relatively low burn-up fuel rods, but proved reliable when extended to higher burn-up levels in the range 30-40 MWd/kgUO_2. However, recent data obtained at Halden from a gas flow rod in the disk irradiation rig IFA-569 and re-fabricated high burn-up fuel show that the onset of release in the range 50-60 MWd/kgUO_2 is substantially lower than predicted using the original criterion, see Figure 1. This is not an artifact due to changes in rod thermal performance, e.g. by degradation of fuel thermal conductivity, but a genuine trend in the release processes; see also [3]. The origin of this trend is unknown and clearly there is a requirement for more data in the range 40-60 MWd/kgUO_2 in order to prescribe the form of the threshold in this region.

RADIOACTIVE FGR MEASURED BY SWEEP GAS EXPERIMENTS

Complementary to experiments using sealed rods, the use of sweep gas experiments have added substantially to our knowledge of fuel rod thermal performance and fission gas release. In these experiments, gas lines are attached to both ends of the fuel rod. This allows the introduction of a gas to pass through the free volume and carry entrained gases released from the fuel to a gamma detector situated outside but adjacent to the reactor. In this way, stable fission gas release can be inferred from measurements on the long lived isotope ^{85}Kr with a half life of ~10 years as well as the release of radioactive fission products, e.g. the radiologically important isotope ^{131}I from measurements of short lived krypton and xenon with half lives spanning ~90 secs to around 5 days. Experiments to measure the release of these short lived rare gases have also made a significant contribution to our understanding of stable gas release, in particular in the determination of the in-pile diffusion coefficient and the processes occurring at grain boundaries.

HALDEN EXPERIENCE IN SWEEP GAS EXPERIMENTS

The first Halden gas flow experiment was designated IFA-430 (Instrumented Fuel Assembly) which commenced irradiation in late 1978 and remained in the reactor for six years. The rig incorporated 4 PWR design rods, although only two were designed as gas flow rods. The principal aim of the experiment was to investigate axial gas flow as a possible limiting factor for clad ballooning during LOCA. All four rods employed 1.2 m long fuel stacks with the gas flow rods comprising 3 sub-stacks with pressure transducers fitted between to measure axial pressure gradients during steady and transient flow conditions. Although many useful fission product release data were obtained from this assembly, the information was of limited applicability because of the long fuel stack and the range of power and burn-up along the length of the fuel column.

This experiment was soon followed by a further gas flow rig, IFA-504 designed specifically for fission product release studies, [4]. The assembly consisted of four rods with short active fuel lengths of 700 mm of different pellet design. Two rods contained solid pellets with pellets sourced from separate manufactures, one hollow rod and one fuelled with niobia doped UO_2 pellets. This assembly was loaded in December 1980 and is still operating successfully to date at a burn-up in excess of 75 MWd/kgUO_2 after 19 years continuous irradiation. Over this time the experiment has produced unique data on fuel thermal performance, hydraulic diameter as well as fission product release.

Based on the success of IFA-504, Nuclear Electric (UK), now British Energy, commissioned a similar experiment, IFA-558 to investigate the effect of internal pressure on the release of short lived fission products. The assembly carried 6 identical fuel rods 700 mm long containing hollow pellets of BNFL CONPOR fuel. The operating pressure in pairs of rods was maintained at 2, 20 and 40 bar during the entire irradiation except when being flushed periodically to measure release. After measuring short lived species by gamma counting, the gas from individual rods was trapped on liquid nitrogen cooled charcoal and stored until short lived fission products had decayed. The gas was then expanded past the gamma detector and the quantity of the long lived ^{85}Kr measured. Thus data were obtained simultaneously for both short and long lived fission gases.

The sweep gas technique has also been used on two experiments, IFA-563 and IFA-569 where the fuel was in the form of 1 mm thick disks of UO_2 sandwiched between disks of molybdenum to carry away most of the heat generated by fission. In this way the fuel operated at a near uniform temperature controlled by the fuel-clad gap and its gas composition.

Finally, sweep gas lines have been attached to re-instrumented fuel pre-irradiated to high burn-up in commercial reactors. Two loadings of this series of experiments have been performed, one containing pre-irradiated UO_2 fuel and the other containing pre-irradiated MOX fuel.

Analysis of Sweep Gas Experiments

The fractional release of a radioactive fission product is measured as the ratio of the rate of release from the fuel, R in atoms/s, divided by the birth rate, also in atoms/s. For constant irradiation conditions over a period of around three half-lives, the system is at radioactive equilibrium and the total release $(R/B)_{total}$ is the sum of two terms:

$$(R/B)_{total} = (R/B)_{diffusion} + (R/B)_{\lambda\text{-independent}} \qquad /2/$$

The first term results from release by atomic diffusion and is dependent on temperature via a diffusion coefficient and a radioactive decay constant λ; for a surface to volume ratio (S/V) and (R/B) < 0.1:

$$\left(R/B\right)_{diffusion} = \left(S/V\right)\sqrt{\frac{\alpha \cdot D}{\lambda}} \qquad /3/$$

where α is a constant for each isotope representing diffusion by the precursor to the isotope under consideration. The second term is also proportional to (S/V) but is independent of half life and represents the contribution from knock-out and direct recoil. The parameters of interest in these equations are: the diffusion coefficient D which is common for all isotopes of krypton and xenon and hence the stable isotopes of these species, the surface to volume ratio (S/V), as this changes from one material to another and with irradiation. The equation for $(R/B)_{total}$ is often written in a phenomenological form:

$$\left(R/B\right)_{total} = A + B\sqrt{\frac{\alpha}{\lambda}} \qquad /4/$$

where the coefficients A and B are referred to as the *recoil* and *slope* respectively and for a given gas flow measurement, are common for a range of species.

The Diffusion Coefficient

By comparing the release from polycrystalline UO_2 with release from single crystal material of known (S/V), an absolute determination of diffusion coefficient was obtained for the rare gases [5,6]. This was found to comprise three terms: a high temperature intrinsic diffusion coefficient, an intermediate term depending on temperature and rating and a final athermal term observed at low temperature which was proportional to rating. However, the low levels of release at low temperatures from the small amount of material used in these experiments, (~mgs), reduced the accuracy of determining this third component. This is not the case for the

sweep gas experiments performed at Halden, where the active fuel column can weigh ~ 0.5 kg. Data from IFA-430, IFA-504 and IFA-558 suggested that this third term was not athermal but had a small temperature dependence. This was explored further in the start-up ramp for IFA-563, which confirmed the earlier findings, Figure 2. Thus the final diffusion coefficient D (m^2/s) in terms of the mass rating R (W/gU) and the temperature TK (K), was revised as follows:

$$D = D_1 + D_2 + D_3$$

where:

$$D_1 = 7.6 \cdot 10^{-10} \cdot e^{-35000/TK} \qquad /5/$$

$$D_2 = 1.38 \cdot 10^{-16} \cdot R^{1/2} \cdot e^{-13800/TK}$$

$$D_3 = 7.67 \cdot 10^{-22} \cdot R \cdot e^{-2785/TK}$$

This diffusion coefficient has been used to analyze much of the data from the gas flow rigs with particular reference to its applicability to the lifetime of the isotopes measured. It had been noticed [6] that employing the 3 terms in a fuel performance code to estimate stable FGR, the code systematically over predicted the release at low powers. Consequently, when employed for stable gases, only the first two terms of the diffusion coefficient were used. Prior to interlinkage of grain boundary porosity, the value of (S/V) is approximately the same throughout the pellets and the resulting release of a radioactive isotope will be proportional to a volumetric average of the square root of the diffusion coefficient. If the fuel temperature is also averaged in the same way, it is possible to identify a measured (R/B) with a characteristic diffusion coefficient and temperature. In this way, for each gas flow measurement, the diffusion coefficient can be calculated for a range of isotopes of different half lives. This has been applied to a full range of isotopes including ^{131m}Xe (12 days), ^{133}Xe (5 days). A compilation of the results is shown in Figure 3, where it can be seen that these long lived species are best represented by omitting the third term D_3. Thus stable and long lived species should be modelled using $D_1 + D_2$ whilst for short lived species, the full three term diffusion coefficient should be employed. This is not fully understood, although an attractive explanation in terms of a fractal representation of the free surface has been proposed. (R J White private communication, 1999). Here, the diffusion coefficient is D_1+D_2 and the difference in long and short-lived release is because the effective (S/V) is smaller for long-lived than short-lived species because of the distance that species can diffuse before release and/or decay.

Effect on (R/B) on crossing the FGR threshold

Just as there is a threshold for stable FGR, the same threshold applies to radioactive fission gases. This was well demonstrated in IFA-558 where measurement of stable and radioactive FGR were made as the fuel was coaxed across the empirical threshold. The short lived species were analyzed to calculate the slope and recoil coefficients A and B and these are shown along with the centreline temperature, empirical threshold and stable fractional release in Figure 4. Here it can be seen that whenever the temperature crosses the threshold, there is a gradual increase in the fraction of stable gas released and a simultaneous increase in the coefficients A and B. Note also that when the temperature drops below the threshold, the coefficients also fall showing that the rate of radioactive fission gas release reduces. The behaviour of the radioactive species can be interpreted in terms of surface area, thus identifying the empirical threshold with the interlinkage of porosity along grain boundaries.

THE RELEASE OF RADIOACTIVE IODINE SPECIES

The release of radioactive iodine from irradiated fuel poses little problem as long as the integrity of the cladding is maintained, because the iodine contributes little to the internal pressurization of the fuel rod. The situation is radically changed in the event of clad failure, particularly if this is associated with a breach of the reactor containment as in this case, the escape of iodine can pose a radiological health hazard. The effects of radioactive iodine are generally described by the term 'Dose Equivalent Iodine' (DEI), which attempts to quantify the health hazard in terms of a weighted sum of the five radioactive iodine fission products. Approximately half of the DEI arises from ^{131}I so calculating this component of release in fault situations is of great importance.

The measurement of Radioactive Iodine

From an experimental point of view, the iodine isotopes of interest are ^{135}I, ^{133}I and ^{131}I with half lives of 6.72 hours, 20.9 hours and 8.04 days respectively. Iodine isotopes are solid except at high temperatures and are not transported through the unheated flow lines to the gamma detector. Assessment of their release therefore presents some problems and must be performed indirectly by measurement of their xenon decay products. The situation is further complicated by the fact that the decay products, ^{135}Xe, ^{135m}Xe, ^{133}Xe and ^{131m}Xe are themselves released in sufficient quantities as to render at-power measurement difficult. This situation is circumvented by exploiting the fact that production and release of the isotopes effectively ceases at reactor shut down. Any excess xenon detected after shut-down must have arisen from decay of iodine isotopes already released and plated out on cooler parts of the gas circuit. Therefore, at shut-down, the rods are flushed thoroughly to remove any xenon actually released as xenon. This is followed by a number of on-line flow measurements taken at intervals over the following 24 hours. In this way the release of ^{135}I and ^{133}I can be inferred from the ^{135}Xe, ^{135m}Xe and ^{133}Xe activity.

The determination of ^{131}I release is more complicated. 99% of its decay results in the stable ^{131}Xe isotope, the remaining 1.086% yields ^{131m}Xe which has a half life of 11.9 days and whose gamma energy is in close proximity to a strong gamma ray from the decay of ^{133}Xe (5.29 days half-life). The technique adopted exploits the different half-lives of the isotopes in the decay chain. If the rod is sealed, after 12-14 days, the concentration of ^{131m}Xe reaches a maximum and when swept out to the gamma detector, it can be distinguished from any residual amounts of ^{133}Xe and used to estimate the quantity of ^{131}I released immediately prior to shut-down. The requirement for a long shut-down for this measurement means that only a few estimates of ^{131}I release have been possible.

Iodine Diffusion Coefficient

The diffusion coefficient described in equation /5/ applies strictly to the rare gases krypton and xenon. During experiments immediately preceding those from which the diffusion coefficient was derived, Turnbull and Friskney [7] investigated the release from small samples of both rare gases and volatile species including caesium, tellurium and iodine. Here the released volatile species were trapped out on a 'cold finger' situated above the heated specimens during irradiation. This was removed at the end of each irradiation cycle and the

fission products collected and measured. At a specimen temperatures of ~1400-1500 °C it was found that to a good approximation both gaseous and volatile species were released from the fuel with identical kinetics, Figure 5. This study was extended by Friskney and Turnbull [8] to cover a wider range of temperatures, 770-1450 °C. Here, iodine diffusion coefficients derived from plate out measurements and from analysis of precursor mobility using the method of Friskney and Speight [9] were compared to those of the rare gases. They concluded that over this temperature range, there was no discernible difference between the diffusion coefficient for iodine and that for krypton and xenon. It appeared therefore that equation /5/ can be used equally for the release of iodine isotopes, and as will be seen in the next section, this conclusion has been substantiated and refined with data from Halden sweep gas experiments.

Data on Iodine release

In all, a total of 21 direct measurements of ^{131}I release were made from the Halden gas flow experiments and these are given in Table 1. The paucity of data is because of the difficulty in making these direct measurements. Because of this, a means of using data from the rare gases was devised in order to increase the ^{131}I database. In the early 1980s, Turnbull [10] analysed fission gas release from a number of swept fuel experiments and based on the results of the experiments discussed above, assumed that the release of ^{131}I was essentially by single atom diffusion and hence could be calculated by simply scaling by the square root of the ratio of the half-lives of a chosen gaseous fission product and ^{131}I. Since the longest lived rare gas for which reliable data were generally found was ^{85m}Kr with a 4.48 hour half life, this isotope was chosen for the calculation. The release to birth ratio (R/B) for ^{131}I could therefore be written as:

$$\left(R/B\right)_{131} = \left(R/B\right)_{85m} \times \sqrt{\frac{\lambda_{85m}}{\lambda_{131}}} \qquad /6/$$

This implies that (R/B) for ^{131}I is of the order of 6.56 times that for ^{85m}Kr.

From more recent studies using the Halden experiments, it is clear that this method contains a number of conservative assumptions:

1. The scaling process neglects the fact that ^{85m}Kr release is enhanced by rapid diffusion of its ^{87}Br precursor. This will not be the case for iodine isotopes.
2. The scaling process ignores the presence of a recoil release component, (eq. /4/).
3. Release of the shorter lived ^{85m}Kr is best described using all three of the diffusion coefficient contributions, $D_1 + D_2 + D_3$ in eq. /5/ whilst ^{131}I is best described using only $D_1 + D_2$.

The first assumption is relatively small and the second is easily corrected by replacing eq. /6/ with the following, using the nomenclature of eq /4/:

$$\left(R/B\right)_{131} = A + B\sqrt{\frac{1}{\lambda_{131}}} \qquad /7/$$

Figure 6 shows the results of comparing 'directly' measured (R/B) ^{131}I with that derived from ^{85m}Kr using the original scaling method, labelled 'K' and using eq. /7/ above, labelled 'R'. The results displayed in the figure confirm that both scaling methods are indeed pessimistic when compared with the actual measured values for ^{131}I. For the original scaling method, the predicted/measured statistics are P/M = 4.6 ×÷ 1.74 and for the recoil and slope scaling method P/M = 2.71 ×÷ 1.74. The revised method is clearly less pessimistic yet still overestimates by a factor approaching 3.

Correction for the difference in diffusion coefficient requires more computation and requires an estimate for the volume averaged temperature. In which case, with values of the coefficients A and B, derived from the rare gases, the equivalent fractional release for ^{131}I is given by:

$$\left(R/B\right)_{131} = A + B \times \sqrt{\frac{(D_1 + D_2)}{(D_1 + D_2 + D_3) \cdot \lambda_{131}}} \qquad /8/$$

This correction has been applied to the data for IFA-504 and IFA-558 and the results identified as the points 'D' included in Figure 6. For these P/M = 0.864 ×÷ 1.72, but if the lowest data point is removed, P/M = 1.26 ×÷ 1.62. This method is much closer to a best estimate evaluation with predicted values occurring either side of the 'true' value.

REVISION OF THE ANS 5.4 MODEL FOR CALCULATING RADIOACTIVE FISSION PRODUCT RELEASE

The current ANS 5.4 model is known to significantly overpredict the quantities of ^{131}I released into the fuel-clad interspace for intact fuel rods, with values closer to 10% than the <1% observed. The American Nuclear Society has therefore set up a Working Group to revise the model in the light of data now available. Such data are available from experiments performed at AECL Chalk River, CEA Grenoble and of course Halden, as described here.

For the purposes of developing and validating a new model, the Halden Project propose to make all their gas flow experimental data available. This will include direct measurements of iodine and (R/B) values derived from rare gas data corrected by 'recoil plus slope scaling' and the 'diffusion corrected scaling' methods described above. Both these methods have their own merits. The new method because it produces best estimate values and the recoil plus slope method because it produces systematically conservative values. In safety analyses it is preferable to provide pessimistic assessments rather than ones that are best estimate which could possibly underestimate release and its consequences. For this reason, it is suggested that the revised model should be developed and benchmarked against directly measured iodine release and data derived using the 'recoil plus slope' method.

REFERENCES

1. C. Vitanza, E. Kolstad and U. Graziani,: "Fission Gas Release from UO_2 Pellet Fuel at High Burn-up", ANS Topical Meeting on Light Water Reactor Fuel Performance, Portland, Oregon, 29 April-3 May, 1979.
2. M. V. Speight, Nucl. Sci. and Engineering, 37, 180, 1969.
3. R. Manzel, R. Eberle: "Fission Gas Release at High Burn-up and the Influence of the Pellet Rim", International Topical Meeting on LWR Fuel Performance, Avignon, France, April 1991.
4. E. Kolstad and C. Vitanza: "Fuel Rod and Core Materials Investigations Related to LWR Extended Burn-up Operation", J Nucl. Mater. 104-112, 188, 1992.
5. J. A. Turnbull, C. A. Friskney, J. R. Findley, F. A. Johnson and A. J. Walter: " The Diffusion Coefficient of Gaseous and Volatile Species during the Irradiation of Uranium Dioxide", J Nucl. Mater. 107, 168-184, 1982.
6. J. A. Turnbull, R. J. White and C. Wise: "The diffusion coefficient for fission gas atoms in uranium dioxide", Technical Committee Meeting on Water Reactor Fuel Element Computer Modelling in Steady-State, Transient and Accident Conditions, Preston England, 19-22 Sept. 1988.
7. J. A. Turnbull and C. A. Friskney: "The Relation between Microstructure and the Release of Unstable Fission Products during High Temperature Irradiation of Uranium Dioxide", J. Nucl. Mater. 71, 238-248, 1978.
8. C. A. Friskney and J. A. Turnbull: "The Characteristics of Fission Gas Release from Uranium Dioxide during Irradiation", J. Nucl. Mater. 79, 184-198, 1979.
9. C. A. Friskney and M. V. Speight: "A Calculation on the In-Pile Diffusional Release of Fission Products forming a General Decay Chain", J. Nucl. Mater. 62, 89-94, 1976.
10. J. A. Turnbull: "A Model for Calculating the Gap Inventory of 131I in Intact Fuel Rods", British Nuclear Energy Society Conference on Nuclear Fuel Performance, paper 56, Stratford-upon-Avon, 1985.

Table 1

Comparison between measured ^{131}I and release estimated from rare gas data by different methods

Rod	Burn-up MWd/kgUO2	Measured	85mKr scaling	Recoil + slope scaling	Diffusion corrected scaling
430-2	6.5	1.2E-4	1.6E-3	1.6E-3	
	7.7	3.8E-4	7.2E-4	7.2E-4	
	12.6	1.2E-3	3.8E-3	3.8E-3	
	16.9	1.2E-3	1.2E-2	1.2E-2	
504-1	9.3	1.2E-4	4.8E-4	2.7E-4	5.4E-5
	46.4	2.6E-3	1.1E-2	9.2E-3	4.87E-3
504-2	2.1	2.1E-4	1.2E-3	6.7E-4	2.8E-4
	9.3	1.5E-4	3.9E-4	2.6E-4	5.7E-5
	49.4	9.6E-4	8.7E-3	4.0E-3	1.57E-3
504-3	2.1	2.5E-4	5.9E-4	4.3E-4	1.9E-4
	9.3	1.2E-4	2.2E-4	1.4E-4	3.4E-5
	49.4	2.8E-3	9.4E-3	5.2E-3	4.5E-3
504-4	2.1	2.5E-4	1.3E-3	7.5E-4	2.4E-4
	9.3	1.2E-4	5.4E-4	5.0E-4	9.9E-5
	48.4	2.6E-3	1.3E-2	8.4E-3	1.6E-3
558-1	30.3	3.5E-4	1.2E-3	6.6E-4	4.8E-4
	31.9	5.7E-4	1.2E-3	8.1E-4	3.1E-4
	34.3	2.9E-4	1.3E-3	7.6E-4	3.4E-4
558-3	29.1	4.1E-4	1.9E-3	1.1E-3	5.9E-4
558-6	31.6	3.8E-4	1.5E-3	8.4E-4	3.1E-4
	33.9	2.7E-4	1.5E-3	8.4E-4	3.4E-4

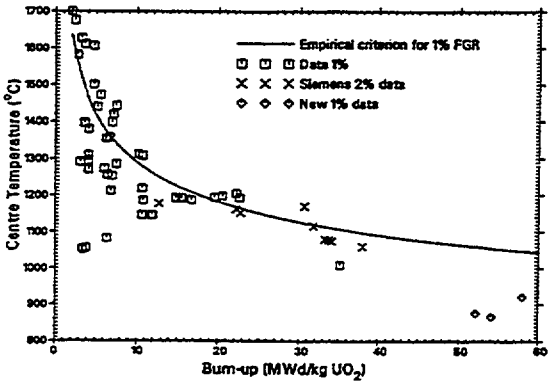

Figure 1 Empirical criterion for the onset of FGR and supporting data

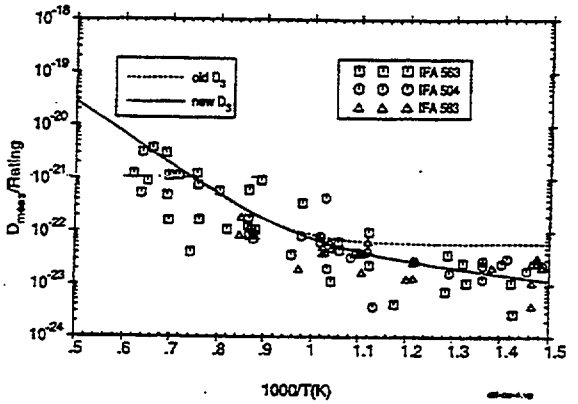

Figure 2 Revised formulation of low temperature term in the rare gas diffusion coefficient

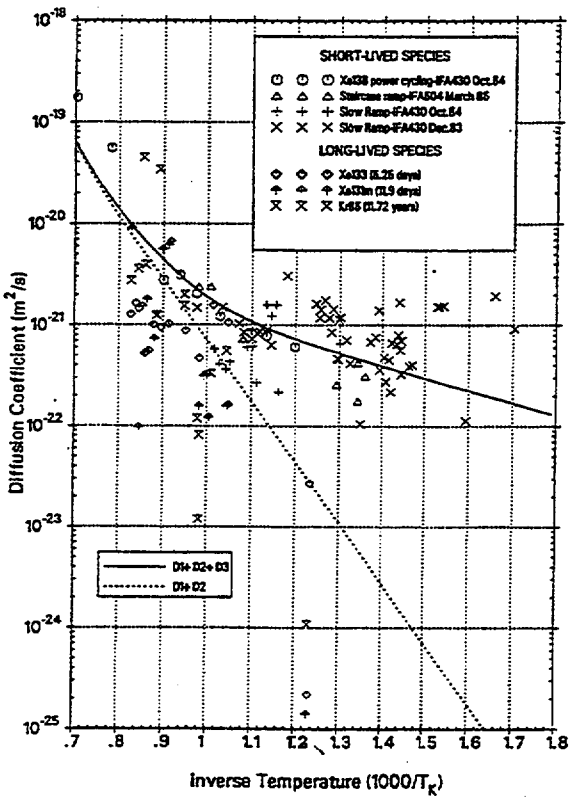

Figure 3 Diffusivity plot showing both short-lived and long-lived isotope release from Halden Gas Flow Rigs

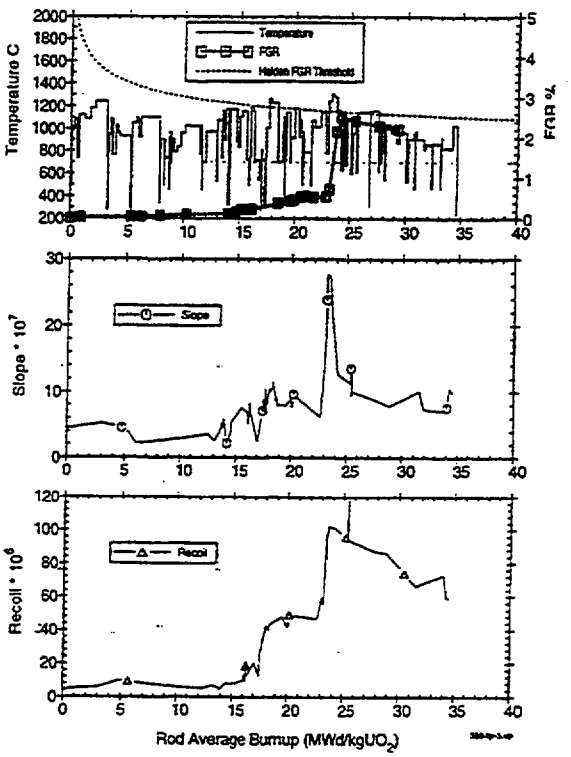

Figure 4 Fission product release data for IFA-558 showing stable FGR and short-lived parameters

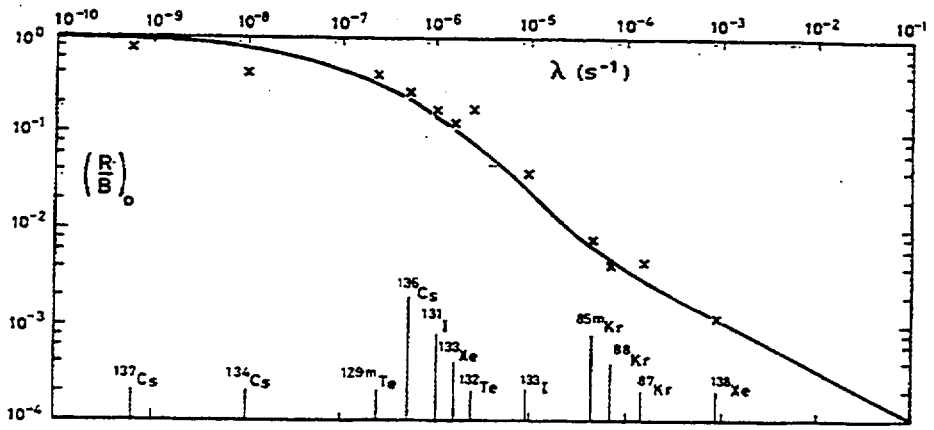

Figure 5 Fractional release: (R/B) for a range of gaseous and volatile fission products versus decay constant taken from reference [7]

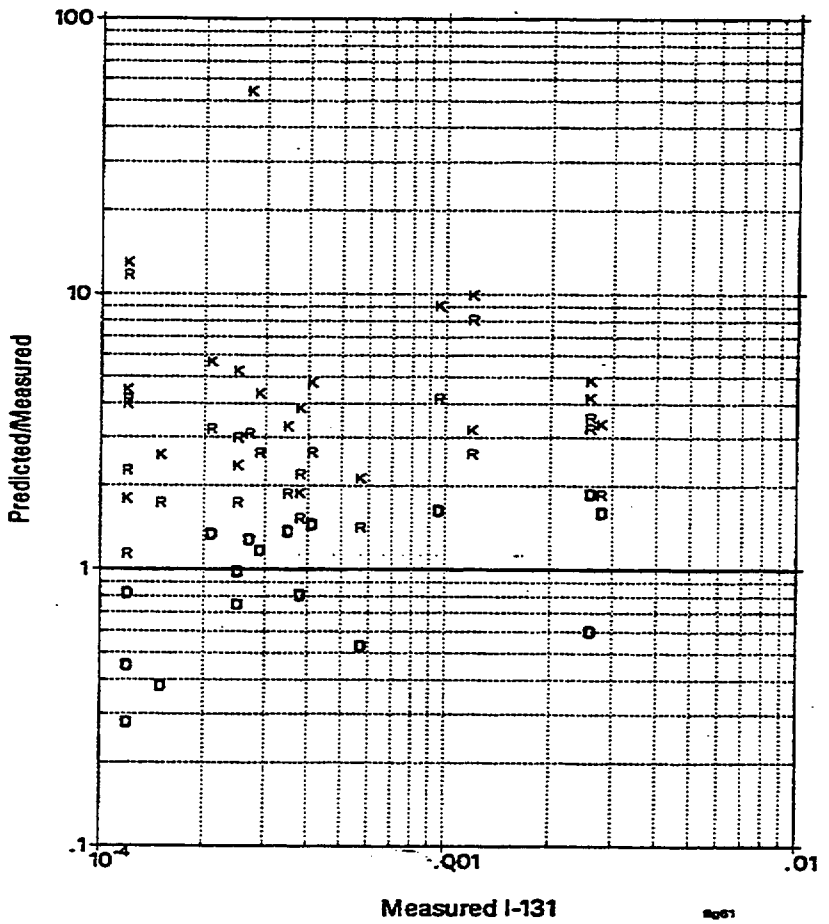

Figure 6 Values of predicted to measured ratio (P/M) for ^{131}I release using various methods of derivation from measured rare gas data as described in the text.

Short-Time Creep and Rupture Tests on High Burnup Fuel Rod Cladding

W. Goll / Siemens Nuclear Power GmbH,
E. Toscano / European Commission, JRC-Karlsruhe, ITU
H. Spilker / Gesellschaft für Nuklear-Behälter mbH

This study was performed by order and in co-operation with the German utilities.

1. Abstract

Short-time creep and rupture tests were performed to assess the strain potential of cladding of high burnt fuel rods under conditions of dry storage. The tests comprised irradiated corrosion-optimized Zry-4 cladding samples from fuel rods with burnups of up to 64 MWd/kgU and were carried out at temperatures of 573 and 643 K at cladding stresses of about 400 and 600 MPa. The stresses, much higher than those occurring in a fuel rod, were chosen to reach circumferential elongations of about 2 % within an envisaged testing time of 3-4 days. The creep tests were followed by a low temperature test at 423 K and 100 MPa to assess the long-term behavior of the cladding ductility especially with regard to the effect of a higher hydrogen content in the cladding due to the high burnup.

The creep tests showed considerable uniform plastic elongations at these high burnups. It was demonstrated that around 600 K a uniform plastic strain of at least 2 % is reached without cladding failure.

The low temperature tests at 423 K for up to 5 days revealed no cladding failure under these conditions of reduced cladding ductility. It can be concluded that the increased hydrogen content has no adverse effect on the cladding performance even at long storage times.

2. Introduction

The behavior of fuel assemblies (FA) under dry storage conditions was assessed about ten years ago. Over the last years, however, the discharge burnup of the FAs has been increased. Therefore, the Gesellschaft für Nuklear-Behälter mbH ordered new tests at Siemens AG. The tests were performed at the European Institute for Transuranium Elements (ITU), Karlsruhe, within the frame of a contract between Siemens AG and ITU.

The increased burnup will result in an increase in neutron fluence and corrosion layer thickness with higher hydrogen content as a consequence. Since the mechanical properties of Zircaloy change with neutron fluence and hydrogen content /1/, it is therefore necessary to confirm the cladding ductility of the fuel rods at this higher burnup level.

Whereas the irradiation hardening due to the neutron fluence shows saturation early during irradiation, the influence of the hydrogen on the cladding ductility has to be considered with increasing burnup.

Hydrogen is produced during the corrosion reaction and, with increasing oxide layer thicknesses, an increased amount of hydrogen is found in the cladding. If its solubility limit of e.g. about 150 ppm at operating temperature is exceeded, the hydrogen will precipitate as δ-ZrH platelets. Their orientation depends on texture and stress during precipitation /2/.

The creep tests were performed with the objective of reaching a hoop strain of about 2 % within several days, this means much faster than under conditions of dry storage but at comparable storage temperatures of 573 and 643 K.

Since at lower temperatures (< 520 K) the influence of the hydrogen on the cladding ductility is more pronounced than at higher temperatures, a test following the creep test was made to assess if there are any adverse effects in connection with the cooling down under dry storage conditions. Therefore, so called ductility tests were performed, in which the cladding was slowly cooled down to 423 K and held at a stress of 100 MPa for up to 5 days.

3. Materials

The cladding material used in the tests was prepared from two standard fuel rods (see Tab. 1) with an outer diameter of 10.75 mm and a wall thickness of 0.73 mm. The cladding consisted of corrosion-optimized Zircaloy-4 with 1.29 w/o Sn, 0.22 w/o Fe, and 0.12 w/o Cr. The annealing parameter was about $2.2 \cdot 10^{-17}$ h. In the as-fabricated state the cladding had a tensile strength of 776 N/mm^2 at room temperature and of 423 N/mm^2 at 673 K.

- **Manufacturing data:**

Cladding outer diameter	10.75	mm	
Cladding wall thickness	0.73	mm	
Alloying constituents	1.29	w/o	Sn
	0.22	w/o	Fe
	0.12	w/o	Cr
Annealing parameter	$2.2 \cdot 10^{-17}$ h		
Tensile strength	776	N/mm² (room temperature)	
	423	N/mm² (673 K)	

- **Irradiation data:**

	Rod A	Rod B	
Burnup (rod average)	54	64	MWd/kgU
Neutron fluence (>1 MeV)	9.5	$12.1 \cdot 10^{21}$	n/cm²

Tab. 1 Characteristic Data of the Irradiated Rods

The rods A and B were irradiated in a commercial PWR for four and five irradiation cycles up to rod average burnups of 54 and 64 MWd/kgU equivalent to neutron fluences of $9.5 \cdot 10^{21}$ and $12.1 \cdot 10^{21}$ cm^{-2} (E_n>1 MeV), respectively.

The irradiation behavior of the rods was deduced from non-destructive examinations performed on rod B and on comparable rods. The diameter change of rods from the same batch is shown in Fig. 1 as a function of the burnup. It can be seen that the cladding of rod A experienced a maximum diameter decrease of 0.8 - 0.9 %, whereas cladding of rod B was additionally strained back by about 0.2 %.

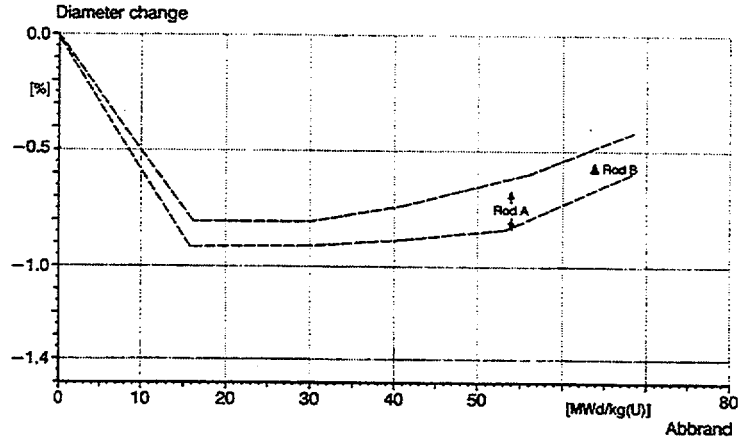

Fig. 1 Diameter Behavior of the Cladding During Reactor Operation

Fig. 2 shows the axial oxide layer profiles of the rods. The oxide layer of rod B was measured nondestructively by the eddy current technique and averaged over the rod circumference over an axial length of 40 mm. The axial oxide layer profile of rod A was estimated from a comparable oxide layer profile that was adjusted by means of oxide layer thicknesses obtained metallographically at three axial rod positions.

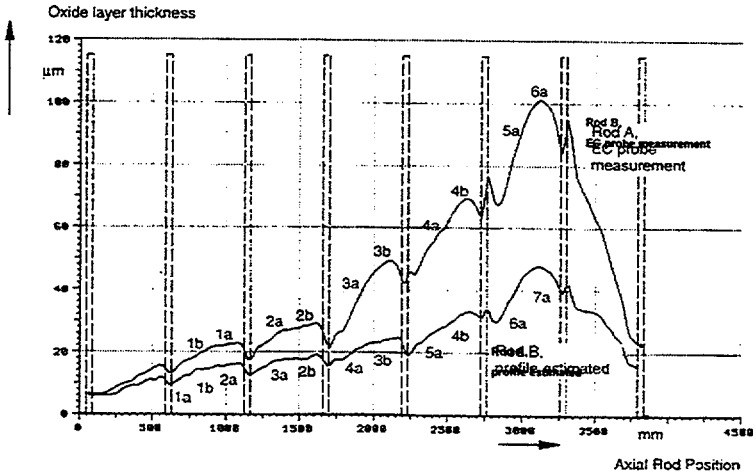

Fig. 2 Axial Oxide Layer Ticknesses of Rod A and B and Sample Positions

The 4-cycle rod A had an oxide layer thickness up to 47 µm and the 5-cycle rod B a layer thickness of up to 100 µm.

4. Experimental Setup

The creep tests were performed with a test device and a sample preparation technique that was developed and installed by the European Institute for Transuranium Elements (ITU) at Karlsruhe.

The creep test samples were cut from the rods A and B with a sample length of 170 mm. The fuel was removed mechanically by means of a commercial drilling machine (see Fig. 3). The diameter of the drilling tool was optimized to remove a maximum amount of fuel, without scratching the cladding to avoid possible crack initiation. After removal of the fuel the sample was shortened to cut cladding regions possibly damaged by the clamping of the drilling machine. The test samples were then 150 mm in length which, taking into account the grip length, ensures an unsupported length of about 100 mm. The sample was filled with steel mandrels to minimize the energy inventory of the oil. Both ends were closed with high precision plugs and seals. In order to screw the fittings to the sample, a special machine was developed based on a pneumatic wrench able to perform a sufficiently strong but smooth tightening of the fittings.

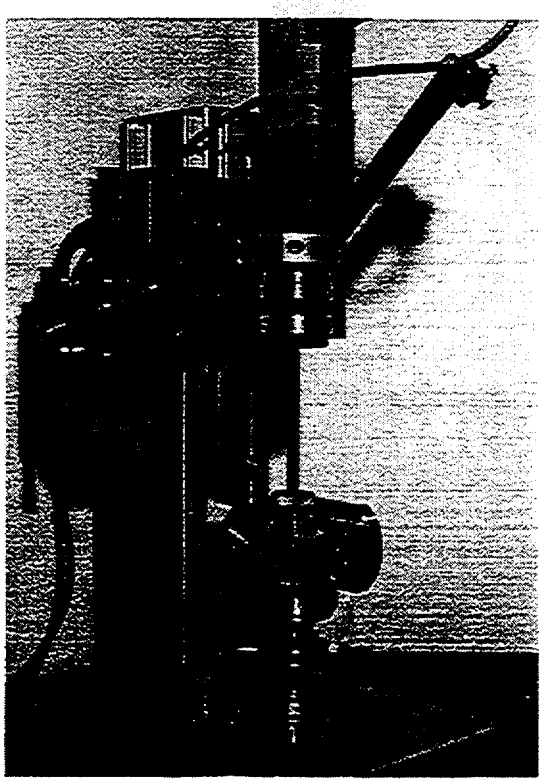

Fig. 3 Removal of the Fuel with a Drilling Device

In Fig. 4 the scheme of the measurement device is shown. The sample was pressurized with oil and heated in a furnace. A uniform sample temperature was assured by using a furnace with three heating zones and an internal double wall lining containing Cs. The temperature gradient over the whole sample length amounted to only ± 0.2 K. To achieve oil pressures of more than 100 MPa an intensifier piston was used. The device was controlled by a data sampling system, which allowed the temperature, pressure and displacement of the intensifier piston to be monitored and to be stored at preset time intervals. The displacement of the intensifier piston could be calibrated to obtain the strain of the sample during testing. Additionally, the diameter of the sample was measured before and after testing by means of two knives connected to a linear variable differential transformer (LVDT). The sample was measured azimuthally every 45° and axially every 5 mm. The plastic hoop strain of the sample was calculated from both measurements.

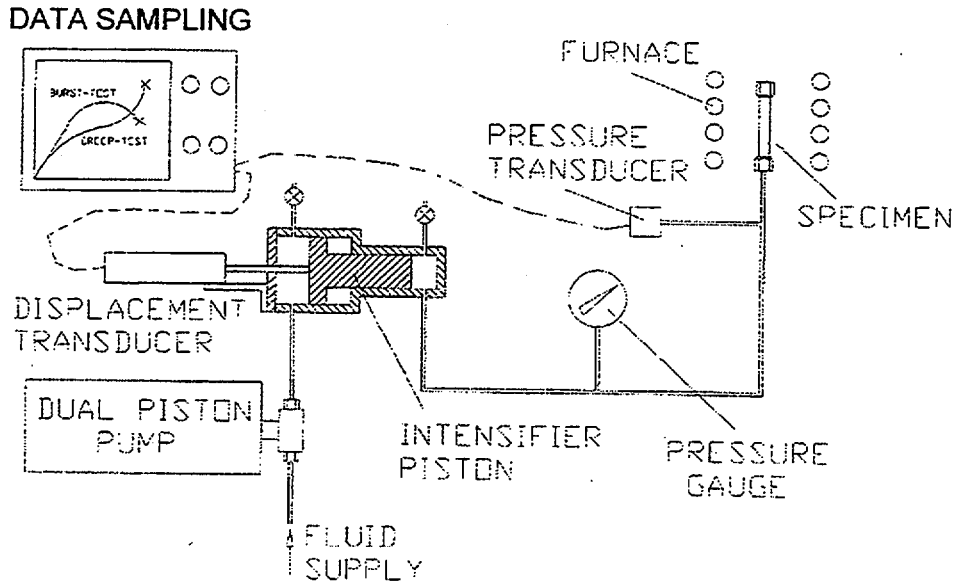

Fig. 4 Schematic Measurement Device

5. Tests

Fig. 5 shows the schematic sequence of the tests for a maximum temperature of 643 K. The test with a maximum temperature of 573 K was carried out in the same way. Both tests were designed to reach a plastic hoop strain of about 2 % within 3 to 4 days. The appropriate pressure was estimated and the sample pressurised with a rate less than 35 MPa/min. Having reached this estimated pressure, the strain rate was determined from the change of the oil inventory and the pressure corrected if necessary.

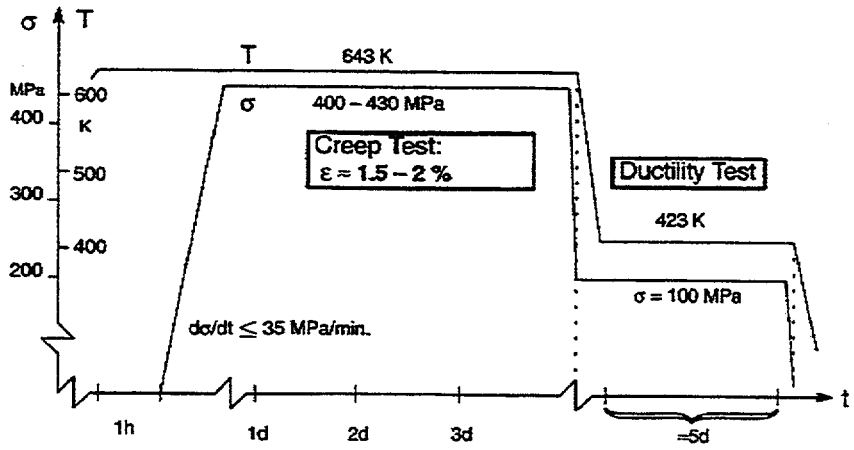

Fig. 5 Testing Sequence

In case of intact samples, the creep phase was followed by a ductility test at 423 K and reduced pressure (100 MPa). The ductility test was planned to last up to about 5 days.

6. Results

The results of the creep tests on the rods A and B are presented in Tabs. 2 and 3. The cladding stress needed to achieve the required creep rate was in the range of 400 to 430 MPa at 643 K and of about 600 MPa at 573 K. At 643 K the samples reached uniform plastic elongations between 0.3 and 7.4 %. The low value of 0.3 % resulted from an early defect in the clamping region. At 573 K the range of uniform plastic elongation was 1.0 to 3.5 %. In this case of low temperature, it was difficult to maintain the tightness of the clamping for a sufficient long time.

Rod-Designation	Test Conditions		Uniform Plastic Elongation	Ductility Test 100 Mpa, 423 K	Comment
	Stress MPa	Time h	%	Time h	
	Temp. 643 K				
A_1a	320	72	4.5	90	Sample intact
A_2a	430	30	7.4	100	Sample intact
A_3a	430	2	0.3		Clamping failed
A_4a	430	54	4.2	62	Sample intact
A_5a	400	129	≈ 6*		Sample failed
A_6a	410	74	2.3	89	Sample intact
A_7a	410	67	≈ 4.5*		Sample failed
	Temp. 573 K				
A_1b	630	65	1.2		Clamping unstable
A_2b	620	44	1.0	109	Sample intact
A_3b	620	189	2.4	26	Sample intact
A_4b	620	69	3.5	92	Sample intact

* averaged over intact region

Tab. 2 Results of the Creep Tests on Rod A Samples

Rod-Designation	Test Conditions		Uniform Plastic Elongation	Ductility Test 100 Mpa, 423 K Time	Comment
	Stress MPa	Time h	%	h	
	Temp. 643 K				
B_1a	400	100	2.5	90	Sample intact
B_2a	400	124	3.1	63	Sample intact
B_3a	420	111	4.1	119	Sample intact
B_4a	410	137	4-6*		Sample failed
B_5a	400	88	≈ 5*		Sample failed
B_6a	410	55	3.0		Sample failed
	Temp. 573 K				
B_1b	620	143	1.9	120	Sample intact
B_2b	620	143	1.1	97	Sample intact
B_3b	620	119	1.4		Defect near clamping
B_4b	630	13	> 2.5		Repaired sample failed

* averaged over intact region

Tab. 3 Results of the Creep Tests on Rod B Samples

The results are plotted in Fig. 6. It can be seen that no cladding failure occurred below 2 % uniform plastic strain. Above 2 % elongation, rupture was observed on six out of fifteen samples. Before failure, the elongation vs. time curve derived from the oil inventory, always showed that the samples were in ternary creep stage. This is an indication for high local ductility of the cladding. A systematic influence of oxide layer and hydrogen content on the creep behavior was not detected.

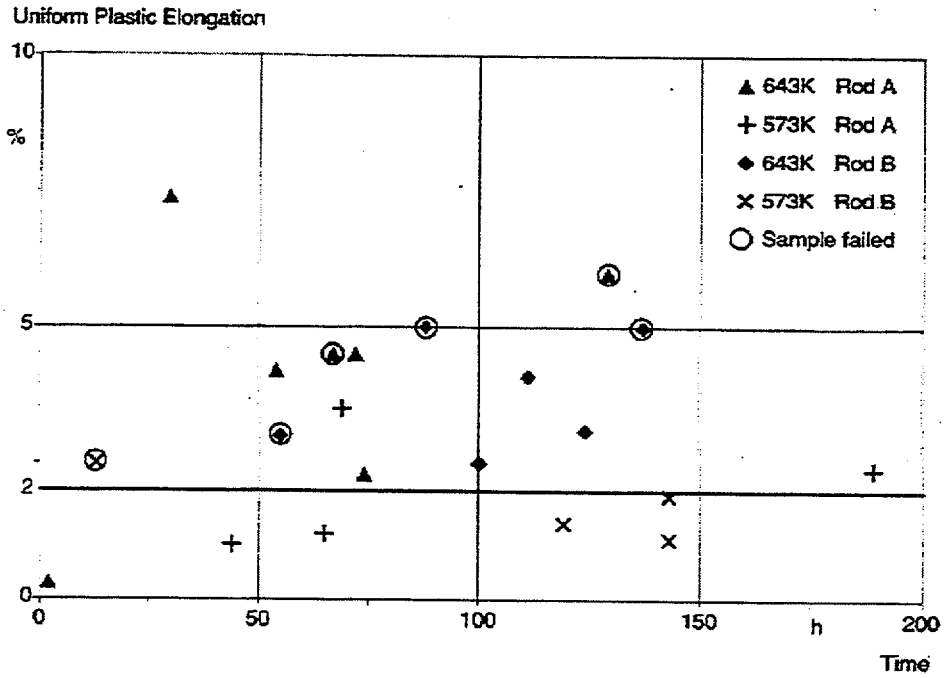

Fig. 6 Results: Uniform Plastic Strain

All intact samples were submitted to a ductility test at 423 K to test the influence of the hydrogen at low temperatures and the effects of cladding stresses comparable to those found in high burnup rods due to their internal pressure. All samples tested remained intact.

The behavior of the hydrogen in the cladding was investigated by metallographic examinations performed after testing. Fig. 7 shows the hydride distribution of the intact sample A_3b tested at 573 K. The tangentially oriented platelets reflect the typical distribution immediately after discharge from the reactor.

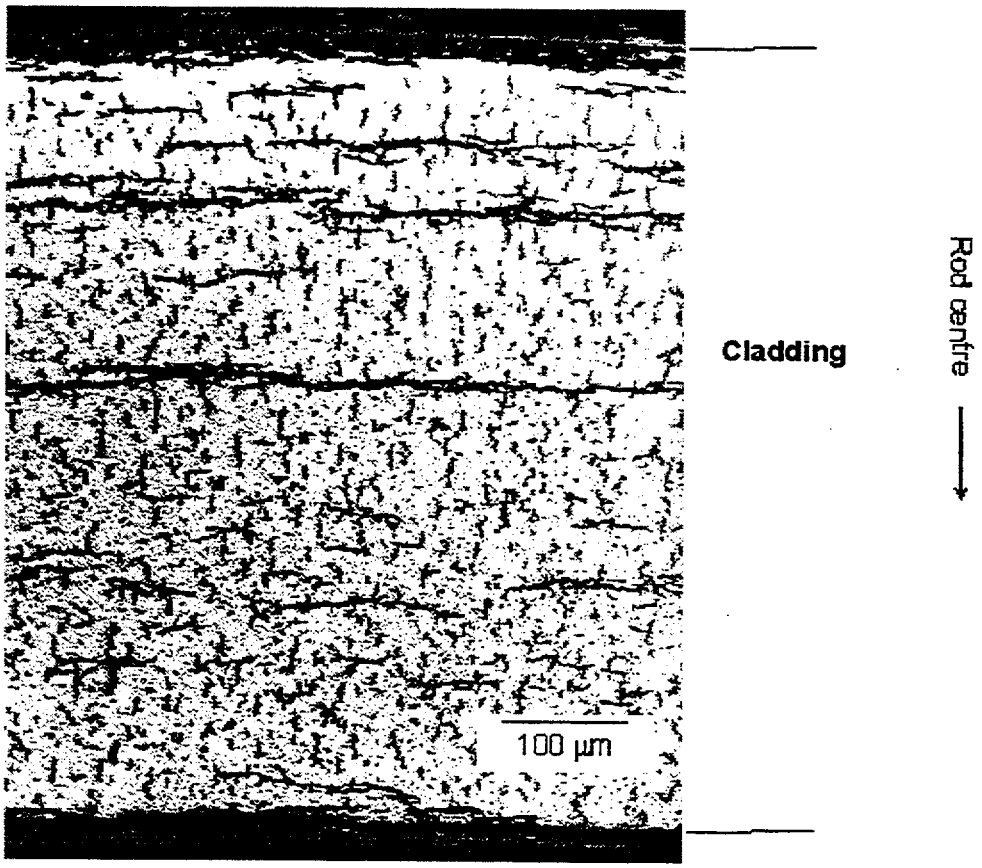

Fig. 7 Metallographic Examination of Sample A_3b after 573K-Creep and 423K-DuctilityTesting

During testing at 573 K part of the platelets was dissolved and precipitated under stress (100 MPa) during the cool down phase of about 3 h to the ductility test. This led to the precipitation of radially oriented platelets, however, without cladding failure.

7. Conclusions

The results of the short-time creep-rupture tests can be summarized as follows:

- The creep tests performed at 400 to 600 MPa and 600 K demonstrated that rods with burnups of up to 64 MWd/kgU and corrosion-optimized Zircaloy-4 cladding types can withstand **uniform plastic strains of at least 2 % without failure.** Above 2 % uniform plastic strain 6 out of 15 samples failed under these conservative short-time conditions. However, all ruptures occurred after the onset of the ternary creep phase indicating a considerable local cladding ductility.

- The ductility tests performed at 423 K at cladding stresses of 100 MPa showed **no failure even if radially oriented hydrides occurred.** This is in agreement with other findings on crack propagation /2,3/. Since the hydrogen was precipitated in the cladding during several hours, the tests were far away from a quenching situation and can be regarded as representative for even longer cooling down times.

8. Literature

/1/ W. Jahreiß, R. Manzel, E. Ortlieb
'Einfluß des Wasserstoffgehaltes und der Bestrahlung auf das mechanische Verhalten von Brennelementstrukturteilen aus Zircaloy',
Jahrestagung Kerntechnik '93, 25. - 27. Mai 1993, Seite 303 ff.

/2/ D.O Northwood and U. Kosasih
'Hydrides and delayed hydrogen cracking in zirconium and its alloys'
International Metals Reviews, 1983, Vol. 28, No. 2

/3/ M. Peehs, F. Garzarolli and W. Goll,
'Assessment of Dry Storage Performance of Spent LWR Fuel Assemblies with Increasing Burn-up', International Symposium on Storage of Spent Fuel From Power Reactors, Vienna, 9 - 13 November 1998

Definition and Status of the CABRI International Program for High Burn-Up Fuel Studies

J. Papin, J-C. Melis

Institut de Protection et de Sûreté Nucléaire
Département de Recherches en Sécurité
CE-Cadarache
13108 St Paul-lez-Durance
France

C. Lecomte

Institut de Protection et de Sûreté Nucléaire

Avenue du Général De Gaulle
92140 Clamart
France

Abstract

Following the CABRI-REP Na program initiated in the early 90s, the CABRI-PWL program is now prepared in the frame of a broad international cooperation with the aim to provide data and knowledge for high burn-up advanced fuels submitted to a reactivity initiated accident under more representative reactor conditions.

Twelve tests are foreseen, the two first being planned in 2002 in the CABRI sodium loop allowing obtainment of preliminary results on advanced fuels, the other ten being scheduled in the years 2005-2007 after renewal of the CABRI facility. These tests will be associated to clad mechanical characterization providing a complete data set for different fuel types tested in similar conditions.

The CABRI PWL program will allow establishing data under more representative reactor conditions that will provide the industry and their respective regulatory agencies with the necessary knowledge for further fuel management evolutions.

1 / Introduction

Economic considerations are currently leading most utilities to increase the burn-up of the UO_2 fuel in their power plants. For instance in France, Electricité de France (EdF) has recently received authorization from the safety authority to burn its fuel up to 52 GWd/t (fuel assembly average) and anticipates a further burn-up increase to 60 GWd/t in future years.

For the same economic considerations, some utilities have introduced mixed-oxide (MOX) fuel. EdF for example has been using MOX fuel for ten years and the next short-term objective is to reach similar high burn-up level in MOX and UO_2 assemblies in the new fuel management strategies ("Parité MOX").

One of the key requirements when increasing burn-up has been the need to improve cladding resistance to corrosion. This has led to the development of new cladding alloys like ZIRLO, M5 and Duplex. However, the increase of burn-up and the introduction of MOX fuel have also created a need to (a) verify the adequacy of safety criteria that were previously defined for lower fuel burn-up, or to modify those criteria, (b) demonstrate good behavior of the fuel during normal operation and during design-basis

accidents such as loss-of-coolant accidents (LOCAs) and reactivity-initiated accidents (RIAs) and (c) evaluate the safety margins.

With this background, the "Institut de Protection et de Sûreté Nucléaire" (IPSN) initiated a research program in 1993, called Cabri-REP-Na, to study the behavior of high-burn-up UO_2 and MOX fuel under RIA conditions. This program was conducted in collaboration with EdF and with participation of the USNRC. It has led to a significant improvement of the knowledge on high burn-up fuel behavior during RIA transients [1] [2] [3].

However, the remaining questions resulting from lack of representative conditions and the need to assess the behavior of advanced fuels in prototypical PWR conditions led the IPSN to propose an international RIA program in the CABRI reactor equipped with a Pressurized Water Loop (called CABRI-PWL program) which is described hereafter.

2 / Background and objectives of the CABRI PWL program

In the early 90s, the utility's request for authorization to increase burn-up in the French PWRs led to a need of extension of the RIA data base which had been previously established for fresh or low irradiated UO_2 fuel (~ 30 GWd/t) and resulted from SPERT and PBF testing programs.

As a first step of investigation in France, the CABRI REP Na experimental program has been launched in the sodium loop of the CABRI reactor [4] in which consequences of a fast power transient applied to a single fuel rod could be studied in a sodium coolant environment.

From 1993 to 1998, seven tests with UO_2 fuel and three tests with MOX fuel have been performed using mostly refabricated rods from PWR fuel, with low internal pressure (0.3 MPa He pressure, consistent with sodium channel pressure).

The following parameters were studied:

- rod burn-up from 33 to 64 GWd/t,
- cladding corrosion thickness from 4 to 130 μm of ZrO_2,
- corrosion conditions from uniform to spalled with hydride blisters resulting from reactor operation,
- power transients starting from almost zero power to different energy levels and with various pulse widths leading to different energy injection rates.

In parallel to the REP-Na experiments, the SCANAIR code [5] was developed in order to interpret the test results, perform sensitivity studies and translate the results to reactor conditions.

Separate-effects tests are also being conducted for the study of the cladding mechanical properties (PROMETRA [6]), the clad-fluid heat transfer under fast transients (PATRICIA) and the transient behavior of fission gases (SILENE-RIA).

The lack of adequacy of the present safety criteria for high burn-up UO_2 and MOX fuel was evidenced through the REP-Na tests which led to rod failure at enthalpy levels from 30 to 120 cal/g (radial

average). Similar conclusion was derived from tests performed in the NSRR facility in Japan and showing low energy failure of high burn-up UO_2 fuel.

Key parameters influencing the fuel behavior were also identified through this program such as cladding corrosion associated to oxide spalling, energy injection rate (pulse width), contribution of fission gases on clad loading [7]. The possibility of transient oxide spalling above certain corrosion thickness has also been evidenced and could lead to potential local departure from nucleate boiling in water conditions.

The CABRI-REP Na program has provided key results supporting the licensing authorization given to EDF to increase the fuel burn-up up to 52 GWd/t (mean assembly); nevertheless, questions still remain in order to understand the effect of DNB on cladding failure, the influence of internal rod pressure, and the possibility of fuel-coolant interactions after failure.

The complexity of these phenomena and their important coupling make it difficult to extrapolate the current results to higher burn-up without experimental confirmation with integral tests under representative PWR conditions. Moreover, lack of representativity was also identified in separate effects tests such as the PROMETRA mechanical program under RIA conditions, preventing reliable prediction of the rod behavior on the sole basis of such separate effects experiments at the present time. Thus, prototypical PWR conditions are particularly important for the qualification of any further fuel burn-up increases in power reactors.

These are the reasons why IPSN has decided to replace the present sodium loop in Cabri with a pressurized water loop (PWL) and to propose an international program called Cabri-PWL.

Twelve tests have been proposed for the Cabri-PWL program; they include high burn-up fuel tests combined with mechanical tests in order to provide the necessary understanding to extrapolate to a broad spectrum of reactor conditions. Six test series have been identified:

- S0 - two tests in the sodium loop using advanced fuels (rods with Zirlo and M5 cladding already committed)
- S1 - two tests in the water loop with the same advanced fuels in order to provide a link to Cabri-REP-Na tests
- S2 - tests with ultra high burn-up fuel (80-100 GWd/t, one DUPLEX rod committed)
- S3 - tests specifically designed to improve the understanding of RIA phenomena
- S4 - tests with MOX fuel
- S5 - complementary tests (open)

It is to be noticed that, among these tests, the first test to be realized in the pressurized water loop will contribute to the qualification of the loop and therefore will be defined with a particular attention.

These integral tests will be coupled with separate-effect tests (mechanical testing, fission gas behavior experiments) and code development to facilitate translation to power reactor conditions, development of safety criteria or limits and evaluation of the safety margins.

3 / The status of the CABRI-PWL program

* Test facility and planning

In the frame of the CABRI-PWL program and in view of additional long term needs, the lifetime of the CABRI reactor, originally built in 1962, will be extended for at least fifteen years, through a complete renovation associated with the implementation of the pressurized water loop.

At the present time, the test facility is operating with the sodium loop and will be shut down in early 2001 after the realization of two RIA tests in 2000 using one UO_2 5 cycles rod with M5 cladding and one MOX 5 cycles rod with standard Zr4 cladding.

However, taking into account the urgent needs from the utilities and safety experts for evaluation of the very high burn-up advanced fuels, an experimental window will be opened in 2002 allowing the performance of the S0 series of the CABRI-PWL program and potential domestic tests.

The reactor will then be shut down in 2003-2004 for completion of the renovation and installation of the water loop. Completion of the ten tests (series S1-S5) in the Cabri-PWL program will take place in 2005-2007.

At the present time, the detailed design of the water loop is drawn and the preparatory work for safety authorizations is underway. The design of the test section is also drawn. The first step of renovation work is prepared and work will be initiated beginning 2001.

In parallel, the change from sodium to pressurized water coolant led to initiate intensive R&D work for the use of sensors with fast transient response and ability to operate in reactor under high temperature and water pressure. The objective is to implement high quality measurement devices allowing reliable quantification of the studied phenomena, thus enabling physical understanding and models development with focus on: transient fuel and clad deformations, rod failure detection and mechanisms, fission gas release kinetics and contribution to clad loading, clad spalling occurrence, DNB occurrence and post-DNB behavior, and post-failure events (fuel dispersal, fuel coolant interaction, fission gas escape and mechanical energy release).

* Organization of the CABRI-PWL project

The CABRI-PWL program is now being settled as an international program due to its commonly agreed objectives; it will gather the scientific and industrial community involved in high burn-up fuel studies.

Two complementary agreements are proposed to the international community in order to provide consistency as well as flexibility with respect to each partner:

- an Umbrella agreement, established under the auspices of OECD ; it will provide the common governing rules of the Project and is structured in a manner similar to other OECD-NEA projects (Steering Committee and Technical Advisory Group) ;

- bi-lateral agreements which will contain the financial provisions agreed upon with each Project participant as well as specific forms of participation.

In the frame of bilateral agreements, the access to the CABRI-REP-Na tests performed with UO_2 fuel until 1998 will be provided, as well as the SCANAIR code.

At the present time, thirteen countries (represented by both safety organizations and industry) have expressed their intention to participate to the CABRI-PWL program during the OECD start-up meeting of December 99, and some of them have already signed the Umbrella agreement.

Bilateral agreements are also under elaboration and one of them has been signed.

In the frame of the TAG meetings, which already started in 2000, intensive technical discussions are underway for the precise definition of the test matrix and the choice of the fuel rods. In addition, an associated out-of-pile clad mechanical testing program and pre- and post-test examination programs are being defined inside the whole project in order to get the appropriate data for interpretation of the results.

This will constitute a key feature of the CABRI-PWL program dealing with different types of advanced fuels tested in similar conditions and in international context.

4 / Conclusion

Following the CABRI-REP Na program initiated in the early 90s, the CABRI-PWL program is now prepared in the frame of a broad international cooperation with the aim to provide data and knowledge for high burn-up advanced fuels submitted to a reactivity initiated accident under more representative reactor conditions.

One of the key features of this program is that different advanced fuel rods will be tested in similar conditions by out-of-pile and integral CABRI in-pile experiments, and the results will be discussed within the international partners of the program.

The CABRI PWL program will therefore allow establishing validated data under more representative reactor conditions that will provide the industry and their respective regulatory agencies with the necessary knowledge for further fuel management evolutions.

References:

[1] "French Studies on High-Burnup Fuel Transient Behavior under RIA Conditions," J. Papin et al, *Nuclear Safety*, Vol. 37, 1996, pp. 289-327.

[2] "High burn-up effects on fuel behavior under accident conditions: the tests CABRI REP Na" F. Schmitz and J. Papin, J. Nucl. Mater., 270 (1999) 55-64

[3] "Further results and analysis of MOX fuel behavior under reactivity accident conditions in CABRI" J. Papin, F. Schmitz, B. Cazalis, 27th WRSM, October 1999, Bethesda, USA

[4] "SURA: a Test Facility to Investigate the Safety of LMFBR and PWR Fuels," C. Marquie et al, IAEA International Symposium on Research Reactor Utilization, Lisbon, 1999.

[5] "Status of development of the SCANAIR code for the description of fuel behavior under reactivity initiated accident", E. Féderici, F. Lamare, V. Bessiron and J. Papin, International Topical Meeting on Light Water Reactor Fuel Performance, Park City, Utah, April 10-13, 2000.

[6] "The PROMETRA programme: assessment of mechanical properties of Zircaloy 4 cladding during an RIA", M. Balourdet, C. Bernaudat, V. Basini and N. Hourdequin, SMIRT-15 meeting, Seoul, Korea, August, 1999

[7] "The role of grain boundary gases in high burn-up fuel under reactivity initiated accident", F. Lemoine, J. Papin, JM. Frizonnet, B. Cazalis, H. Rigat, International Seminar on Fission Gas Behavior in Water Reactor Fuels, September 26-29th 2000

HIGH BURNUP BWR FUEL RESPONSE TO REACTIVITY TRANSIENTS AND A COMPARISON WITH PWR FUEL RESPONSE

Toyoshi FUKETA, Takehiko NAKAMURA, Kazuyuki KUSAGAYA
Hideo SASAJIMA and Hiroshi UETSUKA
Department of Reactor Safety Research
Japan Atomic Energy Research Institute
Tokai-mura, Ibaraki-ken, 319-1195 JAPAN

The NSRR experiments, FK-6 and FK-7, with 61 MWd/kgU BWR fuels resulted in significant cladding failure and fuel dispersal. The results indicate that an intense PCMI loading due to tight pellet-cladding bonding, radially oriented hydride clusters in the cladding, possible reductions of cladding ductility and fracture toughness caused crack initiation, propagation and fuel failure. Due to the PCMI loading mechanism with the tight pellet-cladding bonding and cladding failure with very small strain, small differences in size of pulse could give different failure energy in subsequent FK-9. The FK test series indicates that fission gas release during pulse-irradiation is strongly influenced by base-irradiation conditions in BWR.

I. INTRODUCTION

To study fuel behavior under reactivity-initiated accident (RIA) conditions, we have performed more than sixty experiments in the Nuclear Safety Research Reactor (NSRR) with irradiated LWR fuel rods since 1989. Among twenty-two PWR fuel experiments,[1-4] four tests at burnups of 48 to 50 MWd/kgU resulted in fuel failure and provided key information regarding hydride-assisted pellet-cladding mechanical interaction (PCMI) failure,[4,5] fuel dispersal and mechanical energy generation. Fuel failure has not been observed in all of ten BWR fuel experiments[6,7] at burnups up to 56 MWd/kgU, but three of four BWR fuel experiments at a burnup of 61 MWd/kgU resulted in significant cladding failure and fuel dispersal.

II. TEST FUEL RODS AND PULSE-IRRADIATION CONDITIONS

The NSRR program for irradiated BWR fuels includes two series of experiments; TS test series[6] with 7x7 rods at a burnup of 26 MWd/kgU and subsequent FK test series at burnups of 41 to 61 MWd/kgU. Table 1 shows a test matrix of the FK test series. In the first five tests, FK-1 through FK-5, cladding failure did not occur. Tests FK-1, FK-2 and FK-3[7] were conducted with 8x8BJ Step I type rods with Zr-liner cladding at burnups of 41 to 45 MWd/kgU irradiated for 5 cycles in the 1st Fukushima plant unit 3. The subsequent two tests, FK-4 and FK-5,[8] used 8x8 Step II type rods with Zr-liner cladding at a burnup of 56 MWd/kgU irradiated for 4 cycles in the 2nd Fukushima plant unit 2.

The test fuel rods in the FK-6 through FK-9 were the same type of rod as FK-4 and FK-5 but were irradiated for 5 cycles in the same unit, and the burnup reached 61 MWd/kgU. Linear heat rate during the

irradiation in the BWR reached 35.1 kW/m at a peak, and decreased to 8.9 kW/m at the end of the last cycle. It should be noted that the linear heat rate during the last cycle was very low and only 10.9 kW/m at maximum. Oxide layer formed in the cladding outer surface during base-irradiation in the BWR was about 20 μm in thickness, and hydrogen absorbed into the cladding was less than 140 ppm. Fission gas release during the irradiation in the BWR was 14% in mother rod of FK-6 and FK-7, and 12% in that of FK-8 and FK-9. Figure 1 shows schematics of the test fuel rod in FK-6 through FK-9. As-fabricated Zircaloy-2 cladding with zirconium linear has outer diameter of 12.27 mm and thickness of 0.86 mm, and radial gap between fuel pellet and cladding inner surface was 0.1 mm.

In the test FK-6 and FK-7 the maximum pulse available in the NSRR was used. The expected peak fuel enthalpies were 548 J/g (131 cal/g) and 540 J/g (129 cal/g), respectively. A difference between FK-6 and FK-7 in terms of test conditions was the initial rod internal pressure, 0.1 MPa for FK-6 and 1.5 MPa (simulating EOL gas pressure) for FK-7. In the FK-8 and FK-9 a smaller and wider pulse was used and tests rods were pressurized to 1.5 MPa. In the four tests, FK-6 through FK-9, cladding surface and coolant temperatures, rod and capsule internal pressures were measured during the pulse-irradiations. Sensors for cladding and pellet stack axial elongations were installed in FK-6. Instead of the elongation sensors, water column velocity sensor was used in FK-7 through FK-9 in order to evaluate mechanical energy generation[9] following to cladding failure.

Table 1 NSRR/High burnup BWR fuel tests (FK test series)

Test ID	Test Fuel	Fuel Burnup (MWd/kgU)	Fill gas pressure of test rod (MPa)	Peak Fuel Enthalpy (J/g)	Result
FK-1	BWR, 8x8BJ Step I, 5 cycles Zr-liner	45	0.3	544	No failure
FK-2		45	0.3	293	No failure
FK-3		41	0.3	607	No failure
FK-4	BWR, 8x8 Step II, 4 cycles Zr-liner	56	0.5	586	No failure
FK-5		56	0.5	293	No failure
FK-6	BWR, 8x8 Step II, 5 cycles Zr-liner	61	0.1	548	Failed at 293 J/g (70 cal/g), 100% fuel dispersed
FK-7		61	1.5	540	Failed at 260 J/g (62 cal/g), 100% fuel dispersed
FK-8		61	1.5	272	No failure
FK-9		61	1.5	389	Failed at 360 J/g (86 cal/g), 100% fuel dispersed

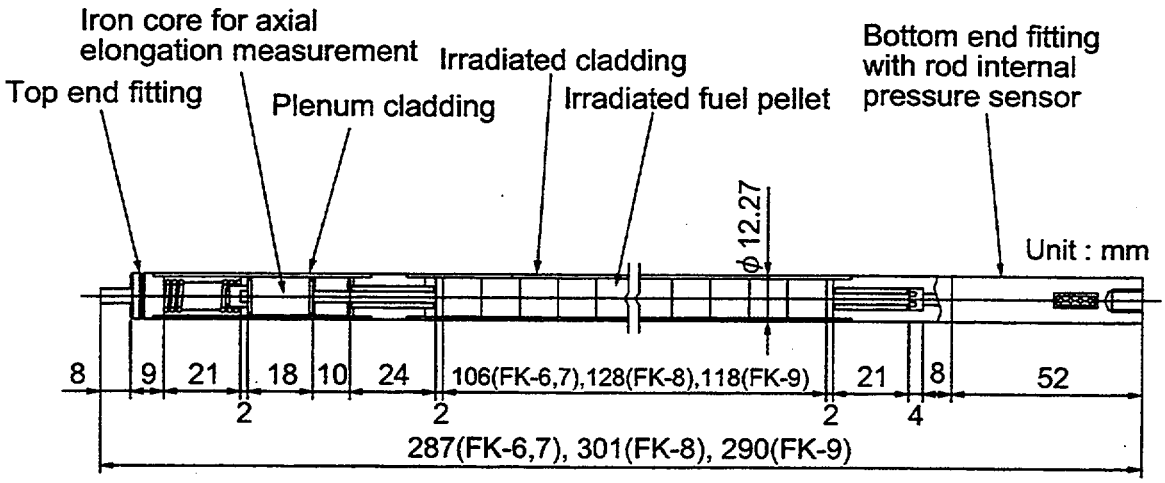

Fig. 1 Test fuel rod in FK-6 through FK-9.

III. FUEL FAILURES IN FK-6 AND FK-7

The Step-II fuel rods in FK-4 and FK-5 have a narrower pellet-to-cladding gap and higher fuel density than in the Step-I rods in FK-1 through FK-3. General behavior of the Step-II rods in FK-4 and FK-5, however, was quite similar to that of the Step I rod. The cladding conditions of the Step-II rods in terms of oxide thickness and hydrogen content were similar to those of the Step-I rod, about 20 μm oxide and 60 ppm hydrogen. The cladding was ductile enough to survive PCMI loading during the pulse-irradiation in the FK-1 through FK-5. Figure 2 shows residual hoop strain of un-failed cladding in experiments FK-1 through FK-5, tests TS, and PWR fuel experiments as a function of peak fuel enthalpy. Residual hoop strain in BWR experiments increases at a higher enthalpy level and is much smaller than in PWR fuels. The wider pellet-to-cladding gap due to the smaller creep down in BWRs could cause the PCMI loading to be milder than in the 50 MWd/kgU PWR fuel experiments.

Extensive bonding, however, occurred between the Zr-liner and the fuel pellets in the Step-II rods with a higher burnup of 61 MWd/kgU, and the pellet-to-cladding gap was completely closed during the irradiation in the BWR. Test fuel rods sampled from the 61 MWd/kgU BWR rods then failed in tests FK-6

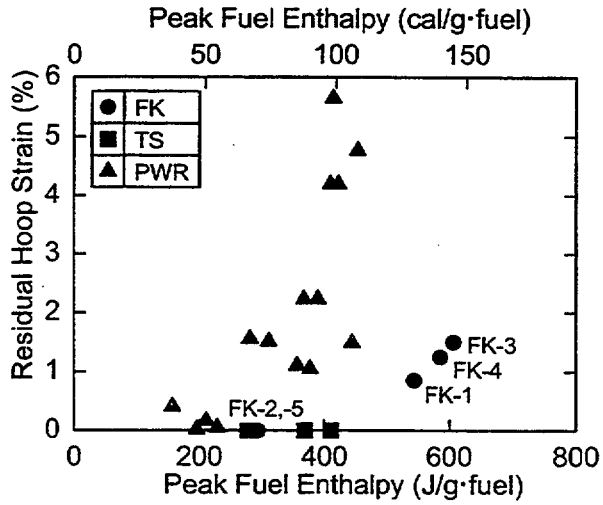

Fig. 2 Residual hoop strain of post-test cladding as a function of peak fuel enthalpy.

and FK-7, which were performed on February and March 2000. Transient data obtained during the FK-6 are shown in Fig. 3. Spikes appeared in traces of rod internal and capsule internal pressures, and indicated an occurrence of cladding failure. The fuel rod failed during the pulse-irradiation at fuel enthalpy of 293 J/g (70 cal/g) in the FK-6. A post-test appearance of the failed cladding of the FK-6 is shown in Fig. 4. The cladding was broken apart into three pieces, and all of the fuel pellets was dispersed into the capsule water. The cracks seen in the photographs suggest that both radial and axial loadings occurred in the cladding during the pulse. The result suggests the occurrence of an intense PCMI loading due to the pellet-cladding bonding. In the previous PWR fuel experiment HBO-1[1] resulting in fuel failure, the cladding was broken apart into two pieces since a crack propagated to the welded position of irradiated cladding and bottom-end-fitting, and all of the fuel pellets were collected from capsule water. However, cracks generated in the test propagated axially. In rest of the PWR fuel experiments resulting in

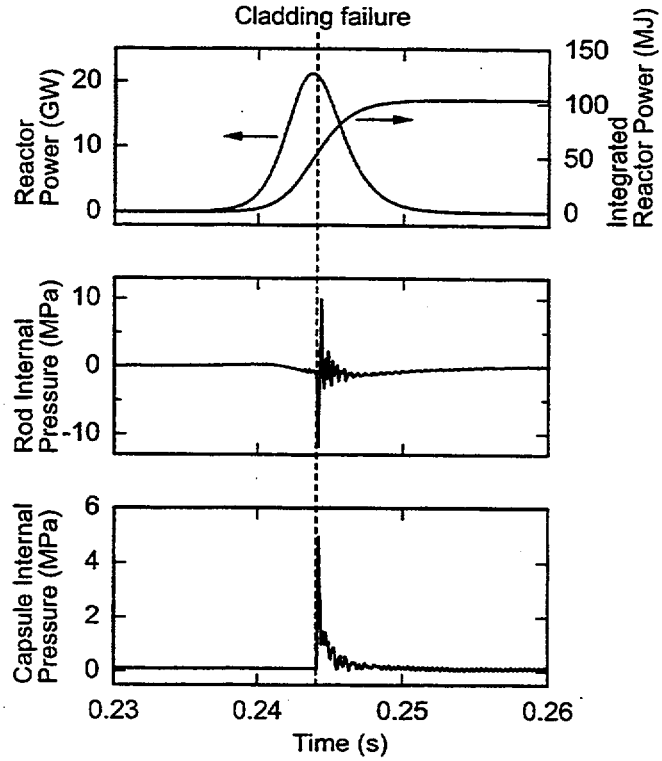

Fig. 3 Transient data in FK-6.

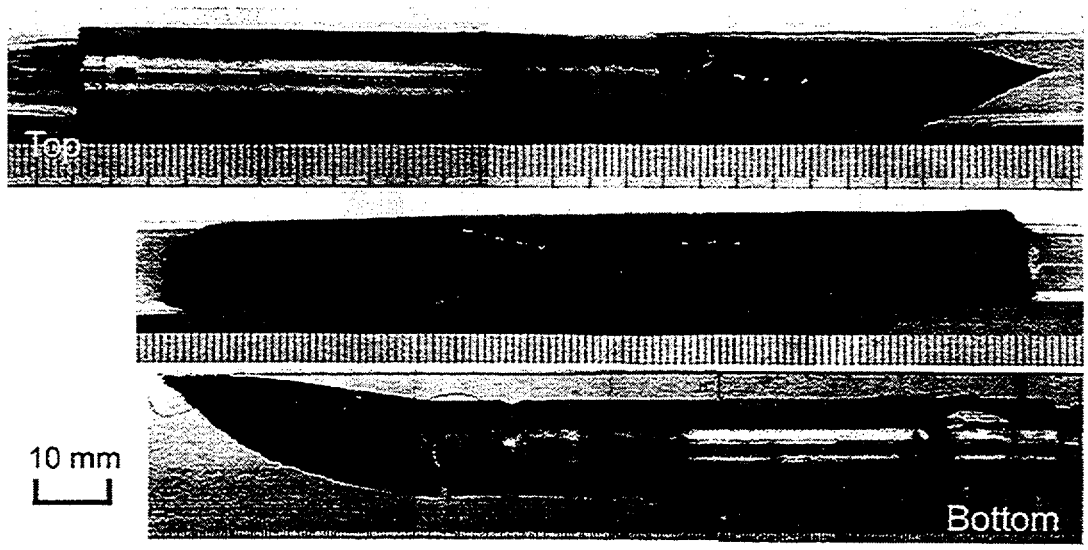

Fig. 4 Post-test appearance of test rod in FK-6.

fuel failure, e.g. HBO-5[2] and TK-2,[4] only a long axial crack appeared in the failed rod and fuel dispersal were very limited. Only 5% and 7% of fuel pellets were dispersed in the HBO-5 and TK-2, respectively.

Transient records and a post-test appearance of the subsequent test FK-7 are shown in Figs. 5 and 6, respectively. A large spike in trace of capsule internal pressure indicated an occurrence of cladding failure, and fuel enthalpy reached 260 J/g (62 cal/g) by the time of the failure in the FK-7. As stated previously, water column velocity sensor is installed in the FK-7, and a half wavelength in the signal corresponds to the 3-mm displacement of the water column. The signal shows an occurrence of water hammer immediately after the cladding failure. The post-test appearance of the failed cladding in the FK-7 was quite similar to that of the FK-6. The cladding was broken apart also into three pieces, and all of the fuel pellets were dispersed into the capsule water.

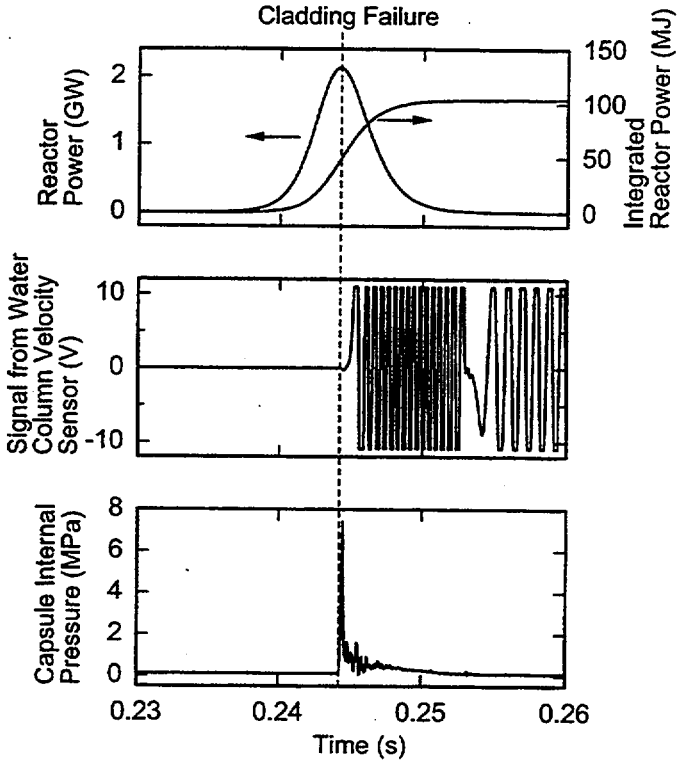

Fig. 5 Transient data in FK-7.

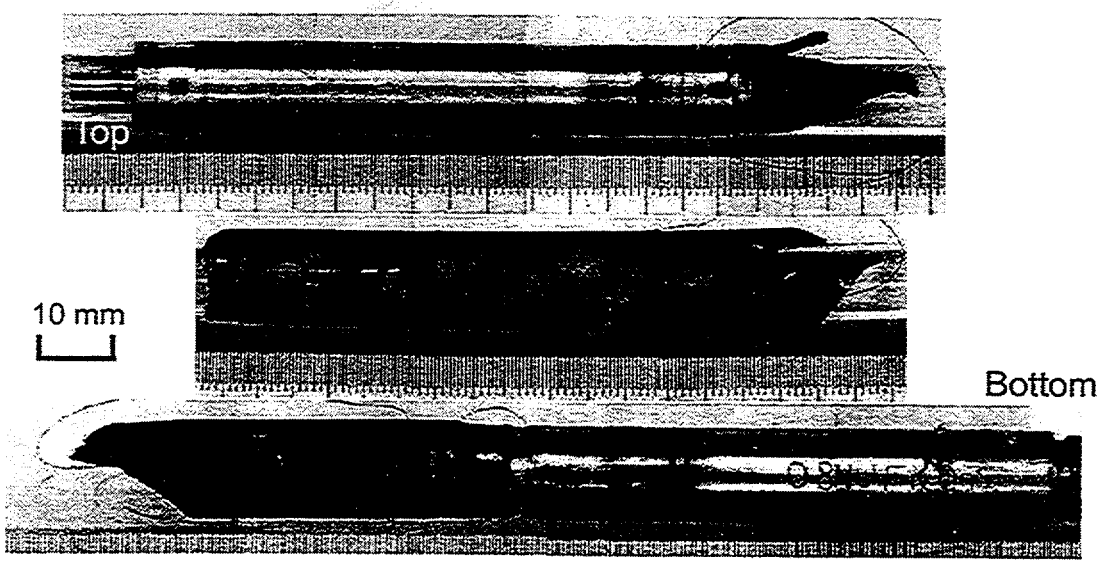

Fig. 6 Post-test appearance of test rod in FK-7.

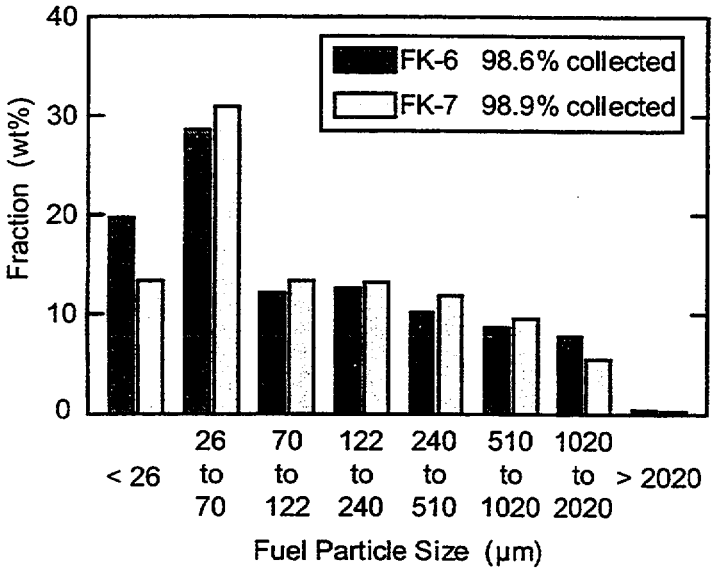

Fig. 7 Size distribution of fuel particles collected in FK-6 and FK-7.

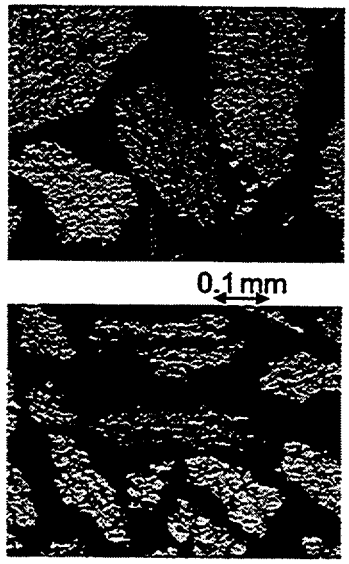

Fig. 8 Cross-section of relatively large fuel particles collected in FK-6.

About 99% of fuel pellets were collected from capsule water after the both experiments, and fuel particles were sieved in order to obtain size distribution. The results showed that about half of fuel pellets became particles smaller than 0.1 mm, as shown in Fig. 7. Median diameter (volume-surface mean diameter) of the fuel particles were 43 μm and 56 μm in the FK-6 and FK-7, respectively. Cross-sectional view of relatively large fuel particles is shown in Fig. 8. The collected fuel particles were not once-molten, as can be expected from the low maximum fuel temperature (1400 K or lower evaluated with FRAP-T6 code) at failure. Although the fragmented particles remained in the solid phase, mechanical energy was generated during the tests.

Figure 9 shows radial cross-section of cladding failed in the FK-6. Although a region next to zirconium liner seemed a little ductile, cracks propagated with brittle nature. Hydrogen concentration in the cladding is not high, less than 140 ppm, but hydride clusters are not circumferentially oriented. Some radially oriented hydride clusters can be seen in the pictures. Figure 10 compares radial cross-sections of cracks in the previous experiment HBO-1 and the FK-6. In the HBO-1 with 50 MWd/kgU PWR fuel, brittle fracture appeared in the peripheral region, and ductile fracture in inner region. Hydride clusters were radially localized in the periphery (forming hydride-rim), and were circumferentially oriented in stress relieved Zry-4 cladding of the HBO-1. On the other hand, hydride clusters were not radially localized, but radially oriented hydride clusters were formed in recrystallized Zry-2 cladding of the FK-6. These radially oriented hydride clusters may have an influence on crack initiation and propagation. Figures 11 and 12 show fracture surface of cladding failed in the FK-6. The fracture surface in zirconium liner looks most brittle, and a layer next to the liner looks ductile. Most of peripheral layer shows brittle fracture surface with partially ductile region. Although the data are preliminary, a photo-image analysis

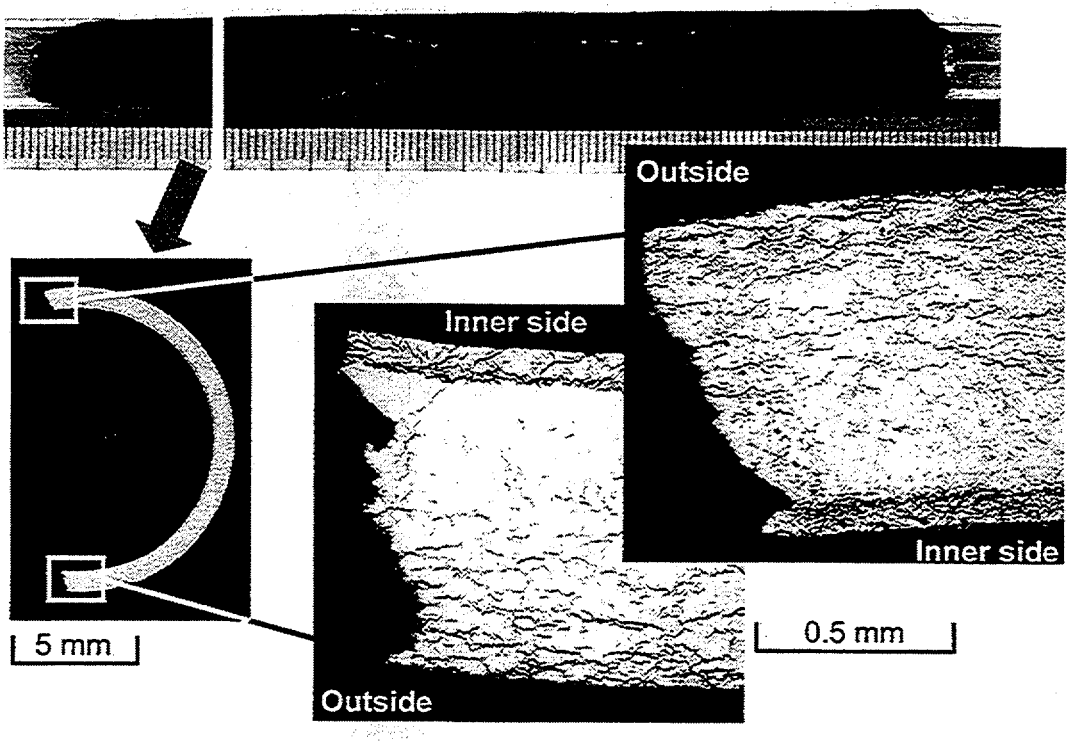

Fig. 9 Radial cross-section of failed cladding of FK-6.

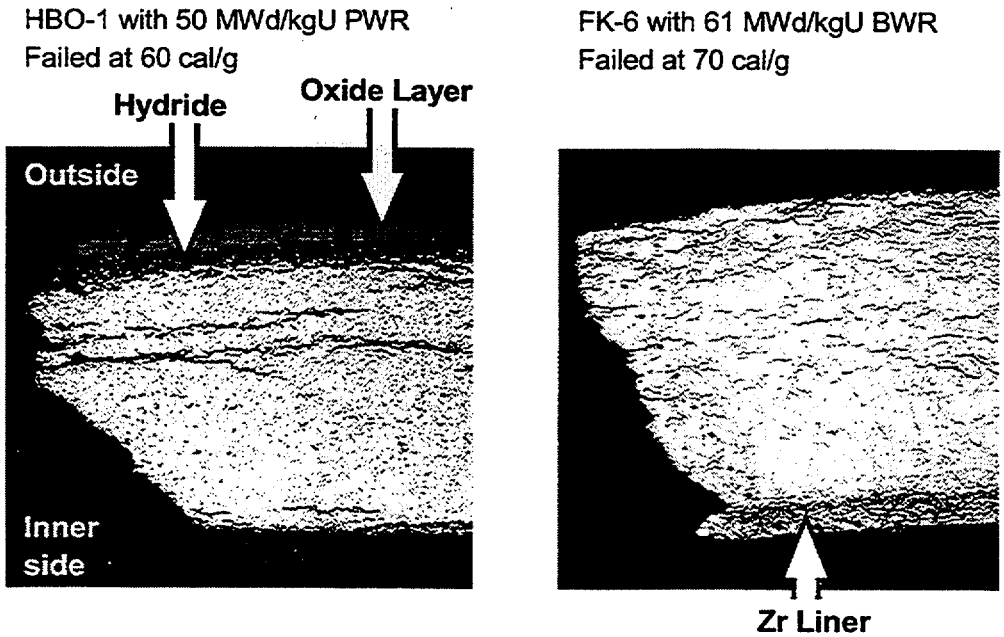

Fig. 10 Radial cross-sections of cracks in PWR fuel experiment HBO-1 and BWR fuel experiment FK-6.

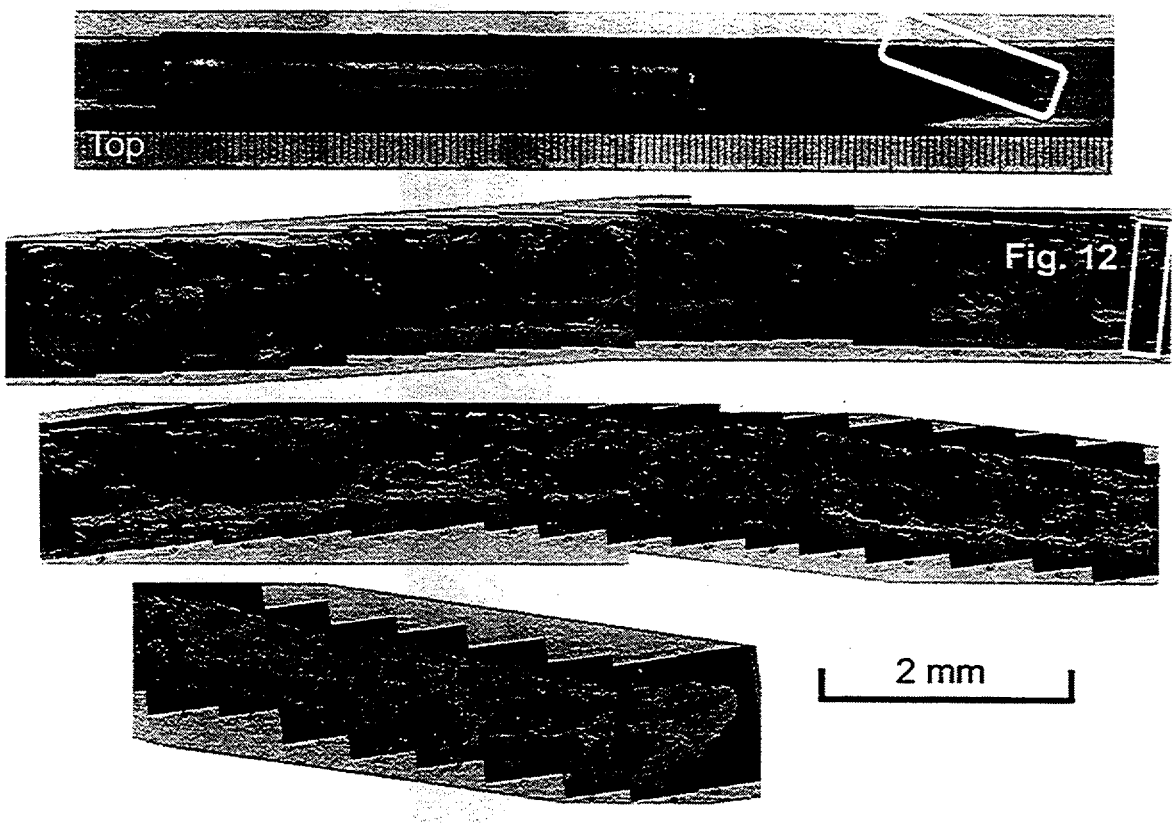

Fig. 11 Fracture surface of failed cladding of FK-6.

on the cross-section of the FK-6 cladding shows a residual hoop strain of approximately 0.1%. A possible decrease in fracture toughness[10] with increasing reactor exposure may explain the brittle fracture morphology seen in the surfaces.

The fuel rods failed during the pulse-irradiations at fuel enthalpies of 293 J/g (70 cal/g) for FK-6 and 260 J/g (62 cal/g) for FK-7. Japanese Nuclear Safety Commission adopted new regulatory criteria on April 1998 regarding a failure of burnup fuel during a reactivity-initiated event, and a threshold of PCMI failure was newly defined in terms of enthalpy increase and fuel burnup. Both the fuel enthalpies at failure in the FK-6 and FK-7 were higher than the PCMI failure threshold, which is 209 J/g (50 cal/g) in the burnup region, and hence the results from the FK-6 and FK-7 do not suggest any immediate regulatory action. The data, however, provide a better understanding of failure mechanism in high burnup BWR fuels and may help in development of new fuel for higher burnup application.

III. FK-8 AND FK-9 WITH MILDER PULSES AND COMPARISONS WITH FK-6 AND FK-7

The 61 MWd/kgU BWR fuels were tested also in recent two experiments FK-8 and FK-9 performed on October and November 2000. In the previous FK-6 and FK-7, maximum pulses available in the NSRR were used. On the other hand, smaller and a little wider pulses were used in the FK-8 and FK-9. Test rods

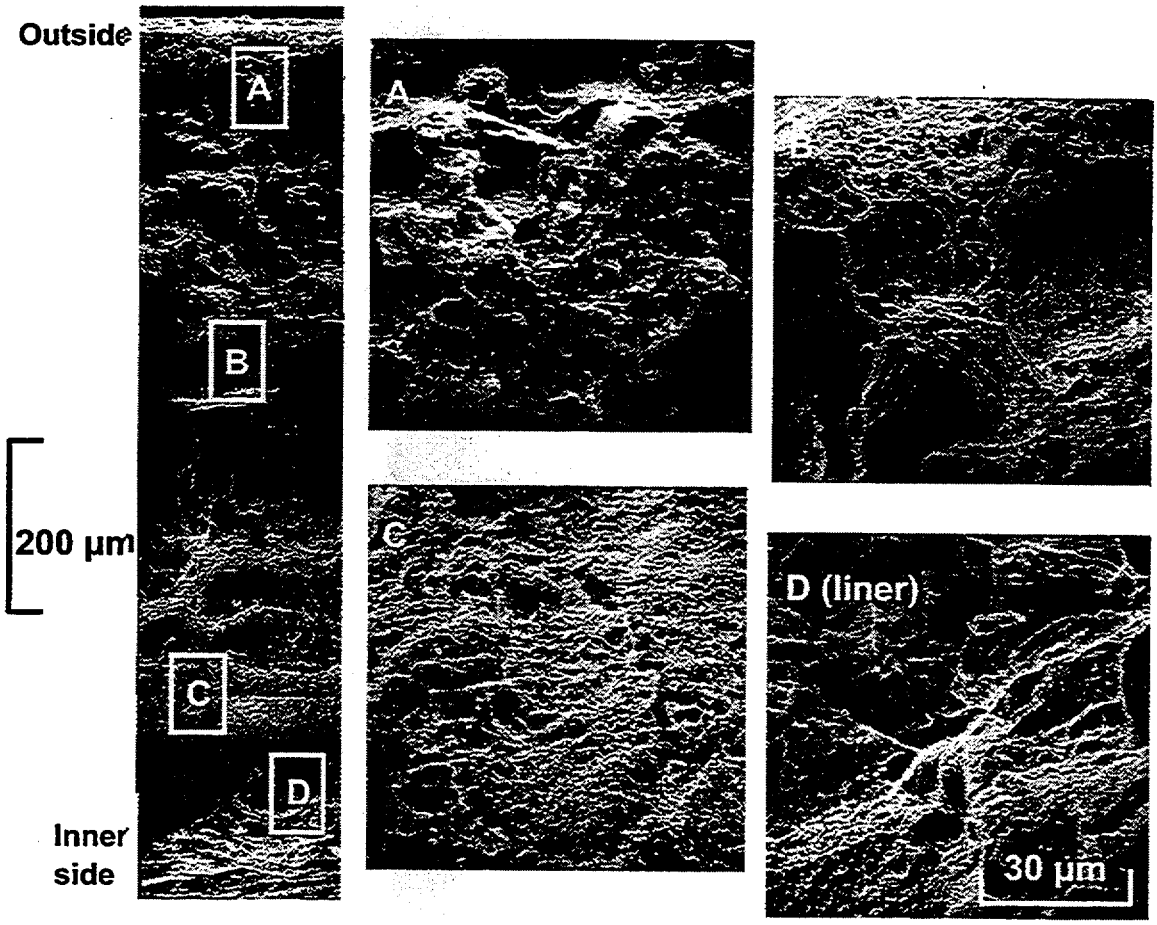

Fig. 12 Fracture surface of failed cladding of FK-6.

in the FK-8 and FK-9 were pre-pressurized to 1.5 MPa as was in the FK-7. A size of pulse was fixed in the FK-8 in order to obtain a peak fuel enthalpy of 272 J/g (65 cal/g), which corresponds to fuel enthalpy at failure in the previous FK-7. A pulse width (a full width at half maximum) was 4.3 ms in the FK-6 and FK-7, but became 7.3 ms in the FK-8. Cladding failure did not occur in the FK-8, and post-test cladding showed very small residual strain.

In the latest FK-9, a mid-size pulse with a width of 5.7 ms was used for a peak fuel enthalpy of 389 J/g (93 cal/g). Then, cladding failed at 360 J/g (86 cal/g), and all of fuel pellets were collected from capsule water. Figure 13 compares transient records of reactor power and capsule internal pressure in the FK-7 and FK-9. It can be expected that an effect of pulse size appears most dramatically in experiments with test fuel rods with extremely embrittled cladding, such as PWR cladding with pre-existing oxide spallation.[11] Since this kind of cladding fails with very small strain, small differences in thermal expansion of fuel pellets may give different failure energies. The 61 MWd/kgU BWR cladding tested in the FK-6 through FK-9 may have significant reduction in ductility and fracture toughness. The brittle type fracture morphology seen in the post-test fuels indicates that the rods could fail with very small strain,

which is probably less than 1% of total hoop strain and about 0.1% of plastic strain. In combination with tight pellet-cladding bonding, small differences in loading conditions could result in different failure energies. According to analyses[12] with FRAP-T6 code, calculated strain without fission gas loading (fission-gas-induced pellet expansion)[4] is similar to the measured cladding strain, and suggests that an effect of fission gas on cladding deformation is limited. In terms of strain rates and cladding temperatures at failures, differences are not significant between predicted and measured values. Since the analyses are still preliminary, an effect of pulse size on failure enthalpy will be examined further.

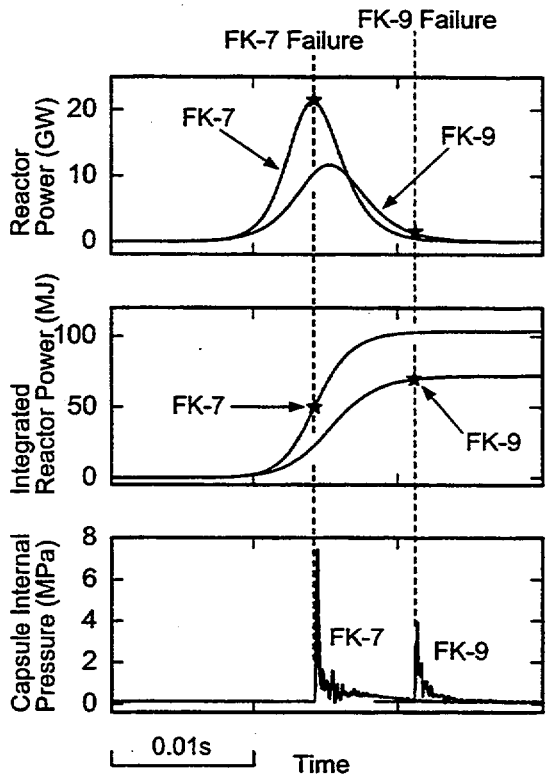

Fig. 13 Transient records of reactor power and capsule internal pressure in FK-7 and FK-9.

IV. FISSION GAS RELEASE

Fission gas release during pulse-irradiations was evaluated from rod puncture and gas analysis, or capsule cover gas sampling and analysis. Figure 14 shows fission gas release during pulse-irradiation as a function of fission gas release during base-irradiation in BWR. The value from the most recent FK-9 is from a preliminary evaluation. Fission gas release during pulse-irradiation correlates well with that during base-irradiation, and the larger fission gas release during base-irradiation results in the larger fission gas release during pulse-irradiation. The results indicate that fission gas release in BWR fuels during pulse-irradiation is strongly influenced by base-irradiation conditions in BWR, e.g. linear heat rate, and release paths generated during base-irradiation play a role also during the transient.

Correlation between peak fuel enthalpy and fission gas release during pulse-irradiation is shown in Fig. 15. Fission gas release during base-irradiation is 12% or higher in fuels tested in FK-4 through FK-9, whereas it is lower than 2% in fuels of FK-1 through FK-3. In each group, FK-1 through FK-3 or FK-4 through FK-9, a higher fuel enthalpy resulted in larger fission gas release during the pulse.

Strong influence of cladding failure and subsequent pellet fragmentation cannot be seen on fission gas release, as far as one compares data of FK-6 and FK-7 with that of FK-4 in Figs. 14 and 15. Considering peak fuel enthalpy during pulse-irradiation, however, fission gas release is relatively large in FK-9 which had cladding failure. It is premature to neglect influence of cladding failure and pellet fragmentation on fission gas release.

The local burnup in pellet peripheral region becomes much higher than the average at high burnup, and a ratio of xenon/krypton (Xe/Kr) varies with the local burnup in radial direction of fuel pellet.

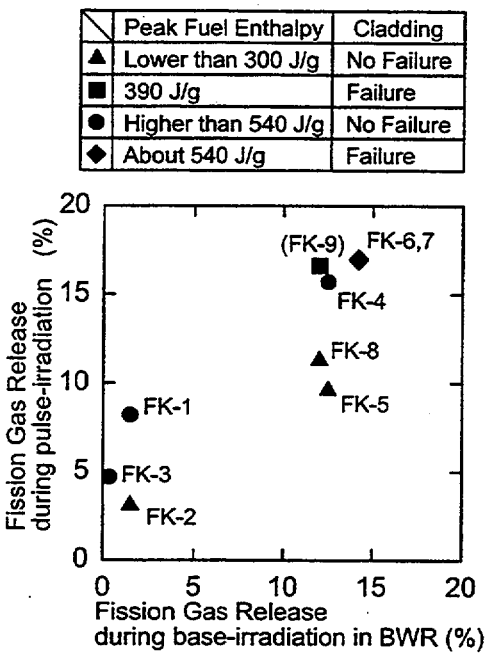

Fig. 14 Fission gas release during pulse-irradiation as a function of fission gas release during base-irradiation in BWR.

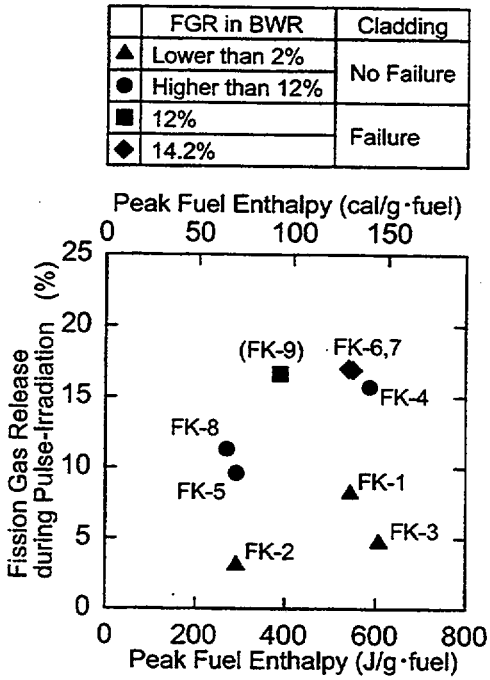

Fig. 15 Fission gas release during pulse-irradiation as a function of peak fuel enthalpy.

Accordingly, the Xe/Kr ratio of the collected gas provides information regarding radial position where accumulated fission gas was released in pellet.[13] In the Step I fuels at burnups from 41 to 45 MWd/kgU, which were tested in FK-1 through FK-3, the Xe/Kr ratio of gas released during pulse-irradiation was equivalent to the ratio of gas released in BWR and the ratio corresponding the average burnup. This suggests that fission gas was uniformly released from fuel pellet inside region as well as peripheral region during the pulse-irradiations of the FK-1 through FK-3. Among the Step II fuels at burnups from 56 to 61 MWd/kgU, which were tested in FK-4 through FK-9, the ratio of gas released during the FK-6 and FK-7 was equivalent to the ratio of gas released in BWR, but the ratio in the FK-4, FK-5, FK-8 and FK-9 was higher than the ratio of gas released in BWR. The results indicate that fission gas uniformly released in the FK-6 and FK-7, but fission gas release was larger in pellet peripheral region during pulse-irradiations of the FK-4, FK-5, FK-8 and FK-9. Differences in fission gas release during base-irradiation may explain the different ratios in the two groups. Fuels tested in the FK-6 and FK-7 released 14.2% gas in BWR, and fuels of the FK-4, FK-5, FK-8 and FK-9 released 12.0% to 12.5% gas during the base-irradiation. The uniform release in the FK-6 and FK-7 appears to be due to cladding failure and fuel fragmentation during both tests. The FK-9 also resulted in failure, however, gave a ratio equivalent to the un-failed FK-8.

V. SUMMARY

The NSRR experiments, FK-6 and FK-7, with 61 MWd/kgU BWR fuels resulted in significant cladding failure and fuel dispersal. The fuel rods failed during the pulse-irradiations at fuel enthalpies of 293 J/g (70 cal/g) for FK-6 and 260 J/g (62 cal/g) for FK-7. Both the fuel enthalpies at failure were higher than the Japanese safety criteria, which is 209 J/g (50 cal/g) in the burnup region. In licensing evaluation for Japanese LWRs, failures at the 50 cal/g are assumed for fuels at burnups of 40 to 65 MWd/kgU, and hence the fuel failures are within the assumed consequence. The tests, however, provide valuable information to understand fuel behavior of high burnup BWR fuels during transients. The cladding was broken apart into three pieces in the both tests. Although hydrogen concentration in the cladding was less than 140 ppm, radially oriented hydride clusters were observed and brittle type morphology was seen in entire region of the fracture surface of the failed cladding. The results indicate that an intense PCMI loading due to tight pellet-cladding bonding, radially oriented hydride clusters in the cladding, possible reductions of cladding ductility and fracture toughness caused crack initiation, propagation and failure with very small plastic strain. All of the fuel pellets were finely fragmented and dispersed into the capsule water. Median diameters of the fuel particles were 43 μm and 56 μm in the FK-6 and FK-7, respectively.

The subsequent two experiments, FK-8 and FK-9, were recently performed with 61 MWd/kgU BWR fuels and smaller and a little wider pulses. Fuel failure did not occur in the FK-8 with a peak fuel enthalpy of 272 J/g (65 cal/g), and residual strain of post-test cladding was very limited. The rod failed at 360 J/g (86 cal/g) in the FK-9 with a peak fuel enthalpy of 389 J/g (93 cal/g). Due to the PCMI loading mechanism with the tight pellet-cladding bonding and cladding failure with very small strain, small differences in thermal expansion of fuel pellets could give different failure energies. A negligible role of fission gas expansion was predicted in the present case.

Fission gas release during pulse-irradiation correlates well with release during base-irradiation in BWR, and the larger fission gas release during base-irradiation results in the larger fission gas release during pulse-irradiation. The results indicate that fission gas release in BWR fuels during pulse-irradiation is strongly influenced by base-irradiation conditions in BWR. In the data from FK-4, FK-6 and FK-7, strong influence of cladding failure and subsequent pellet fragmentation cannot be seen on fission gas release, but it is premature to neglect the influence.

ACKNOWLEDGMENTS

The authors would like to acknowledge and express their appreciation for the time and effort devoted by numerous engineers and technicians in JAERI, in particular, NSRR Operation Division for performing pulse-irradiation experiments, Department of Hot Laboratories for conducting pre- and post-test fuel examinations, and Department of Safety Research Technical Support for mass spectrometry. Comments from R. O. Meyer of USNRC (U. S. Nuclear Regulatory Commission), C. E. Beyer of PNNL (Pacific Northwest National Laboratory) and H. M. Chung of ANL (Argonne National Laboratory) are appreciated. Direct and indirect contributions from NUPEC (Nuclear Power Engineering Cooperation), JNF (Japan Nuclear Fuel Co., Ltd.) and NFD (Nippon Nuclear Fuel Development Co., Ltd.) are also acknowledged. The FK experiments have been conducted with fuel rods from TEPCO (Tokyo Electric

Power Company, Inc.).

REFERENCES

(1) Fuketa, T., Mori, Y., Sasajima, H., Ishijima, K. and Fujishiro, T., "Behavior of High Burnup PWR Fuel Under a Simulated RIA Conditions in the NSRR", *Proc. CSNI Specialist Mtg. on Transient Behavior of High Burnup Fuel*, Cadarache, France, September 12-14, 1995, NEA/CSNI/R(95)22, pp.59-85, (1996).

(2) Fuketa, T., Nagase, F., Ishijima, K. and Fujishiro, T., "NSRR/RIA Experiments with High-Burnup PWR Fuels", *Nuclear Safety*, Vol.37, No.4, pp.328-342, (1996).

(3) Fuketa, T., Sasajima, H., Mori, Y. and Ishijima, K., "Fuel Failure and Fission Gas Release in High Burnup PWR Fuels under RIA Conditions", *J. Nucl. Mater.*, Vol.248, pp.249-256, (1997)

(4) Fuketa, T., Sasajima, H. and Sugiyama, T., "Behavior of High Burnup PWR Fuels with Low-Tin Zircaloy-4 Cladding Under Reactivity-Initiated-Accident Conditions", *Nucl. Technol.*, Vol.133, No.1, pp.50-62, (2001).

(5) Meyer, R., McCardell, R., Chung, H., Diamond, D. and Scott, H., "A Regulatory Assessment of Test Data for Reactivity-Initiated Accidents", *Nuclear Safety*, Vol.37, No.4, pp.271-288, (1996).

(6) Nakamura, T., Yoshinaga, M., Sobajima, M., Ishijima, K. and Fujishiro, T., "Boiling Water Reactor Fuel Behavior at Burnup of 26 GWd/tonne U Under Reactivity-Initiated Accident Conditions", *Nucl. Technol.*, Vol.108, No.1, pp.45-60, (1994).

(7) Nakamura, T., Yoshinaga, M., Takahashi, M., Okonogi, K. and Ishijima, K., "Boiling Water Reactor Fuel Behavior under Reactivity-Initiated-Accident Conditions at Burnup of 41 to 45 GWd/tonne U", *Nucl. Technol.*, Vol.129, No.2, pp.141-151, (2000).

(8) Fuketa, T., Nakamura, T., Sasajima, H. Nagase, F., Uetsuka, H., Kikuchi, K. and Abe, T., "Behavior of PWR and BWR Fuels During Reactivity-Initiated Accident Conditions", *Proc. Int. Top. Mtg. on Light Water Reactor Fuel Performance*, Apr. 10-13, Park City, Utah, U.S.A., CD-ROM, (2000)

(9) Sugiyama, T. and Fuketa, T., "Mechanical Energy Generation during High Burnup Fuel Failure under Reactivity Initiated Accident Conditions", *J. Nucl. Sci. Technol.*, Vol.37, No.10, pp.877-886, (2000).

(10) Kreyns, P. H., Bourgeois, W. F., White, C. J., Charpentier, P. L., Kammenzind, B. F. and Franklin, D. G., "Embrittlement of Reactor Core Materials", *Zirconium in the Nuclear Industry: 11th Int. Symp.*, ASTM STP 1295, Bradley, E. R. and Sabol, G. P.(Eds.), ASTM, pp.758-782, (1996).

(11) Schmitz, F. and Papin, J., "REP-Na 10, another RIA Test with a Spalled High Burnup Rod and with a Pulse Width of 30 ms", *Proc. 26th Water Reactor Safety Information Mtg.*, Bethesda, Maryland, October 26-28, 1998, NUREG /CP-0166, Vol.3, p.243, (1999).

(12) Nakamura, T., Kusagaya, K., Fuketa, T. and Uetsuka, H., "High Burnup BWR Fuel behavior under Simulated Reactivity Initiated Accident Conditions", *Nucl. Technol.*, to be submitted.

(13) Sasajima, H., Nakamura, J., Fuketa, T. and Uetsuka, H., "Fission Gas Release Behavior of High Burnup UO_2 Fuel under Reactivity Initiated Accident Conditions", *J. Nucl. Sci. Technol.*, Vol.36, No.11, pp.1101-1104, (1999).

THE HISTORY OF LOCA EMBRITTLEMENT CRITERIA

G. Hache
Institut de Protection et de Sureté Nucléaire
Cadarache, France

H. M. Chung
Argonne National Laboratory
Argonne, Illinois, USA

Abstract

Performance of high-burnup fuel and fuel cladding fabricated from new types of alloys (such as Zirlo, M5, MDA, and duplex alloys) under loss-of-coolant-accident (LOCA) situations is not well understood at this time. To correctly interpret the results of investigations on the performance of the old and new types of fuel cladding, especially at high burnup, it is necessary to accurately understand the history and relevant databases of current LOCA embrittlement criteria. In this paper, documented records of the 1973 Emergency Core Cooling System (ECCS) Rule-Making Hearing were carefully examined to clarify the rationale and data bases used to establish the 1204°C peak cladding temperature and 17% maximum oxidation limits. A large amount of data, obtained for zero- or low-burnup Zircaloy cladding and reported in literature only after the 1973 Rule-Making Hearing, were also evaluated and compared with the current criteria to better quantify the margin of safety under LOCA conditions.

1. Introduction

Because of major advantages in fuel-cycle costs, reactor operation, and waste management, the current trend in the nuclear industry is to increase fuel discharge burnup. At high burnup, fuel rods fabricated from conventional Zircaloys often exhibit significant degradation in microstructure. This is especially pronounced in pressurized-water reactor (PWR) rods fabricated from standard Zircaloy-4 in which significant oxidation, hydriding, and oxide spallation can occur. Thus, many fuel vendors have developed and proposed the use of new cladding alloys, such as low-tin Zircaloy-4, Zirlo, M5, MDA, duplex cladding, and Zr-lined Zircaloy-2. Performance of these alloys under loss-of-coolant-accident (LOCA) situations, especially at high burnup, is not well understood at this time. Therefore, it is important to verify the safety margins for high-burnup fuel and fuels clad with new alloys. In recognition of this, LOCA-related behavior of various types of high-burnup fuel cladding is being actively investigated in several countries [1-6]. However, to correctly interpret the results of such investigations, and if necessary, to establish new embrittlement thresholds that maintain an adequate safety margin for high-

burnup operation, it appears necessary to accurately understand the rationale, history, and data bases used to establish the current LOCA criteria, i.e., maximum cladding temperature limit of 1204°C (2200°F) and maximum oxidation limit of 17%. For this purpose, documented records of the 1973 Atomic Energy Commission (AEC) Emergency Core Cooling System (ECCS) Rule-Making Hearing were carefully examined and the relevant databases were reevaluated in this paper. Since the establishment of the current criteria, large amounts of data were obtained in many countries for zero- or low-burnup fuel cladding. The results of these investigations were also critically evaluated to determine the validity of the current criteria and safety margins for a wider range of conditions.

2. Primary Objectives of Current Criteria

In 1967, an Advisory Task Force on Power Reactor Emergency Cooling [7], appointed to provide "additional assurance that substantial meltdown is prevented" by core cooling systems, concluded that:

> "The analysis of (a LOCA) requires that the core be maintained in place and essentially intact to preserve the heat-transfer area and coolant-flow geometry. Without preservation of heat-transfer area and coolant-flow geometry, fuel-element melting and core disassembly would be expected... Continuity of emergency core cooling **must be maintained after termination of the temperature transient for an indefinite period until the heat generation decays to an insignificant level**, or until disposition of the core is made."

This rationale makes it plainly clear that it is most important to preserve the heat transfer area and the coolant flow geometry not only during the short-term portion of the core temperature transient but also for long term.

Consistent with the conclusions of the Ergen Task Force, the U.S. Atomic Energy Commission (AEC) promulgated Criterion 35 of the General Design Criteria [8] which states that: "... fuel and clad damage that could interfere with **continued effective core cooling** is prevented." It also promulgated Criterion 3 of the Interim Acceptance Criteria for ECCS for LWR [9] which states that: "The clad temperature transient is terminated at a time when the core geometry is still amenable to cooling, and before the cladding is so embrittled as to fail **during or after quenching**."

These criteria were subjected to a Rule-Making Hearing in 1973, which was extensively documented in the Journal of Nuclear Safety in 1974 [10,11]. During the hearing process, the last part of the Criterion 3 was replaced by the modified Criterion 1 and the new Criterion 2 of the Code of Federal Regulations, Title 10, Part 50.46, Article (b), commonly referred to as 10 CFR 50.46 [12]. Thus, the AEC Commissioners wrote:

"In view of the fundamental and historical importance of maintaining core coolability, we retain this criterion as a basic objective, in a more general form than it appeared in the Interim Acceptance Criteria. It is not controversial as a criterion... Although most of the attention of the ECCS hearings has been focused on the events of the first few minutes after a postulated major cooling line break, up to the time that the cladding would be cooled to a temperature of 300°F or less, the **long-term maintenance of cooling** would be equally important [13]."

There are two key factors to consider to evaluate the change in coolable geometry of core, a brittle mode and a ductile mode of deformation in fuel cladding. The ductile mode is related to cladding ballooning, burst, and coolant channel blockage. This mode will not be treated in this paper. Our focus in this paper is on the change in coolable geometry due to cladding embrittlement and failure.

3. Metallurgy of Cladding Embrittlement

In 1960s, Wilson and Barnes performed laboratory tests simulating steam reactions with Zircaloy-clad fuel rods at high temperatures. They observed embrittlement of oxidized cladding well below the melting temperature of Zircaloy, either during the test itself or during removal of the specimen from the oxidizing furnace. The results were reported in Argonne National Laboratory (ANL) progress reports and synthesized later in Ref. 14. At the same period, investigators in Oak Ridge National Laboratory (ORNL) conducted TREAT Test No. 6 with Zircaloy cladding in steam and observed that the specimen was severely embrittled by oxidation [15]. Also at about the same period, many tests were conducted that simulated reactivity-initiated accident (RIA) in SPERT-CDC and TREAT reactors. Results of metallurgical examination in these tests showed that embrittlement was caused by severe microstructural modification of the cladding. Brittle cladding cross sections exhibited oxide layer, oxygen-stabilized alpha-phase layer and a region of acicular prior beta-phase. The results were later reported by Fujishiro et al. [16].

As a result of these observations, the scientific community was alerted to the fact that oxidation of Zircaloys above the alpha-to-beta transformation temperature results in the formation of inherently brittle phases, i.e., Zr oxide, oxygen stabilized alpha-Zr (fcc structure), and diffusion of oxygen into the underlying beta phase (bcc structure). This is shown schematically in Fig. 1. Ductility of cladding could be severely degraded if the degree of oxidation is high. It was also realized that, if the embrittled cladding fragments into small pieces, the coolability of the core could be seriously impaired.

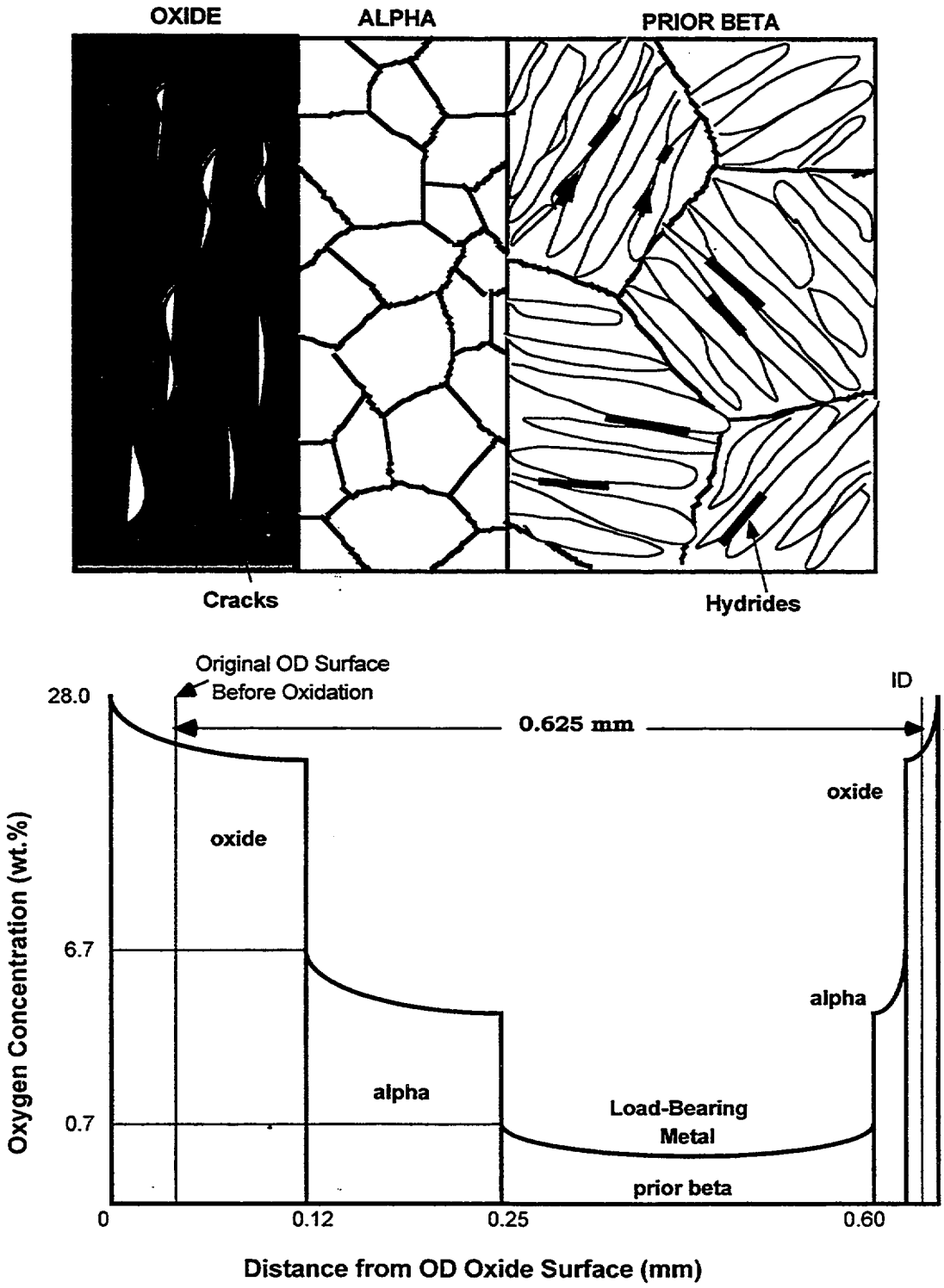

Fig. 1. Schematic illustration of microstructure (top) and oxygen distribution (bottom) in oxide, stabilized alpha, and prior-beta (transformed-beta) layers in Zircaloy cladding after oxidation near 1200°C.

Significantly embrittled cladding can fragment during the quenching phase of a LOCA. The action of rewetting by ECCS water involves the collapse of the vapor film that covers the cladding outer-diameter (OD) surface prior to subsequent transition to nucleate boiling. This event takes place at a more or less constant temperature, i.e., the Leidenfrost temperature. For oxidized Zircaloy-4 cladding rewetted by bottom-flooding water, ANL investigators reported that rewetting occurs in the range of 475-600°C [17]. The abrupt change in the heat transfer conditions induces large thermal-shock stress, which can fracture the cladding, if it is sufficiently embrittled by oxidation.

Below the Leidenfrost temperature, there is continued risk of fragmentation after quenching. In accordance with the opinions of the Ergen Task Force and the AEC staff and commissioners mentioned earlier, other experts also wrote a similar opinion for OECD Committee on Safety of Nuclear Installations (CSNI) [18]: "The ability of the cladding to withstand the thermal-shock stresses of quenching during rewetting **or post-LOCA forces** is related to the extent and detailed nature of oxidation during the transient. **The post-LOCA forces, which need to be taken into account, are the hydraulic, seismic, handling, and transport forces.**"

There are two primary factors that exacerbate the susceptibility of oxidized cladding to post-quench embrittlement in comparison with susceptibility to fragmentation during quenching: i.e., (1) more pronounced effect of oxygen dissolved in beta phase at lower temperature of loading (i.e., more pronounced after quench than during quench) and (2) more pronounced effect of hydrogen uptake which may occur during irradiation (e.g., in high-burnup Zircaloy-4) or during transient oxidation in steam (e.g., from cladding inner surface in contact with stagnant steam near a ballooned and burst region). For cooling rates typical of bottom flooding of core (i.e., 1-5°C/s), most hydrogen atoms remain in solution in the beta phase at Leidenfrost temperature, and in such state, hydrogen has little effect on the fracture resistance of an oxidized Zircaloy. However, when load is imposed at temperatures below the Leidenfrost temperature, precipitated hydrides strongly influence the fracture resistance of cladding. Eutectoid decomposition of hydrogen-stabilized beta phase at temperatures below ≈550°C [19] is the major factor that causes this deleterious effect (see Fig. 2).

4. Opinion of Regulatory Staff and Commissioners during 1973 Rule-Making Hearing

4.1 Reluctance to Neglect Effects of Mechanical Constraints

Some factors during a LOCA, such as ballooning of the rod near the spacer grid, rod-grid spring chemical interaction, and the friction between the fuel rod and spacer grids, can restrict the axial movement of the cladding. Also, guide tubes in a PWR fuel assembly are mechanically fixed to the spacer grids.

Because of these factors, fuel rods during reflooding will be subject to tensile load that is produced due to the differential axial shrinkage between a cladding and the guide tube. Rods may interact each other due to ballooning or bowing. For high-burnup fuels in which tight pellet-cladding bonding is common, axial shrinkage can be restricted if the tight bonding remains unchanged after ballooning and burst. These constraints will remain after quench, when deleterious effects of oxygen and hydrogen are far more pronounced.

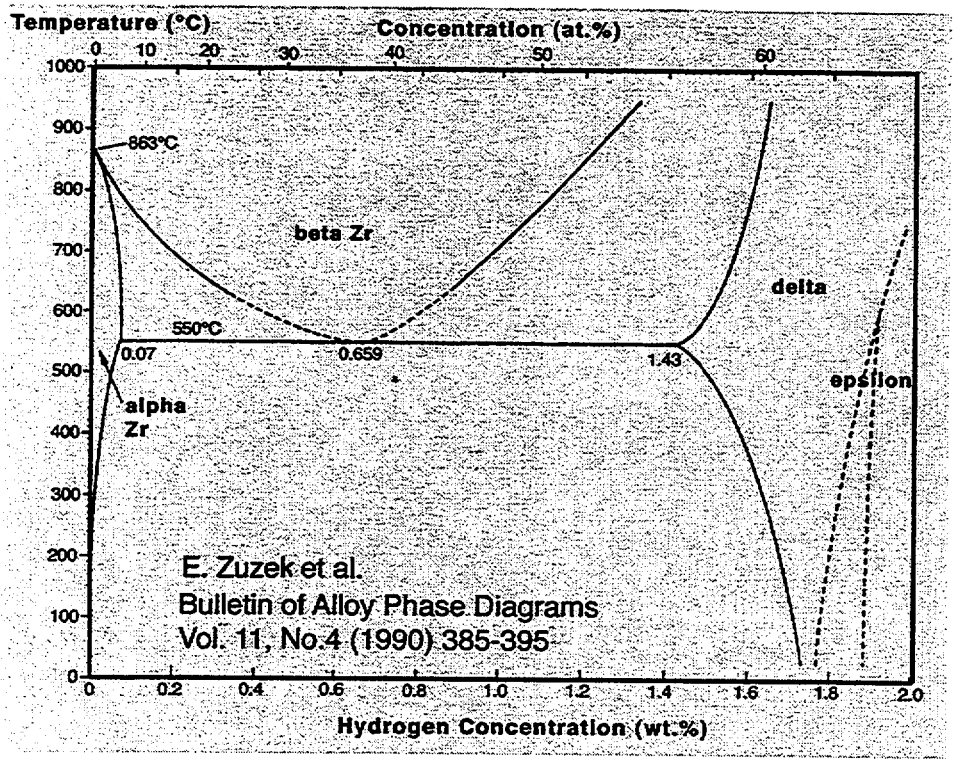

Figure 2.

Zr-H binary phase diagram (from E. Zuzek et al., Bulletin of Alloy Phase Diagrams, Vol. 11, No. 4, 1990, pp. 385-395).

In recognition of this, the AEC Staff wrote during the 1973 Rule-Making Hearing that "**the loads due to assembly restraint and rod-to-rod interaction may not be small compared to the thermal shock load and cannot be neglected** [20]." Subsequently, it was concluded that: "The staff believes that quench loads are likely the major loads, but **the staff does not believe that the evidence is as yet conclusive enough to ignore all other loads** [21]."

Then, the Commissioners added: "**There is some lack of certainty as to just what nature of stresses would be encountered during the LOCA**.... (We want) to draw attention to the fact that **it may not be possible to anticipate and calculate all of the stresses to which fuel rods would be subjected in a LOCA**. Although we believe the calculations of thermal shock stresses are worthwhile and informative, we agree with the regulatory staff that they are not sufficiently well defined to depend on for regulatory purposes [13]."

Before 1973, no thermal-shock quench test was performed on mechanically constrained cladding specimens. Then in early 1980s, Uetsuka et al. performed quenching tests on cladding sections under severely constrained condition [22]. In their experiment, cladding tube was fixed at the bottom but was allowed to freely elongate in axial direction during oxidation at high temperature. As a result, cladding length increased freely because of thermal expansion and oxide-induced creep. At the end of the isothermal oxidation, the specimen top was fixed to the crosshead of an Instron tensile facility. Then, the load-time curve was continuously monitored during quenching. Thus, at Leidenfrost temperature; the cladding tube was subjected to combined axial-tensile and thermal-shock stresses. The results of the tests are summarized in the Fig. 3. Similar tests were also performed on unconstrained tubes (Fig. 4).

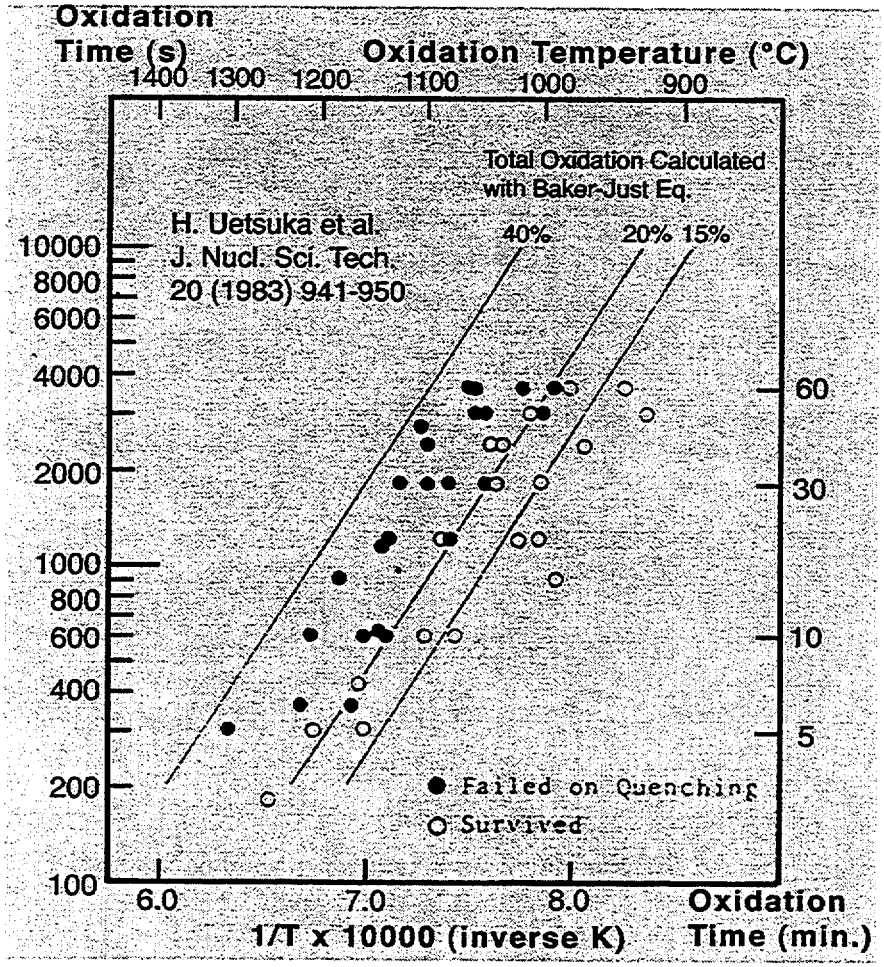

Figure 3.

Failure-nonfailure boundary for fully constrained Zircaloy-4 after oxidation in steam and quenching as function of oxidation time and temperature; total oxidation calculated with Baker-Just equation is also indicated (from Uetsuska et al., J. Nucl. Sci. Tech. 20, 1983, pp. 941-950).

A comparison of the results from the two contrasting types of test shows a large effect of the mechanical constraint. However, it is difficult to conclude whether the degree of constraint in the experiments of Uetsuka et al. is prototypic of a LOCA or unrealistically too severe. The 17% oxidation limit, calculated with Baker-Just correlation, appears to be adequate for protection of

constrained rods against thermal-shock failure (Fig. 3), whereas a large margin is evident for unconstrained rods (Fig. 4).

Unlike other bundle tests such as NRU, REBEKA, JAERI and ORNL multirod tests that were entirely devoted to the study of ballooning, burst, and flow-channel blockage, some of the tests in Phebus LOCA program was devoted to the study of embrittlement [23]. The fragmented Rod 18 of the Test 219, exposed to ≈1330°C, is especially interesting (see Fig. 5). For this oxidation temperature, results of calculation with PRECIP-II Code [24] indicates that the O content in the beta phase was higher than 0.9 wt.%, a threshold O concentration found to be associated with thermal-shock failure or survival [17]. Rod 18 fragmented despite it was oxidized to an equivalent-cladding reacted (ECR) value of only ≈16%. This observation indicates a deleterious bundle effect, i.e., an additional mechanical constraint.

As a conclusion, results of the JAERI constraint quench test and the PHEBUS-LOCA Test appear to justify the reluctance of the AEC staff and commissioners to neglect the effect of mechanical constraints on the susceptibility to thermal-shock failure.

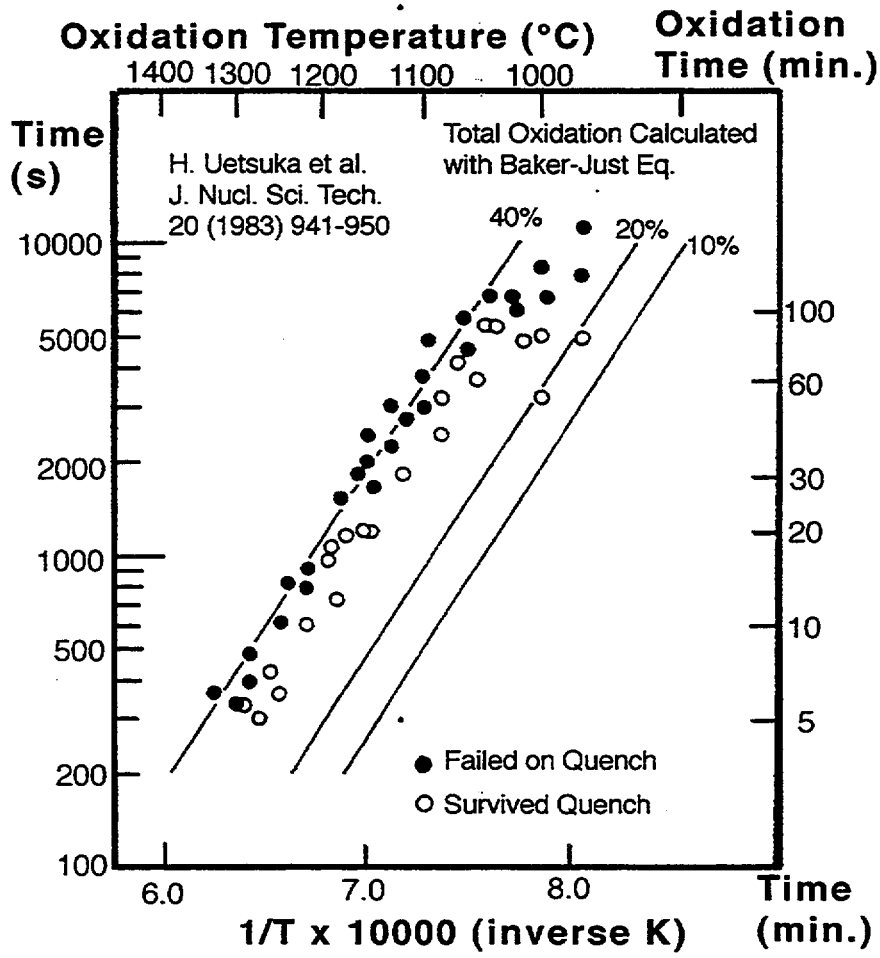

Figure 4.

Failure-nonfailure boundary for unconstrained Zircaloy-4 after oxidation in steam and quenching as function of oxidation time and temperature; total oxidation calculated with Baker-Just equation is also shown (from Uetsuska et al., J. Nucl. Sci. Tech. 20, 1983, pp. 941-950).

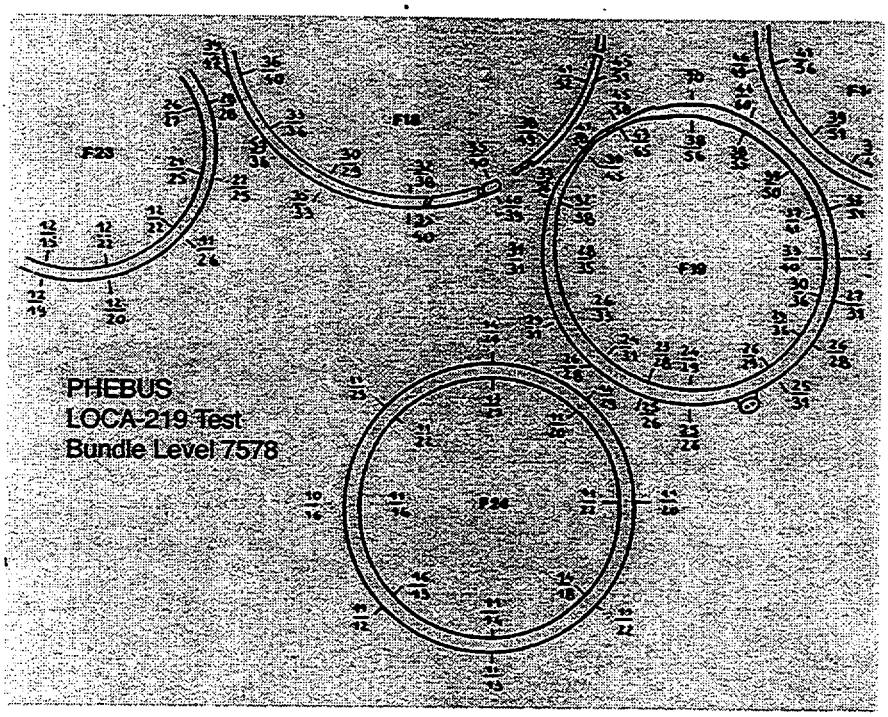

Figure 5.

Cross-section of portion of fuel assembly from PHEBUS LOCA-219 Test (Ref. 23), showing fragmentation of cladding.

4.2 Preservation of Ductility and Consideration of Results from Unconstrained Quench Test

At the end of the 1973 Hearing, the AEC Commissioners wrote: "...Nevertheless we find the quench results encouraging in that they provide assurance that the 2200°F limit is conservative. Our selection of the 2200°F limit results primarily from **our belief that retention of ductility in the Zircaloy is the best guarantee of its remaining intact during the hypothetical LOCA**... The thermal shock tests are reassuring, but **their use for licensing purposes** would involve an assumption of knowledge of the detailed process taking place in the core during a LOCA **that we do not believe is justified** [13]."

Without much ambiguity, this conclusion clearly expressed the belief that retention of ductility was considered the best guarantee against potential fragmentation under various types of loading (thermal-shock, bundle constraints, hydraulic, handling, and seismic forces). During the 1973 Hearing, results from unconstrained quench tests (simple thermal-shock test) were considered only corroborative and reassuring. However, their use for regulatory purposes was not accepted.

Results of later investigations on unconstrained or partially constrained cladding [17,18] showed a large margin of survival under thermal shock relative to 17%-ECR and 2200°F (1204°C) peak temperature limits. Such results are summarized in Fig. 6. No fragmentation occurred for ECR < 17% for all

oxidation temperatures, whereas significant margin of survival was observed for oxidation temperatures <1204°C. The results in Fig. 6 were limited for thermal-shock tests in which cladding tube or ring was directly quenched from the maximum oxidation temperature without slow cooling through the range of beta-to-alpha-prime transformation. For slow-cooling conditions, more pronounced margin of survival was observed [17].

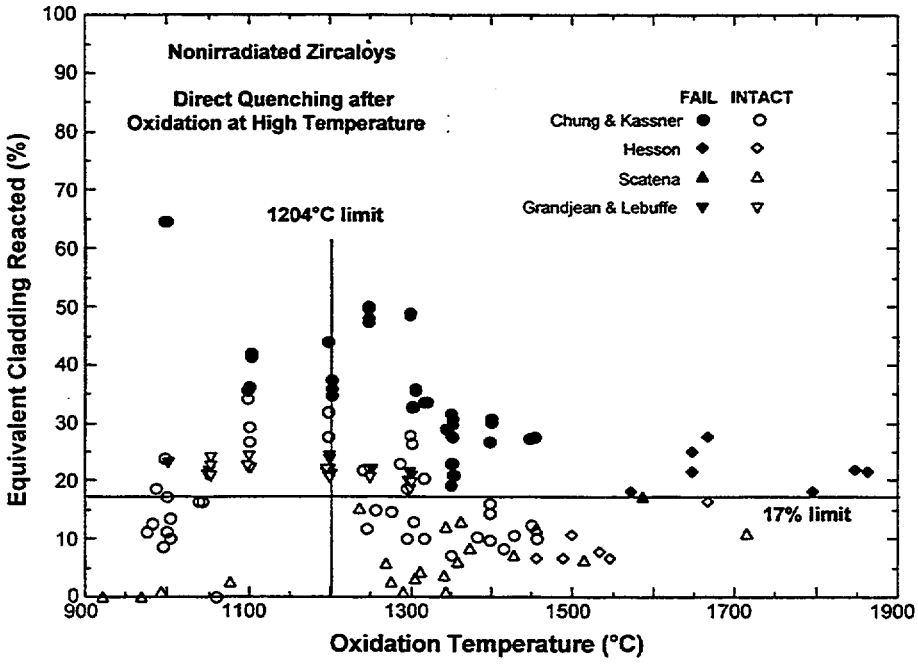

Figure 6. Failure boundary of partially constrained Zircaloy cladding tubes or unconstrained rings after oxidation at high temperature and direct quenching from peak oxidation temperature (from Refs. 17 and 29).

5. 17%-Oxidation Criterion

5.1 Establishment of 17% Criterion During 1973 Rule-Making Hearing

The rationale for establishment of the two criteria in 10 CFR 50.46(b) is described in this section. As indicated in a few reports [17,18] that reviewed the results of the LOCA-related tests performed before and after the 1973 Hearing, the 17%-ECR and 1204°C criteria were primarily based on the results of post-quench ductility tests conducted by Hobson [25,26].

Figure 7 summarizes the results of Hobson's ring compression tests performed at 23-150°C. Zircaloy-4 cladding tubes were oxidized in steam on two sides, followed by direct quenching into water. Then, short ring specimens cut from the oxidized tube were either compressed slowly to a total deflection of 3.8 mm or squashed by impact loading. After the test, the broken pieces of the ring was assembled back to determine the degree of brittleness. Zero ductility was defined on the basis of the macroscopic geometry of the broken pieces and the morphology of the fracture surface on microscopic scale. Each data point in Fig. 7 indicates failure type, test identification number, oxidation time in min., oxidation temperature in °F, and first maximum load in pound.

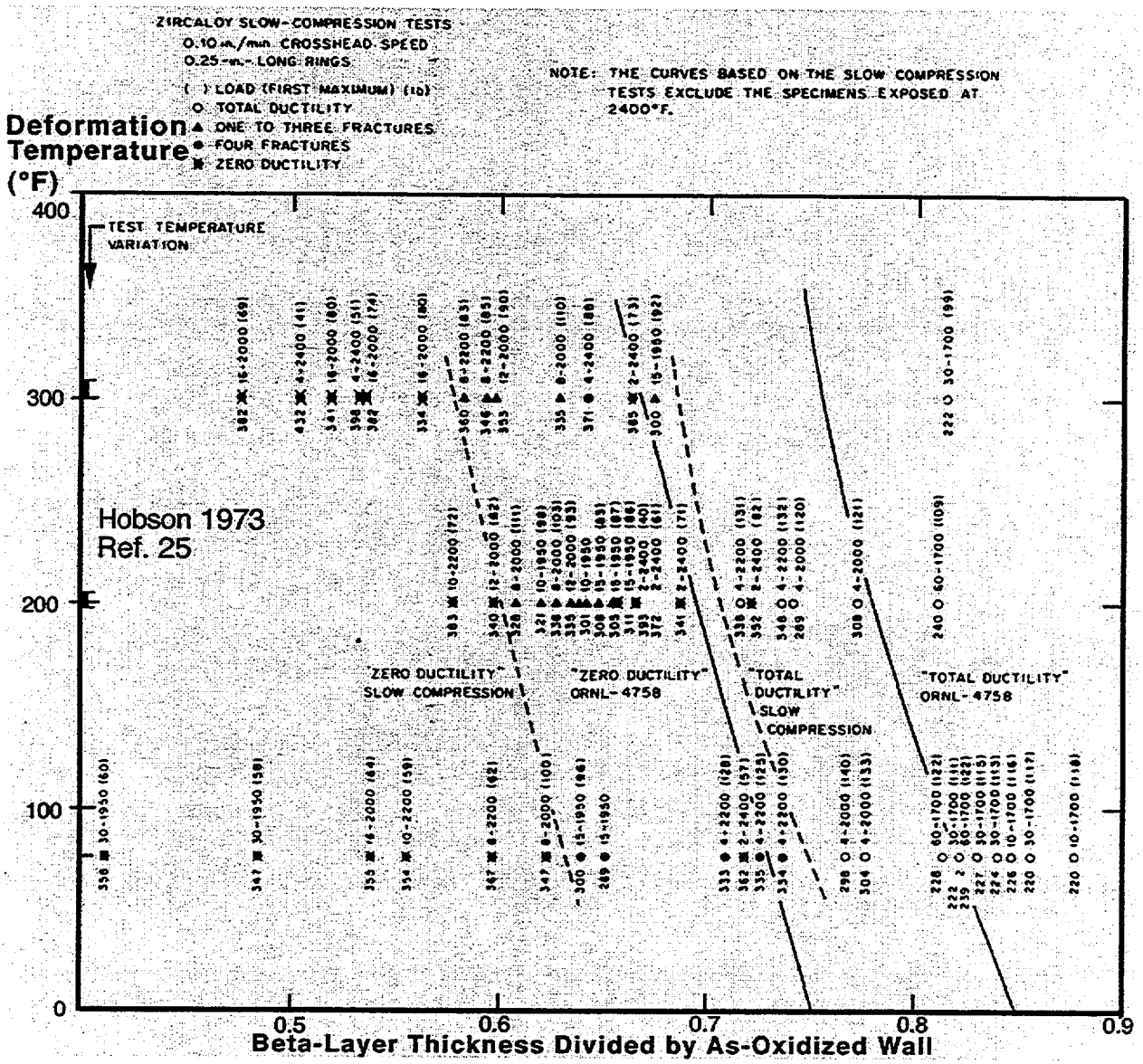

Figure 7.

Ductility of two-side-oxidized Zircaloy rings as function of slow- or fast-compression temperature and fraction of transformed-beta-layer (from Hobson, Ref. 25 and 26).

The dashed line on the left side of Fig. 7 denotes the zero ductility domain for slow-compression rate. This domain is valid only for oxidation temperatures of <2200°F or <1204°C. During the 1973 Hearing, ORNL investigators suggested to consider a zero-ductility temperature (ZDT) no higher than the saturation temperature during reflood, i.e., ≈135°C. Zero-ductility threshold at this temperature is equivalent to a beta-layer fraction of ≈0.58, or a fraction of combined oxide layer plus alpha layer thickness (defined as X_T) of ≈0.42 (based

on as-oxidized cladding wall). The latter fraction corresponds to ≈0.44 if it is calculated based on fresh nonoxidized cladding wall (defined as Wo).

The threshold fractional thickness of the combined oxide and alpha layer (X_T/Wo, defined as Xoa in Fig. 8) of 0.44, which corresponds to zero ductility threshold for slow compression at 135°C, was the key number in the establishment of 17% oxidation criterion in the 1973 Hearing. During the hearing, the AEC Regulatory Staff wrote:

> "Giving due credit to the numerous quench experiments and the ORNL zero ductility experimental data points for both impact and slow compression, the staff suggests that an embrittlement criterion be based on a **calculated X_T/Wo that shall not exceed 0.44. This is equivalent to a zero ductility temperature of about ... 275°F based on the slow compression tests** [20]."

Then, it was concluded:

> "To preclude clad fragmentation and to account for effects noted in the tests described above, **a limit of X_T/Wo ≤ 0.44** was earlier suggested by the Regulatory staff as an embrittlement criterion (Exhibit 1113, page 18-18). This limit was inferred from quench tests and mechanical tests. Criterion (b)(2) is now proposed as a better method of specifying a similar limit on the extent of cladding oxidation. The bases for proposing this method are described below: (The) use (of the **17 percent reaction limit) with the Baker-Just equation** is conservative when compared to the previously suggested limits of **X_T/Wo ≤ 0.44**. This is shown in Figure 8 (of this paper) for isothermal conditions. Four lines of **constant calculated X_T/Wo** (two for 0.44 and two for 0.35) are constructed on the plot of percent reaction versus a parameter proportional to the square root of exposure time. The solid X_T/Wo lines are based on Pawel's equation (Exhibit 1133) (Ref. 27 of this paper), and the dashed lines are based on Exhibit 09, page 9, Figure 5 (Ref. 25 of this paper). As can be seen, **the X_T/Wo = 0.44 lines are both above the 17 percent reaction line..."**

Results of a total of five key tests and calculations are summarized in Fig. 8, a complex but the most important step used to reach the 17% oxidation limit. They are: (1) equivalent cladding reacted (ECR) calculated as function of oxidation temperature and square root of time based on Baker-Just correlation, (2) two broken curves which define the time and temperature to reach the threshold fractional thickness of the combined oxide and alpha layer (denoted as Xoa) of 0.44 and 0.35, as determined based on the data given in Ref. 25, Page 9, Fig.5, (3) two solid curves that define the time and temperature to reach the threshold fractional thickness of the combined oxide and alpha layer of 0.44

and 0.35, as determined based on the method of Ref. 27, (4) six ECR-(time)$^{0.5}$ curves from the thermal-shock tests of Hesson et al., Ref. 14, and (5) results from Combustion Engineering (CE) ring compression tests after one-sided oxidation.

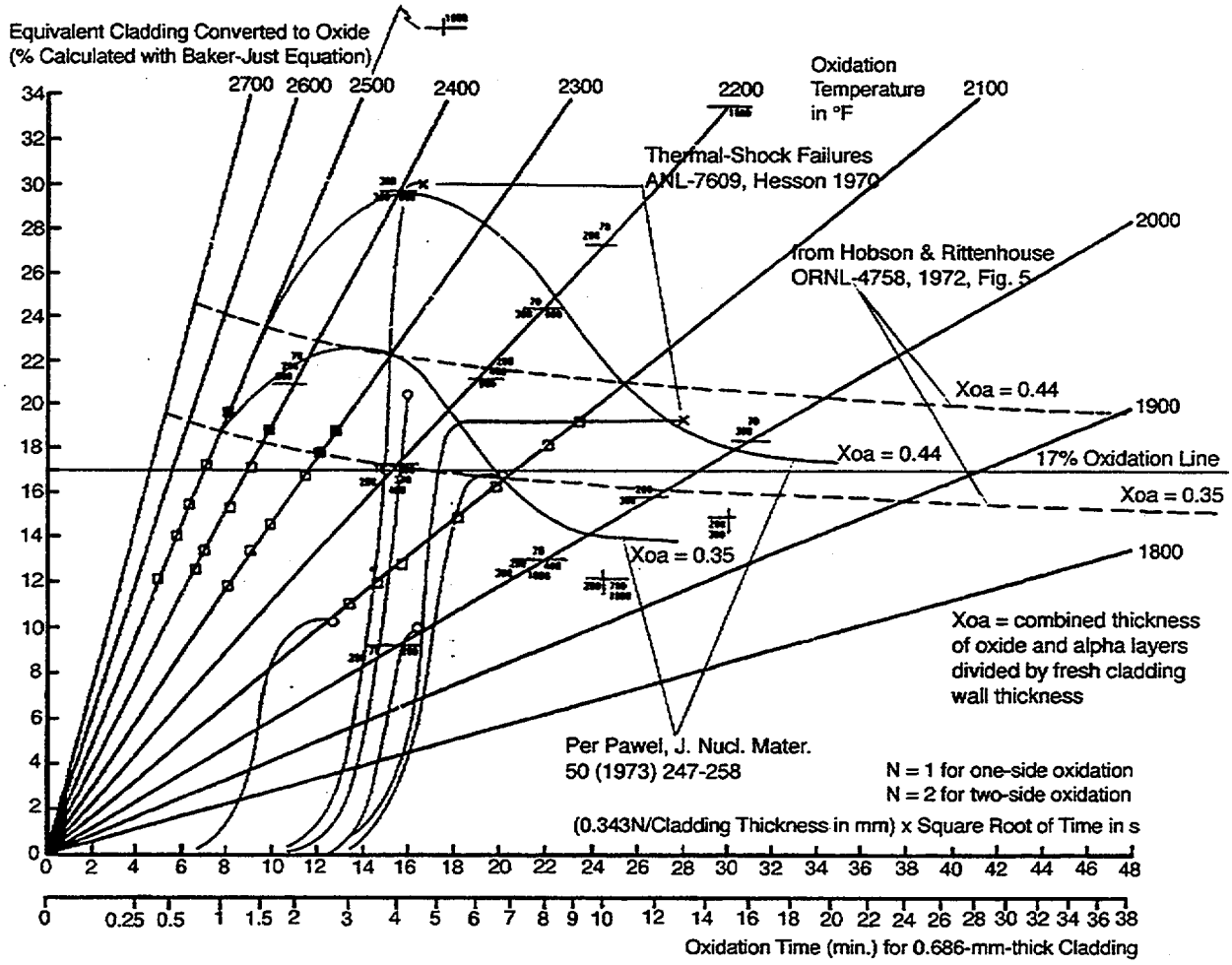

Figure 8.

Summary of multistep procedure used to establish 17% oxidation criterion during 1973 Rule-Making Hearing (from Docket RM-50-1, April 16, 1973). Note equivalent cladding oxidized was calculated per Baker-Just correlation. For comparison, time to reach threshold fraction of combined oxide and alpha layers of 0.44 is shown as determined per Hobson and Rittenhouse (ORNL-4758, January 1972) and Pawel (J. Nucl. Mater. 50, 1973, pp. 247-258).

By definition, **ECR parameter varies depending on cladding wall thickness,** either due to differences in fuel design or due to ballooning and

burst during the heatup phase in a LOCA. Figure 8 shows how to take account of the effects of variations in wall thickness and one- vs. two-sided oxidation.

Two of Hesson's thermal-shock experiments resulted in cladding fragmentation at calculated ECR values of ≈19 and ≈30%, as indicated in the figure. The other four did not fail at ECR values of ≈21, ≈16.5, ≈10, and ≈9.5%. The time-temperature transients in Hesson's tests were integrated also by **using the Baker-Just equation.**

The CE data, discussed in the Hearing, are represented by squares on the oxidation isotherms of 2500, 2400, 2300, and 2100°F. If the sample fractured on compression by CE's load standard, it was considered to have failed and is denoted with a filled square. Open squares denote CE's non-failed specimens. By the CE's load standard, only those samples with calculated ECR values >17% failed.

Based on the results given in Fig. 7 and the five sets of information shown in Fig. 8, one can conclude that **no samples tested by slow compression at >135°C failed with zero ductility if equivalent cladding reacted (ECR), calculated on the basis of Baker-Just correlation, was less than 17%.** Furthermore, all samples oxidized to <17% ECR (again calculated with Baker-Just correlation) survived direct quenching.

In summary, the AEC Commissioners concluded that the very good consistency between the **17% limit, if calculated with the Baker-Just equation,** and a wide variety of experiments supports adoption of this procedure [21], and it was further stated:

> "There is relatively good agreement among the industrial participants as to what the limit on total oxidation should be.... The regulatory staff in their concluding statement compared various measures of oxidation and concluded that a 17 % total oxidation limit is satisfactory, **if calculated by the Baker-Just equation**... As argued by the regulatory staff, it appears that the 17% oxidation limit is within the Rittenhouse criteria. Thus a remarkable uniformity of opinion seems to exist with regard to the 17% oxidation limit [13]."

It is clear that the primary **rationale of the 17% criterion is retention of cladding ductility** at temperatures higher than 275°F (135°C, i.e., the saturation temperature during reflood). Of major importance in this proceeding is that the **threshold ECR value of 17% is tied with the use of Baker-Just correlation.** That is, the 17% ECR criterion is specific to Baker-Just correlation that must be used to determine the degree of total oxidation. If an oxidation correlation other than the Baker-Just equation (e.g., Cathcart-Pawel correlation) were used, the threshold ECR would have been less than 17%.

This means that use of a best-estimate correlation may not necessarily be conservative in evaluating post-quench cladding ductility.

5.2 Other Embrittlement Criteria Proposed after the 1973 Hearing

Few months after the 1973 Hearing, Pawel proposed a new criterion based on <95 % saturation of the average oxygen concentration in the beta phase [27]. However, such a criterion fails to recognize that in addition to a sufficiently low O concentration, a minimum thickness of beta layer is required to ensure adequate resistance to failure. Such criterion is less facilitated to handle, especially during non-isothermal LOCA transients, and it requires a computer code that can accurately calculate O diffusion under moving-phase-boundary conditions, a task more difficult than the calculation of a simple parabolic oxidation correlation. Nevertheless, many of such computer codes have been developed after the 1973 Hearing, e.g., those reported in Refs. 17 and 24.

Sawatzky performed room-temperature tensile tests on specimens exposed to high-temperature spikes in steam [28]. Based on results of microhardness measurement, the distribution of O in the transformed beta (or prior beta) layer was found to be nonuniform, an observation confirmed subsequently by ANL investigators by Auger electron spectroscopy (Fig. 32-43, Ref. 17). In spite of total oxidation of only 16 %, a specimen with average O concentration >0.8 wt% in the prior beta exhibited very low strength and negligible elongation, whereas a specimen with O content <0.6 wt% in the prior beta retained some ductility. Based on this observation, Sawatzky proposed to replace the 1204°C PCT and the 17% ECR criteria by a unified criterion, that is, oxygen concentration in beta layer shall be <0.7 wt% over at least half of the cladding thickness. At temperatures >1280°C, Sawatzky's criterion is virtually identical to Pawel's criterion (see Fig. 9).

Validity of the three criteria illustrated in Fig. 9 is, however, subject to variations in cladding wall thickness, because the time to reach the specified threshold state of material is strongly influenced by the clad wall thickness which may vary with fuel design and the degree of ballooning and burst. Thus, it was deemed desirable to develop a unified embrittlement criterion that would be valid independent of variations in wall thickness and oxidation temperature [17].

5.3 One- vs. Two-Side Oxidation and Thermal-Shock Failure

Grandjean et al. have reported results of extensive thermal-shock tests which were performed in TAGCIS facility [29,30]. Hydrogen uptake in their short ring specimens was not excessive. In their investigation, ECR was calculated with PECLOX oxidation code [31], and failure-survival behavior was determined based on the result of gas-leakage check. The results of the tests were included in Fig. 6. The effect of one- vs, two-side oxidation on thermal-

shock failure was the focus of investigation. As indicated in Fig. 8, such effect was considered negligible in establishing the 17% ECR limit in the 1973 Rule-Making Hearing. Interestingly, Grandjean et al.'s failure threshold for two-side oxidation appears to be slightly higher than the threshold for one-sided oxidation, i.e., ≈21 vs. ≈20% ECR. Nonetheless, this study provides an independent confirmation of the validity of the 17% ECR criterion relative to susceptibility to thermal-shock failure.

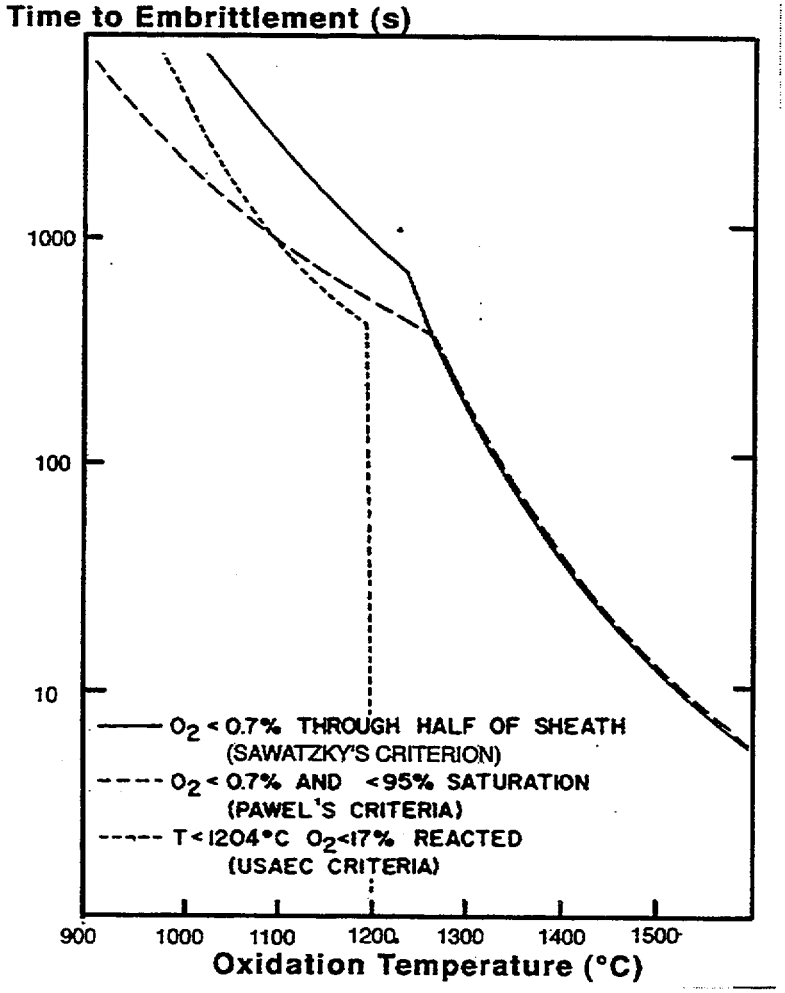

Figure 9.

Comparison of current embrittlement criteria with those proposed by Pawel (Ref. 27) and Sawatzky (Ref. 28).

5.4 17% Oxidation Limit and Impact Failure at Small Hydrogen Uptake

After the 1973 Hearing, ANL investigators conducted impact tests to provide an independent verification of the validity of 17% ECR threshold with respect to cladding resistance to impact failure [17]. Impact tests were performed at room temperature on non-pressurized open-ended Zircaloy-4 tubes that were oxidized on two sides in steam at 1100-1400°C and cooled through the beta-to-alpha-prime transformation range at 5 or ≈100°C/s. Because the sample was oxidized on both OD and ID sides, hydrogen uptake was limited to <130 wppm. Therefore, microstructure and oxygen and hydrogen distributions in the specimens were similar to those of the ring-

compression specimens of Hobson [25,26] that were cooled fast through the beta-to-alpha-prime transformation range.

It was found that slow-cooled specimens were more resistant to impact failure than fast-cooled specimens (Fig. 65, Ref. 17]. Results obtained for slow-cooled specimens are summarized in Fig. 10. The ECR values in Fig. 10 were directly determined based on measured phase layer thickness, therefore, are considered more accurate than values calculated based on Baker-Just correlation. The results in Fig. 10 show that for cladding oxidized at <1315°C to <17% ECR, a sufficient level of resistance to impact failure is retained at 23°C, i.e., failure impact energy of >0.8 J.

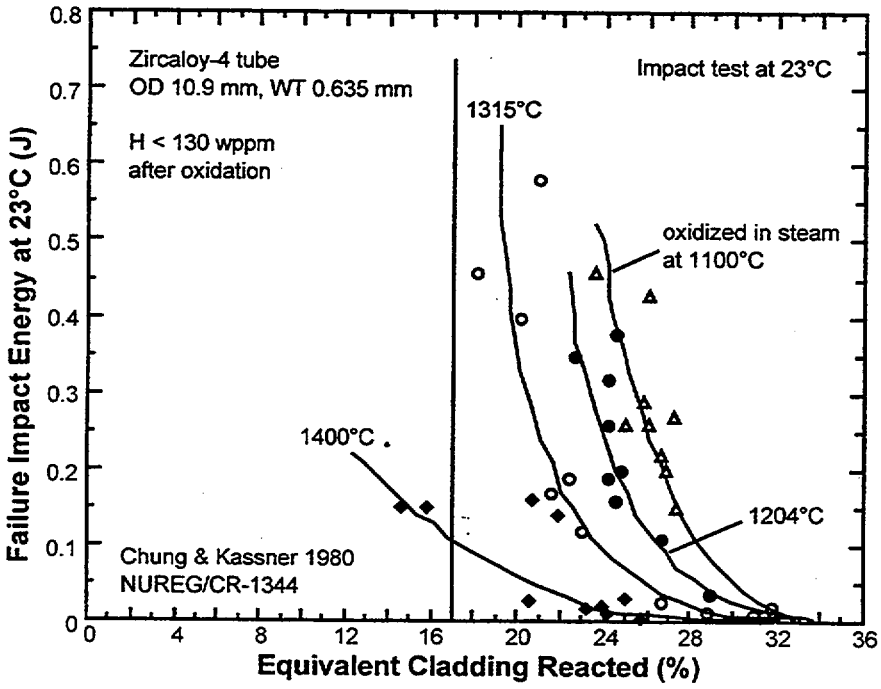

Figure 10.

Failure impact energy vs. equivalent cladding reacted, from tests at 23°C on undeformed Zircaloy-4 tube oxidized on two-sides and cooled at 5°C/s (Ref. 17).

5.5 17% Limit and Ring-Compression Ductility at Small Hydrogen Uptake

As shown in Fig. 8, the 17% threshold ECR was derived by indirect multistep procedure. Of particular importance in this procedure is the accuracy of two key factors, i.e., (1) temperature measurement in the experiments of Baker-Just and Hobson-Rittenhouse [25,26] and (2) definition of nil-ductility as given in Fig. 7. In consideration of this, ANL investigators performed independent compression tests at room temperature on short Zircaloy-4 ring specimens. Rings were sectioned from long tubes that were oxidized in steam at 1100-1400°C and cooled through the beta-to-alpha-prime transformation range at 5 or ≈100°C/s. Hydrogen uptake in the ring specimens was <130 wppm. This procedure reproduced the conditions of the ring-compression tests of Hobson. In the ANL compression tests, however, load-

deflection curves were obtained to better quantify the degree of remaining ductility and the magnitude of load that a ring can sustain.

It was found that slow-cooled specimens retained more ductility than fast-cooled specimens under otherwise identical conditions (Fig. 67, Ref. 17]. Figure 11 summarizes results obtained for a slow-cooling rate of ≈5°C/s, a rate probably more prototypic of a LOCA than fast cooling. The ECR values in the figure were determined based on measured phase layer thickness and time-temperature history. This result shows that for cladding oxidized at <1315°C to <17% ECR, ductility is retained at 23°C (i.e., relative diametral deflection >16%); no brittle failure was observed. This experiment provides an independent confirmation of the validity of the 17% oxidation limit for undeformed Zircaloy specimens that contain hydrogen <130 wppm.

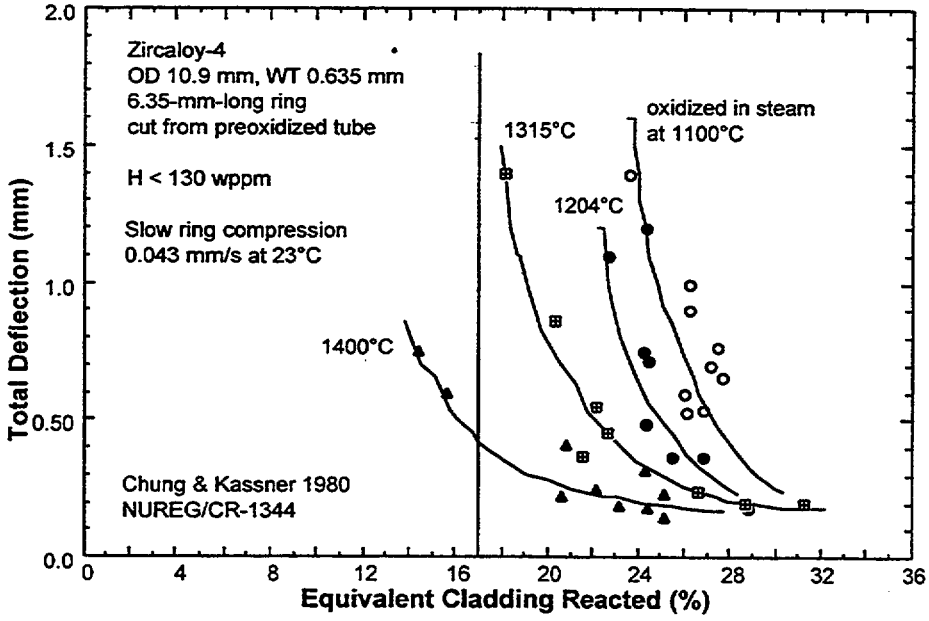

Figure 11.

Total deflection at 23°C vs. equivalent cladding reacted, from ring-compression tests on Zircaloy-4 oxidized on two-sides and cooled at 5°C/s (Ref. 17).

5.6 Resistance to Impact Failure at Large Hydrogen Uptake

In addition to the impact tests on non-ruptured empty tubes, ANL investigators performed 0.15- and 0.3-J pendulum impact tests at 23°C on pressurized Zircaloy-4 tubes that were burst, oxidized, cooled at ≈5°C/s, and survived quenching thermal shock [17]. The CSNI experts [18] considered that: "Ambient impact of 0.3 J were thought to be a reasonable approximation to post LOCA quench ambient impact loads." The results of the 0.3-J impact tests, summarized in Fig. 12, indicate that the 17%-ECR limit is adequate to prevent a burst-and-oxidized cladding from failure under 0.3-J impact at 23°C, as long as peak cladding temperature remained ≤1204°C. The ECR values in the figure were determined based on measured thickness of oxide, alpha, and

beta phase layers, rather than calculated based on Baker-Just correlation, and hence, are considered more accurate.

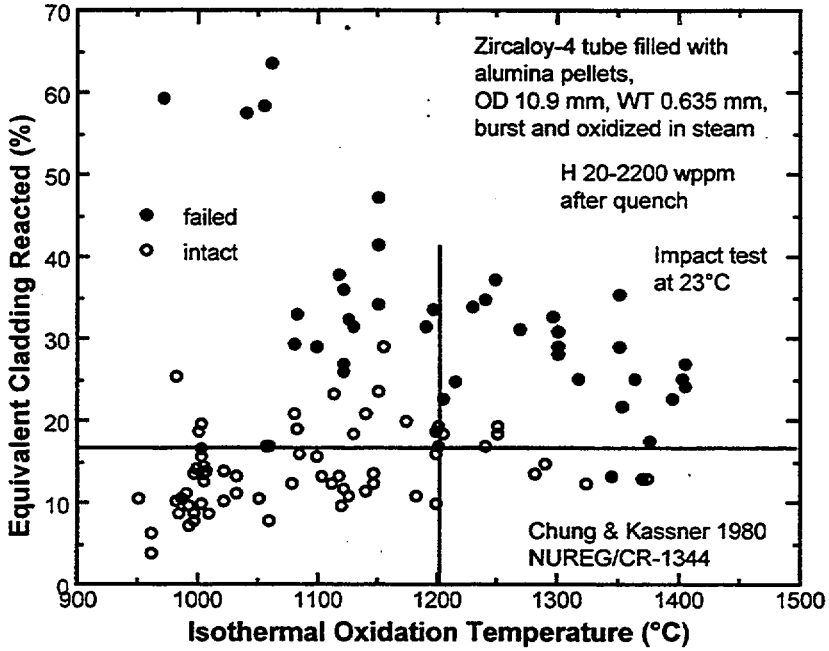

Figure 12.

Impact failure threshold as function of equivalent cladding reacted and oxidation temperature of burst, oxidized, slow-cooled, and quenched Zircaloy-4 tube containing 20-2200 wppm hydrogen (from Ref. 17).

In contrast to two-side-oxidized non-pressurized non-ruptured tubes in which hydrogen uptake was small (<130 wppm), burst Zircaloy-4 tubes exhibited peculiar oxidation behavior near the burst opening. The inner-diameter (ID) surfaces of the top and bottom "necks," ≈30-mm away from the burst center, were exposed to hydrogen-rich stagnant steam-hydrogen mixture which is produced because of poor mixing of steam and hydrogen at the narrow gap between the alumina pellets and the ID surface of the necks. As a consequence, thick breakaway oxides formed at 900-1120°C [17], and hydrogen uptake as high as ≈2200 wppm was observed at the "necked" regions. Subsequently, JAERI investigators confirmed occurrence of the same phenomenon [32,33].

The results from the same tests shown in Fig. 12 were converted to failure-survival map based on average hydrogen content of the impact-loaded local region and the thickness of transformed-beta layer containing <0.7 wt.% oxygen. This failure-survival map is shown in Fig. 13. On the basis of the figure, ANL investigators proposed to replace the 1204°C PCT and 17% ECR criteria by a unified criterion which specifies that the thickness of transformed-beta layer containing <0.7 wt.% oxygen shall be >0.3 mm [17]. The criterion implicitly incorporates a limit in peak cladding temperature. This limiting temperature corresponds to the temperature at which oxygen solubility is 0.7 wt.% in Zircaloy that contains 700-1200 wppm hydrogen. This temperature is believed to be between 1200 and 1250°C, although the exact data from

applicable Zircaloy-O-H ternary diagrams are not. This criterion is not subject to variations in cladding wall thickness and oxidation temperature.

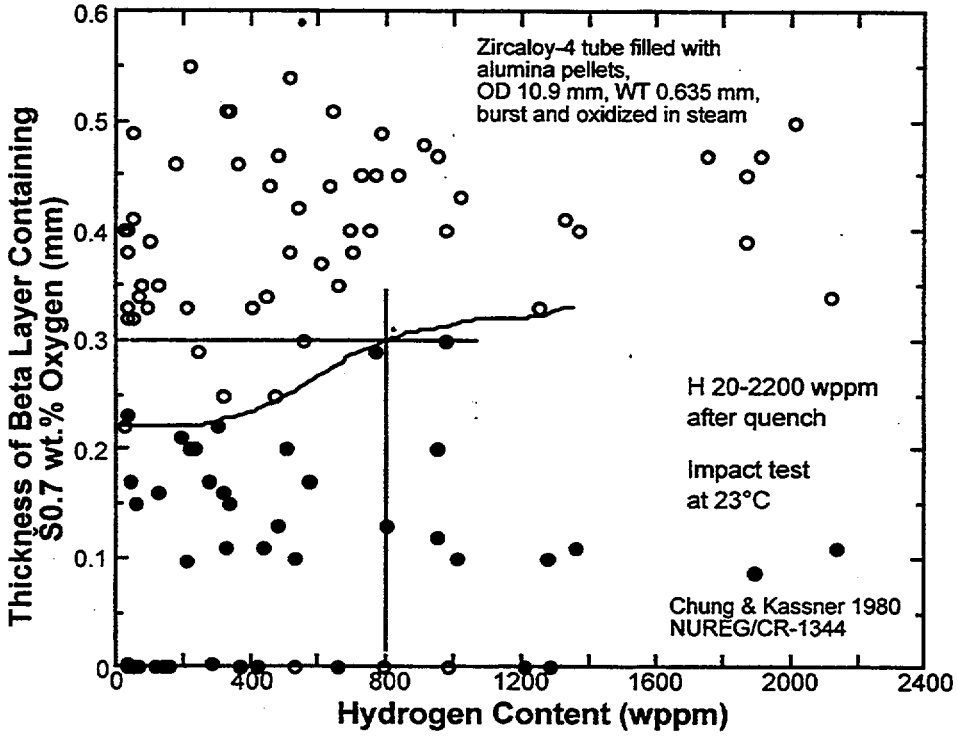

Figure 13.

Impact failure map as function of hydrogen content and thickness of beta layer containing ≤0.7 wt.% oxygen; Zircaloy-4 tube burst, oxidized, slow-cooled, and quenched (from Ref. 17).

The results in Fig. 13 show that for a given thickness and a given oxygen content in transformed-beta layer, resistance of cladding to impact failure is significantly reduced if hydrogen uptake exceeds ≈700 wppm. Such situation does not occur in non-pressurized, non-ruptured, two-side-oxidized Zircaloy cladding, such as those tested by Hobson [26] or discussed in Figs. 10 or 11.

5.7 Ring-Compression Ductility at Large Hydrogen Uptake

Investigators in ANL [17] and JAERI [32,33] conducted extensive tests on tube or ring specimens of Zircaloy-4 that contained high concentrations of hydrogen. In the former investigation, Zircaloy-4 tubes filled with alumina "pellets" were pressurized, heated, burst, oxidized, slow-cooled, and quenched with bottom-flooding water. Then, the tubes that survived the quenching thermal shock were compressed diametrically at 23°C [17]. Such specimens contained H up to ≈2200 wppm. In the latter investigation, short rings, sectioned from tubes that were exposed to similar conditions, were compressed at 100°C. The ring specimens contained H up to ≈1800 wppm. Typical distributions of oxide layer thickness, hydrogen concentration, and ring deflection to failure are shown in Fig. 14. The top and bottom "necks" that contained the highest concentration of hydrogen and the thinnest transformed-beta layer exhibited the lowest ductility.

However, ANL investigators observed that the rate of hydrogen generation, amount of hydrogen uptake, and hence, the degree of embrittlement of the necked regions are strongly influenced by the method of heating cladding tubes during LOCA-like transients, i.e., more uniform (indirect heating in JAERI) vs. less uniform (direct heating in ANL) heating [17]. This is schematically illustrated in Fig. 15.

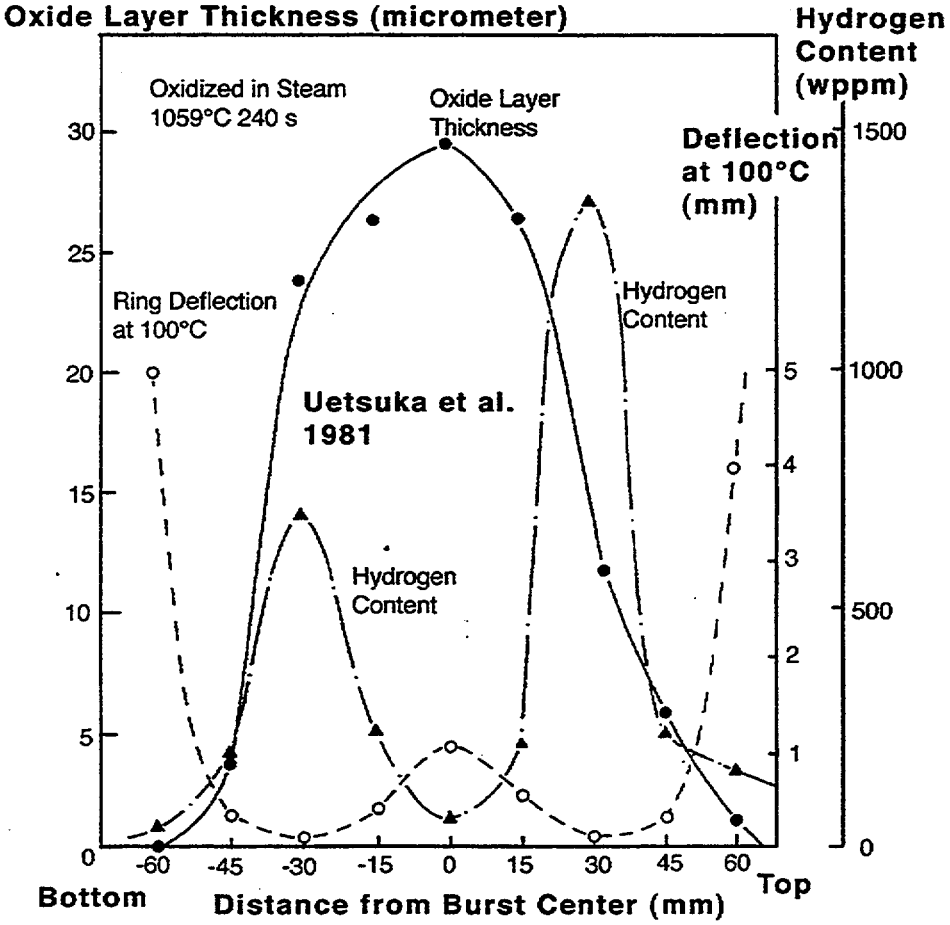

Figure 14.

Distributions of hydrogen content, inner-diameter oxide layer thickness, and total deflection at 100°C of ring specimens sectioned from burst region (from Uetsuka et al., Refs. 32 and 33).

The effect of hydrogen uptake on post-quench ductility, determined either from diametral-compression test of burst-and-oxidized tubes at 23°C [17] or compression at 100°C of ring specimens sectioned from burst-and-oxidized tubes [32,33], is summarized in Fig. 16. At hydrogen uptake >700 wppm, significant embrittlement of cladding is evident, even if total oxidation is <17% (see Fig. 14). Similar dependencies of plastic deflection on beta-layer oxygen content and total hydrogen content have been also reported in Fig. 88, Ref. 17 and Fig. 89, Ref. 17, respectively. These results show that post-quench ductility of Zircaloy is strongly influenced by not only oxidation but also hydrogen uptake. This is shown in Fig. 17. Apparently, the important effect of

hydrogen uptake on post-quench ductility was not well realized at the time of 1973 Hearing.

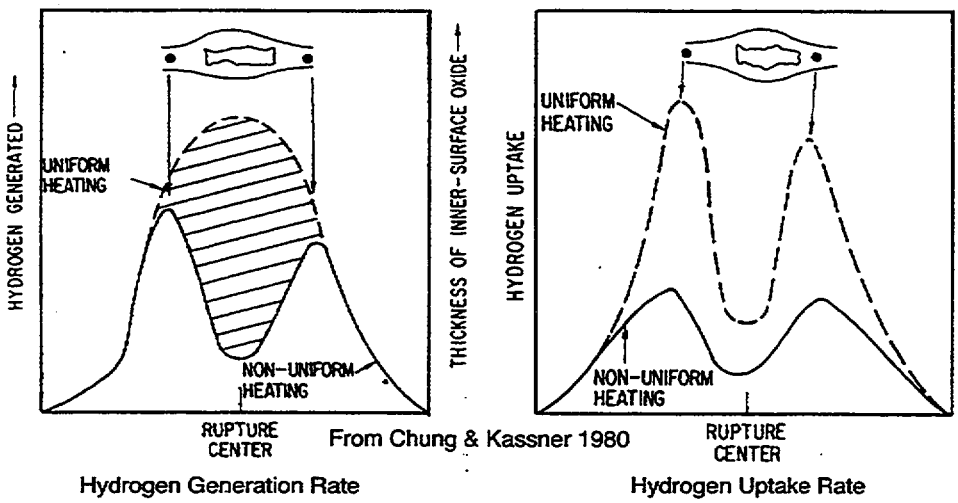

Figure 15.

Effect of heating method (uniform vs. nonuniform heating) on hydrogen generation and uptake near burst opening (from Ref. 17)

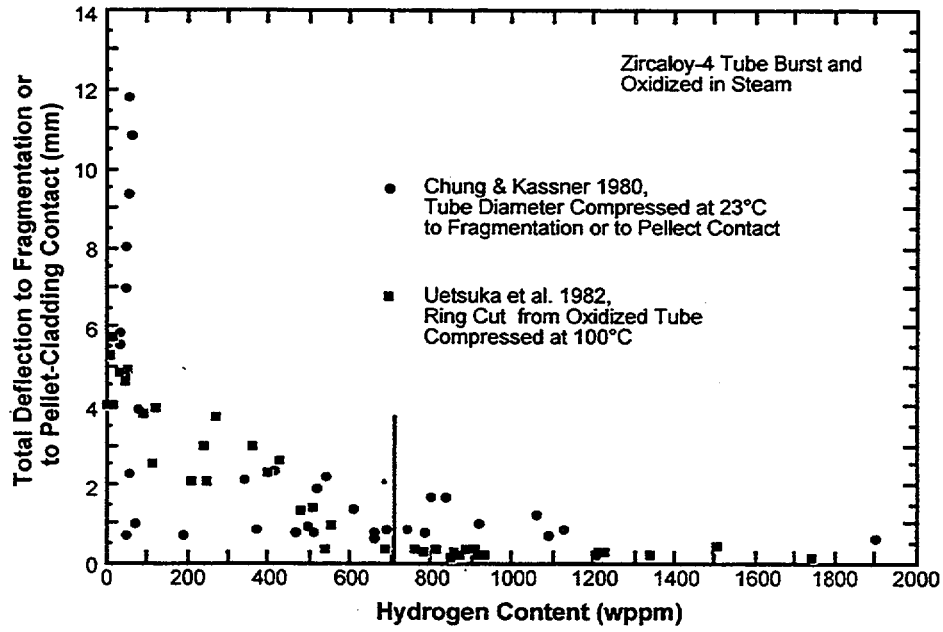

Figure 16.

Effect of hydrogen uptake on diametral deflection of burst, oxidized, and quenched Zircaloy-4 tube or sectioned ring.

Essentially similar observation has also been reported by Komatsu et al. [34,35]. They reported that the load to initial ring cracking is strongly influenced by total oxidation and hydrogen uptake. For oxidation temperatures >1260°C in which the oxygen content in the beta layer exceeds ≈0.7 wt.% in short period of time, the embrittling effect of oxygen appears to be predominant (see Fig. 18). The "zero-ductility" region denoted in Fig. 18 appears to have been determined based on a threshold load to initial cracking rather than based

on ductility consideration. As such, this "zero-ductility" threshold differs significantly from that defined by Hobson [25,26].

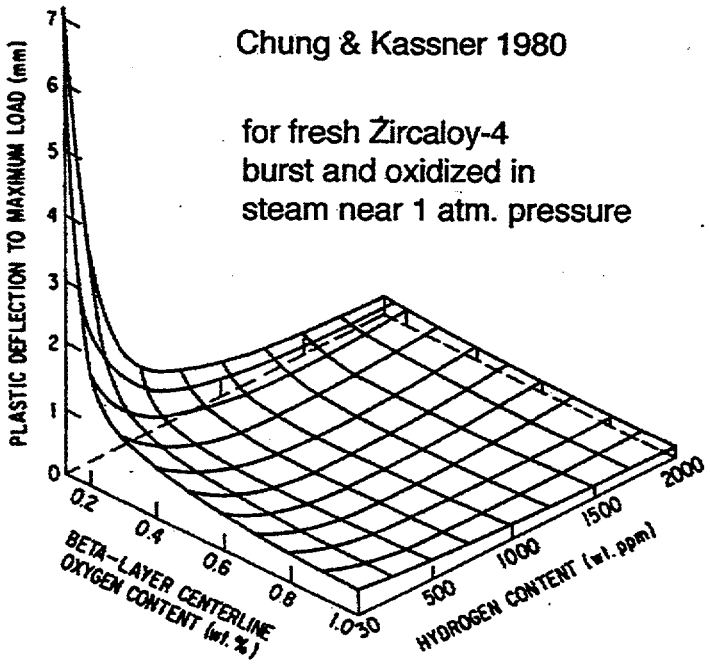

Figure 17.

Post-quench ductility shown as function of oxidation (beta-layer centerline oxygen content) and total hydrogen content, from diametral compression test at 23°C on burst, oxidized, slow-cooled, and quenched Zircaloy-4 tubes (for database see Ref. 17).

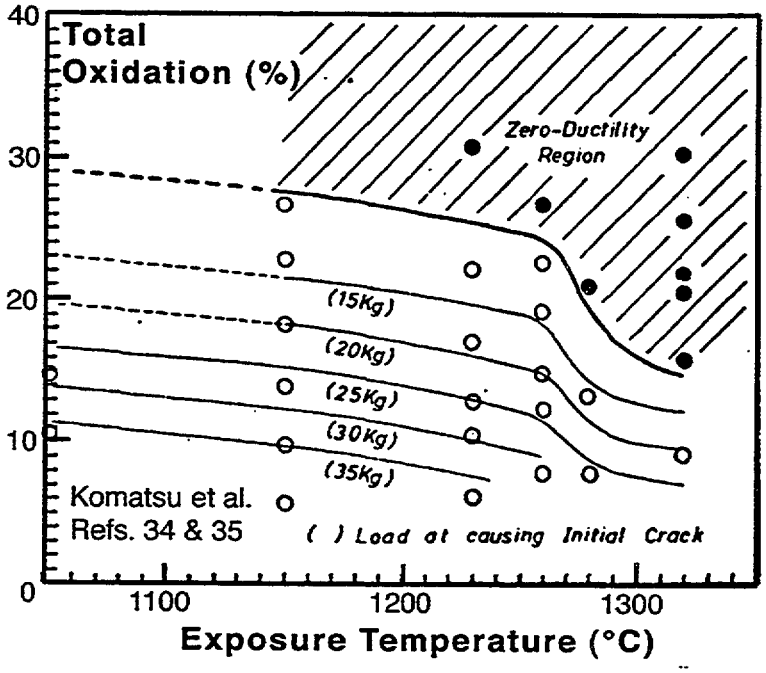

Figure 18.

Applied load at initial cracking of ring as function of total oxidation and exposure temperature, from Komatsu et al., Refs. 34 and 35.

5.8 17% Oxidation Criterion - Summary

It is clear that the primary rationale of the 17% ECR criterion is retention of cladding ductility at temperatures higher than 275°F (135°C), i.e., the saturation temperature during reflood. The threshold ECR value of 17% is tied

with the use of Baker-Just correlation. If a best-estimate correlation other than Baker-Just equation (e.g., Cathcart-Pawel correlation) were used, the threshold ECR would have been <17%.

Investigations conducted after the 1973 Rule-Making Hearing showed that for oxidation temperatures ≤1204°C, the 17% oxidation limit (as calculated with Baker-Just correlation) is adequate to ensure survival of fully constrained or unconstrained cladding under quenching thermal shock. It was also shown that the 17% limit (ECR determined on the basis of measured phase layer thickness) is adequate to ensure retention of ductility and resistance to 0.3-J impact failure in non-irradiated, non-ruptured, two-side-oxidized Zircaloy cladding in which hydrogen uptake during a LOCA-like transient is small.

However, the 17% limit appears to be inadequate to ensure post-quench ductility for hydrogen uptake >700 wppm. Such level of large hydrogen uptake could occur in some types of fuel rods during normal operation, especially at high burnup, or during a LOCA-like transient in localized regions in a ballooned and ruptured node.

6. 1204°C (2200°F) Peak Cladding Temperature Criterion

6.1 Selection of 1204°C Criterion in 1973 Hearing

From the results of posttest metallographic analysis of the slow-ring-compression specimens, Hobson [26] observed a good correlation between zero ductility temperature (ZDT) and fractional thickness of transformed-beta layer (or the sum of oxide plus alpha layer thickness) as long as the specimen was oxidized at ≤2200°F (1204°C) (see Fig. 7). However, in spite of comparable thickness of transformed beta layer, specimens oxidized at 2400°F (1315°C) were far more brittle. This observation was explained on the basis of excessive solid-solution hardening of transformed-beta phase at high oxygen concentrations. For mechanical properties near room temperature the critical concentration of oxygen in the transformed-beta was estimated to be ≈0.7 wt%. Above this concentration, transformed beta phase becomes brittle near room temperature. Because of the solubility limit of oxygen in the beta phase, this high O concentration cannot be reached at 2200°F (1204°C) but can be reached at 2400°F (1315°C). Hobson concluded that: "embrittlement is not simply a function of the extent of oxidation alone, but is related in yet another way to the exposure temperature."

During the 1973 Rule-Making Hearing, AEC Staff endorsed Hobson's conclusion and wrote: "The staff recognizes the importance of oxygen concentration in the beta phase in determining the load bearing ability of Zircaloy cladding, and the implication from the recent compression tests that this may not be satisfactorily characterized above 2200°F by a ZDT as a

function of remaining beta fraction only. We therefore believe that **peak cladding temperatures should be limited to 2200°F** [20]."

Subsequently, it was also concluded that:

"Additional metallurgical and slow compression mechanical tests on other quenched samples from the ORNL experiments indicated that an important consideration was the amount and distribution of oxygen in the nominally ductile prior-beta phase. However, these factors could not be correlated as functions of time and temperature in the same manner as the (combined oxide and alpha layer) penetration. In particular, the slow compression tests indicated a greater degradation in cladding ductility at higher temperatures than would be expected from considerations of (combined oxide and alpha layer) penetration alone. It was on this basis that **the staff previously suggested a 2200°F maximum cladding temperature**... What was observed in the slow compression tests was that 6 samples exposed at 2400°F for only two minutes and with relatively high values of Fw (Fw being fractional thickness of prior beta, all greater than 0.65) all fractured with nil ductility... Only when brittle failure was detected at high Fw in the slow compression tests did the suspicion arise that ductility was a function of both Fw and the exposure temperature... As the temperature rises above 2200-2300°F, solid solution hardening in the beta phase appears to contribute significantly to formation of a brittle structure. That is, brittle failure occurs even though alpha incursions are not observed, and the fraction of remaining beta is greater than that observed in lower temperature tests. This is confirmed by examination of the six samples from the ORNL exposed at 2400°F for two minutes (Exhibit 1126)... From the foregoing, there is ample evidence that load bearing ability and ductility decrease with increasing exposure temperatures, even for transients with comparable Fw. Increased solubility of oxygen in the prior-beta phase has been discussed as a contributing factor... The staff believes that because of high temperature degradation ... phenomena (... strongly suggested by the experimental evidence cited), **the suggested 2200°F limit should be imposed** [21]."

Then it was added:

"The situation is complicated by the fact that not all of the prior beta phase is equally strong or ductile, since these properties depend on the amount of dissolved oxygen. This fact has been suspected for some time... From the phase diagram, given by both Scatena and Westinghouse, it is obvious that it is possible for the beta phase zirconium to take on a higher oxygen content at 2600°F than at 2000°F. Furthermore, since the diffusion rate depends exponentially upon temperature, one might expect a greater incursion of oxygen into the beta phase for a given thickness of oxide and stabilized alpha phase at higher temperatures... Others (than Hobson) have also observed that the resistance to rupture depends upon the temperature at which oxidation occurs

as well as the extent of oxidation... To recapitulate, measures of Zircaloy oxidation, whether by percent, X_T, or F_W, are largely or wholly determined from the brittle layers of zirconium oxide or stabilized alpha phase, while the ductility and strength of oxidized zirconium depend upon the condition and the thickness of the prior beta phase... Thus a criterion based **solely on the extent of total oxidation is not enough, and some additional criterion is needed** to assure that the prior beta phase is not too brittle. The specification of a maximum temperature of 2200°F will accomplish this **adequately. The data cited in exhibit 1113 would not support a choice of a less conservative limit** [13]."

Few months after the Hearing, Pawel [27] explained Hobson's observation based on data that indicate oxygen solubility in the beta Zr at 2200-2400°F (1204-1316°C) is ≈0.7 wt.%. The O solubility in beta Zircaloy is significantly influenced by not only temperature but also the concentration of hydrogen, a strong beta stabilizer. Nevertheless, Pawel endorsed that: "...the above reasoning easily explains why the mechanical or load bearing properties of the oxidized specimens should not be a unique function of the extent of (total) oxidation." Consequently, Pawel proposed to replace the peak cladding temperature (PCT) criterion by a new criterion that specifies the average oxygen concentration in the beta phase shall be less than 0.7 wt% [see Fig. 9].

6.2 1204°C Limit vs. In-Pile Test Results

In 1970s, high-temperature oxidation and embrittlement behaviors were investigated extensively in TREAT and PBF test reactors. During the TREAT-FRF2 test, a seven-rod cluster was oxidized at 2400°F (≈1315°C) [36]. According to hardness measurements, all rods contained portions that possessed no ductility at room temperature. Three rods were broken accidentally during handling in ORNL hot cell, which indicates the degree of brittleness of a badly embrittled rod and the magnitude of a typical load during handling in hot cell (see Fig. 19).

Some fuel rods tested in the Power Burst Facility (PBF) were also known to have failed during handling or posttest examination in hot cell. This information is summarized in Fig. 20 [37]. Total oxidation of several failed rods were <17 %. Of particular interest is Rod IE-019 of Test IE 5, because ballooning and burst occurred in the rod before exposure to temperatures >1100°C. In spite of the fact that ECR was only ≈12%, the rod broke into pieces after exposure to an "equivalent" oxidation temperature of ≈1262°C. Most likely, actual peak temperature was higher than this equivalent temperature. Rod A-0021 also ruptured before entering high temperature transient; this caused ingress of steam to the rod interior. The rod failed after exposure to ≈1307°C, although ECR was only ≈6%. Hydrogen uptake in the two rods was excessive because of exposure to stagnant steam near the rupture opening.

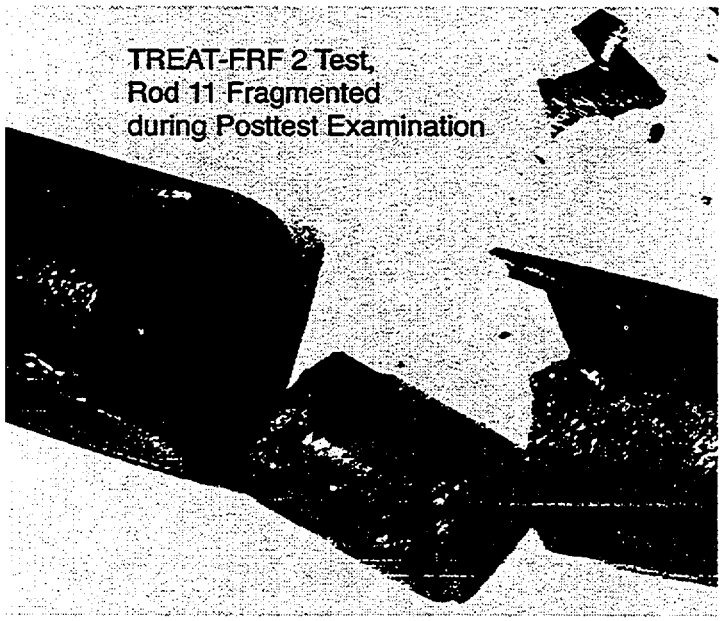

Figure 19.

Fuel pellet released through fragmented cladding section of Rod 11, TREAT-FRF 2 Test (from Ref. 37).

It is not clear if the failure behavior of Rods IE-019 and A-0021 is predicted based on Pawel's criterion (Fig. 9). However, because the exposure temperatures of the rods exceeded ≈1262°C, the thickness of beta layer that contained ≤0.7 wt.% oxygen should have been zero or close to zero. However, because oxygen solubility in beta is influenced by hydrogen and because accurate peak temperatures reached in the rods are not well known, it is difficult to calculate accurately the thickness of beta layer that contains O ≤0.7 wt.%. Therefore, it is not clear if the failure behavior of the two rods is consistent with the criterion shown in Fig. 13.

As long as clad oxidation temperature was limited to ≤1204°C, a handling failure at measured ECR <17% was not observed from the TREAT and PBF tests or the ANL 0.3-J impact tests (see Fig. 20). This observation clearly demonstrates the importance of the 1204°C PCT limit. That is, the 1204°C PCT and the 17% ECR limits are inseparable, and as such, constitute an integral criterion.

6.3 Summary of 1204°C Criterion

The 2200°F (1204°C) peak cladding temperature (PCT) criterion was selected on the basis of Hobson's slow-ring-compression tests that were performed at 25-150°C. Samples oxidized at 2400°F (1315°C) were far more brittle than samples oxidized at <2200°F (<1204°C) in spite of comparable level of total oxidation. This is because oxygen solid-solution hardening of the prior-beta phase is excessive at oxygen concentrations >0.7 wt%.

The selection of the 1204°C criterion was subsequently justified by the observations from the ANL 0.3-J impact tests and the handling failure of rods

tested in the Power Burst Facility. These results also take into account of the effect of large hydrogen uptake that occurred near the burst opening. Consideration of potential for runaway oxidation alone would have lead to a PCT limit somewhat higher than 2200°F (1204°C). In conjunction with the 17% oxidation criterion, the primary objective of the PCT criterion is to ensure adequate margin of protection against post-quench failure that may occur under hydraulic, impact, handling, and seismic loading.

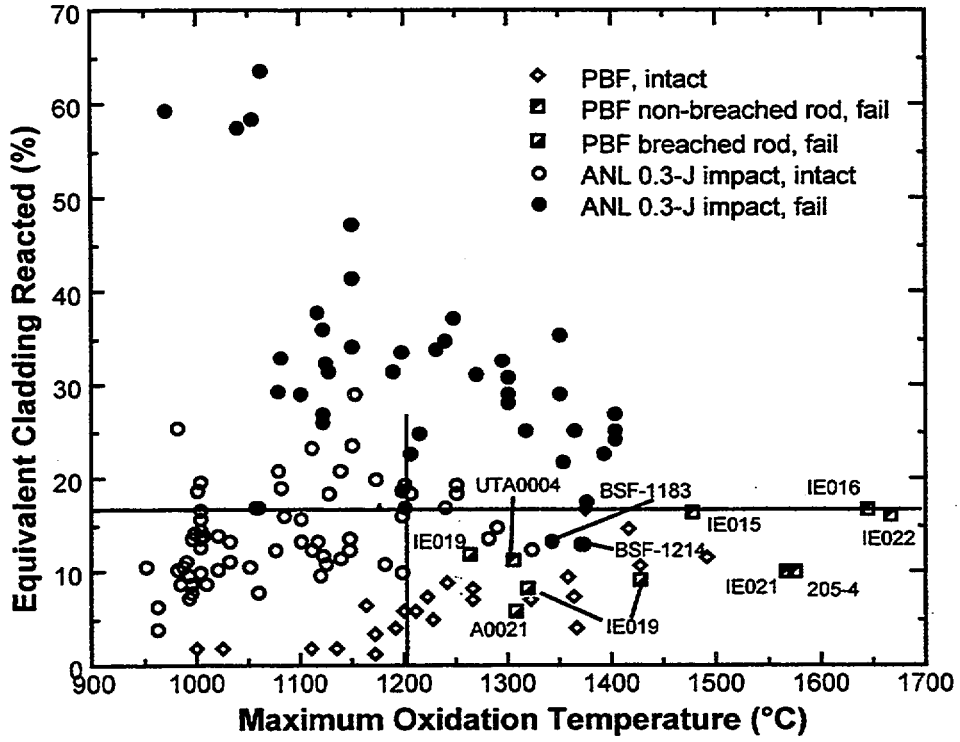

Figure 20.

Comparison of data from hot-cell handling failure of Zircaloy rods exposed to high temperature in Power Burst Facility (Ref. 37) and 0.3-J impact tests in ANL (Ref. 17).

7. Conclusions

1. In the 1973 Rule-Making Hearing, the U. S. Atomic Energy Commission (AEC) staff and commissioners were clearly reluctant to neglect the effect of mechanical constraints on the susceptibility of oxidized fuel cladding to thermal-shock fragmentation. Subsequent test results appear to justify this rationale. Results from unconstrained or partially constrained quench tests were considered only corroborative; their use for regulatory purposes was not accepted.

2. The AEC staff and commissioners and OECD-CSNI specialists were of the opinion that retention of ductility was the best guarantee against potential fragmentation of fuel cladding under various types of not-so-well-quantified loading, such as thermal shock, hydraulic, and seismic forces, and the forces related with handling and transportation.

3. Primary rationale of the 17% oxidation criterion was retention of cladding ductility at temperatures higher than 275°F (135°C), i.e., the saturation temperature during reflood. The threshold equivalent cladding reacted (ECR) of 17% is tied with the use of Baker-Just correlation. If a best-estimate correlation other than Baker-Just equation (e.g., Cathcart-Pawel correlation) had been used, the threshold ECR would have been <17%.

4. Investigations conducted after the 1973 Rule-Making Hearing show that for oxidation temperatures ≤1204°C, the 17% oxidation limit (calculated with Baker-Just correlation) is adequate to ensure survival of unconstrained or fully constrained cladding under quenching thermal shock. It was also shown that the 17% limit (ECR determined on the basis of measured phase layer thickness) is adequate to ensure retention of ductility and resistance to 0.3-J impact failure in non-irradiated non-ruptured two-side-oxidized Zircaloy cladding in which hydrogen uptake during a LOCA-like transient is small.

5. However, the 17% ECR limit appears to be inadequate to ensure post-quench ductility at hydrogen concentrations >700 wppm. A major finding from tests performed after the 1973 Rule-Making Hearing shows that post-quench ductility is strongly influenced by not only oxidation but also hydrogen uptake. It seems that this effect of large hydrogen uptake was not known at the time of 1973 Hearing.

6. By definition, an embrittlement criterion expressed in terms of ECR is subject to uncertainties because calculated ECR varies with variations in cladding wall thickness and the degree of ballooning.

7. The 1204°C peak cladding temperature (PCT) limit was selected on the basis of slow-ring-compression tests that were performed at 25-150°C. Samples oxidized at 1315°C were far more brittle than samples oxidized at 1204°C in spite of comparable level of total oxidation. This is because oxygen solid-solution hardening of the prior-beta phase is excessive at oxygen concentrations >0.7wt%. Consideration of potential for runaway oxidation was a secondary factor in selecting the 1204°C limit. The 1204°C limit was subsequently justified by the observations from impact tests and handling failure of fuel rods exposed to high temperatures in the Power Burst Facility. The 1204°C PCT and the 17% ECR limits are inseparable, and as such, constitute an integral criterion.

8. The degree of oxygen saturation and the thickness of beta layer that contains oxygen concentrations ≤0.7 wt.% were important parameters used by investigators to develop new embrittlement criteria based on beta phase thickness rather than total oxidation. Such a criterion is not subject to inherent uncertainties associated with variations in cladding wall thickness and pre-LOCA oxidation.

9. Post-quench ductility and toughness are determined primarily by the thickness and the mechanical properties of transformed-beta layer. The mechanical properties are strongly influenced by several factors such as: oxygen solubility in beta, concentrations of alpha- (tin and oxygen) and beta-stabilizing elements (niobium and hydrogen), the nature of beta-to-alpha-prime transformation, redistribution of oxygen, niobium, and hydrogen during the transformation, and precipitation of hydrides. Significantly large hydrogen uptake can occur in some types of fuel cladding, during normal operation to high burnup, during breakaway oxidation at <1120°C, and, for localized regions near a rupture opening, during LOCA transients. Hydrogen uptake and its effect on the properties of transformed beta could differ significantly in Zircaloys and in niobium-containing alloys. Considering these factors, it is recommended to obtain a better understanding of the effects of more realistic hydrogen uptake and niobium addition on the properties of transformed-beta layer and post-quench ductility.

Acknowledgments

The authors would like to express thanks to C. Grandjean, R. O. Meyer, and S. Basu for helpful discussions.

References

1. Grandjean, C. et al., "Oxidation and quenching experiments with high burnup cladding under LOCA conditions," Proc. 26th Water Reactor Safety Information Meeting, Bethesda, USA, 26-28 October, 1998.
2. Mardon, J.P. et al., "The M5 fuel rod cladding," Proc. ENS TOP'FUEL 99, Avignon, France, 13-15 September, 1999.
3. Nagase, F. et al., "Experiments on high burnup fuel behavior under LOCA conditions at JAERI," Proc. ANS Topical Meeting on LWR fuel Performance, Park City, USA, 10-13 April, 2000.
4. Ozawa, M. et al., "Behavior of irradiated zircaloy4 fuel cladding under simulated LOCA conditions," Proc. 12th Symp. on Zirconium in the Nuclear Industry, Toronto, Canada, 15-18 June, 1998.
5. Aomi, M. et al., "Behavior of irradiated BWR fuel cladding tubes under simulated LOCA conditions," Proc. ANS Topical Meeting on LWR fuel Performance, Park City, USA, 10-13 April, 2000.
6. Chung, H.M. et al., "Test plan for high-burnup fuel cladding behavior under loss-of-coolant accident conditions," Proc. 24th Water Reactor Safety Information Meeting, Bethesda, USA, 21-23 October, 1996.
7. Report of Advisory Task Force on Power Reactor Emergency Cooling, TID-24226, 1967.

8. General Design Criteria for Nuclear Power Plants, U.S. Code of Federal Regulations, Title 10, Part 50, Appendix A, 20 February, 1971, amended.

9. Interim Acceptance Criteria for Emergency Core-Cooling Systems for Light-Water Power Reactors, U.S. Federal Register 36 (125), pp. 12247-12250, 29 June, 1971.

10. Cottrell, W.B., "ECCS rule-making hearing," Nucl. Safety 15 (1974) 30-55.

11. New acceptance criteria for emergency core-cooling systems of light-water-cooled nuclear power reactors, Nucl. Safety 15 (1974) 173-184.

12. Acceptance Criteria for Emergency Core Cooling Systems for Light-Water Nuclear Power Reactors, U.S. Code of Federal Regulations, Title 10, Part 50, Section 46, 4 January, 1974, Amended.

13 Atomic Energy Commission Rule-Making Hearing, Opinion of the Commission, Docket RM-50-1, 28 December, 1973.

14. Hesson, J.C. et al., Laboratory Simulations of Cladding-Steam Reactions Following Loss-of-Coolant Accidents in Water-Cooled Power Reactors, ANL-7609, January 1970.

15. Parker, G.W. et al., "Release of fission products from reactor fuels during transient accidents simulated in TREAT," Proc. Intl. Symp. Fission Product Release and Transport under Accident Conditions, Oak Ridge, USA, 5-7 April, 1965.

16. Fujishiro, T. et al., "Light water reactor fuel response during reactivity initiated accident experiments," NUREG/CR-0269, August 1978.

17. Chung, H.M. and Kassner, T.F., Embrittlement Criteria for Zircaloy Fuel Cladding Applicable to Accident Situations in Light-Water Reactors, NUREG/CR-1344, January 1980.

18. Parsons, P.D. et al., The Deformation, Oxidation and Embrittlement of PWR Fuel Cladding in a Loss-of-Coolant Accident: A State-of-the-Art Report, CSNI Report 129, December 1986.

19. Zuzek, E. et al., "The H-Zr (hydrogen-zirconium) system," Bulletin of Alloy Phase Diagrams, 11 (1990) 385-395.

20. Atomic Energy Commission Rule-Making Hearing, Supplemental Testimony of the Regulatory Staff Docket RM-50-1, 26 October, 1972.

21. Atomic Energy Commission Rule-Making Hearing, Concluding Statement of the Regulatory Staff, Docket RM-50-1, 16 April, 1973.

22. Uetsuka, H. et al., "Failure-bearing capability of oxidized Zircaloy-4 cladding under simulated loss-of-coolant condition," J. Nucl. Sci. Tech. 20 (1983) 941-950.

23. Reocreux, M. and Scott de Martinville, E., "A study of fuel behavior in PWR design basis accident: An analysis of results from the PHEBUS and EDGAR experiments," Nucl. Eng. Design 124 (1990) 363-378.

24. Suzuki, M. and Kawasaki, S., "Development of computer code PRECIP-II for calculation of Zr-steam reaction," J. Nucl. Sci. Tech. 17 (1980) 291.

25. Hobson, D.O., and Rittenhouse, P. L., "Embrittlement of Zircaloy Clad Fuel Rods by Steam During LOCA Transients," ORNL-4758, Oak Ridge National Laboratory, January 1972.

26. Hobson, D.O., "Ductile-brittle behavior of Zircaloy fuel cladding," Proc. ANS Topical Mtg. on Water Reactor Safety, Salt Lake City, 26 March, 1973.

27. Pawel, R.E., "Oxygen diffusion in beta Zircaloy during steam oxidation," J. Nucl. Mater. 50 (1974) 247-258.

28. Sawatzky, A., "Proposed criterion for the oxygen embrittlement of Zircaloy-4 fuel cladding," Proc. 4th Symp. on Zirconium in the Nuclear Industry, Stratford-on-Avon, UK, 27-29 June, 1978.

29. Grandjean, C., "Oxidation and quenching experiments under simulated LOCA conditions with high burnup clad material," Proc. 24th Water Reactor Safety Information Meeting, Bethesda, USA, 21-23 October, 1996.

30. Grandjean, C. et al., "High burnup UO2 fuel LOCA calculations to evaluate the possible impact of fuel relocation after burst," ANL Program Review Meeting, Rockville (USA), 22 October, 1999.

31. Hofmann, P. et al., PECLOX: A Computer Model for the Calculation of the Internal and the External Zircaloy Cladding Oxidation, KFK-4422 Part 2, October 1988.

32. Uetsuka, H. et al., "Zircaloy-4 cladding embrittlement due to inner surface oxidation under simulated loss-of-coolant condition," J. Nucl. Sci. Tech. 18 (1981) 705-717.

33. Uetsuka, H. et al., "Embrittlement of Zircaloy-4 due to oxidation in environment of stagnant steam," J. Nucl. Sci. Tech. 19 (1982), 158-165.

34. Komatsu, K., "The effects of oxidation temperature and slow cooldown on ductile-brittle behavior of Zircaloy fuel cladding," Proc. CSNI Specialists' meeting on the behavior of water reactor fuel elements under accident conditions, Spaatind, Norway, 13-16 September, 1976.

35. Komatsu, K. et al., "Load-bearing capability in deformed and oxidized Zircaloy cladding," Proc. CSNI Specialist Mtg. on Safety Aspects of Fuel Behavior in Off-Normal and Accident Conditions, Espoo, Finland, 1-4 September, 1980.

36. Lorenz, R.A., "Fuel rod failure under loss-of-coolant conditions in TREAT," Nucl. Tech. 11 (1971) 502-520.

37. Haggag, F. M., Zircaloy-Cladding-Embrittlement Criteria: Comparison of In-Pile and Out-of-Pile Results, NUREG/CR-2757, July 1982.

HIGH TEMPERATURE STEAM OXIDATION OF ZIRCALOY CLADDING FROM HIGH BURNUP FUEL RODS*

Y. Yan, T.S. Bray, H.C. Tsai and M.C. Billone

Argonne National Laboratory (ANL)
Argonne, Illinois, USA

Abstract

The ANL Cladding Metallurgy at High Burnup program is being conducted to provide data in support of efforts to model the behavior of high burnup fuel rods during Loss of Coolant Accident (LOCA) and Reactivity-Initiated Accident (RIA) events and to assess directly the LOCA criteria licensing limits for high burnup fuel. One demonstration TMI-1 PWR rod (≈50 GWd/MTU) and seven high burnup (≤57 GWd/MTU) Limerick BWR fuel rods have been provided by EPRI for the test program; a similar number of H.B. Robinson PWR fuel rods (≈70 GWd/MTU) will be provided at a later time. The major program tasks are: characterization of fuel and cladding, studies of cladding high temperature steam oxidation kinetics, LOCA-criteria testing, and studies of cladding mechanical properties (uniaxial tensile, plane strain, biaxial, and bending). The focus of this paper is on the results of the oxidation kinetics study and its impact on LOCA-criteria test planning. Metallographic results are presented for archival and irradiated Limerick Zircaloy-2 cladding samples exposed to high temperature (≈1204°C) steam for 5-40 minutes. Quantitative weight gain measurements based on total sample weight gain data, oxygen increase data and metallographic data are presented for the archival samples. These data are compared to predicted values from a best-estimate model (Cathcart-Pawel) to assess the relative merits of the three measurement techniques.

Introduction

To ensure adequate ductility during Emergency Core Cooling System (ECCS) quench and during possible post-LOCA seismic events, the current LOCA licensing criteria (10 CFR50.46) limit the peak cladding temperature to 2200°F (1204°C) and the peak Equivalent Cladding Reacted (ECR) to 17% during high temperature steam oxidation. In addition, as discussed in NRC Information Notice 98-29, the ECR is to be based on the total oxidation, including oxide layers formed during normal reactor operation. For PWR cladding, high burnup operation may result in coolant-side oxidation thicknesses of up to ≈100 μm, corresponding to ≈10-14% ECR. This leaves very little margin for LOCA transient oxidation. Although this approach may ensure an adequate safety margin for high burnup fuel, the in-reactor-formed oxide layer may not affect all of the mechanisms responsible for cladding ductility loss during ECCS quench, and its inclusion may be overly conservative. The primary high burnup phenomena that may affect cladding response during ballooning and burst, steam oxidation and quench are: greater loss of base metal thickness during normal operation, increased hydrogen pickup (≈500-700 wppm at 100 μm oxide thickness), greater change in microstructure and precipitate morphology at the higher fluences, and tighter fuel-cladding bonding. The first three phenomena may decrease the ductility of the cladding by decreasing the effective thickness of the prior-β-phase layer and by increasing the H and O transport to that layer during steam oxidation. A tighter fuel-cladding bond may influence ballooning shape and burst extent, as well as induce additional stresses on the cladding during quench. The ANL LOCA-criteria tests

* Work supported by the U.S. Nuclear Regulatory Commission, Office of Nuclear Regulatory Research (RES).

will be conducted with intact fuel rod segments to ensure that the effects of fuel-cladding bonding are included. The oxidation studies are being performed on defueled cladding samples to determine ECR vs. time. Using these oxidation data, LOCA-criteria test times will be determined to correspond to the current criteria limits (ECR=17% based on total oxidation at 1204°C) and to larger and smaller ECR values such that the failure threshold is bracketed in the tests.

The test plan for oxidation studies of high burnup BWR and PWR fuel rod cladding specifies ranges of temperature (900-1300°C) and test time (1-300 minutes). In addition to providing data for LOCA-criteria test planning, the oxidation tests also provide fundamental data for modeling the effects of high burnup operation on high temperature steam oxidation kinetics. Of particular interest in these studies is the influence of the in-reactor-formed oxide layers and associated hydrogen pickup on the oxidation kinetics and phase boundary evolution during steam oxidation. For the TMI-1 demonstration cladding and the high burnup BWR and PWR cladding, fast fluences (E>1 MeV) range from $9\text{-}13\times10^{26}$ n/m^2, outer diameter (OD) oxide layer thicknesses range from 10-110 μm, and hydrogen contents range from about 70 to 700 wppm. In order to determine the effects of these parameters on oxidation kinetics, unirradiated archival BWR and PWR cladding samples are tested concurrently with high burnup samples to allow a direct comparison of the results.

The oxidation studies work to date has focused on thermal and metallurgical benchmarking, testing of unirradiated Zircaloy-2 and -4, testing of irradiated TMI-1 PWR cladding and testing of irradiated Limerick BWR cladding. The thermal benchmarking consists of comparison of thermal couple readings at various axial and circumferential locations above and below the sample, as well as inside the sample, to ensure temperature uniformity. Metallographic benchmarking has consisted of oxide, α-phase and prior-β-phase thickness measurements vs. axial and circumferential locations for unirradiated cladding. Most of the benchmarking has been performed for 1204°C tests. Samples (25-mm-long) of archival and irradiated Limerick cladding have been tested initially in sequence at several 1204°C hold times. Results are reported for unirradiated (qualitative and quantitative) and irradiated (qualitative) Limerick BWR Zircaloy-2 cladding exposed to 1204°C steam for hold times of 5-40 minutes. The measurements consist of: pre-test characterization of ID and OD oxide layer thicknesses, oxygen and hydrogen concentrations; and post-test weight gain, oxide and phase layer thicknesses, and oxygen and hydrogen concentrations.

Cladding Characterization

The archival Limerick tubing has the dimensions typical of the GE-11 (9-by-9 fuel rod array) design: outer diameter (OD) of 11.18 mm and thickness of ≈0.7 mm. Based on metallographic results, the ID Zr barrier is ≈0.1-mm thick and the remaining Zircaloy-2 cladding is ≈0.6-mm thick. The oxygen content has been measured to be in the range of 0.10-0.11 wt.%, depending on sample preparation and cleaning techniques. The reference value used to analyze the oxygen change during steam oxidation is 0.11 wt.%.

The irradiated Limerick BWR cladding samples have been taken from grid span 4 of a fuel rod irradiated to an axially averaged burnup of 56 GWd/MTU. Based on metallographic examinations, the inner-surface barrier oxide layer is about 10-15 μm. The outer-surface oxide layer varies circumferentially from about 3 μm to 18 μm, with local pockets as deep as 30 μm. In the regions of thin oxide layers, tenacious crud deposits of 5-10 μm are observed. For post-test analysis of steam oxidation metallographic data, the average OD oxide thickness of 7±4 μm is used. Based on Leco determinator measurements, the oxygen content of the irradiated cladding is 0.70±0.09 wt.% and the hydrogen content is 72±7 wppm. These values include O and H in crud, outer and inner surface oxide layers and the base metal. At room temperature, the hydrogen is in the form of hydrides concentrated at the outer surface (radial), the inner barrier surface (radial) and in the central region of the cladding ("X" patterns).

Experimental Apparatus

The schematic of the experimental apparatus is shown in Fig. 1. All components, except for the control and monitoring system and the furnace power source, are located in one of the Alpha-Gamma Hot Cells. The atmosphere of these cells is nitrogen with a low, controlled oxygen level. The furnace is a 400-mm-long quad-elliptic, focused radiant heater with a uniform heating zone >250 mm. It is centered with respect to the 52.6-mm-ID quartz tube, which contains the test train and the flowing steam. The test train containing the sample is centered relative to the quartz tube by the perforated spacer disc shown in Fig. 1. Because of the focused heating source, centering of the test sample with respect to the centerline of the furnace is necessary in order to generate uniform surface heating and temperature profiles. Water is first preheated to <100°C and then turned into steam exiting the boiler. The steam flows into the quartz tube and exits out the top of the system into the hot cell. For ease of assembly and disassembly, the interface between the quartz tube and the top of the boiler is not sealed (i.e., the quartz tube sits on top of the boiler). Tests were conducted with average steam flow rates in the range of 1.0-2.0 mg/s per cm^2 of steam-flow area. The steam rate was deduced from water consumption during the test; it was not measured directly. The system is designed to produce one-sided (outer-surface) oxidation of the sample.

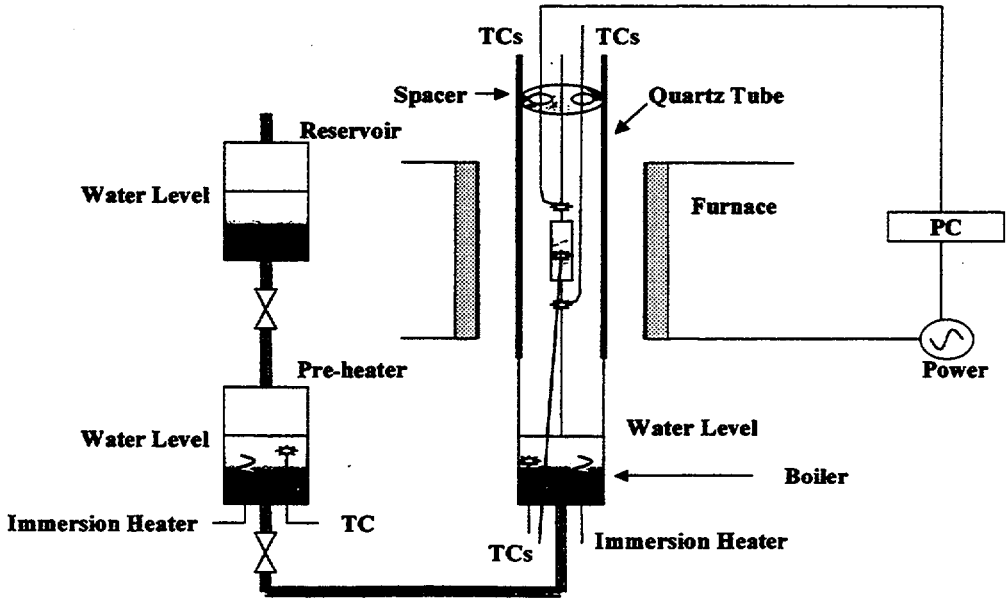

Fig. 1. Schematic of the oxidation kinetics studies apparatus. All components, except the PC and power source, are located in a nitrogen-atmosphere alpha-gamma hot cell.

Figure 2 shows the dual-sample design that will be used in future testing. The two 25.4-mm-long samples are separated from the Inconel holders and stem (running through the interior of the samples) by alumina inserts. On both sides of the alumina inserts are zirconia washers under slight compression to partially inhibit steam from entering the interior of the sample. A slow argon purge flows through the sample interior to sweep away steam that may leak in through the interfaces. This design will allow simultaneous testing of irradiated and archival samples and a direct comparison of the results under identical test conditions.

Figure 3 shows an earlier single-sample design used for thermal and metallurgical benchmarking, as well as for conducting the first series of Limerick tests at 1204°C. The top two thermocouples are located ≈6 mm above the Zircaloy sample. They are inserted into wells – 180° apart – and they have been benchmarked against an additional TC welded directly to the Inconel at the same axial location. The two bottom thermocouples are located ≈6 mm below the sample and are also inserted into wells. These were included in early benchmarking tests. However, they were omitted during the Limerick testing because they proved less reliable due to the difficulty of assembly and the effect of fin cooling from the thermocouple leads extending out into the steam flow regime. In addition to the thermocouples observed in Fig. 3, a freestanding thermocouple is inserted down the center of the sample to the midplane.

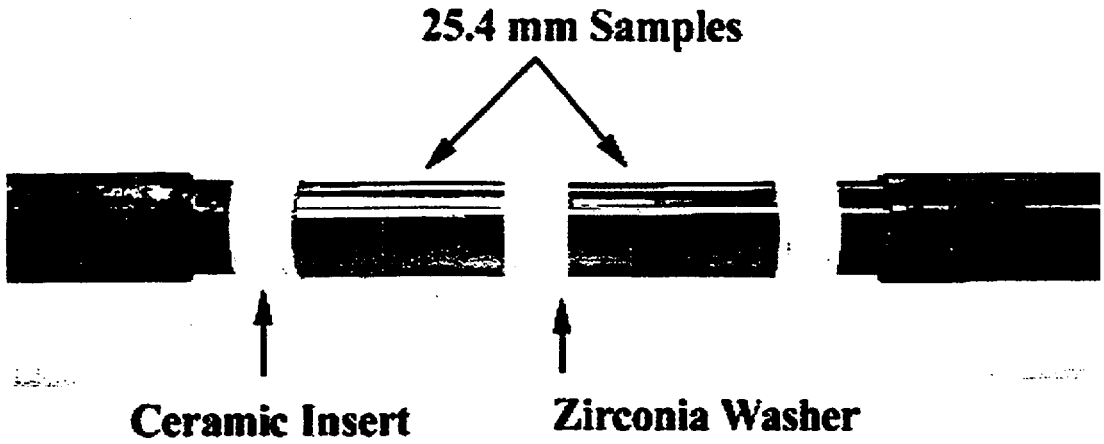

Fig. 2. Sample and holder design for testing pairs of 25.4-mm-long unirradiated and irradiated samples.

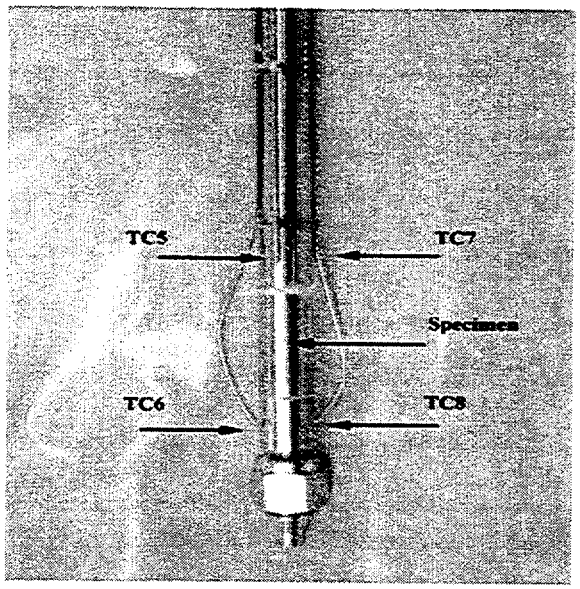

Fig. 3. Single (25.4-mm-long) sample design used for thermal benchmarking and the initial series of Limerick Zircaloy-2 steam oxidation tests. In addition to the four thermocouples shown, there is a fifth thermocouple suspended within the sample at its midplane.

Test Conditions

Figure 4 shows the temperature histories for the four tests (LOU) using unirradiated, archival Limerick Zircaloy-2. The plots represent the recording of the thermocouple used to control the power to the furnace. In addition to these plots, data were recorded from the other top thermocouple and the interior thermocouple. As has been mentioned previously, the bottom two thermocouples were not used during the Limerick cladding test program. The Limerick steam oxidation test conditions are summarized in Table 1. The steady state temperatures (T_s) listed in Table 1 were determined by a weighted averaging of the three thermocouple readings during the hold time. The equivalent times were determined using the Cathcart-Pawel (CP) model described in Ref. 1. This weight gain model was integrated over the actual temperature history, including the ramp, to generate a best-estimate model prediction of the weight gain during each individual test. The model was again used to determine the time at the steady temperature T_s to generate the same weight gain as was calculated for the actual temperature history. It is a better representation of the effective test time than either the total test time (including the ramp) or the hold time (excluding the ramp). However, the significance of this time depends on the degree to which the data are consistent with the model predictions. In the present work, it is not used to compare data to model predictions.

Experimental Results for Archival (Unirradiated) Samples

The results of the archival sample tests were analyzed in detail to provide baseline data for the comparison to the results of the tests with Limerick irradiated samples and to check on the reliability of the data determined from three independent measurement techniques: increase in total sample weight, increase in oxygen content at the sample midplane, and weight gain deduced from the metallography.

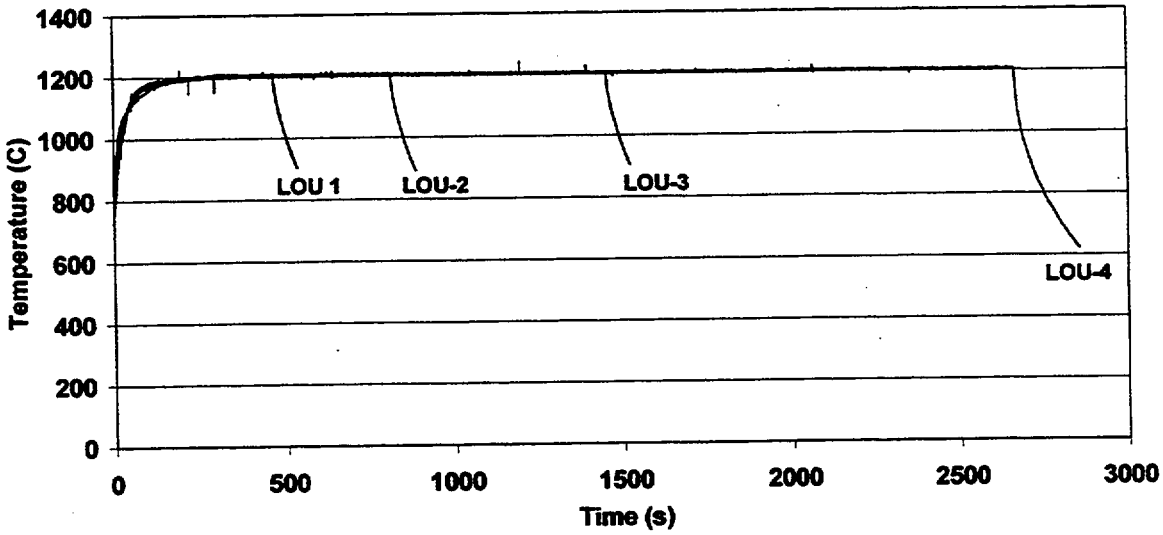

Fig. 4. Summary of the temperature histories (as recorded by the control thermocouple) for the steam oxidation tests (LOU 1-4) conducted with unirradiated, archival Limerick Zircaloy-2 cladding.

Table 1. Experimental Conditions for the Limerick Steam Oxidation Tests; unirradiated (U) Zry-2 is archival cladding (11.18-mm OD/9.75-mm ID), irradiated (I) Zry-2 is from Limerick rod F9

Test ID	Sample Cond.	Sample Length mm	Steady Temp. (T_s) °C	Total Time s	Equiv. Time s	Steam Rate mg/cm^2-s
LOU-1	U	25.3	1204	534	405	2.0
LOU-2	U	25.8	1204	888	746	1.2
LOU-3	U	25.9	1193	1524	1382	1.8
LOU-4	U	25.5	1204	2718	2583	1.8
LOI-1	I	25.4	1204	498	370	1.0
LOI-1	I	25.4	1211	810	657	2.0
LOI-3	I	25.4	1197	1506	1368	1.5
LOI-4	I	25.4	1226	2592	2468	1.8

The weight gain determined from the total change in sample weight is the easiest to determine as it merely involves weighing the sample before and after the test. However, as it includes possible non-uniform end effects, oxidation at the inner surface of the cladding, and non-uniformities throughout the sample, it may not be the most reliable method. Post-test measurement of the oxygen content within a specimen at the midplane of the sample has the advantage of eliminating end effects, but it may include

possible inner-surface oxidation. There is also the possibility of losing some brittle oxide during sample preparation. Using metallography to determine weight gain at the sample midplane may be the most reliable method, as it includes neither end effects nor inner-surface oxidation. It also has the advantage of visualization of the oxide, alpha and prior-beta layers and their interfaces. This allows direct comparison between measured and predicted oxide layer thickness, as well as weight gain. In order to compare the results from the three methods, the total sample weight gain is normalized to the steam-exposed cladding outer surface area.

Normalized Weight Gain Determined from Change in Sample Weight

The C-P predicted weight gains for the nominally 5-, 10-, 20- and 40-minute tests are 13.4, 18.2, 23.5 and 33.9 mg/cm^2, respectively. As has been mentioned before, these predicted values are determined by integrating the C-P model over the experimental temperature history for each test. Sample weight gain data could only be obtained from three of the four tests, as the 40-minute test resulted in such a brittle sample that a chunk of the material was lost during disassembly. The measured normalized weight gains for the 5-, 10- and 20-minute tests are 16.8, 25.7 and 26.5 mg/cm^2, respectively. These values fall between the best-estimate C-P predictions [1] and the upperbound Baker-Just predictions [2]. The high measured sample weight gains (≈25% higher than predicted values) appear to be due to the presence of local regions of enhanced oxidation (see Discussion section).

Normalized Weight Gain Determined from Change in Oxygen Content

Because of the oxygen saturation level of the Leco Oxygen Determinator, specimens cut from the midplane of the oxidation sample had to be further subdivided by making radial cuts such that each Leco specimens were <0.1 g. The procedure involves cutting ≈6-mm-long rings from the midplane and then sectioning radially into smaller pieces. Some of the oxide may be lost during the radial sectioning. As can be seen from Fig. 5, weight gain determined from change in oxygen content agrees reasonably well with the C-P best estimat predictions for the 5-minute test (66-μm oxide layer) and the 10-minute test (89-μm oxide layer), but it falls short of the predicted value for the 20-minute test (129-μm oxide layer). Thus, although direct determination of the oxygen content is still considered to be a reliable method for determining weight gain during steam oxidation, the method of specimen preparation needs to be improved to avoid loss of brittle oxide particularly for oxide layers > ≈100 μm.

Normalized Weight Gain Determined from Metallography

The procedure for determining weight gain from the metallography is as follows: a specimen is prepared at the sample midplane. Using an optical metallograph, photomicrographs are taken at eight circumferential locations representing ≈40% of the circumference. For most cases, metallographs from as-polished specimens were used for the analyses. The thicknesses of oxide, alpha, and prior-beta layers were determined from the photomicrographs by digitalizing the images, using the ImagePro software package, and employing a linear-intercept technique to determine the average layer thicknesses. In doing this averaging, only regions of uniform layer growth were considered. The results are summarized in Table 2, and they are compared to the C-P predicted values in Fig. 5. The agreement between the weight gain determined from metallography and the C-P model is excellent.

Experimental Results for Irradiated Limerick Samples

For the irradiated samples, only sample weight gain and oxide layer thickness measurements were performed. Similar to the results for the unirradiated samples, the total sample weight gains were higher

Table 2. Summary of Results of Archival (Unirradiated) Limerick Zircaloy-2 Steam Oxidation Tests

T_s °C	C-P Equiv. Time s	Weight Gain, mg/cm^2			Thickness, μm		
		From Sample Weight	From Oxygen Analysis	Calc. From Met.	Oxide Layer	Alpha Layer	Beta Layer
1204	405	16.8	13.1	13.2	66	89	591[a]
1204	746	25.7	19.2	17.3	89	111	524[a]
1193	1382	26.5	20.9	24.0	129	145	467[a]
1204	2583	---	25.0	32.9	179	203	385[a]

[a]Includes Zr barrier

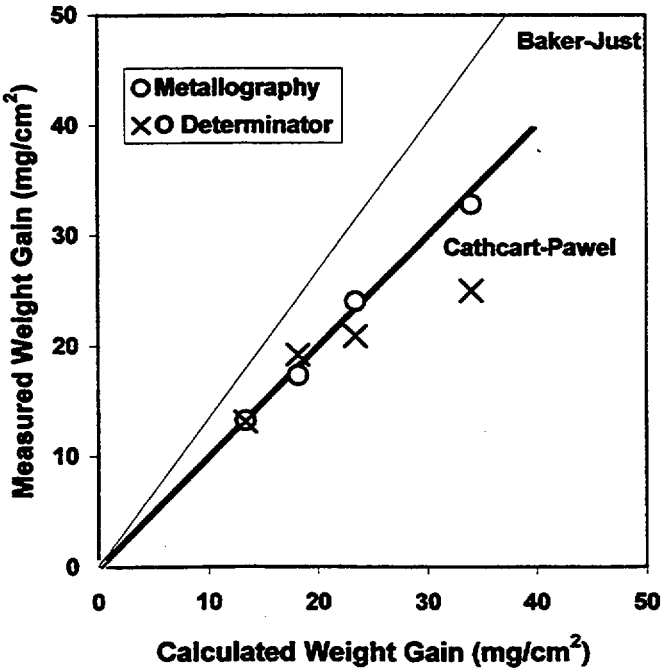

Fig. 5. Weight gain data from metallography and Leco Oxygen Determinator vs. Cathcart-Pawel model predictions for unirradiated Limerick Zry-2 oxidized in steam at ≈1204°C for nominal times of 5, 10, 20 and 40 minutes. Also shown are the Baker-Just model predictions.

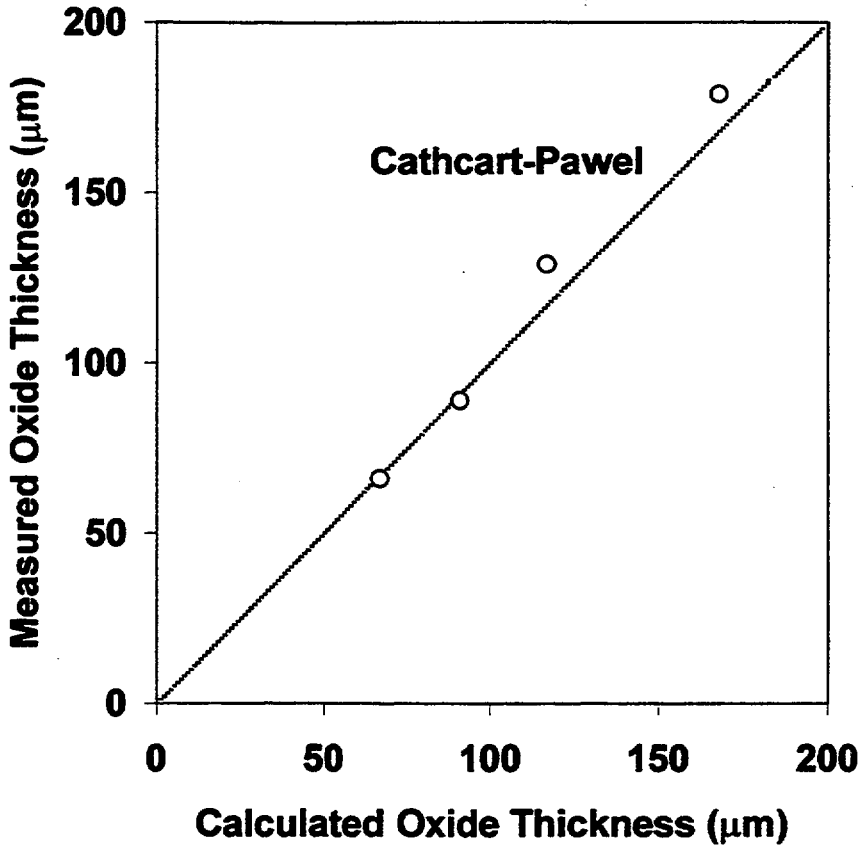

Fig. 6. Comparison of oxide layer thickness data (from sample midplane metallography) vs. best-estimate model (Cathcart-Pawel) predictions for unirradiated Limerick Zry-2 oxidized in steam at 1204°C for nominal times of 5, 10, 20 and 40 minutes.

than predicted by the C-P best estimate model. However, in this case the higher weight gains were due to the combination of local regions of enhanced oxidation, wavy interface regions between the oxide and alpha layers, and larger-than-predicted uniform oxide layers. It is not clear at this point whether the irradiated samples are more susceptible to the possible environmental artifacts than the unirradiated samples or whether the steam-oxidation rate is higher. These tests need to be repeated with better control of the steam environment between the sample and the quartz tube before the data can be reported with confidence.

Discussion

The agreement between measured (from metallography) and predicted weight gains and oxide layer thicknesses is excellent for the tests with unirradiated samples when only regions of uniform layer growth are considered. Figure 7 shows the uniform layers for tests with both unirradiated and irradiated samples. The interfacial layers are well defined for the unirradiated sample. For the irradiated sample, the oxide-alpha layer boundary is well defined, but the alpha-beta boundary is uneven because of alpha incursions into the prior beta layer. These micrographs are from etched samples using polarized light.

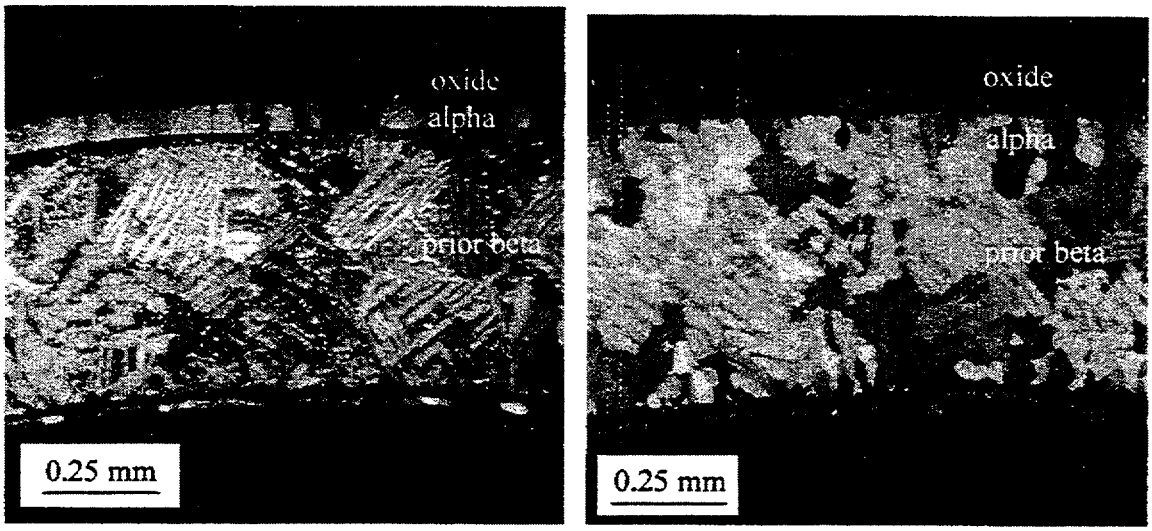

(a) (b)

Fig. 7. Uniform-oxide, alpha and prior-beta phase layers in (a) 5-minute test at 1204°C with unirradiated Zircaloy-2 and (b) 10-minute test at 1204°C with irradiated Limerick Zircaloy-2

All of the micrographs shown in this paper and used for the results given in Table 2 were taken from specimens at the midplane of the sample. For some of the tests, specimens were also taken ≈3 mm from the sample ends. Comparison of micrographs from the two locations suggests that end effects are minimal. However, examination of micrographs from different circumferential locations at the midplane revealed local regions of enhanced oxide growth (Fig. 8a) and regions of wavy interface between the oxide and alpha layers (Fig. 8b). The outer surfaces of these samples exhibit local regions of grayish-white oxide protrusions that correlate with the regions of enhanced oxide growth. Based on SEM results, these silvery protrusions are oxide nodules with crater-like holes and radial cracks that would promote enhanced oxidation. For a nodule such as the one shown in Fig. 8a, the planar diameter of the outer surface nodule is ≈2 mm and the diameter of the crater-like defect is ≈100-300 μm. In steam oxidation tests, such behavior has been referred to as "anomalous oxide growth" [3]. For outer-surface anomalous oxide, the behavior has been correlated with cladding tensile stresses. For inner-surface oxide, the behavior has been attributed to steam containing relatively high H_2 content. However, the time-temperature regimes for observing such behavior are not consistent with those of the current tests. Also, neither the tensile stresses nor high H_2 concentrations in the steam are likely for the current tests.

For the current tests, it is possible that some N_2 from the hot cell environment entered the test chamber because the quartz tube merely rests on the boiler. Also, the procedure used to center the furnace to the quartz tube may result in some tipping of the tube relative to the boiler interface. Cathcart, Pawel, et al. [1] did oxidation tests on Zry-4 at 1100°C and 1300°C with up to 10 molar % N_2 in steam. Although no nitrogen effect was observed, their tests were at different temperatures and shorter times than the ANL tests. No direct evidence was found in the ANL post-test analyses that N_2 entered the test chamber and caused the local regions of enhanced oxidation. Nor was evidence found of excessive nitrogen content in the oxide layer or the base Zry-2 metal. However, indirect evidence suggests that this may have occurred.

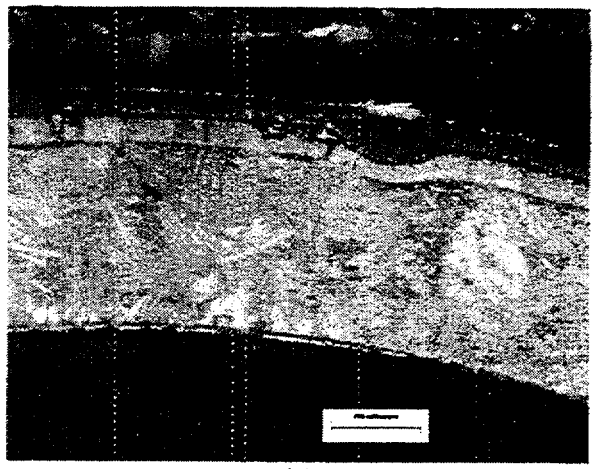

(a)

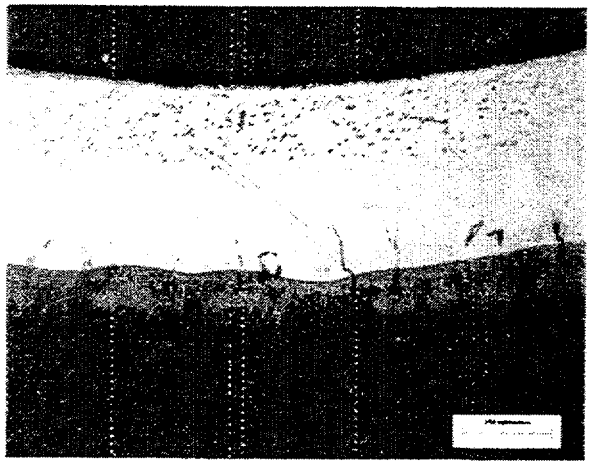

(b)

Fig. 8. Regions of enhanced oxide layer growth and uneven oxide-alpha interface for unirradiated Zry-2 sample after 5 min. in steam at 1204°C; and (b) irradiated Limerick Zry-2 cladding after 20 min. in steam at 1197°C. Note: scale bars are approximate for these figures.

In the LOCA Mock-up Apparatus, longer samples of unirradiated Zry-2 have been exposed to steam at 1204°C for times comparable to those in Table 1. These are out-of-cell tests conducted in an air environment external to the test chamber. However, the test chamber is sealed at the quartz-boiler interface and it is purged with inert gas prior to the introduction of the steam. No "anomalous" or enhanced oxide layer regions have been observed in these tests. Also, oxide layer thicknesses measured after these tests agree quite well with the C-P model predictions. Thus, it appears that the local enhancement of the oxidation layer growth rate is an experimental artifact of the in-cell apparatus, possibly due to a combination of N_2 ingress and uneven steam flow. In future work, the in-cell oxidation kinetics apparatus will be modified to accommodate a seal between the quartz tube and the boiler by adapting the base plate already in use for the LOCA Mock-up Apparatus. The quartz tube may also be purged with inert gas prior to steam ingress. Once the design change has been implemented and validated, oxidation kinetics testing will resume with the dual-sample design (see Fig. 2).

Conclusions

One-sided (outer-surface) oxidation kinetics studies have been conducted on archival and irradiated Limerick BWR Zircaloy-2 cladding exposed to steam at 1204°C for nominal times of 5, 10, 20 and 40 minutes. The results from the tests with unirradiated samples have been analyzed in depth and compared to the Cathcart-Pawel model predictions for weight gain and oxide layer thickness. Of the three independent methods for data determination – sample weight gain, chemical analysis of oxygen increase, and oxide layer thickness increase and weight gain deduced from the metallography – the metallographic approach proved to be the most reliable for the tests conducted. Both the oxide layer thicknesses and weight gains deduced from metallographic determination of oxide, alpha and prior-beta layer thicknesses are in excellent agreement with the Cathcart-Pawel model predictions. In addition, the metallographic approach was able to identify local regions of enhanced oxide layer growth – an apparent experimental artifact of the current test apparatus. Regions of uniform oxide layer growth were used in the comparison of data to best estimate model predictions. The weight gains deduced from sample weight change were ≈25% higher than predicted values. Although these results are within the scatter band of reported data from previous tests, they are unreliable because the method averages regions of both uniform and enhanced oxide layer growth. Chemical analysis of the oxygen contents before and after the tests is a useful method for determining weight gain. The weight gains deduced from samples with oxide layers < ≈100 μm were in excellent agreement with the best-estimate predictions. However, for samples with thicker oxide layers, loss of some oxide was experienced during cross-sectional and radial cutting of the specimens for Leco analysis. Once the method of sample preparation is improved, the results from the chemical analysis of oxygen increase might be as reliable as the results obtained from the metallography.

Sample weight gain and metallographic analyses were performed on the four tests with irradiated samples. Both sets of results are higher than the Cathcart-Pawel model predictions. The sample weight gain results are not considered to be reliable for the reasons cited above for the unirradiated samples. It is not clear at this point whether the larger-than-predicted uniform oxide layers are characteristic of the irradiated material or are caused by environmental artifacts in the test chamber. The tests will be repeated with a sealed interface between the steam generator and the quartz tube test chamber to eliminate the possible effects of excess N_2 (from the hot cell environment) and to better control the steam flow. Test results from the out-of-cell LOCA Mock-up apparatus, which uses a sealed interface, indicate that predictable steam-induced black oxide layers are formed at 1204°C with no evidence of external regions of silvery, cracked oxide nodules or enhanced oxide growth.

References

1. J.V. Cathcart, R.E. Pawel, R.A. McKee, R.E. Druscel, G.J. Yurek, J.J. Cambell and S.H. Jury, "Zirconium Metal-Water Oxidation Kinetics IV. Reaction Rate Studies", ORNL/NUREG-17, Aug. 1977.

2. L. Baker and L.C. Just, "Studies of Metal-Water Reactions at High Temperatures; III. Experimental and Theoretical Studies of the Zirconium-Water Reaction," ANL-6548, May 1962.

3. H.M. Chung and T.F. Kassner, "Embrittlement Criteria for Zircaloy Fuel Cladding Applicable to Accident Situations in Light-Water Reactors: Summary Report", ANL-79-48, NUREC/CR-1344, Jan. 1980.

DEVELOPMENT AND ASSESSMENT OF THE FRAPTRAN TRANSIENT FUEL ROD CODE

ME Cunningham, CE Beyer, FE Panisko; Pacific Northwest National Laboratory
HH Scott, U.S. Nuclear Regulatory Commission
GA Berna; Gary A. Berna Consulting

ABSTRACT

The FRAPTRAN computer code is being developed for the U.S. Nuclear Regulatory Commission (NRC) to calculate fuel behavior during power and/or cooling transients such as reactivity accidents, boiling-water reactor power oscillations without scram, and loss-of-coolant-accidents at burnup levels up to at least 65 MWd/kgM. FRAPTRAN will serve as a tool for: analysis of fuel response to these postulated design-basis accidents; understanding and interpretation of experimental results; and guiding of planned experimental work.

INTRODUCTION

The FRAPTRAN computer code is being developed for the U.S. Nuclear Regulatory Commission (NRC) to calculate single-rod fuel behavior during postulated design-basis accidents at burnup levels up to 65 MWd/kgM. Such accidents include power and/or cooling transients such as reactivity accidents, boiling-water reactor (BWR) power oscillations without scram, and loss-of-coolant-accidents (LOCAs). FRAPTRAN will be used to provide insight into fuel performance during the transients and help guide experimental programs. Development of the FRAPTRAN code is being done subsequent to, and building on, development of the FRAPCON-3 computer code, which has been released (Berna et al. 1997).

FRAPTRAN is intended to be used for numerous applications, including auditing fuel-related models in licensee's evaluation models, performing special studies such as fission product release for timing of containment valve operation, estimating margin to damage limits for reactivity accidents and LOCAs, planning experimental tests and analyzing results, scaling pulse test data to adjust for different test temperatures, translating Zircaloy test results to other cladding alloys using mechanical properties, and estimating cladding response to BWR power oscillations for which integral tests will not likely be performed. FRAPTRAN will be used to perform sensitivity analyses of the effects of parameters such as fuel-cladding gap size, rod internal gas pressure, and cladding ductility and strength on the response of a fuel rod to a postulated transient. Fuel rod responses of interest often include fuel and cladding temperature, cladding strain, location of ballooning, cladding oxidation, etc.

FRAPTRAN is intended to address a wide span of power levels, cladding temperatures, and time scales as illustrated in Figure 1. At one extreme, a postulated reactivity accident can cause very large power increases in a few assemblies in less than a second with fuel failure occurring through pellet-cladding mechanical interaction. LOCAs lie at the other extreme where power levels are at decay heat levels, but cooling is lost leading to high cladding temperatures and failure by ballooning over a time span of minutes. In between these two extremes, BWR power and coolant flow oscillations over a span of a few minutes could lead to cladding temperatures high enough for ballooning and failure, or pellet-cladding mechanical interaction could play a role in fuel failure.

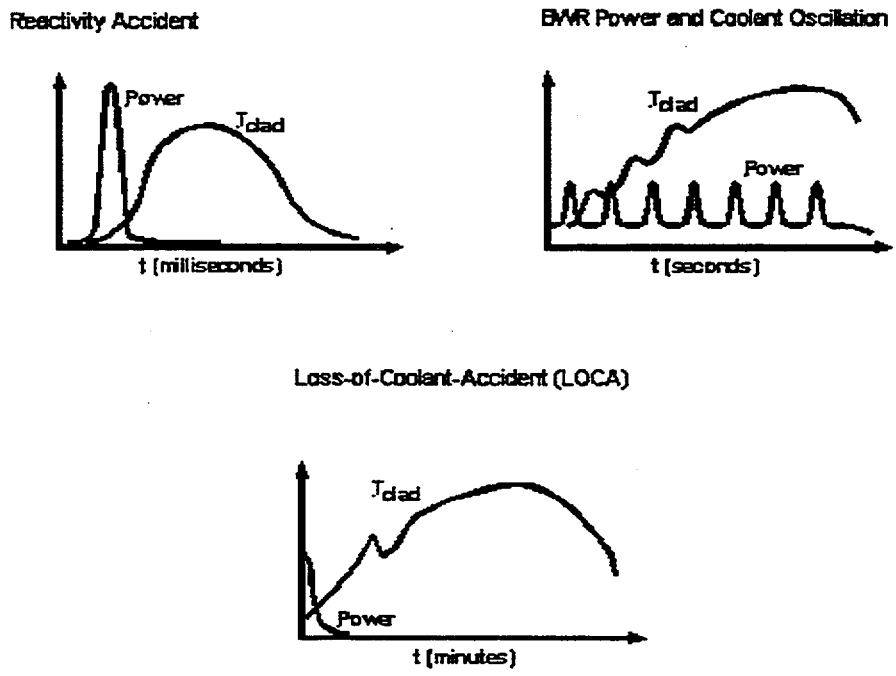

FIGURE 1. Illustration of the Wide Range of Potential Transients to be Addressed by FRAPTRAN

Provided in the following sections are a brief description of FRAPTRAN, a summary of the code assessment, and an example application of FRAPTRAN to evaluating potential fuel response to a BWR power oscillation scenario.

FRAPTRAN DESCRIPTION

FRAPTRAN uses a finite difference thermal model, the FRACAS-1 solid-pellet mechanical model, and material properties from MATPRO-Version 11, Revision 2 (Hagrman, Reymann, and Mason 1981) to calculate the thermal-mechanical response of a fuel rod to transient power and coolant conditions. Principal assumptions for the thermal solution include no longitudinal heat conduction and that steady-state critical heat flux correlations and surface heat transfer correlations are valid under transient conditions. Principal assumptions for the mechanical solution include thin wall cladding, the incremental theory of plasticity, the Prandtl-Reuss flow rule, isotropic work hardening, and no axial slippage when fuel and cladding are in contact. The use of the solid-pellet mechanical model assumes that once the fuel and cladding are in contact, the cladding must follow the fuel without any deformation imposed on the fuel by the interaction.

To facilitate the development of FRAPTRAN, the code has been developed from the FRAP-T6 computer code (Siefken et al. 1981); Version 21 from 1997 was the starting point. The general approach has been to implement applicable existing high-burnup models from FRAPCON-3 rather than developing new models; not tuning models to match experimental data (i.e., more first principles); not substantially changing the code structure (with the exception of deleting dynamic dimensioning); removing no longer needed or used coding in consultation with the NRC; correcting known or found problems in FRAP-T6; and improving ease of use.

The principal model updates to improve high-burnup performance have been to the fuel thermal conductivity and Zircaloy cladding mechanical properties. These models were updated in FRAPCON-3 (Lanning, Beyer, and Painter 1997) to improve thermal and mechanical performance predictions, and the same models are now incorporated in FRAPTRAN. The new fuel thermal conductivity model incorporates a burnup dependency (decreased thermal conductivity with increasing burnup) plus a gadolinia dependency. Use of this model also requires detailed specification of the axial and radial burnup profiles for a rod. The new Zircaloy cladding properties are improved for high burnup by including a dependency on excess hydrogen in the cladding, from oxidation of the Zircaloy, in addition to an effect from fast neutron fluence.

Other features of FRAPTRAN include updating the fuel-cladding solid gap conductance model to match that used in FRAPCON-3 (Lanning, Beyer, and Painter 1997); using an equal-area fuel ring node structure to better evaluate the high-burnup fuel rim region; inputting data using the free-format NAMELIST option for improved user ease; maintaining a link between FRAPCON-3 and FRAPTRAN for the specification of burnup-dependent parameters needed to define FRAPTRAN input; removal of dynamic-dimensioning (returning to fixed dimensioning) for improved ability to work with the source coding; and increasing the problem input options by allowing axial and radial profiles of burnup and power profiles (needed with the new fuel thermal conductivity model), user specification of the initial thickness of the cladding outer surface oxide, and user specification of excess hydrogen concentration in the cladding (needed with the new cladding mechanical properties). The user also has the option of specifying transient rod-average fission gas release and fuel swelling; these options were added to aid in evaluating fuel rod response during reactivity accidents.

FRAPTRAN ASSESSMENT

An assessment data base has been selected that emphasizes reactivity accident and LOCA experiments because these accidents will be a focus for FRAPTRAN application and span the range of anticipated transient conditions. A large emphasis is placed on experiments that investigate the effects of burnup on fuel rod behavior during design basis accidents. In particular, these include the reactivity accident tests conducted by a) the Japan Atomic Energy Research Institute (JAERI) in the NSRR facility (Fuketa et al. 2000) and b) the Institut de Protection et de Sûreté Nucléaire (IPSN) (Papin and Schmitz 1997) in the CABRI reactor. There is a lack of LOCA assessment cases using irradiated fuel rods at high-burnup levels. For assessing performance in predicting LOCA behavior, the LOCA experiments conducted in the National Research Universal (NRU) reactor (Wilson et al. 1983) will primarily be used. Provided in Table 1 is a summary of the selected integral assessment cases.

The assessment of FRAPTRAN is in process and will continue into 2001. Current results support that FRAPTRAN is meeting the objective of providing improved results for high-burnup analyses. Provided in Figure 2 is a plot of predicted fuel centerline temperature for a beginning-of-life power ascension that shows good agreement with the measured temperatures and the FRAPCON-3 calculation (Lanning et al. 1997). Provided in Figure 3 is a plot of FRAPTRAN-predicted peak total cladding elongation for the CABRI and NSRR reactivity experiments as a function of the measured peak cladding elongation. This illustrates a good comparison to total cladding elongation from reactivity accident tests on high burnup fuel rods. Provided in Figure 4 is a comparison of predicted and measured fuel centerline temperature during the scram phase of the PBF LOC-11C test (Larson et al. 1979). This illustrates a good comparison to transient temperature data at low burnup.

TABLE 1. Integral Assessment Cases for FRAPTRAN

Case	Rod Type	Reactor	Rod Burnup	Other Comments
A. Reactivity Accidents				
1) HBO-6	PWR 17x17	NSRR	49 MWd/kgM	80 cal/g, 4.4ms, 1.2% diametral strain
2) MH-3	PWR 14x14	NSRR	39 MWd/kgM	65 cal/g, 4.5ms, 1.6% diametral strain
3) GK-1	PWR 14x14	NSRR	42 MWd/kgM	93 cal/g, 4.6ms, 2.5% diametral strain
4) OI-2	PWR 17x17	NSRR	39 MWd/kgM	108 cal/g, 4.4ms, 4.8% diametral strain
5) TS-5	BWR 7x7	NSRR	26 MWd/kgM	98 cal/g, 4.6ms, 0% diametral strain
6) FK-1	BWR 8x8	NSRR	45 MWd/kgM	112 cal/g, 3.5ms, 0.9% diametral strain
7) REP-Na 3	PWR	CABRI	53 MWd/kgM	125 cal/g, 9.5ms, 2.% diametral strain
8) REP-Na 4	PWR	CABRI	62 MWd/kgM	96 cal/g, 64ms, 0.4% diametral strain
9) REP-Na 5	PWR	CABRI	64 MWd/kgM	115 cal/g, 9ms, 1.1% diametral strain
10) IGR-H5T	VVER	IGR	50 MWd/kgM	153 cal/g, 760 ms, 6.5% diametral strain, failed
B. LOCAs				
11) NRU MT-1, MT-4	PWR	NRU	0	11 full-length rods, adiabatic heatup; clad temperature, gas pressure
12) NRU MT-6A	PWR	NRU	~0	21 full-length rods; clad temperature, gas pressure
13) PBF LOC-11C	PWR	PBF	0	4-rod test train; target peak cladding temperature of 1000K
14) TREAT FRF-2	BWR	TREAT	0	power ramp, adiabatic heatup
15) Phebus-218	PWR	Phebus	0	international standard problem; 5x5 bundle
C. Other Cases				
16) FRAP-T6 Standard Problem	PWR	Assumed PWR	0	hypothetical PWR double-ended cold leg break
17) IFA-508, Rod 11	PWR	HBWR	~0	fuel temperature initial power ascension
18) IFA-533 (IFA-409)	PWR	HBR	45 MWd/kgM	centerline temperature during scram
19) PBF IE-1, Rod 7	Saxton PWR	PBF	7 MWd/kgM	
20) PBF PR-1	BWR-type	PBF	0 MWd/kgM	4-rod test train, 1 failed; power-cooling mismatch

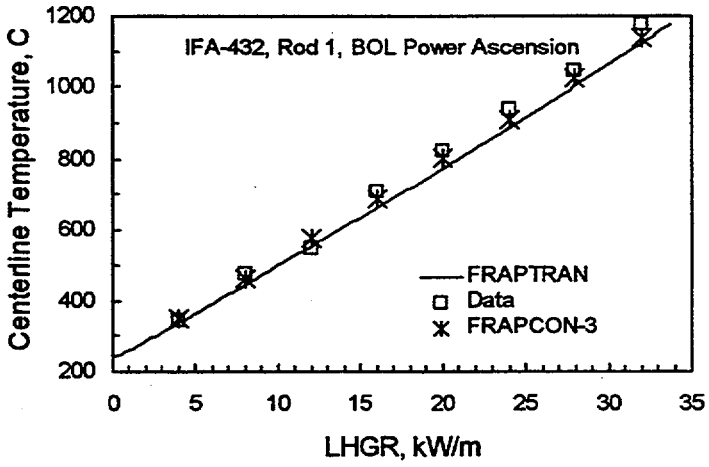

FIGURE 2. Comparison of FRAPTRAN-Calculated Fuel Centerline Temperature for BOL Power Ascension of IFA-432, Rod 1, to Measured Data and FRAPCON-3 Calculation

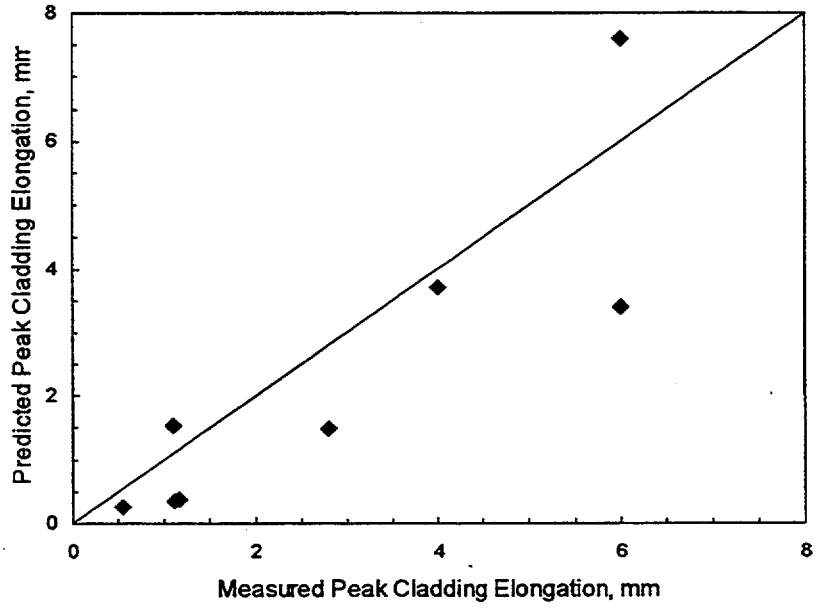

FIGURE 3. Comparison of FRAPTRAN-Predicted Peak Cladding Elongation vs. Measured Peak Cladding Elongation for Reactivity Accident Tests

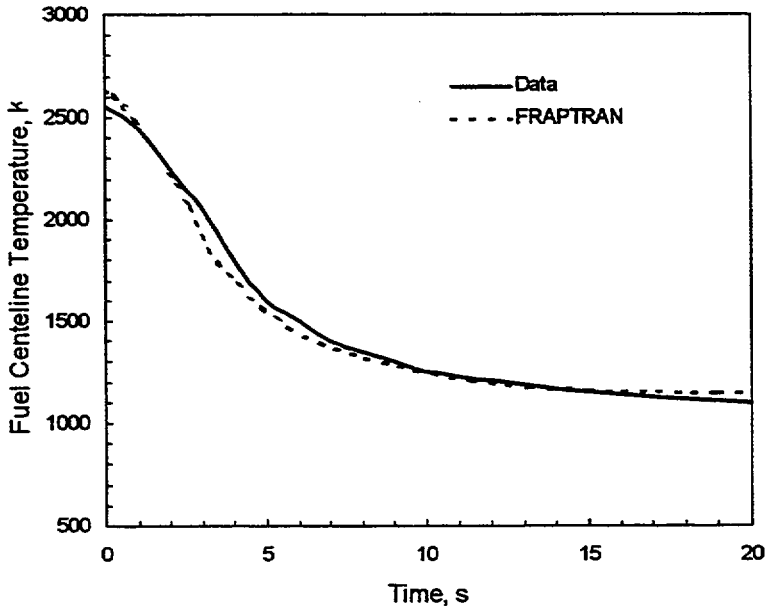

FIGURE 4. Comparison of Predicted and Measured Fuel Centerline Temperatures for a Scram (PBF LOC-11C)

FRAPTRAN APPLICATION

FRAPTRAN is already being used to support evaluations of the recent reactivity accident experiments such as evaluating the effects of pulse width and cladding ductility on fuel response. In the area of guidance for planned and potential experimental programs, the code will be used to evaluate the physical characteristics of the fuel rods that will be used by Argonne National Laboratory (ANL) for upcoming mechanical property testing of high-burnup cladding. Evaluations will include effects such as cold fuel-cladding gap size and cladding strength. The code will also be used to evaluate the planned LOCA tests such as extent of cladding oxidation and ballooning of the test rods. FRAPTRAN has also been used to evaluate the possibility that test rigs in the Halden Boiling Water Reactor might simulate fuel response during BWR power oscillations without scram (Cunningham and Scott 1999). This analysis has shown significant fuel performance sensitivities to the assumed oscillating power levels and coolant conditions.

To illustrate an application, FRAPTRAN is being used to evaluate possible BWR power oscillations without scram. An example of this type of transient is the following scenario (Boyack et al. 2000; www.nrc.org/RES/pirt): A BWR has its recirculation pumps trip and coolant flow drops from 75% of full flow to 30% without the reactor scramming; power then drops from 84% of rated to 40%. The reactor enters natural circulation flow, at 30% of full-flow, and power oscillations (because of coolant density variations) begin about five minutes after the pump trip; these oscillations have a period of about 2.5 seconds. At about seven minutes after pump trip the power oscillations are up to about 120% of rated. The power oscillations continue to increase in magnitude to approximately 1300% of rated power by nine minutes after pump trip. At twelve minutes, the limit cycle is reached and boron injection begins to shut down the reactor. To complicate this scenario, the flow rate also begins to decrease and oscillate in opposite phase to the power cycles. As a result of the increasing power levels and decreasing flow rates, fuel and cladding temperatures

increase with time because there is insufficient cooling between the power peaks to fully dissipate the fuel rod heat. These power peaks, and increased temperatures, can lead to pellet-cladding mechanical interaction and possibly even ballooning if cladding temperatures rise sufficiently and fuel rod gas pressures reach sufficient levels. Should cladding temperatures reach sufficient levels, even cladding dry out is possible.

A very simple approximation of the above BWR transient scenario is evaluated here using FRAPTRAN. The assumed BWR rod is the Monticello rod used in the FRAPCON-3 integral assessment (Lanning et al. 1997). This rod was irradiated to a rod-average burnup of 45 MWd/kgM with an end-of-life fission gas release of 5%. Provided in Table 2 are rod design parameters and FRAPCON-3 calculated end-of-life conditions for this rod.

TABLE 2. BWR Rod Design Parameters and EOL Conditions for Assumed BWR Transient Scenario

Parameter	As-Fabricated	At 45 MWd/kgM
Fuel Active Length	3.658 m	same
Plenum Length	0.286 m	same
Plenum Volume	2.62×10^{-5} m^3	same
Gas Composition and Pressure	100% helium, 0.1 MPa at 300K	16% He, 13% Kr, 71% Xe, 1.86 MPa at 572K
Cladding Outer Diameter	0.01252 m	0.01249 m
Cladding Inner Diameter	0.01080 m	0.01077
Fuel-Cladding Radial Gap Thickness	114.0×10^{-6} m	69.0×10^{-6} m
Fuel Pellet Diameter	0.01057 m	0.01063 m
Coolant Pressure	7.16 MPa	same
Coolant Inlet Temperature	542K	same
Coolant Mass Flux	1350 kg/s-m^2	See Figure 5
Rod Pitch	0.01626 m	same

The simplified BWR power and coolant transient history input to FRAPTRAN is illustrated in Figure 5. This transient is assumed to begin from 8 kW/m (40% of nominal operating power), with the power peaks increasing with each cycle to a peak of 200 kW/m (a 1000% increase over the nominal power level of 20 kW/m). The power peaks have a base width of 0.6 second and, between the power peaks, the rod-average power is assumed to be 4 kW/m for a length of 1.9 seconds. The coolant flow is assumed to begin at about 40% of full flow, and then oscillate and slowly decrease with each oscillation; this postulated coolant flow history is also illustrated in Figure 5 Local coolant conditions were calculated using the thermal-hydraulic models internal to FRAPTRAN. Coolant inlet enthalpy, pressure, and coolant mass flux were specified as a function of time along with the Babcock&Wilcox correlation (Gellerstedt et al. 1969) for critical heat flux[(a)] and the cluster geometry form of the Groeneveld correlation for film boiling.

(a) The B&W correlation was used because the General Electric correlation for critical heat flux was found to fail for steam quality greater than 0.84, which was calculated for this application.

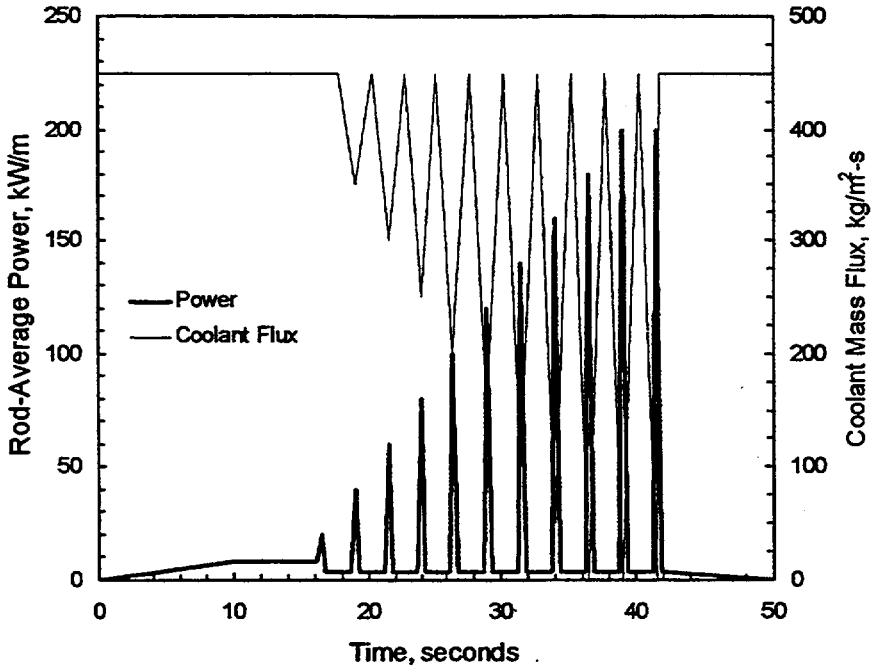

FIGURE 5: Assumed Oscillating Power and Coolant Flow Histories for FRAPTRAN Calculations

To prepare the input for FRAPTRAN, the FRAPCON-3 code was run to define the fuel rod pre-transient conditions. Burnup-dependent variables from FRAPCON-3 used for FRAPTRAN include radial dimensions (accounting for burnup dependent fuel, cladding, and gap dimensional changes), fill gas composition and pressure, and radial profiles of power and burnup at each axial node (for a full-length BWR rod). The FRAPCON-3 calculation resulted in an open fuel-cladding gap at 45 MWd/kgM and fission gas release of 5% for a gas mixture of 16% helium, 13% krypton, and 71% xenon at 1.9 MPa at 570K. A full-length rod was modeled with 12 equal-spaced axial nodes.

A simple parametric study of transient fuel response using FRAPTRAN was conducted beginning with the fuel rod conditions defined by FRAPCON-3. Parameters that were varied included varying the coolant flow rate from full flow (1350 kg/m^2-s) to constant reduced flow (450 kg/m^2-s) to oscillating and reducing flow (Figure 5); decreasing fuel-cladding gap size so that fuel-cladding contact would occur at 8 kW/m prior to the first power cycle; and increasing fuel rod gas pressure up to system pressure at 8 kW/m prior to the first power cycle. The variations in gap size and gas pressure, when combined with the cooling variations, lead to significant differences in cladding behavior during the postulated transient.

Some representative results of the calculations are provided in Figures 6-10, and are discussed in the following. Six of the parametric cases that were run are presented here, and are summarized along with key results in Table 3.

Provided in Figure 6 is the time history for cladding inner surface temperature showing the effect of the three different coolant flow assumptions. Case 1 assumes full flow (1350 kw/m^2-s) with no oscillation and it can be seen that, while cladding temperature does increase with each power cycle, cladding temperature remains

below about 650K. In contrast, when coolant flow is reduced, a point is reached in the history when cladding temperature strongly increases. This is further illustrated in Figure 7 where the cladding temperature history for selected axial nodes is presented for Case 3. It can be seen that the nodes at peak power in the middle of the rod (axial nodes 6, 7, and 8) increase in temperature first and reach the highest temperature (for clarity, not all axial nodes are shown in the figure). The cladding temperature history for Case 3 (Figure 7) is representative of the temperature histories for cases 4 (increased gas pressure), 5 (decreased fuel-cladding gap), and 6 (increased gas pressure with reduced fuel-cladding gap).

It should be noted that the thermal-hydraulic modeling in FRAPTRAN is not fully adequate for this type of transient. This is indicated by other studies of this scenario, using more detailed thermal-hydraulic modeling, predicting shorter axial rod sections experiencing dry out. In addition, the critical heat flux correlation used by FRAPTRAN is being applied outside of its data base range. Finally, this scenario involves axial variations in the coolant flow which are not modeled by FRAPTRAN.

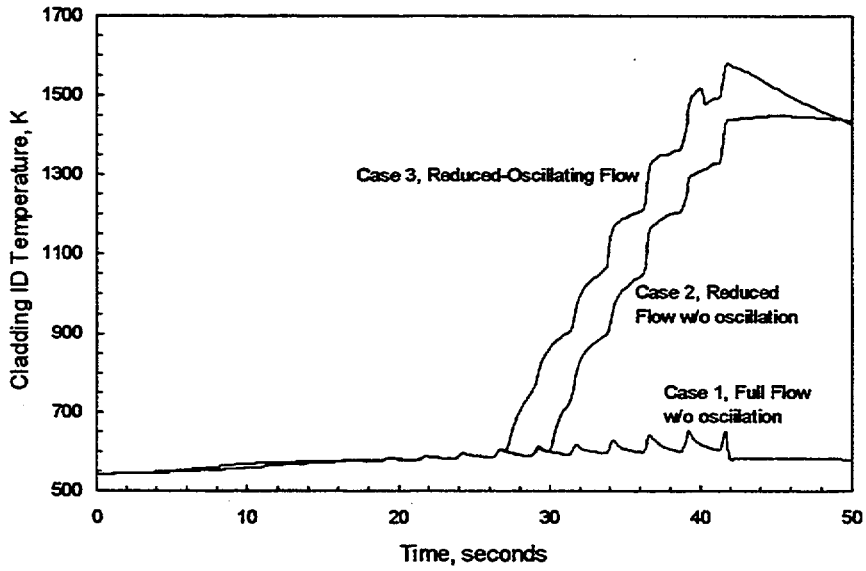

FIGURE 6. Peak Cladding Inside Surface Temperature for Three Coolant Flow Cases

The cladding mechanical response associated with the cladding (and fuel) temperatures is presented in Figures 8, 9, and 10. The axial variation in cladding permanent hoop strain for cases 2 through 6 is presented in Figure 8. Low values of permanent hoop strain at the end of the transient are seen for cases 2, 3, and 5. In contrast, Case 4, with high gas pressure, resulted in large permanent hoop strain along a significant length of the rod. It is recognized that experimental evidence does not support the predicted long axial extent of ballooning predicted for Case 4. Case 6, with high gas pressure and closed fuel-cladding gap, resulted in low permanent hoop strain similar to Case 5 (closed fuel-cladding gap) over most of the length of the rod, but with significant hoop strain at the top of the rod.

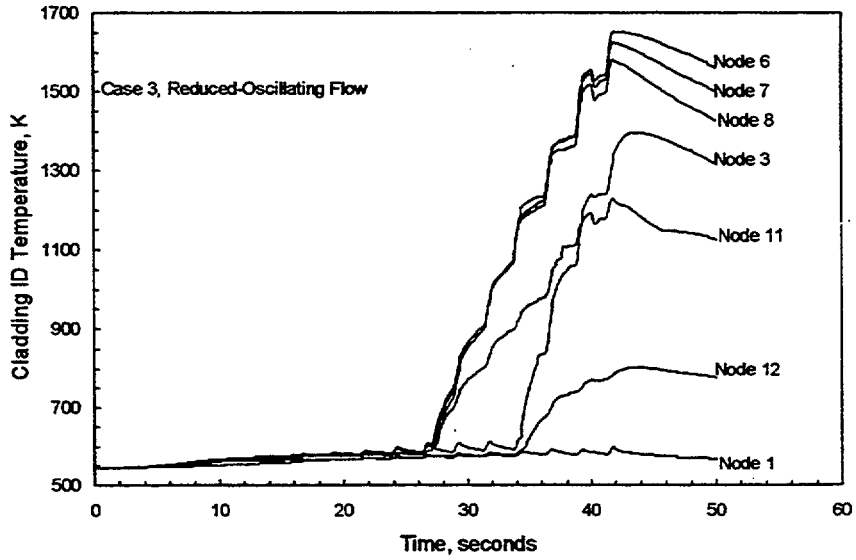

FIGURE 7. Example of Time and Axial Position Variation in Cladding Inside Surface Temperature (Case 3, Reduced and Oscillating Coolant Flow)

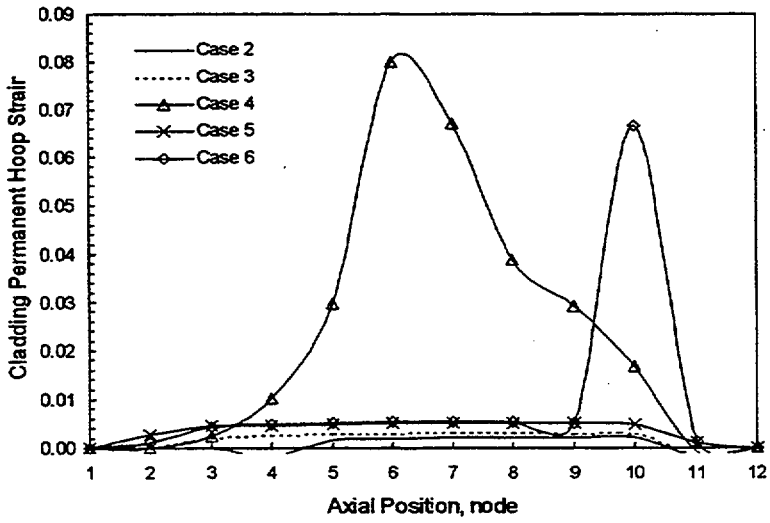

FIGURE 8. Axial Variation in Cladding Permanent Hoop Strain for Selected Cases

The time and axial dependence of permanent hoop strain for the high gas pressure Case 4 is presented in Figure 9. It may be seen that fuel-cladding interaction began at about 34 seconds (during the eighth power cycle), and then increased strongly as cladding temperatures increased (see Figure 7 for representative cladding temperatures). For the closed fuel-cladding gap case (Case 5), pellet-cladding mechanical interaction began during the sixth power cycle (about 30 seconds) and increased with each cycle (see Figure 10).

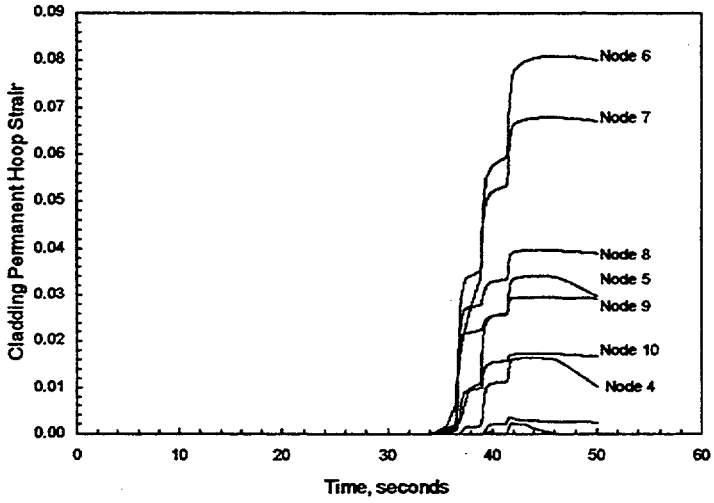

FIGURE 9. Example of Time History for Cladding Permanent Hoop Strain, Case 4, with Cladding Ballooning

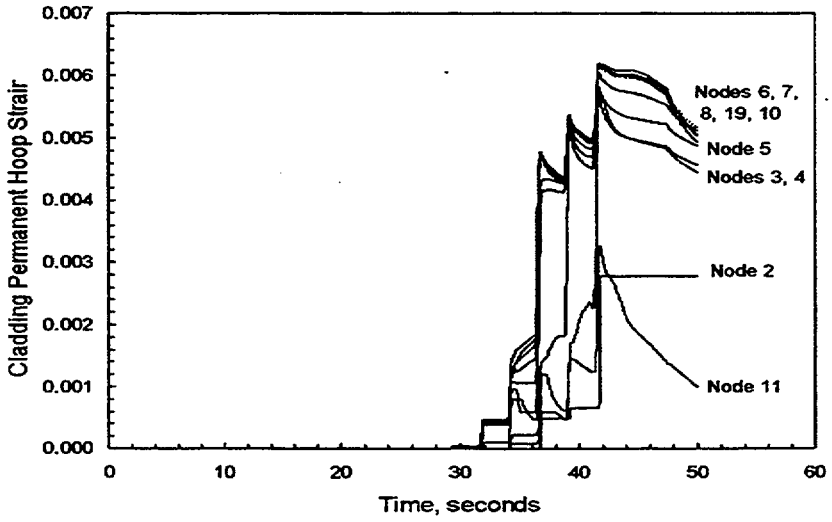

FIGURE 10. Example of Time History for Cladding Permanent Hoop Strain, Case 5, with Pellet-Cladding Mechanical Interaction

It can be seen from Figures 6-10 and Table 3 that the results are highly dependent on the assumptions. In general, all cases show initial pellet-cladding mechanical interaction, with the magnitude being dependent on the initial fuel-cladding gap size. If the cooling becomes sufficiently degraded for cladding temperatures to increase to greater than 1000K, then the cladding is predicted to "collapse" onto the fuel if rod gas pressure is less than coolant system pressure, or to "balloon" if rod gas pressure is greater than coolant system pressure.

TABLE 3. Summary of Parametric Cases and Principal Results

Case for Parametric Study	Peak Cladding Temperature	Cladding Response
1. Base rod input, oscillating power, full coolant flow	650K	Very slight PCMI during last power oscillation
2. Base rod input, oscillating power, reduced coolant flow (40%) without oscillation	1450K	0.38% peak permanent strain; PCMI beginning after seventh cycle; some cladding "collapse" onto the fuel
3. Base rod input, oscillating power reduced coolant flow with oscillation (Figure 5)	1650K	0.42% peak permanent strain; PCMI beginning after sixth cycle; some cladding "collapse" onto the fuel
4. Rod gas pressure increased to system pressure at 8 kW/m, oscillating power, reduced coolant flow with oscillation	1450K	8.1% peak permanent strain; cladding ballooning at axial nodes 6-7
5. Fuel-cladding gap closed at 8 kW/m, base rod gas pressure, oscillating power, reduced coolant flow with oscillation	1620K	0.6% peak permanent strain; PCMI interaction before ballooning
6. Combination of cases 4 and 5; i.e., closed fuel-cladding gap with high gas pressure	1590K	7.0% peak permanent strain; PCMI strains at nodes other than node 10 where ballooning apparently occurred

SUMMARY AND STATUS

The current status of the FRAPTRAN effort is as follows: principal code development is completed, assessment cases have been run and evaluated, the code description and assessment reports have been written, and a peer review is in process. The code description and assessment reports will be finalized considering the peer review comments, and then the code will be issued in 2001. As material properties models are improved in the future, for example from the work being done by ANL on high-burnup cladding, those models will be incorporated in MATPRO for use by FRAPTRAN.

REFERENCES

Berna, G.A., et al. 1997. *FRAPCON-3: A Computer Code for the Calculation of Steady-State, Thermal-Mechanical Behavior of Oxide Fuel Rods for High Burnup.* NUREG/CR-6534, Vol. 2 (PNNL-11513), Pacific Northwest National Laboratory, Richland, Washington.

Boyack, B.E., et al. 2000. *Phenomenon Identification and Ranking Tables (PIRTs) for Power Oscillations Without Scram in Boiling Water Reactors Containing High Burnup Fuel,* LA-UR-00-3122 DRAFT, Los Alamos National Laboratory, Los Alamos, New Mexico.

Cunningham, M.E., and H.H. Scott. 1999. "FRAPTRAN Calculations of Possible Rapid Power Oscillation Experiments in the HBWR," presented at the Enlarged Halden Program Group Meeting, Loen, Norway, May 24-29, 1999.

Fuketa, T., et al. 2000. "Behavior of PWR and BWR Fuels During Reactivity-Initiated Accident Conditions," in *Proceedings of the International Topical Meeting on Light Water Reactor Performance,* Park City, Utah, April 10-13, 2000.

Gellerstedt, J.S., et al. 1969. "Correlation of Critical Heat Flux in a Bundle Cooled by Pressurized Water," *Two-Phase Flow and Heat Transfer in Rod B undles,* Symposium presented at the Winter Annual Meeting of the American Society of Mechanical Engineers, Los Angeles, California, pp. 63-71.

Hagrman, D.L., G.A. Reymann, and R.E. Mason. 1981. *MATPRO-Version 11 (Revision 2): A Handbook of Materials Properties for Use in the Analysis of Light Water Reactor Fuel Rod Behavior,* NUREG/CR-0497 (TREE-1280, Rev. 2), Idaho National Engineering Laboratory, Idaho Falls, Idaho.

Lanning, D.D., et al. 1997. *FRAPCON-3: Integral Assessment,* NUREG/CR-6534, Vol. 3 (PNNL-11513), Pacific Northwest National Laboratory, Richland, Washington.

Lanning, D.D., C.E. Beyer, and C.L. Painter. 1997. *FRAPCON-3: Modifications to Fuel Rod Material Properties and Performance Models for High-Burnup Application,* NUREG/CR-6534, Vol. 1 (PNNL-11513), Pacific Northwest National Laboratory, Richland, Washington.

Larson, J.R., et al. 1979. *PBF-LOCA Test Series; Test LOC-11 Test Results Report.* NUREG/CR-0618, Idaho National Engineering Laboratory, Idaho Falls, Idaho.

Papin, J., and F. Schmitz. 1997. "The Status of the CABRI REP-Na Test Program: Present Understanding and Still Pending Questions," in *Proceedings of the Twenty-Fifth Water Reactor Safety Meeting,* NUREG/CP-106, Volume 2, US Nuclear Regulatory Commission, Washington, D.C.

Siefken, L.J., et al. 1981. *FRAP-T6: A Computer Code for the Transient Analysis of Oxide Fuel Rods.* NUREG/CR-2148 (EGG-2104), and Addendum dated June 1983, Idaho National Engineering Laboratory, Idaho Falls, Idaho.

Wilson, C.L., et al. 1983. *LOCA Simulation in NRU Program; Data Report for the Fourth Materials Experiment (MT-4).* NUREG/CR-3272 (PNL-4669), Pacific Northwest National Laboratory, Richland, Washington.

PWR Owners Group Perspective of NRC Research Performed for GSI-191, "Assessment of Debris Accumulation on PWR Sump Performance"

Timothy S. Andreychek
Westinghouse Electric Company, LLC
Representing B&WOG, CEOG and WOG
andreyts@westinghouse.com
412-374-6246

PWR Owners Group Perspective of NRC Research for GSI-191

- Background
- PWR Owners Groups' Activities
- NEI Initiatives
- NRC Research followed by PWR Industry
- PWR Industry Expectations

PWR Owners Group Perspective of NRC Research for GSI-191

Background

- Post accident sump performance of on-going concern to NRC
  - USI A43 (1985)
  - Subsequent Information Notices
  - Recent BWR Issues
- PWR Owners committed to working with NRC to address concerns

PWR Owners Group Perspective of NRC Research for GSI-191

PWR Owners' Groups Activities

- Active Support of NRC Research
  - Participation in Public Meetings
  - Submitted focused, directed comments
  - Encouraged plants to participate in NRC research
  - Shared PWR Industry Initiatives
    - Debris Transport
    - Risk Informed Approach
  - Support of NRC PIRT panels
  - Support of related NEI Initiatives

PWR Owners Group Perspective of NRC Research for GSI-191

NEI Initiatives

- Serves as formal interface with NRC
- Formed Task Force to follow issues
  - Focused PWR Industry forum for discussion of issues, NRC initiatives
  - Collect and submit comments from Public Meetings
  - PWR Sump Design Survey
    - Initiated in response to NRC request
    - Collected and issued information to NRC

PWR Owners Group Perspective of NRC Research for GSI-191

NRC PWR Sump Performance Research

- Dual focus
  - Materials science study of qualified coating failures
    - Analytical models; fracture mechanics approach
    - Materials data; testing of coatings
  - Sump screen blockage
    - Technically complete and logical approach
    - Integrates industry data, testing, analysis and risk analysis
- Provided for PWR Industry Involvement

PWR Owners Group Perspective of NRC Research for GSI-191

NRC Research followed by PWR Industry

- Qualified Coatings Failure Research
- Debris Transport Research
- Risk Calculations
- Debris Generation Research

These topics appeared to be both important to the overall safety assessment of post-accident sump performance, and were the focus of mutual NRC / PWR Industry interest

PWR Owners Group Perspective of NRC Research for GSI-191

NRC Qualified Coatings Failure Research

- Until recently, little impact on debris transport
- Recent testing shows possible failure mechanism
  - Dose rate and submergence appear to be drivers
  - Failure mechanisms not fully understood
  - Understanding of commonality of failure mechanisms to all qualified coatings not understood at this time
  - Applicability of data to operating plants not established
- Industry comments have been provided via NEI

PWR Owners Group Perspective of NRC Research for GSI-191

NRC Debris Transport Research

- Uses NEI containment sump survey data
- Debris transport testing
  - Initial flume tests
    - RMI behavior similar to that observed in USI-A43 testing
    - Coatings debris tested did not transport
    - Fibrous materials, calcium silicate show transportability
    - Strong industry interaction with program via site visit
  - Awaiting follow-on testing

PWR Owners Group Perspective of NRC Research for GSI-191

NRC Risk Calculations

- NRC Contractor Approach
  - Mature effort; computation models developed
  - To be completed towards end of program
  - Work and status presented at public meeting in March 2000
    - Industry comments focused on model details and usage
    - NRC agreed to additional public meeting
  - Unclear of how risk calculations will be used in or to support NRC decision-making process
  - This activity is not a Risk Informed process
- PWR Industry asked to share how they would apply a Risk Informed process to this issue

PWR Owners Group Perspective of NRC Research for GSI-191

PWR Industry Risk Informed Approach

- Based on Regulatory Guide 1.174, "An Approach for Using Probabilistic Risk Assessment in Risk-Informed Decisions on Plant-Specific Changes to the Licensing Basis."
- Six step approach defined:
  - Phenomenological (deterministic) tasks
    - Identification of events and sequences that can cause debris generation
    - Assessment of debris generation by these events
    - Assessment of debris transport with respect to plant geometry/features
    - Assessment of susceptibility to sump blockage
  - Risk evaluation tasks
    - Determination of risk impact due to sump blockage
    - Alternate actions or accident management to prevent core damage due to sump blockage.

PWR Owners Group Perspective of NRC Research for GSI-191

NRC Debris Generation Research

- Available data is for air / steam jets
  - Applicability to PWR conditions not clear
  - NRC and PWR Industry agree with need for testing at PWR conditions
- NRC Program
  - To be performed jointly with Ontario Power
  - Initiation of testing reported to be eminent
  - Program details not yet shared with Industry

PWR Owners Group Perspective of NRC Research for GSI-191

PWR INDUSTRY EXPECTATIONS

- Continued high level of cooperation with, support of, NRC research programs
- Continued inclusion of PWR Industry in research via PIRT panels and public meetings
- Address post-accident sump operation concerns
  - Maintain, improve safety
- Other uses and benefits of NRC research
  - Support license renewal
  - Increase flexibility of maintenance

PRESSURIZED WATER REACTOR SUMP SCREEN BLOCKAGE STUDY: APPROACH BEING USED

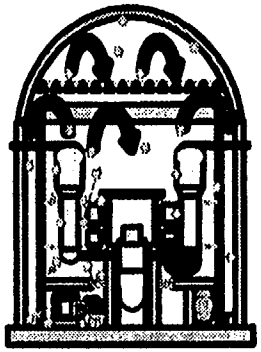

U.S. NUCLEAR REGULATORY COMMISSION
OFFICE OF NUCLEAR REGULATORY RESEARCH
DIVISION OF ENGINEERING TECHNOLOGY
ENGINEERING RESEARCH APPLICATIONS BRANCH

MICHAEL MARSHALL,
PROJECT MANAGER & MECHANICAL ENGINEER
MXM2@NRC.GOV
301-415-5895

Overview of Safety Concern

Primary Concern: The Accumulation of Debris on Sump Screens (or Strainers) Will Increase the Resistance Across the Screen (or Strainer) and Thus Reduce the Net Positive Suction Head Available to the Emergency Core Cooling System Pumps Drawing Suction From the Sump.

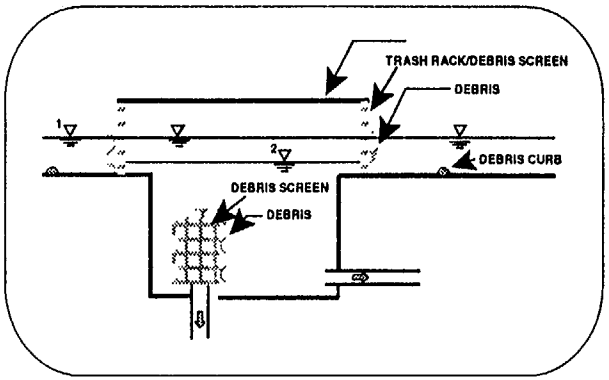

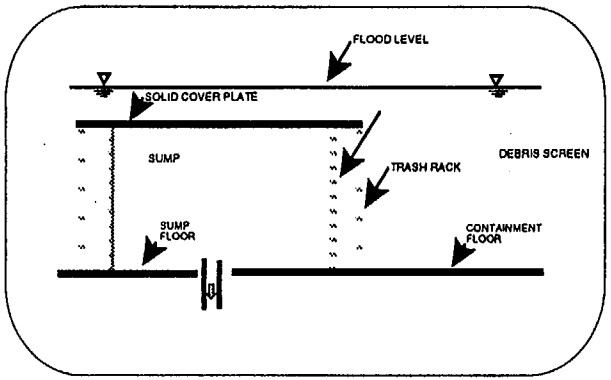

Other Concern: The Accumulation of Debris at the Sump Screen or Along the Flowpaths on the Containment Floor May Form Dams That Prevent or Impede the Flow of Water Into the Sump and Thus the Water in the Sump Can Be Drawn Down Which Will Reduce the Net Positive Suction Head Available to the Emergency Core Cooling System Pumps and Effectively Reduce the Water Inventory in the Sump.

Overview of Study

Sponsor

Primary Contractor

The University of New Mexico

Sub Contractor

Integrated Analysis

- To Extent Practical Calculations and Models Will be "Realistic" (i.e., best estimate)
- Identify Important Phenomena and Plant Features
- Identify Important Parameters
- Identify (or Develop) and Evaluate Models
- Models May Be Empirical, Theoretical, or Combination
- Conduct Experiments
- Compare Models to Separate Effects Experiments
- Integrate Models

Overview of Approach

- Identify Debris Sources
- Estimate Amount of Debris Generated
- Estimate Amount of Debris Transported
- Estimate Head Loss Caused by Debris
- Compare Head Loss to NPSH Margin

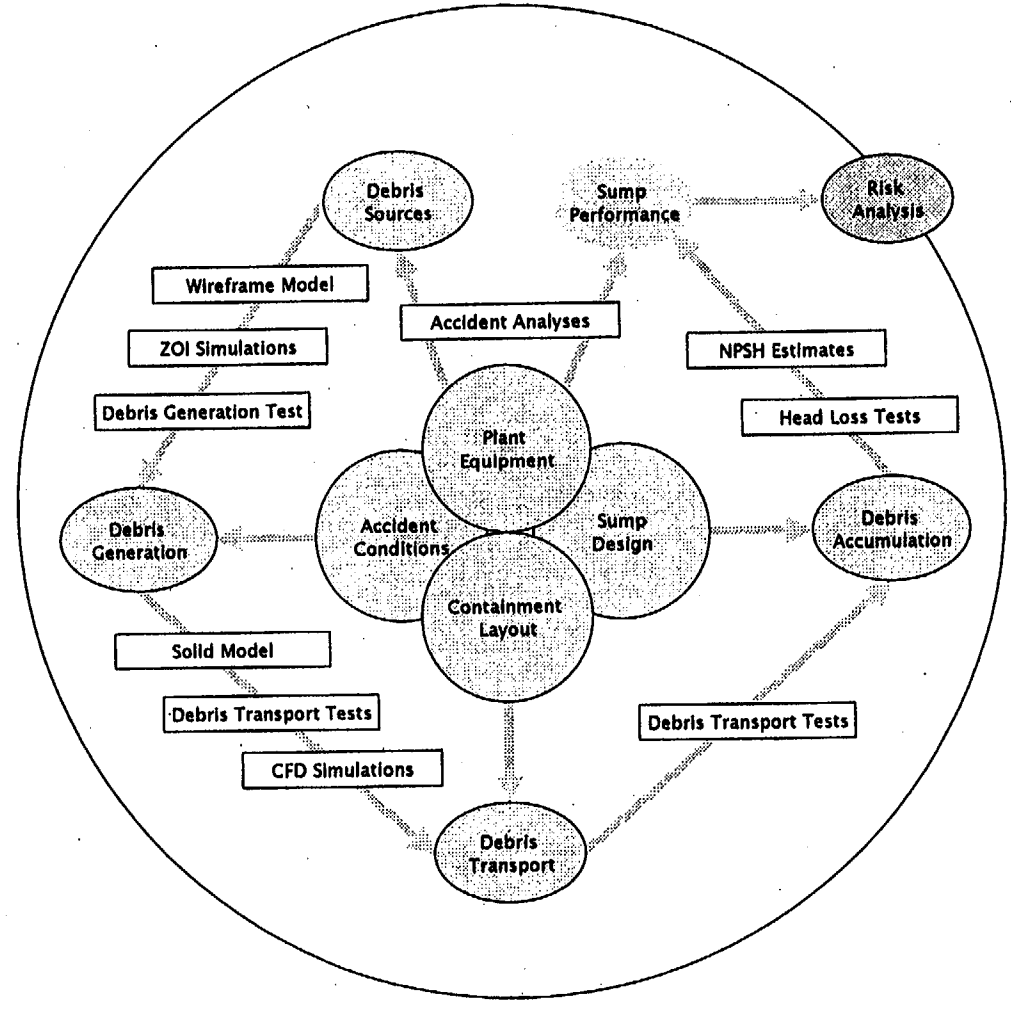

Reference Plant and Accidents

Reference Plant

- 4-Loop Westinghouse
- Large Dry Containment
- One Sump
- Low Set Point for Sprays

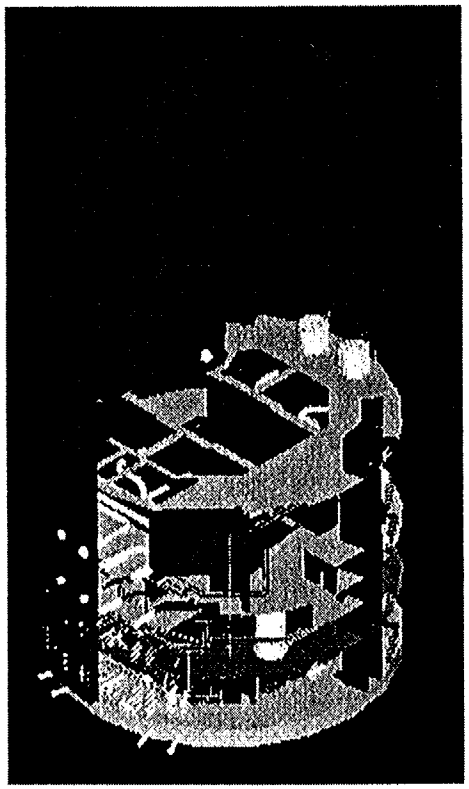

Postulated Accidents

- Large Loss of Coolant Accident
- Medium Loss of Coolant Accident
- Interfacing Systems Loss of Coolant Accident
- Small Loss of Coolant Accident
- Pressurizer Surge Line Break
- Failure of Safety or Relief Valves to Close

☞ The reference plant(s) is based on an operating PWR , but a number of changes have been made to better represent the predominate features found in the majority of operating PWRs.

DEBRIS TYPES

DEBRIS SOURCES IN REFERENCE PLANT

- Thermal Insulations
  - Fiberglass
  - Calcium Silicate
  - SS Reflective Metallic
- Fire Barriers
  - Kaowool
  - Marinite
- Coatings
  - Inorganic Zinc primer and Epxoy Phenlic TopCoat on Steel
  - Epoxy Primer and Epoxy Topcoat on Steel
  - Surfacer and Epoxy Topcoat on concrete

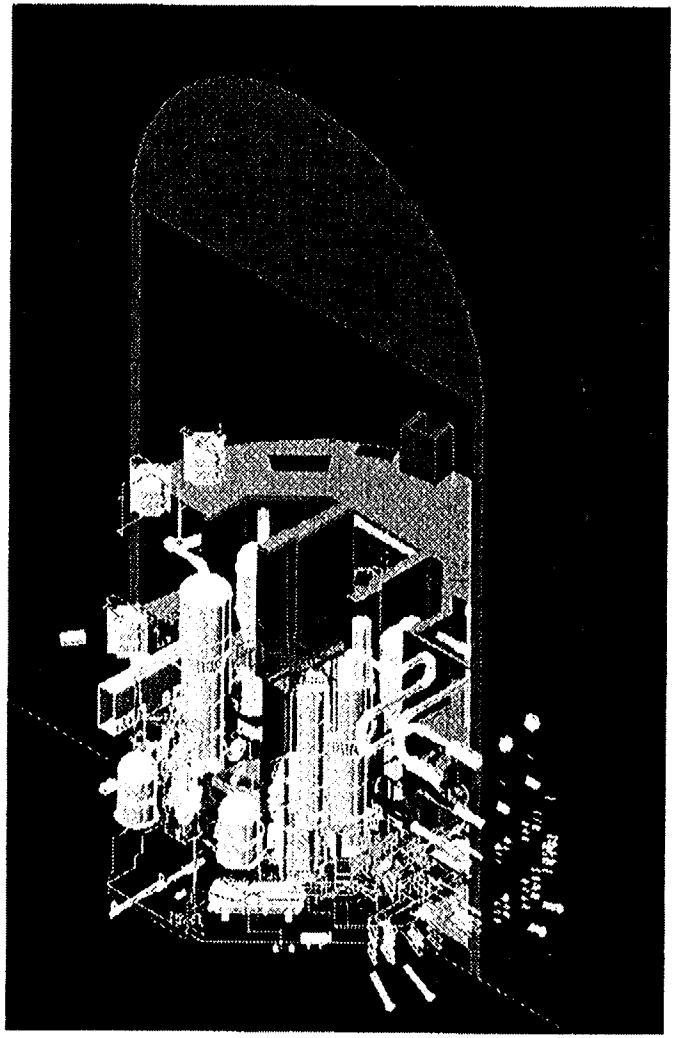

DEBRIS LOCATION

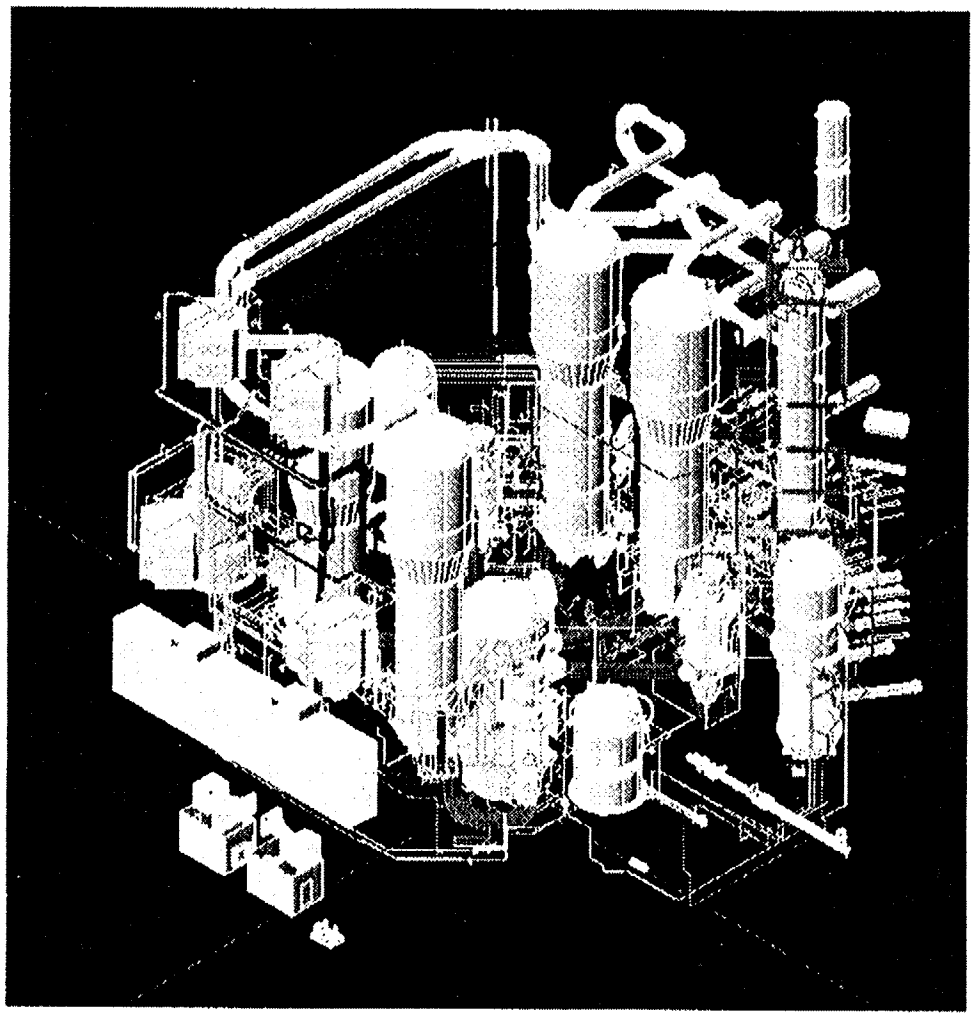

CONSIDERING

- RG 1.82, Rev. 2 - BWR
- Weld Locations
- Most Likely Breaks
- FSARs That Used BTP MEB 3-1

DEBRIS GENERATION

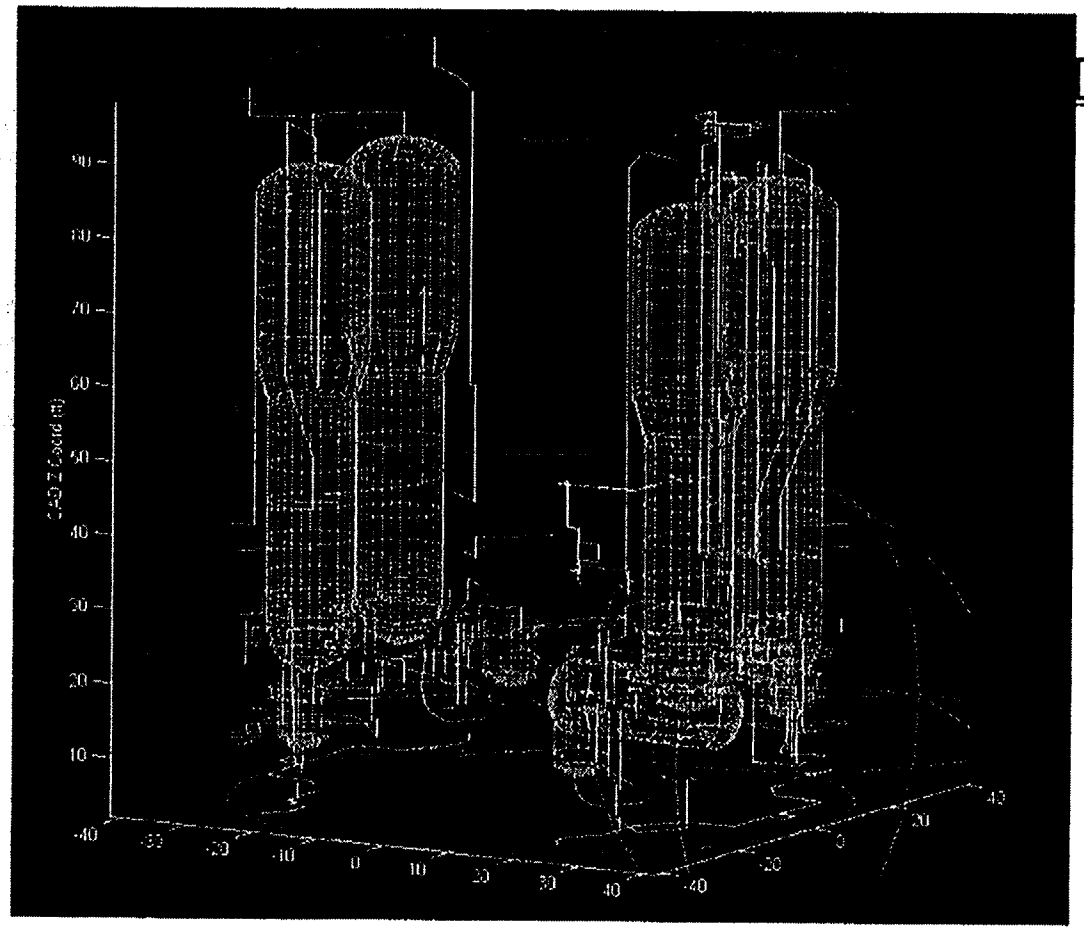

DEBRIS SOURCES

- Source
  - Piping
- Targets
  - Piping
  - Cable Trays
  - Coated Structures

ZONE OF INFLUENCE

- Using
  - Spheres
- Considered
  - Cones

Debris Generation

HOW AMOUNT
GENERATED (will be) ESTIMATED

- Debris Generated by Jet
  - Draw ZOIs for Each Debris Source Around Each Break Location
  - Estimate Amount of Debris Within ZOIs Around Each Break Location
- Debris Generated by Environment
  - Estimate Conditions in Containment at Various Times
  - Compare with Conditions to Create Debris

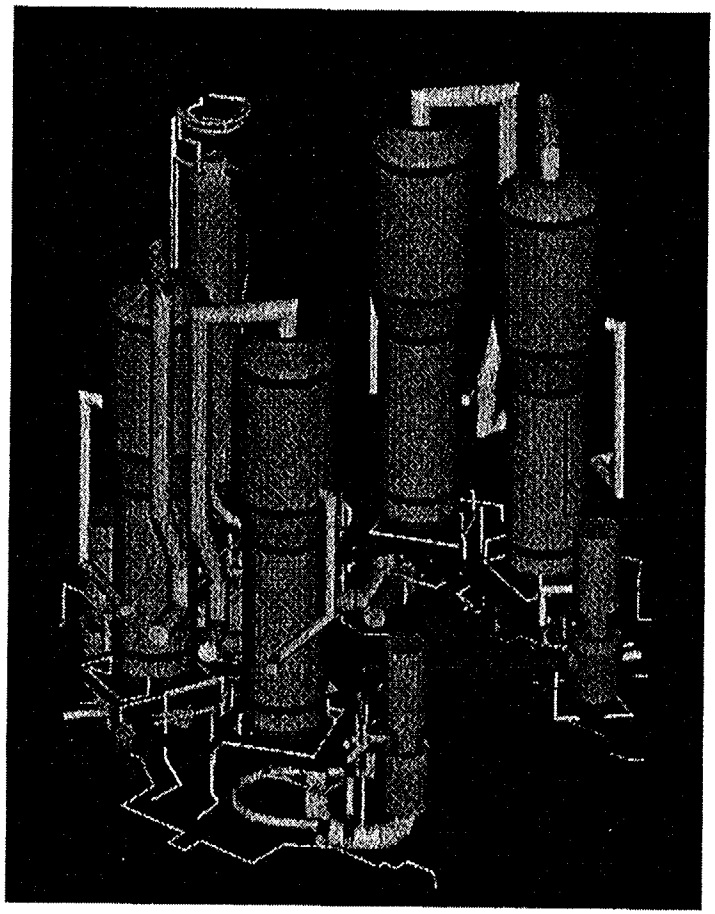

DEBRIS TRANSPORT IN CONTAINMENT

HOW AMOUNT TRANSPORTED (will be) ESTIMATED

- Debris Generated by Jet
  - Divide Containment Into Regions
    - Elevation
    - Obstacles (i.e., gratings)
  - For Each Debris Source Estimate Fraction of Transport to Pool From Region
- Debris Generated by Environment
  - Divide Containment Into Regions
  - For Each Debris Source Estimate Fraction of Transport to Pool From Region at Various Times

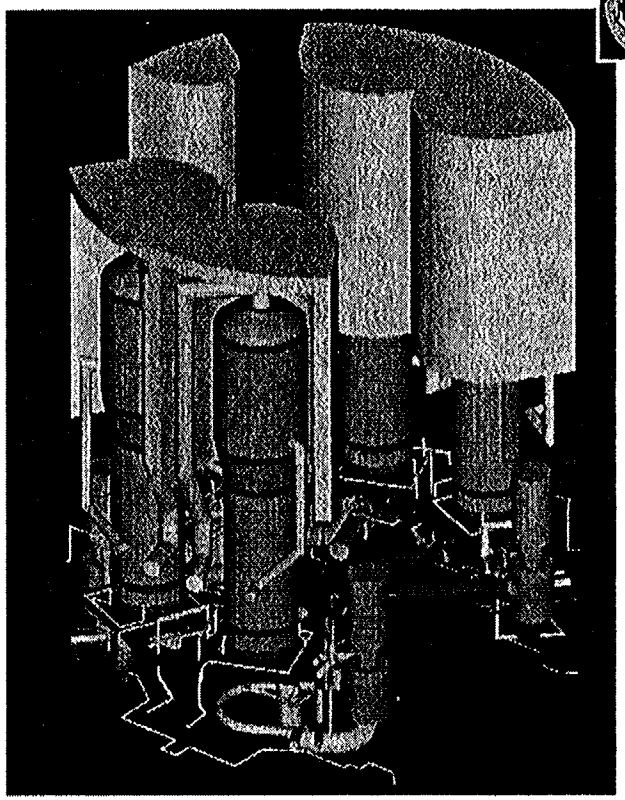

DEBRIS TRANSPORT ON FLOOR

HOW AMOUNT TRANSPORTED (will be) ESTIMATED

- Calculate Pool Height and Conditions at Various Times (i.e., Map Out Flow Fields)
- Compare to Conditions Need to Transport Each Type of Debris Near Sump (i.e., Sump Zone) and Far From Sump

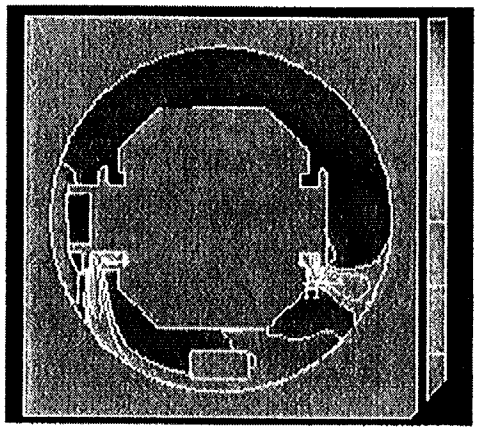

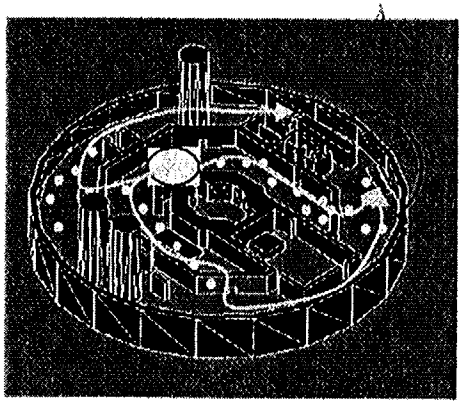

Debris Accumulation and Head Loss

How Magnitude of Head Loss (will be) Estimated

- Estimate Amount of Debris that Reach Screen
- Calculate Flow Velocity at Screen Surface and Curb
- Compare Condition at Screen with Conditions Needed for Debris to Adhere to Screen

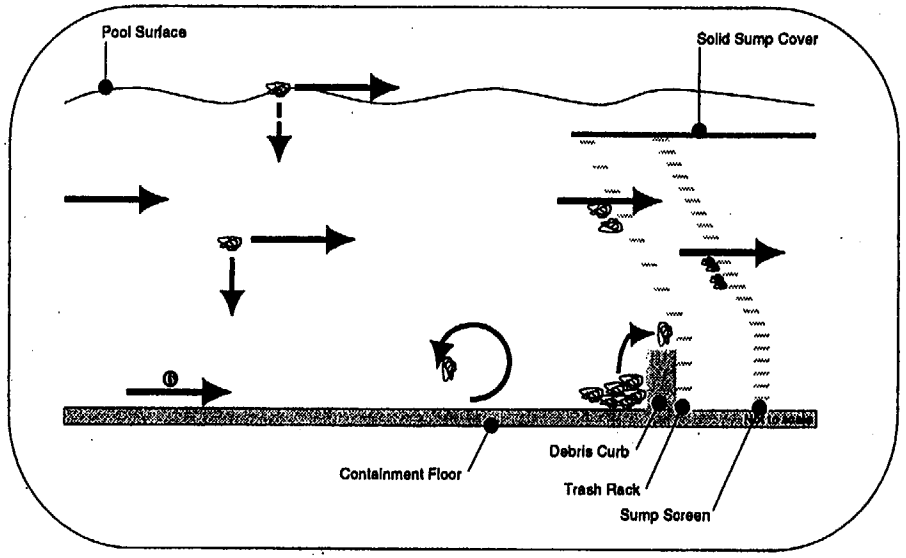

- ❖ Uniform Coverage
  - Empirical Head Loss Calculation
- ❖ Non-Uniform Coverage
  - Calculate Head Loss for Unobstructed Area

PARAMETRIC CALCULATIONS

- Parametric Calculations will be Performed to:
  - Ensure Study Has Generic Applicability
  - Identify Plant Features and Parameters That Most Influence Results

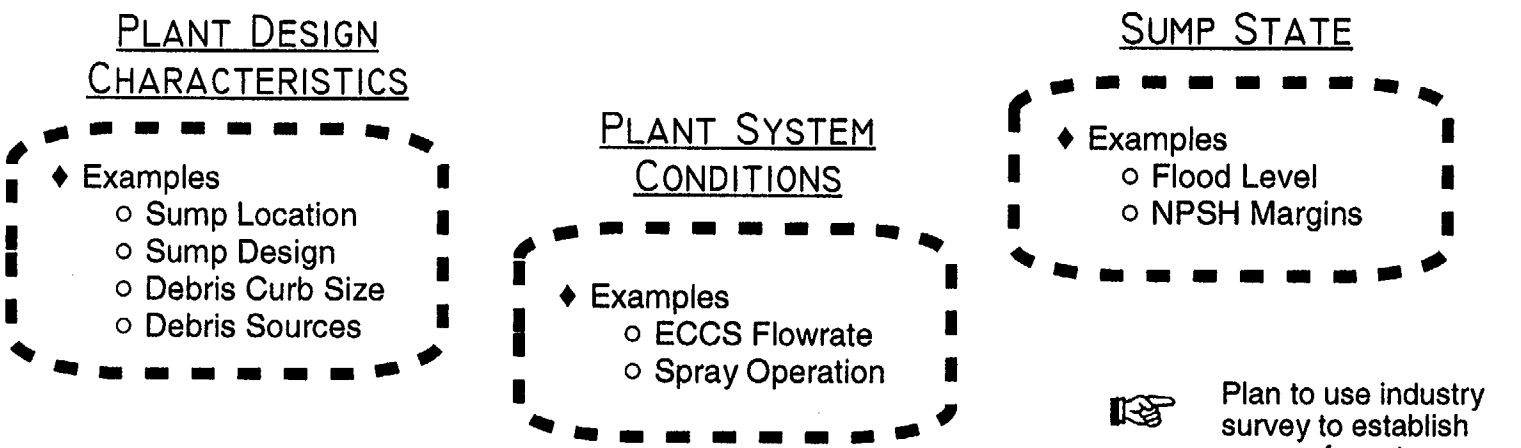

PIRT PROCESS
for
SRTC Containment Coatings Research Program

presented at the
28th Annual Water Reactor Safety Meeting
Bethesda, Maryland

Jon Cavallo
Industry Coating PIRT Panel Chairman
October 24, 2000

Industry Coating PIRT Activity

Industry Coatings PIRT Objectives

- Identify coating systems considered for PIRT process
  - Based on industry usage
  - Steel substrate
  - Concrete substrate
- Identify phenomena and processes for coatings applied inside NPP containments
- Rank those phenomena and processes with respect to their importance to coatings failures

DEFINITIONS

- **Failure:**
  - Disbonding of an applied coating (paint) system into free debris, regardless of size and shape, that is available for transport; a debris source term.
- **Debris Source Terms:**
  - Coating systems that have failed prior to the event.
  - Coating systems that fail as a consequence of the event.

COMPONENTS AND PHENOMENA RANKING SCALES

- **High** – Phenomena has a dominant impact on the primary parameter of interest. Phenomena will be explicitly considered in the implementation of the SRTC research program.
- **Medium** – Phenomena has a moderate influence on the primary parameter of interest. Phenomena will also be considered in the implementation of the SRTC research program.
- **Low** – Phenomena has a small effect on the primary parameter of interest. Phenomena will also be considered in the implementation of the SRTC research program, to the extent possible.

PARTITION COATING SYSTEM INTO COMPONENTS

1. Substrate (Concrete or Steel)
2. Substrate/Primer (Steel) or Substrate/ Surfacer (Concrete) Interface
3. Primer (Steel) or Surfacer (Concrete)
4. Primer/Topcoat (Steel) or Surfacer/Topcoat (Concrete) Interface (not applicable to untopcoated IOZ)
5. Topcoat (not applicable to untopcoated IOZ)

TIME PHASES

Phase 1:	Normal Operation
(-) time	Coating system installation: » Surface Preparation » Coating Application » Curing ILRT
t = 0.0	Start of Power Operations.
t = 40 yr.	LOCA occurs (60 years – plant life extension
Phase 2:	0-40 seconds after initiation of LOCA
Phase 3:	40 seconds - 30 minutes after initiation of LOCA
Phase 4:	30 minutes - 2 hours after initiation of LOCA
Phase 5:	>2 hours after initiation of LOCA

28th Annual Water Reactor Safety
Meeting, Session 4A, October 24, 2000,
Bethesda, Maryland

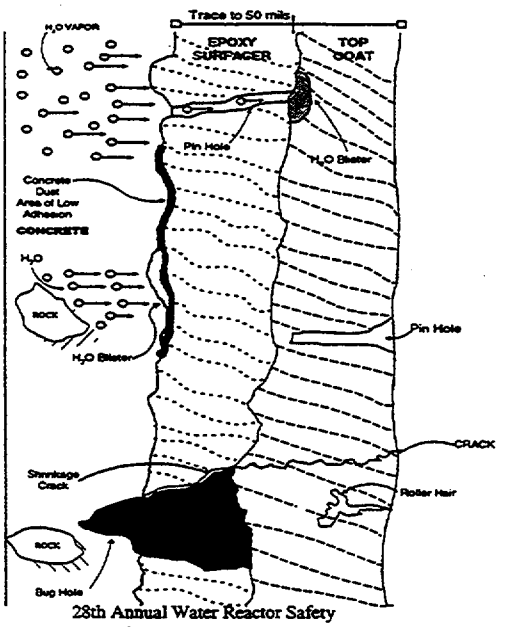

28th Annual Water Reactor Safety
Meeting, Session 4A, October 24, 2000,
Bethesda, Maryland

Concrete Substrate, Surfacer, Epoxy Topcoat - Phase 2

Component	Processes & Phenomena	Rank	Definition
substrate (concrete)	Outgassing / vapor expansion	high	Vapor migration through concrete damage
	Pressure gradients from ILRT's	high	Experience from Phase 1 ILRT shows coatings have come off from rapid depressurizations
	Temperature gradients	low	Would not degrade concrete
	Compression / expansion	low	No evidence of significant impact
	Increased radiation exposure	low	No evidence of significant impact
substrate/surfacer interface	Calcium carbonate buildup	low	Potential pure vapor long term
	Differential expansion/contraction	low	Surfacer designed to withstand expansion/contraction
	Blistering/delamination	high	Maximum pressure and thermal loading
	Vapor buildup	high	Vapor collection under surface
surfacer	Bulk movement	low	No movement of surfacer; thermal expansion of concrete is small
	Environmental exposure	low	Lot of exposure over time to heat
	Coating anomalies	high	Pathway for vapor transmission
	Cracking	low	Not observed from experience; not considered likely
	Chemical exposure	low	Top coat protects the surfacer
	Water diffusion (from concrete)	low	Not by bulk diffusion; can occur through pathways through top coat
	Mechanical damage	low	Does not affect bulk coating integrity; low priority
	Water intrusion pool	n/a	Not in this phase of the event
	Temperature gradient	low	Low, does not affect the surfacer
	Water/air diffusion (from outside the topcoat above submerged level)	low	Low, only through pathways through top coat
	Increased radiation exposure	low	Low; based on test data
surfacer/topcoat interface	Differential expansion/contraction	low	No difference in relative thermal expansion coefficients of the topcoat and surfacer
	Blistering/delamination	high	
	Vapor buildup	high	Vapor collection under the top coat

28th Annual Water Reactor Safety
Meeting, Session 4A, October 24, 2000,
Bethesda, Maryland

TABLE 1

SUMMARY PIRT TABLE

Steel Substrate - Inorganic Zinc Primer - Epoxy Phenolic Top Coat System (PIRT System 1, SRTC System 1)

	Phases →	1	2	3	4	5
	Processes & Phenomena					
IOZ Primer	Film splitting	M	M	M	M	M
	Minor coating anomalies	M	H	M	M	
	Diffusion rate of air/water		L	M	M	H
	Chemical attack			L	M	L
	Moisture & air intrusion through damage sites				M	H
Primer / Top Coat Interface	Differential contraction/ expansion	M	H	H	L	L
	Diffusion rate of air/water		L	H	H	H
Top Coat	Expansion/contraction	M	H	H	L	L
	Environmental exposure	H				
	Mechanical damage	M	L			
	Diffusion of air/water		L	L	L	M
	Immersion to pool surface				L	M

28th Annual Water Reactor Safety
Meeting, Session 4A, October 24, 2000,
Bethesda, Maryland

TABLE 2

SUMMARY PIRT TABLE

Concrete Substrate - Surfacer - Epoxy Top Coat System (PIRT System 6, used by SRTC for SRTC System 2 evaluation)

	Phases →	1	2	3	4	5
	Processes & Phenomena					
Substrate (Concrete)	Outgassing/Vapor Expansion	H	H	H	M	M
	ILRT Pressure Gradients	M	H	H	L	L
Substrate/ Surfacer Interface	Calcium Carbonate Buildup	M				M
	Blistering/Delamination	H	H	H	H	H
	Vapor Buildup	H	H	H	M	M
Surfacer Coating Anomalies	Environmental Exposure	M	L	L	L	M
		H	H	H	M	M
Surfacer/Top Coat Interface	Blistering/Delamination	H	H	H	H	H
	Vapor Buildup	H	H	H	M	M
Top Coat (Epoxy)	Coating Anomalies	H	H	H	M	M
	Environmental Exposure	H	L	L	L	M
	Immersion in Pool					M

28th Annual Water Reactor Safety
Meeting, Session 4A, October 24, 2000,
Bethesda, Maryland

OXIDATION EFFECTS ON EPOXY AND EPOXY PHENOLIC TOPCOATS

- Oxidation damage to exterior surface of topcoats apparently occurs synergistically with radiation (based on SRTC experimental results)
- Based on SRTC experimental results to date, topcoat degradation apparently occurs when topcoat is irradiated, oxidized
  - and immersed
  - or exposed to accident pressure/temperature "pulse" and moisture saturated air
- These phenomena previously unknown to PIRT panel

APPLICATION OF SRTC DATA

- Input to RES PWR Sump Blockage Research Project
- Review and update testing standards (ASTM D4082, D3911)
- Need for better understanding of synergistic effects of radiation integrated exposure, radiation dose rate, LOCA environments and immersion on topcoats of different formulations

Concrete Substrate, Surfacer, Epoxy Topcoat - Phase 2

Component	Processes & Phenomena	Rank	Definition
substrate (concrete)	Outgassing / vapor expansion	high	Vapor migration through concrete damage
	Pressure gradients from ILRTs	high	Experience from Phase 1 ILRT shows coatings have come off from rapid depressurizations
	Temperature gradients	low	Would not degrade concrete
	Compression / expansion	low	No evidence of significant impact
	Increased radiation exposure	low	No evidence of significant impact
substrate/surfacer interface	Calcium carbonate buildup	low	Potential pure vapor long term
	Differential expansion/contraction	low	Surfacer designed to withstand expansion/contraction
	Blistering/delamination	high	Maximum pressure and thermal loading
	Vapor buildup	high	Vapor collection under surface
surfacer	Bulk movement	low	No movement of surfacer; thermal expansion of concrete is small
	Environmental exposure	low	Lot of exposure over time to heat
	Coating anomalies	high	Pathway for vapor transmission
	Cracking	low	Not observed from experience; not considered likely
	Chemical exposure	low	Top coat protects the surfacer
	Water diffusion (from concrete)	low	Not by bulk diffusion; can occur through pathways through top coat
	Mechanical damage	low	Does not affect bulk coating integrity; low priority
	Water intrusion pool	n/a	Not in this phase of the event
	Temperature gradient	low	Low, does not affect the surfacer
	Water/air diffusion (from outside the topcoat above submerged level)	low	Low, only through pathways through top coat
	Increased radiation exposure	low	Low; based on test data
surfacer/topcoat interface	Differential expansion/contraction	low	No difference in relative thermal expansion coefficients of the topcoat and surfacer
	Blistering/delamination	high	
	Vapor buildup	high	Vapor collection under the top coat

28th Annual Water Reactor Safety
Meeting, Session 4A, October 24, 2000,
Bethesda, Maryland

Analysis of Spent Fuel Heatup After Loss of Coolant

Christopher Boyd
US Nuclear Regulatory Commission

ABSTRACT

To provide technical support for the decommissioning rulemaking activity within NRR, the Office of Research has completed a three-dimensional computational fluid dynamics (CFD) analysis of a spent fuel pool and containment building. Prior reported analyses have relied on simplified flow field assumptions which raised questions concerning their validity. The full three-dimensional CFD analysis of the flow field gives the staff a complete picture of this significant phenomena and provides a basis for the assessment of flowfield simplifications made in other models. The primary result is the three-dimensional flowfield. Detailed predictions within the fuel racks lack radiation and clad chemistry models. The model is sized to represent a typical BWR pool and containment building. Predictions are made with fuel loads representative of a fuel pool 2, 3, 4, and 6 years after the reactor is shut down. Sensitivity studies are completed on the ventilation rate, the outer wall heat transfer coefficient, the location of the hottest fuel, fuel burnup, the flow resistance within the racks, and heat conduction within the racks.

INTRODUCTION

In support of the Nuclear Regulatory Commission (NRC) rulemaking activity related to decommissioning, the office of Nuclear Reactor Regulation (NRR) is completing a study on spent fuel pool accident risks. In support, the Office of Nuclear Regulatory Research (RES) is providing technical assistance in several areas. This report documents a thermal-hydraulic evaluation of spent fuel pool heatup after a low-probability complete loss of spent fuel coolant. Computational fluid dynamics (CFD) is used to predict fuel heatup and natural circulation flow paths throughout the spent fuel pool and the upper containment building. The predictions give insights into the phenomena of air cooling which provides most of the heat removal capacity during long-term cooling scenarios after a complete loss of coolant.

Spent fuel pool heatup predictions are typically made using codes tailored to the geometry and physics of spent fuel stored in a rack. Codes of this type include SHARP[1], SFUEL, and COBRA-SFS. The SHARP manual (Ref. 1) provides general background information on some of the important phenomena considered in this type of model. A typical modeling approach is to determine one-dimensional buoyancy-driven flows between idealized upper and lower control volumes tying the fuel bundles together. Codes such as COBRA-SFS and SFUEL incorporate physical models for conduction, radiation, flow losses, clad oxidation chemistry, and other things. The flowfield assumptions, however, simplify the natural circulation flow paths in and around the fuel racks. The assumption of a single well-mixed volume joining each of the

bundles at the top and bottom of the racks does not account for pressure or temperature variations in this region. This idealized upper control volume provides the ultimate heat sink for these models, simulating the entire building and the ventilation system.

Previous studies indicate that in steady-state conditions, the heat produced by the fuel is removed primarily through natural convection flows[2] (Ref 2, p. 47). In addition, the largest source of uncertainty in these fuel heatup predictions is the natural circulation flow rate[3] (Ref 3, p. 57). The RES predictions highlight the natural circulation flows that are simplified in typical spent fuel pool models. The focus of the predictions is on the three-dimensional natural circulation flowfield in and around the fuel pool, racks, and containment building. Physical models for radiation and clad chemistry are not incorporated. The predictions can be used to assess the flowfield assumptions used in other models. The three-dimensional CFD predictions made by RES give valuable insights into the natural circulation air flow which is crucial to spent fuel pool cooling after a complete loss of spent fuel pool coolant.

All code results must be viewed in the light of the assumptions used for the analysis. This CFD model makes simplifying assumptions to represent the complex geometry of the racks and fuel. A porous region provides an equivalent flow resistance for the rack and bundles and aligns the flow in the vertical direction. A volumetric heat source adds the appropriate energy to the fluid in the active fuel region. Predictions are obtained for steady-state conditions to determine the maximum fuel surface temperature for a given pool age and configuration. The CFD predictions do not include models for radiation and clad chemistry. These models are considered important at elevated temperatures ($T > 600$ °C, Ref 2, Figs. 12, 14 and 26). Therefore, the current CFD predictions are more applicable at low temperatures, where these effects are minimal. At elevated temperatures, potential limitations should be kept in mind.

COMPUTATIONAL FLUID DYNAMICS (CFD)

The FLUENT[4] (version 5) CFD code is used to predict the temperature rise in the fuel and the natural circulation flow rates. FLUENT is a commercially available, general-purpose CFD code capable of solving a wide variety of fluid flow and heat transfer problems. The code solves the Reynolds-averaged Navier-Stokes equations a finite volume mesh. The Navier-Stokes equations are the mass, momentum, and energy equations for a continuous fluid. Reynolds-averaging creates the need for turbulence modeling to account for the turbulent diffusion of momentum and energy. The FLUENT code provides several turbulence modeling options and can be applied to almost any geometry.

The predicted results from a CFD analysis are influenced by several steps in the process. In a blind study, where no experimental data are used for bench marking the code, the analyst must rely on accepted CFD practices and engineering judgment to create an acceptable CFD simulation. The basic steps of a CFD analysis are to describe the physical model, develop the CFD model, do sensitivity studies, and validate the solution. Commercial CFD codes are widely used in many industries today. The fundamentals of CFD are to be found in textbooks such as the introductory text by Anderson[5].

PHYSICAL MODEL DESCRIPTION

A simplified model of the containment building, fuel pool, racks, and ventilation system is developed for this investigation. The major parameters used and the physical features of the pool are determined with input from the Office of Nuclear Reactor Regulation (NRR). The model is based upon a boiling water reactor (BWR) containment and fuel pool. The major components are described below.

Pool and Racks

The pool and fuel rack dimensions are typical of a large BWR. The pool is assumed to be completely filled with high-density racking. The racks extend to within 0.15 m (6 in.) of the fuel pool walls. To establish symmetry, the pool is centered on the long axis of the containment building. Figure 1 shows the features of the fuel pool cut along the line of symmetry. The finite volume cells used to represent the rack region in the CFD model are included to highlight the location of the racks. Overall pool dimensions are 9.54 m x 11.08 m x 12 m (l, w, d). The fuel racks sit 0.15 m (5.9 in.) from the pool floor and are 4.3 m (14.1 ft) in height. The high-density racking occupies the entire lower pool (except the 0.15 m gap around the exterior). Figure 2 shows the structure of a typical high-density rack. The square cells which make up the rack share a wall between neighboring cells and there are no open cells. The walls are solid so there is no communication of fluid between cells. Cell pitch is 0.154 m (6 in.). Rack-to-rack spacing is ignored in this model, which is equivalent to assuming a single rack structure with 4200 cells (60 x 70; 9.24 m x 10.78 m). Assuming a full core contains 800 bundles, this pool is racked to hold 5 ¼ cores.

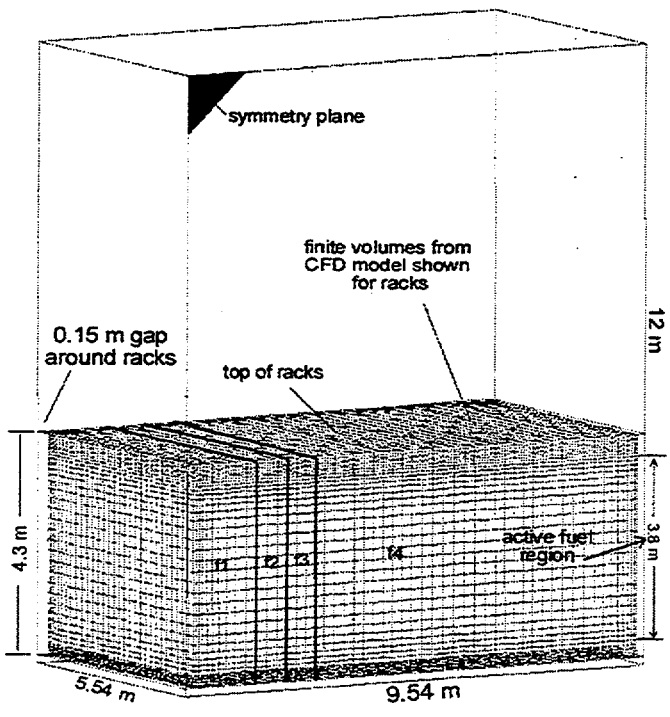

Figure 1. Pool Region and Racks

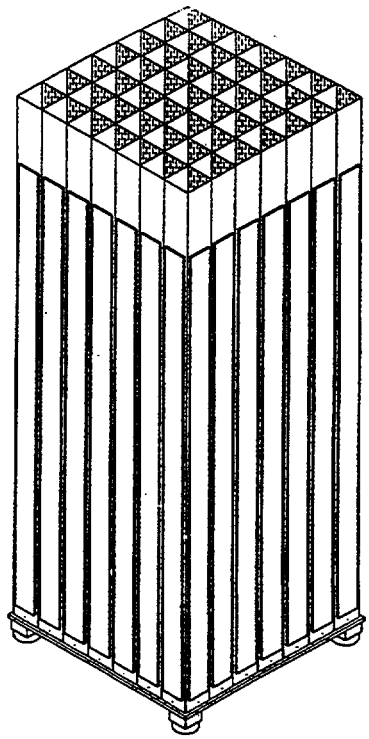

Figure 2. High-Density Fuel Rack

Fuel

A fuel bundle is assumed to occupy each cell of the high-density racking (4200 assemblies). A uniform active (heat generating) length of 3.8 m (12.46 ft) is centered from top to bottom in the racks. Four pool regions are defined with unique characteristics. A hot region with 800 bundles (f1 = 1 core), a second region with 267 bundles (f2 = 1/3 core), a third region with 267 bundles (f3), and a final region with 2866 bundles (f4). Fuel f2 is assumed to be 18 months older than fuel f1 and fuel f3 is 18 months older than fuel f2. Region f4 represents all of the remaining (older) fuel. The fuel layout is illustrated in Figure 1. The hot fuel (f1) is assumed to remain in a contiguous region on the left side of the pool. Fuel f2 is in another contiguous region next to the hottest fuel. Next comes fuel f3. The remaining 2866 bundles, f4, fill out the rack. A sensitivity study is done to look at the effect of moving the hottest fuel, f1, to the center of the pool. Details of the 9x9 BWR fuel bundle geometry are given in reference 8 Table 1 lists the fuel loads applied in this analysis. The fuel loads are given in watts per bundle. These loads are based upon an average burnup of 40 or 50 GWd/MTU, as noted. Most of the sensitivity studies assume an average burnup of 40 GWd/MTU for each fuel region.

Table 1. Fuel Loads for Whole Pool

	No. of cores	**No. of cells**	**Average Watts/bundle after number of years**						
			2 yr (40)*	3 yr (40)*	4 yr (40)*	6yr (40)*	3 yr (50)*	4yr (50)*	6 yr (50)*
f1, Hot	1	800	920	620	462	341	773	576	425
f2, Med Hot	.33	267	536	419	360	296	532	457	376
f3, Med Cold.	.33	267	381	341	304	272	438	390	349
f4, Cold	3.6	2866	201	198	194	190	251	246	241
Total heat load (megawatts) >>>			1.557	1.266	1.103	0.969	1.597	1.39	1.224

* Average Burnup (GWd/MTU)

Containment Building

The main building is sized to represent a BWR containment. No internal structures are modeled. The size and location of the containment relative to the fuel pool is shown in Figure 3. This figure represents the CFD model domain, which is a symmetrical half of the physical structure. The plane of symmetry faces out toward the reader. The containment building is modeled only from the pool surface up to the ceiling. Lower levels are ignored.

Ventilation

A single ventilation input and output are used in the CFD model, which represents half the building and fuel pool. The ventilation opening is 4 m^2 and is shown in Figure 3. The standard ventilation rate is based upon 2 building volumes of air exchanged per hour (Ref. 2, p. 41). The inlet flow provides 2 building volumes of air to the building every hour. Sensitivity studies are

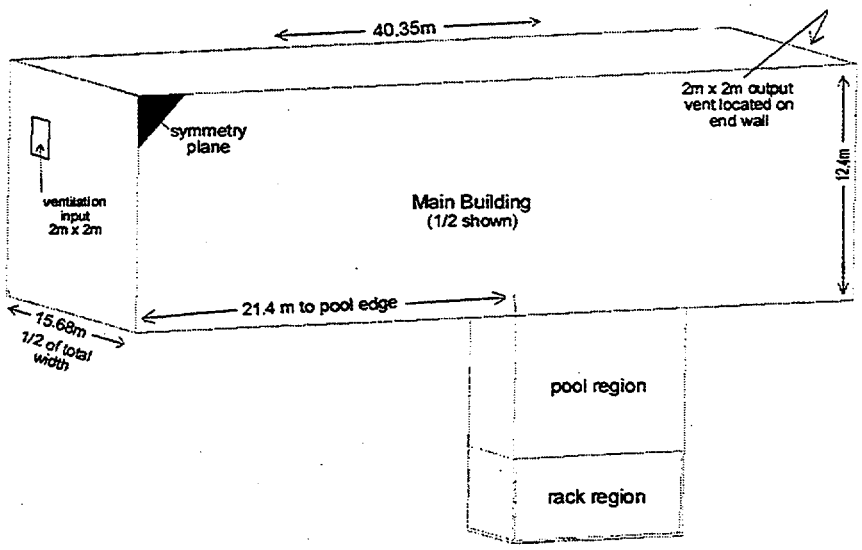

Figure 3. Symmetrical Half of Containment Building and Fuel Pool

performed on this value. Air enters the containment through the inlet vent and is heated by the fuel. Inlet air is set at 27 °C. Air is exhausted on the opposite end of the building through a similar vent opened to the atmosphere. The inlet and outlet vents are positioned 2.68 m from the back wall and ceiling of the containment building.

Wall Heat Transfer

Most of the predictions assume the external building walls are adiabatic. Sensitivity studies are done on the overall heat transfer coefficient at the side walls and ceiling of the containment building. Values of 0, 2, and 4 W/m^2-K are used. Best estimate values range[6] from 1 to 3 W/m^2-K. This range covers various wall types subjected to a 15 mph outdoor wind speed. Outdoor air is assumed to be 27 °C. A value of 2 W/m^2-K is used for best estimate predictions in this report. The pool walls and containment floor are modeled as adiabatic.

CFD MODEL DEVELOPMENT

The physical model described above is represented on a set of finite volumes on which the governing equations are discretized and solved. The Reynolds-averaged Navier-Stokes equations are used. Boundary conditions are applied on the model to facilitate a solution. Developing a CFD model requires a balance between the size and complexity of the model and the need to obtain solutions within available time and computational resources. Although the computational resources available to RES are significant, the scale of this problem dictates that simplifications must be made. The assumptions used to develop the CFD model are discussed below. The model is developed for the FLUENT version 5 unstructured CFD code.

Each prediction is run to find a steady-state solution, using typical CFD modeling options. The solutions give the maximum expected temperature but not the time it takes to reach it. A

transient analysis would require significantly more computer time. The major features of the CFD model are given below.

- steady state Reynolds averaged Navier-Stokes solution
- k-epsilon turbulence model with standard wall functions
- ideal gas, variable thermal properties (air as working fluid)
- gravity
- 675,000+ finite volume cells (tetrahedron and hexagonal mesh)
- segregated solver with 2nd order differencing on momentum and energy
- porous media model of fuel and racks (vertical laminar flow through region)

The clad oxidation reaction energy and radiative heat transfer are not included in this model. The effect of these omissions is considered small at temperatures below 600 °C. Higher temperature results should be viewed with this limitation in mind.

Finite Volume Mesh

The mesh consists of over 675,000 finite volumes. The mesh design minimizes the number of cells used for the model while providing an adequate number of cells to resolve important physical gradients. Cells are constructed to have minimal skew and sides of equal length (aspect ratio = 1) wherever possible. Cell to cell growth is limited to a range between 0 % and 20 %.

Cells in the upper building are large, 1 m^3, to save resources, so excess diffusion is expected in this region. This concession is not considered serious. Flows in the upper building are expected to be more complex (more diffusive) in the typical containment due to internal structures omitted in the CFD model. Any numerical diffusion resulting from the large cells in the upper building will enhance mixing, which is expected to be underpredicted by this model.

Most of the 675,000 cells are located in and around the fuel racks where the highest gradients and most significant phenomena occur. Cell height at the top of the racks is reduced to 1 cm through the use of grid adaption. This fine resolution is needed to resolve the large thermal and velocity gradients predicted in this region. Transitions from the very fine mesh to regions with larger mesh are constructed of tetrahedral elements with a controlled growth rate. This technique eliminates the skew in the hexagonal element regions and provides a smooth transition between cells of different sizes.

Boundary Conditions

Boundary conditions are applied at the walls (both internal and external) and at the inlets and outlets. All external walls use the no-slip condition for the momentum equations. No surface roughness is applied. All external walls are adiabatic except as noted in the sensitivity studies. The surface facing the reader in Figure 3 is a symmetry plane. Internal vertical walls are positioned within the fuel and rack region to separate zones of different fuel ages and to align the flow vertically. These internal walls use a no-shear boundary condition since all flow resistance within the racks and fuel is accounted for by the porous model.

Fresh air enters the building through the 4 m^2 inlet vent (Figure 3). At this location, the flow is aligned normal to the building wall and has a turbulence level of 10%. The inlet velocity is set to yield a volume flow rate equivalent to 2 building volumes per hour (except as noted in

sensitivity studies). The input air is 27 °C. The prescribed inlet velocity is 1.1 m/s. Air exits the model at the opposite end of the building. The exit vent is modeled as a pressure boundary set to atmospheric conditions (101325 Pa, 27 °C).

Material Properties
The working fluid is air modeled as an ideal gas. The temperature-dependent thermal properties are obtained from White's *Viscous Fluid Flow*[7].

Fuel and Racks
The fuel and rack structure are not modeled in detail; the geometry of this region is too complex. CFD modeling of the details of every bundle in a fuel pool is impractical because of memory and processor limitations. To simplify the model, a homogenous non-isotropic porous medium is used to represent the racks and fuel. The volume occupied by the racks is replaced by the porous medium designed to affect the flowfield as the rack structure and fuel would. A porous material does not affect the flow area in the FLUENT model. Flow resistance is set through user-defined viscous and inertial flow loss coefficients. Details of the resistance coefficient determination are given in reference[8] 8. Lateral flow resistance in the porous medium is set two orders of magnitude higher than the vertical resistance to ensure vertical flow through the racks. Several vertical walls are also included in the racks to further guarantee a vertical flow path. The fuel is centered vertically in the racks and has a uniform active heated length of 3.8 m. The width of the active fuel region is 9.24 m, as shown in Figure 1. The individual fuel widths are defined to keep the fuel proportions the same as in Table 1. Fuel regions f1 to f4 are 1.76, 0.5874, 0.5874, and 6.3052 m wide, respectively. Heat is added to the flow as a uniform volumetric heat generation term throughout the volume occupied by the fuel. Axial heating distributions are not considered. Radiation and clad chemistry are also neglected in the model.

Thermal inertia and thermal conduction within the fuel and racks are accounted for in the FLUENT model through the porous media options. The material properties of the medium and the porosity of this region are prescribed to account for the thermal inertia of the racks and fuel and to approximate axial thermal conduction. The FLUENT porous media model assumes isotropic conductivity so the single value affects axial and lateral conduction. A sensitivity study on the thermal conductivity is done to give further insights into the significance of this parameter. Details of the porous media assumptions used to account for thermal inertia and thermal conductivity in the rack region are given in reference 8.

Turbulence Modeling
The k-epsilon turbulence model with standard wall functions is used for this analysis. This model is selected because of its robustness. It is acknowledged that the k-epsilon turbulence model is not ideal for this type of problem. Experimental data are needed to refine the turbulence modeling beyond this standard approach. This subject is beyond the scope of this study.

The flow up (or down) through the bundles is expected to be laminar because of the low Reynolds number in this region. For example, if the velocity of 400 °C air is .243 m/s along the tube bundles (0.1 m/s in the open porous region of the FLUENT model), the Reynolds number based upon hydraulic diameter would be close to 50, indicating laminar flow. To account for this laminar flow, the porous media region representing the racks and fuel is modeled as a

laminar region. In this region, turbulence production and turbulent viscosity are disabled. The FLUENT model transports the turbulent properties through the region unchanged.

Solution Convergence
Final results from this analysis are somewhat unsteady. Variations of +/- 20 °C in the hottest fuel temperatures are typical. To obtain the final predictions, the model is executed until the oscillations are in a steady-state pattern. At this point, variables are recorded during one or more oscillations and an average value is recorded. Initial convergence of the solution is monitored by observing temperatures and velocities at various points in the domain as a function of time. In addition, the residuals (a measure of error) are monitored and minimized for each solution. As a final check, the overall mass and energy balances are verified.

Grid Independence
A grid independence study is not feasible due to the physical scale of the model and the limited computer resources. A high quality mesh is used for this analysis to minimize any grid affects on the results. The effect of the assumptions on the final solution are expected to far outweigh any small effect of the grid on the predictions. Qualitative information on grid independence is given below for completeness.

The final grid for this study contains over 675,000 finite volume cells. In the process of constructing this grid, over 10 separate grids are created and tested. The final grid is a compilation of the lessons learned during this process. The lessons learned included node density requirements for wall functions and large gradients. The final mesh is created with as many cubical elements as possible. Grid stretching and skew are minimized. Mesh size is reduced at the walls to accommodate the wall functions and transitions away from the wall are limited to growth rates between 5% and 20%. To transition between nearly cubical elements of different scales, tetrahedral regions are constructed with growth rates between 5% and 20%. The largest gradients are found just above the fuel racks. In this region, grid adaption is used to reduce the grid size to approximately 0.01 m. Unphysical results were observed in some of the earlier models without this adaption. Grid adaption is also used to refine the mesh in the open region around and below the racks.

COMPLETED PREDICTIONS

CFD results are most valuable when a series of predictions are made with varying assumptions and inputs to assess their impact on the predicted results. This is especially true when there is a lack of data available for model validation. Sensitivities of the final predictions to changes in assumptions and parameters gives valuable insights into the predictions. Table 3 gives the major parameters and assumptions varied for each prediction. As noted in Table 3, several sensitivity studies are completed which include variations of the following parameters:

- decay time and fuel burnup
- ventilation rate
- flow resistance within the fuel and racks
- heat transfer coefficient for external building walls
- fuel loading pattern (location of hottest fuel)
- porous media thermal conductivity

SUMMARY OF ASSUMPTIONS AND LIMITATIONS

The completed CFD predictions give valuable insights into the three-dimensional natural circulation air flows. These flows provide the primary heat removal mechanism in a postulated complete loss of spent fuel pool coolant accident. The final results, however, are still dependent upon the modeling assumptions and limitations. To ensure that these issues are considered along with the final results, some major assumptions and limitations are listed in Table 4.

Table 4. Assumptions and Limitations

Assumptions	Notes/Limitations
building and pool dimensions	building and pool are within typical range but do not represent all configurations
4200 fuel assemblies, high density racks	no rack-to-rack spacing, no open areas in pool
flow resistance in rack/fuel region	determined from a typical configuration, does not apply to all rack designs
0.15 m (6 in.) gap from rack to pool wall	typical for a full pool; some gaps reported as small as 0.05 m (2 in.)
no structures within building	plant-specific structures could affect the flow
model pool and containment above pool surface level	containment only modeled from pool surface up, plant-specific features could affect solution
2 buildings per hour ventilation rate	typical of an operable ventilation system, location of vents could affect the flow patterns
fuel arranged in contiguous regions by age	no checker board pattern for fuel arrangement is attempted, no open cells
decay heat levels	average value used for each fuel grouping, extrapolation of decay heat used for higher burnup fuel
porous media	rack structure is homogenized, heat is added directly to the flow, fuel surface is not modeled, flow resistance is modeled, isotropic conduction
external pool walls are adiabatic	only heat transfer from upper building and ceiling is considered
uniform heat generation in fuel	axial fuel peaking is ignored
radiation	neglected, can be important at elevated T
clad oxidation reaction	neglected, can be important at elevated T
steady-state solution sought	no transient information available during heatup
CFD modeling assumptions and grid	no data used for assessing turbulence modeling, grid independence is not verified

BASE CASE RESULTS

The base case is described in detail to illustrate the flow phenomena predicted and to define some of the parameters used to describe the results. Next, the sensitivity study results are summarized.

The base case assumes a 4 year decay time with the hot fuel located along the left edge of the pool. All external walls are adiabatic. The ventilation rate is based upon two building volumes per hour, which corresponds to an inlet air velocity of 1.1 m/s. The inlet air temperature is 27 °C and the flow has a 10% turbulence level at the inlet. The inlet vent flow area is 4 m^2. Important parameters and phenomena predicted for this case are described below.

Maximum Temperature

The maximum temperature predicted during this scenario varies with time. The peak temperature predicted is 540 °C with variations of +/- 20 °C. Peak temperature is observed near the top of the hottest fuel and on the symmetry plane. Figure 4 shows the computational domain with temperature contours displayed on the surface of the active fuel region. The hottest regions are lightest (whitest) in the figure.

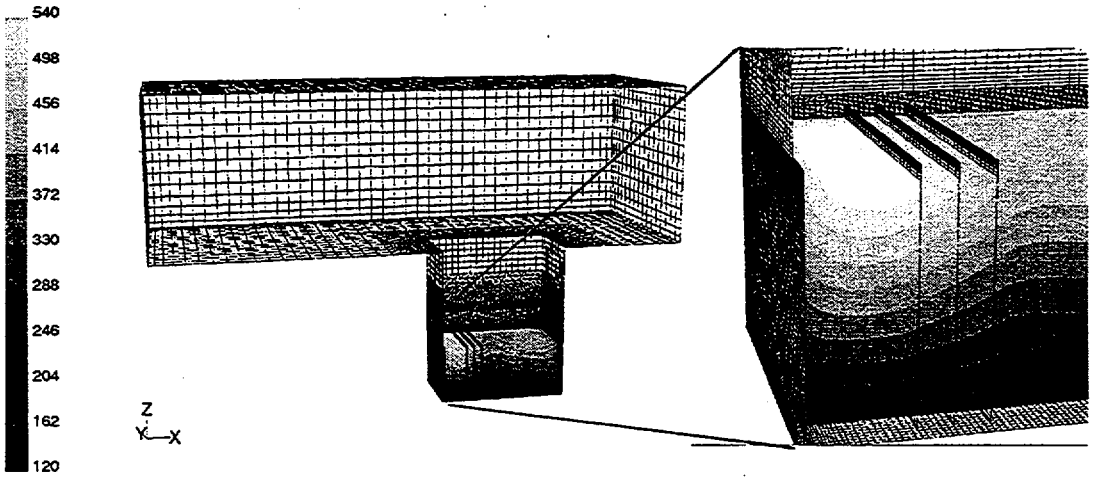

Figure 4. Temperature Contours on Active Fuel Region

Walls between the fuel types are left in place as a visual aid. There is an additional vertical wall in fuel region f1 and several additional walls in fuel region f4 which are not shown to clarify the image. The hottest fuel, f1, is on the left, with a temperature approaching 540 °C. The air entering the bottom of the hottest fuel is approximately 125 °C. Actual fuel surface temperatures can be approximated using Newton's law of cooling. The Nusselt (Nu) number is approximately[9] 9. The difference between the predicted air temperature (assumed to be the mixed mean) and the surface temperature is predicted to be less than 10 °C. This difference is considered negligible compared to other uncertainties and the maximum temperatures are simply reported as the maximum predicted air temperatures.

Global Flow Pattern

The overall flow, although unsteady, displays a predictable pattern. Figures 5, 6, and 7 illustrate the principal convective flow paths. Figure 5 shows the volume of air that is predicted to have temperatures in the range of 132 to 500 °C. These limits are chosen to highlight the hot plume of air rising from the side of the pool containing the hottest fuel. The rising plume stays near the left pool wall until it enters the main building. At this point, the hot air flows towards the roof of the containment with a slight preference towards the outlet vent. The rising hot air hits the ceiling and spreads to cover the entire ceiling with a layer of hot air. Although the air temperature peaks at over 500 °C in the fuel racks, the rising plume of hot air cools

rapidly as it rises. The maximum temperature is 200 °C just a few meters above the fuel racks. As the hot plume reaches the top of the pool, the maximum temperature is 160 °C. The maximum plume temperature is 135 °C when the plume hits the ceiling. Temperatures in the containment are predicted to stratify significantly. The temperature of the hot air on a horizontal plane 0.5 m below the ceiling ranges from 130 to 135 °C. Eliminating the small region occupied by the plume reduces the temperature variation on this horizontal plane to less than 2 °C.

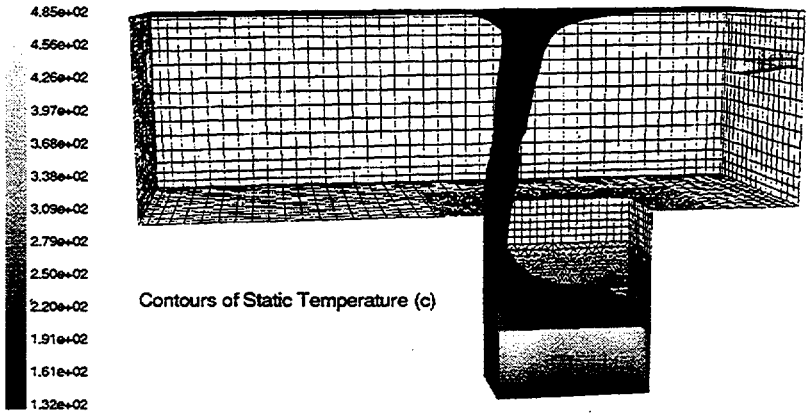

Figure 5. Temperature Contours Showing Rising Hot Plume

Figure 6 shows the inlet air entering the containment and falling to the floor of the building. This relatively cool air spreads around the rising hot plume exiting the pool and falls into the pool on the opposite side. The air on the floor of the containment is relatively well mixed. The temperature range observed on a horizontal plane 0.5 m above the containment floor is 80 to 160 °C. Eliminating the small regions where the inlet plume first hits the floor and where the hot plume rises through this plane results in a temperature range at this elevation of 90 to 110 °C. The average temperature difference between the floor and the ceiling in the containment is approximately 30 °C.

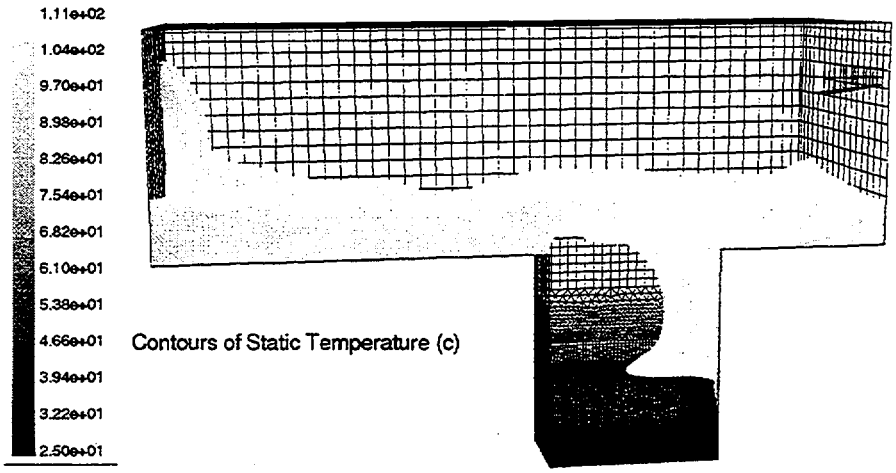

Figure 6. Temperature Contours Showing Cooling Air Flow

A detailed view of the flowfield just above the containment floor is given in Figure 7. This figure shows the velocity vectors on a plane 0.5 m above the floor. The cold inlet plume is predicted to hit the floor and spread out in all directions. The flow travels across the containment floor and around the rising plume. The flow falling into the pool is also clearly visible. The pool edges are not visible. The increase in vector density in the rectangular region around the pool is the result of a mesh density variation near the pool. The mesh density variation in relation to the pool edges is visible in Figure 5. The cold air that enters the fuel pool hits the top of the racks (like a stagnation point) and then flows outward towards the pool walls. Most of the cooling air travels down around the racks (along walls) to the floor of the fuel pool and then up through the fuel.

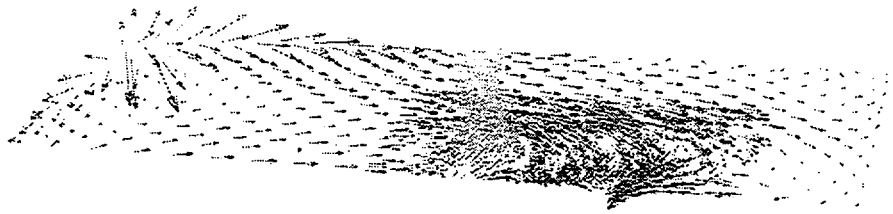

Figure 7. Velocity Vectors in a Plane 0.5 m Above the Containment Floor

Global Energy Balance

To verify a global energy balance, the first law of thermodynamics is applied to the system using a control volume approach. The outlet temperature is computed and compared to the prediction from the FLUENT code. The relevant energy terms are the energy input from the fuel, the energy lost at the external walls by convection, and the energy transported away by the ventilation system. In this case, all the heat generated by the fuel is carried away by the natural circulation flows since the walls are adiabatic. The first law of thermodynamics applied to this steady-state/steady-flow problem results in the following balance of energy equation:

$$\dot{Q}_{fuel} - \dot{Q}_{walls} + \dot{m}(h_{inlet} - h_{outlet}) = 0$$

The terms in the equation represent the energy from the fuel, the energy lost at the walls due to convection, and the net energy change between the inlet and the outlet flows. For this case, total heat from the fuel, Q_{fuel}, is 551,474 W. The wall heat transfer, Q_{wall}, is 0. Assuming 26.85 °C air entering the building through a 4 m^2 inlet vent at 1.10 m/s results in an inlet mass flow rate of 5.178 kg/s. From thermodynamic tables, the inlet enthalpy (h_{inlet}) is 300.19 kJ/kg. Using these values for the total heat load, the mass flow rate, and the inlet enthalpy, the energy balance predicts an outlet enthalpy (h_{outlet}) of 406.69 kJ/kg. From thermodynamic tables, this translates into an outlet temperature of 132.5 °C. The predicted outlet temperature from FLUENT is 132.7 +/- 5 °C. The FLUENT code maintains a global energy balance.

Flow In and Around Racks and Fuel

The flow from the upper building enters the pool and falls to the racks as shown in Figure 6. The flow turns at the rack surface. Some of the flow is entrained by the rising hot air and exits

the pool. Some travels down and around the fuel racks to the pool floor, where it spreads out to cover the region below the racks. As air is pulled up through the fuel and racks, it forms the hot plume visible in Figure 5. The regions of up and down flow in the rack region are illustrated in Figure 8. This figure shows contours of vertical velocity on a horizontal plane at the top of the active fuel region (z = 4.2 m).

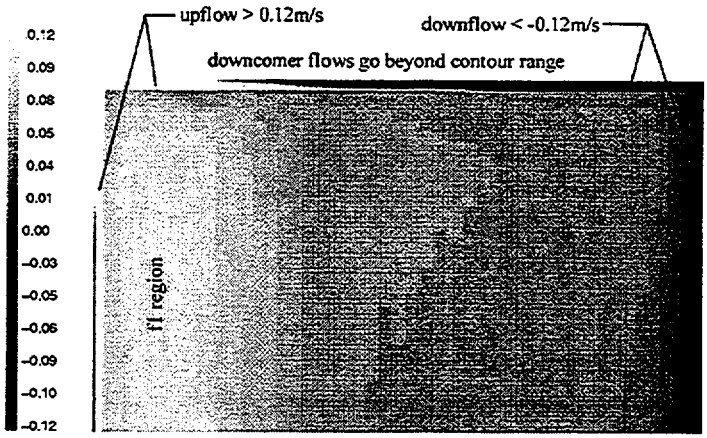

Figure 8. Vertical Velocity (m/s), Horizontal Plane, Top of Active Fuel

The contour ranges are limited to +/- 0.12 m/s to highlight variations in the fuel region. Downcomer velocity magnitudes go beyond these limits, however. Regions where the velocity is above or below the contour ranges are displayed with the maximum or minimum contour range color. The velocity in the fuel is positive (upward) everywhere except a small region near the right downcomer.

A slight upflow is predicted for the left downcomer. This upward flow is the result of several factors. First, the strong plume formed by the hottest fuel blocks downflow on the left side of the pool. In addition, the left downcomer is subject to some buoyant forces due to heat transfer from the hottest fuel adjacent to this region. Entrainment of air in the rising plume on the left side of the pool also promotes upflow in the left downcomer. Finally, a strong right-to-left flow under the fuel racks feeds the flow up through this downcomer.

Most of the flow to cool the fuel enters the region below the racks from the downcomer on the right side of the pool. This region is supplied by a significant downflow of cooling air from the upper building. This air enters the region below the racks and spreads across the floor towards the hottest fuel (f1) region.

Flow in the third downcomer region (top of Figure 8) is more complex. No strong up or down flow is observed. The left side has a slight upflow and the right side has a slight downflow. Large recirculations are observed in this region, making it difficult to generalize the flow path. All fuel and downcomer flows are summarized by the net mass flow rate through each region. Mass flow rates are reported on a horizontal plane at the top of the active fuel region (z = 4.2 m), with positive values indicating upward flow.

Net mass flow through a horizontal plane at the top of the active fuel is given in Table 5 for the four fuel regions and three downcomer regions. The predicted mass flow rates are slightly unsteady. Reported values represent an average mass flow rate for a series of predicted values over time.

Table 5. Mass Flow Rates at Top of Active Fuel, Base Case

Region	Mass Flow Rate (+ upflow, kg/s)	Average Mass Flux (kg/m^2 s)
left downcomer	0.22	0.27
right downcomer	-1.58	-1.90
rear downcomer (top of Fig. 9)	-0.18	-0.13
net downcomer >>	**-1.54**	**-0.51**
f1	0.41	0.043
f2	0.13	0.041
f3	0.12	0.037
f4	0.89	0.018
net fuel >>	**1.54**	**0.031**

Pressure Above and Below Rack

Spatial pressure variations are predicted above and below the racks. These predictions can be used to assess the applicability of the constant pressure boundary condition used in other spent fuel pool models in these regions. All predictions are given as a gauge pressure referenced to the atmospheric pressure at the outlet vent.

Figure 9 shows the predicted pressure on a horizontal plane at an elevation of z = 4.5 m. This plane is 0.05 m (2 in.) above the top of the racks. Pressures vary from 15.25 to 18.25 Pascal (Pa). The average pressure at this elevation is 16.7 Pa. The right side of Figure 9 shows the highest pressure near the symmetry plane. Figure 6 shows why: the relatively cool air flows down the right side of the pool and impinges on the racks there. This region of high pressure is the result of the stagnation region created by the falling plume as it turns 90 degrees to flow along the top of the racks. The stagnation point is on the axis of symmetry near the right downcomer. Flow vectors radiate from this point in all directions across the top of the racks.

The magnitude of the pressure variation across the top of the racks is predicted to be approximately 3 Pa. This value is considered significant relative to the pressure differences encountered. For example, the predicted difference between the average pressure above and below the racks for the base case is 5 Pa. Flow losses are also in this range. Consider air at 900 °C flowing through the racks and fuel at 0.1 m/s. The pressure drop (no gravity) is approximately 15 Pa based upon the flow loss coefficients used. If the air is 400 °C and flowing

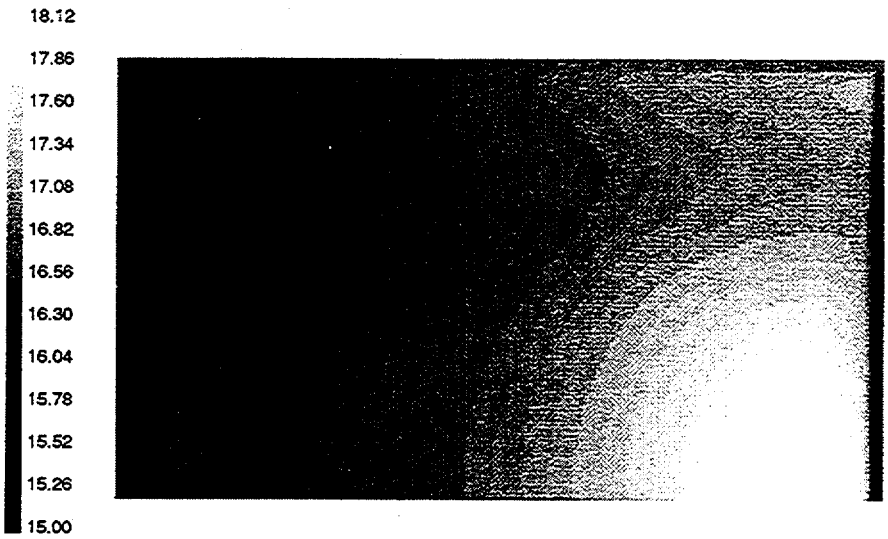

Figure 9. Pressure Contours Above the Fuel Racks, Pa (z = 4.5 m)

at 0.01 m/s, the expected pressure drop is close to 1 Pa. Considering these pressure differences, the 3 Pa variation across the top of the racks could be significant.
Figure 10 shows the predicted pressure contours below the rack at an elevation of 0.1 m. This plane is 0.05 m from the bottom of the racks. Pressures vary from 7.25 to 15.25 Pa; the average pressure is 11.8 Pa. The right side of Figure 10 shows the highest pressure at the bottom of the right downcomer. This is the region where the strong downflow hits the floor and turns to flow along the bottom of the racks. The high velocities leaving this region result in low pressures to the left of the stagnation region. The static pressure slowly increases as the flow slows down on its way to the hottest fuel region at the left. As noted earlier, the reported pressure variations at this plane are significant with respect to other relevant pressure differences in this region.

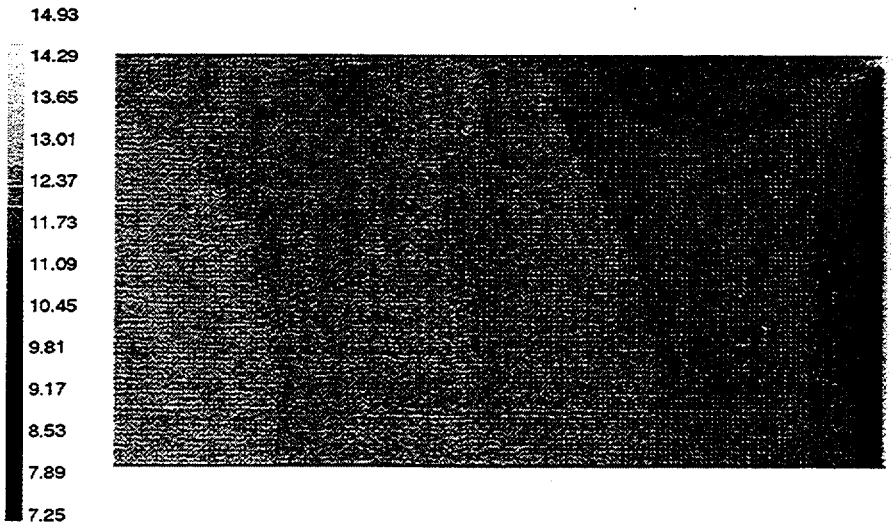

Figure 10. Pressure Contours Below the Fuel Racks, Pa (z = 0.1 m)

Temperatures Above and Below Rack

The temperatures above and below the rack are given by Figures 11 and 12, respectively. These results are highlighted to provide a basis for assessing the constant temperature boundary condition assumed by some spent fuel codes. Temperatures are given on the same horizontal planes used to illustrate pressure in Figures 9 and 10.

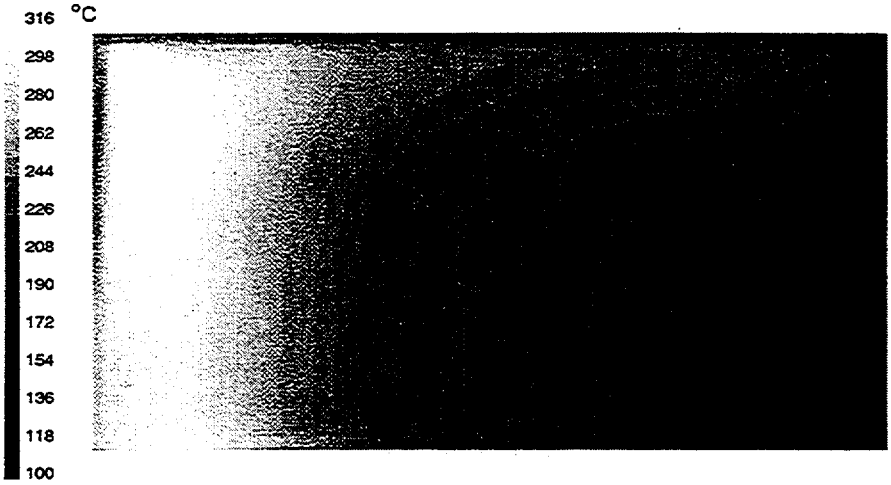

Figure 11. Temperature Contours Above the Fuel Racks (z = 4.5 m)

Figure 12. Temperature Contours Below the Fuel Racks (z = 0.1m)

Temperature contours above the fuel racks (Fig 11.) are consistent with the description of the flow paths given earlier. The stagnation region on the symmetry plane near the right side downcomer has the lowest temperature. This is a result of the cold plume falling into the pool region and stagnating on the racks at this point (see Figure 6). As the flow travels across the racks to the left, it mixes with hotter air exiting the racks. This increase in temperature is clearly

seen in Figure 11. The rising hot plume on the left side of Figure 11 is the hottest region at this level. This area roughly covers the hottest fuel region (f1). The average temperature above the racks at this level is 217 °C. This value is computed over a series of iterations to get a representative value. The spatial variation in temperature at this level is roughly 200 degrees.

Figure 12 shows the temperature contours below the fuel racks. The average temperature for this level is 137 °C. The spatial variation in temperature is nearly 60 degrees. Most of this spatial variation is accounted for by the hot spot near the top right hand corner of Figure 12. This region is caused by a small downflow predicted to occur in the fuel racks in the cells just above this region. This downflow is heated by the fuel before it enters the region below the racks.

The temperature below the racks is nearly equal to the containment outlet vent temperature. This feature of these predictions is coincidental. There is a 30 degree average temperature difference between the floor and ceiling in the containment. The outlet vent is near the ceiling and is exposed to the hotter layers of air in the containment. The air which cools the fuel comes mainly from the floor of the containment. As it travels to the region below the racks, it rises in temperature to nearly equal the outlet vent temperature.

DECAY TIME SENSITIVITY, ADIABATIC WALLS

This sensitivity study focuses on the decay time, defined as the time since reactor shutdown. As decay time increases, the heat load from the fuel decreases. Decay times of 2, 3, 4, and 6 years are studied. The physical and numerical conditions are identical for each case. Only the decay time is varied. Each case is based upon an assumed burnup of 40 GWd/MTU. Predicted temperatures are plotted in Figure 13. Spline fits connect the data. The maximum temperature decreases significantly (511 °C) between 2 and 4 years. From 4 to 6 years, the drop in temperature is only 91 °C. The shape of this curve closely resembles the decay heat curve. It is important to keep in mind the limitations (noted earlier) of these predictions at elevated temperatures. The 2 and 3 year results reach temperatures where the lack of radiation and chemistry models is expected to affect the solution.

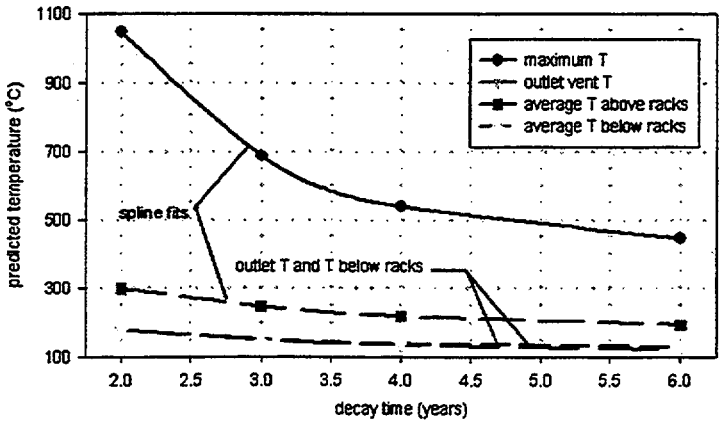

Figure 13. Predicted Peak Temperatures vs. Decay Time, Adiabatic Walls

Temperatures above and below the rack differ by nearly 80 °C. These temperatures decline with decay time as expected. The rate of decline also decreases significantly after 4 years. The outlet vent temperature is predicted to decline in the same manner. One unexpected prediction is the near match between the outlet temperature and the average temperature below the racks. This coincidental result is discussed in a previous section.

The average pressure above and below the racks shows a slight increase as the decay time decreases. This is mainly because the pressure drop at the outlet vent increases as the decay time decreases. The outlet vent is at the end of a 4 m convergent duct protruding out from the containment wall. The pressure drop in this duct increases with the increase in viscosity and velocity associated with lower decay times. The increase in flow resistance through the outlet duct slightly increases the global containment pressure.

The flow patterns for the 2, 3, 4, and 6 year cases are qualitatively the same. Downcomer flows are predicted to distribute in a similar manner. The left downcomer has a slight upflow for each case. The rear downcomer has a similar net downflow. Cooling flow enters the region below the racks mainly through the right downcomer. No clear trend with decay time is observed.

Flow through each of the fuel regions shows a similar pattern. No clear trend is observed with decay time variation. Predictions for the 3, 4, and 6 year cases show nearly identical flow rates through each of the fuel types. The similar flow rates through the fuel indicate that the increases in temperature (lower density) for the lower decay times are offset by similar increases in velocity.

VENTILATION RATE SENSITIVITY

An important input parameter is the ventilation rate. The base ventilation rate assumes 2 building volumes of cool air enter the building each hour. Additional predictions are made with 1, 1.5, and 2.5 building volumes per hour. Each case assumes a 4 year decay time, a 40 Gwd/MTU burnup, and adiabatic external walls. Predicted temperatures are plotted in Figure 14.

The maximum temperature is significantly affected by the ventilation rate. The largest affect occurs when the ventilation rate is reduced from 1.5 to 1 building volume per hour. This trend suggests that reducing the ventilation rate below the 1 building per hour rate would significantly increase the temperature. This is not done because the model is not reliable at higher temperatures. The difference in the maximum predicted temperature between 2 and 2.5 buildings per hour is 19 °C. This is nearly equal to the difference in the predicted exit vent temperature for these two cases. It appears that the effect of increasing the ventilation rate beyond 2 buildings per hour can be approximated by globally adjusting the temperatures to the change in the outlet temperature determined from a global energy balance.

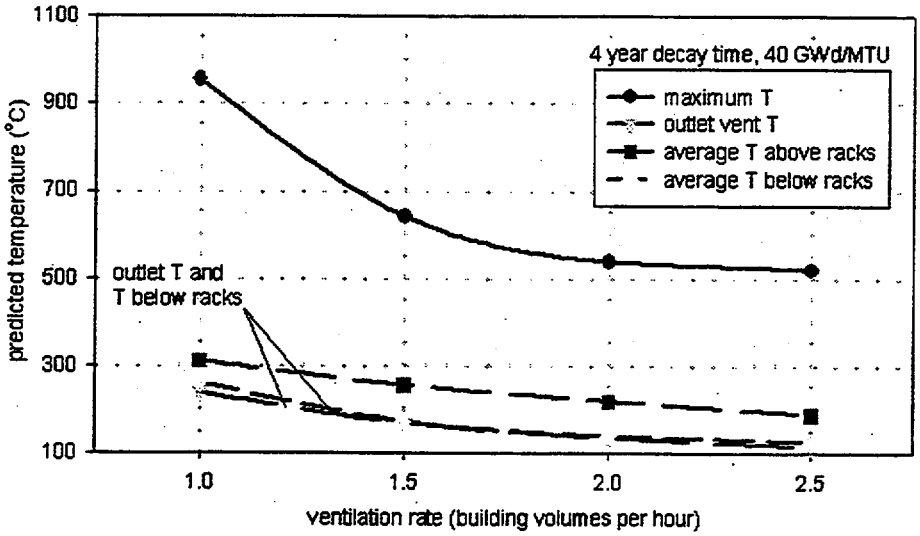

Figure 14. Sensitivity of Peak Temperatures to the Ventilation Rate

At the lower ventilation rate, the mass flow through the fuel drops off. The increased temperature reduces the density and this affects the mass flow. As the ventilation is increased, the mass flow through the fuel increases up to a point. No difference is observed in the mass flow rate through the fuel with the 2 and 2.5 building per hour ventilation rates. It appears that ventilation rates beyond 2 building volumes per hour don't significantly change the mass flow rates through the fuel or the net fuel temperature rise. The net fuel temperature rise is defined as the difference between the outlet vent temperature and the peak fuel temperature. Outlet vent temperature is considered a measure of the overall containment temperature.

WALL HEAT LOSS SENSITIVITY

A sensitivity study is done on the overall heat transfer coefficient between the containment and the exterior environment. Containment wall and ceiling heat transfer coefficients of 2 and 4 W/m^2-K are applied to the base 4 year case. Predicted peak temperature results are plotted in Figure 15. The temperatures drop predictably as the heat transfer coefficient is increased. The drop in the maximum predicted temperature is most significant when the coefficient is changed from 2 to 4 W/m^2-K. The temperatures above and below the racks respond differently. These temperatures change most dramatically when the heat transfer coefficient is changed from 0 to 2 W/m^2-K. The global energy balance also changes most when the coefficient is changed from 0 to 2 W/m^2-K.

The mass flow rates through the fuel region increase slightly as the heat transfer coefficient is increased. The limited data show no clear trend. The increase in the mass flow rate through the fuel is attributable to the lower containment temperatures resulting from the wall heat losses. The lower temperatures produce stronger natural circulation flows, which aid the fuel cooling.

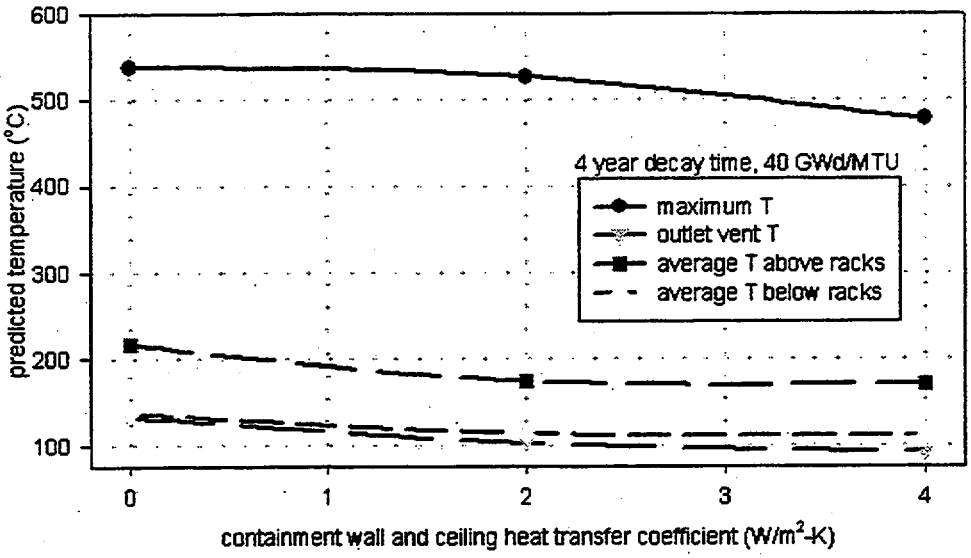

Figure 15. Sensitivity of Temperatures to Wall Heat Transfer Coefficient

The sensitivity of wall heat loss is also observed by comparing the adiabatic and best estimate predictions which use a heat transfer coefficient of 2 W/m^2 K. This comparison, not shown, is completed at 2, 3, 4, and 6 years of decay time with a fuel burnup of 40 GWd/MTU. The temperature reduction resulting from wall heat transfer is greatest at the 2 year decay time due to the higher containment temperatures associated with this case. The peak temperature of the fuel drops by 200 °C when wall heat transfer is applied in this case. At 6 years decay time, the peak temperature drops by 53 °C when wall heat transfer is applied. Temperatures at the outlet and above the fuel racks respond in a similar manner. No clear trend is observed in the average temperature computed below the fuel racks. Mass flow rates through the fuel and downcomers increase in the cases with wall heat transfer. This increased mass flow and reduced temperatures in the containment account for the reduced peak fuel temperatures predicted.

RACK AND FUEL FLOW RESISTANCE SENSITIVITY

The racks and fuel are modeled as a porous medium. The complexity of the physical structure in this area makes a detailed model impractical. A porous resistance is put into this region of the model to account for the viscous and inertial flow losses. Porous resistance is considered a significant parameter in these predictions. Details of the determination of the resistance coefficients are given in reference 8. There is some uncertainty in the data used to determine the loss coefficients, and there are a variety of rack and fuel bundle designs that affect the flow loss. This sensitivity study shows the effect of flow loss variations on the predicted temperatures.

Using the 4 year base case as a starting point, two additional predictions are done with the resistance coefficients changed by +/- 20%. The increased resistance reduces the mass flow rate which increases the temperature rise of the air flowing through the racks. Similarly, with less resistance the mass flow is increased and the temperature rise is reduced. Figure 16

shows the predicted temperature for these cases. The maximum temperature increases with the increased resistance, as expected. This trend is attributable to the mass flow rates discussed above. The largest change occurs when the resistance is increased by 20%. The building outlet temperature is unaffected since the overall energy balance is unchanged. The average temperatures above and below the racks show no significant change.

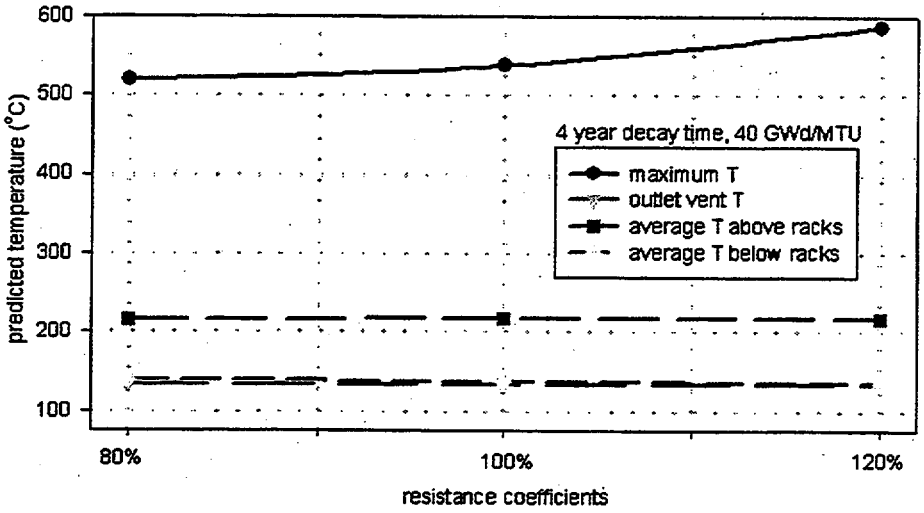

Figure 16. Sensitivity of Peak Temperatures to Flow Resistance

HOTTEST FUEL LOCATION SENSITIVITY

The hottest fuel is placed along the left wall of the fuel pool for each of the predictions described above. The hottest fuel represents the last fuel taken from the reactor when the reactor is shut down. The fuel pool is assumed to be filled from right to left (Figure 1), so that the last fuel taken from the reactor is on the left. As a sensitivity study, the hottest fuel is moved to the center of the pool. Fuel region f2 is next to the hottest fuel on the left. Fuel region f3 is to the right of the hottest fuel. The remaining rack locations are filled in with the oldest fuel, f4. The total fuel load and quantities of each type of fuel are unchanged by this arrangement.

The most conservative (hardest to cool) location for the hottest fuel is not obvious. Placing the hottest fuel in the center of the pool puts the fuel farthest from the downcomer regions supplying the cooling air flow, which could make it harder to cool. However, placing the hottest fuel next to the downcomer can block the cooling air from flowing down through this downcomer. This blockage can result from the rising hot plume. There is no benefit to putting the hot fuel next to a downcomer in this case. Two fuel positions are compared to show the effect of fuel position on the predicted results.

The first case assumes the hot fuel is along the left wall, as described above. Downflow to the left downcomer is blocked off by the rising plume. A small upward flow is established in this downcomer by entrainment and other factors. Cooling air from the right downcomer travels

along the pool floor under the racks to reach the hottest fuel. The average peak temperature in the fuel region is 537 °C.

The predictions from the model with the hottest fuel in the center of the pool are very similar to the base case predictions described above. The hot plume that rises from the center of the pool is swept to the left wall of the pool before rising into containment. The pattern is similar to Figure 5. Cold inlet air falls to the floor of the containment and travels around the pool, as shown in Figure 6. The average maximum temperature in the fuel region for this case is 567 °C. The mass flow rate through the hottest fuel is slightly smaller when this fuel is in the center of the pool. The lack of significant variation in these two cases suggests that the inlet flow path drives the flow patterns in these predictions.

RACK AND FUEL THERMAL CONDUCTIVITY SENSITIVITY

The racks and fuel are modeled as a porous medium because of the physical structure in this area is too complex to model. This porous model requires the user to specify properties to account for given thermal behavior. The thermal property assumptions are given in reference 8. The thermal properties of the porous medium affect the thermal inertia and the conduction flux in the porous region. Thermal inertia is only a factor in transient terms so it is not expected to affect the steady-state results. The thermal conduction term, however, does move fuel energy away from the hottest regions. Thermal conductivity is approximated by assuming one-dimensional conduction in the vertical direction. The FLUENT code assumes isotropic thermal conductivity. The isotropic assumption used by the code and the one-dimensional assumption used to approximate the thermal conductivity are both questionable assumptions. The base case thermal conductivity is reduced by 20% and 50% in separate predictions to quantify the sensitivity of the results to this input parameter.

The maximum temperature is 537, 543, and 570°C for the cases with 0%, 20%, and 50% decreases in the thermal conductivity of the porous medium respectively. The reduction in thermal conductivity slows the conduction of heat away from the hottest regions and accounts for the increase in temperature. The maximum predicted temperature increases by 33 °C as the thermal conductivity in this region is reduced by 50%. This is considered a weak sensitivity. The global flow patterns, the integrated mass flow through the fuel regions, and the global energy balance are not significantly affected by changing the porous model thermal conductivity.

FUEL BURNUP SENSITIVITY

The base case predictions assume an average fuel burnup of 40 GWd/MTU. A sensitivity study is done using an average fuel burnup of 50 GWd/MTU at 4 years decay time. The higher fuel burnup assumption, when applied in this model, increases the energy generation term in the fuel region. The energy associated with a fuel burnup of 50 GWd/MTU is summarized in Table 1. The total pool energy at 4 years for the 50 GWd/MTU burnup falls between the 2 and 3 year cases with a burnup of 40 GWd/MTU.

The temperatures and pressures predicted for the higher burnup case fall between the 2 and 3 year cases at the lower burnup (40 GWd/MTU). This is consistent with the observation noted above concerning the total pool energy. The mass flow rate predictions also generally fall between the 2 and 3 year cases. Similar to the other cases, the majority of the cooling flow travels down the right hand downcomer to the region below the racks. The average maximum temperature in the fuel region for this case is 712 °C. In summary, raising the fuel burnup results in an increase in the energy generation term in the model which is similar to decreasing the decay time for a given burnup.

BEST ESTIMATE CRITICAL DECAY TIME

Predictions are made at several decay times using best-estimate parameters. These parameters include an overall wall heat transfer coefficient of 2 W/m^2-K and a ventilation rate of 2 building volumes per hour. These results represent the best estimate of the fuel temperatures and the convective flowfields, given the assumptions and limitations of this model. The global features of the solutions are similar to the solutions discussed earlier.

The best estimate decay time sensitivity for burnups of 40 and 50 Gwd/MTU are shown in Figure 17. Critical decay time is defined as the post shutdown time required to ensure fuel temperatures don't rise above predefined temperature limits after a complete loss of fuel pool coolant. For temperature limits of 800 and 600 °C, the critical decay times are 26 and 35 months respectively for the 40GWD/MTU burn up case. Assuming the burnup is 50GWd/MTU, the critical decay times are predicted to be 37 and 60 months respectively.

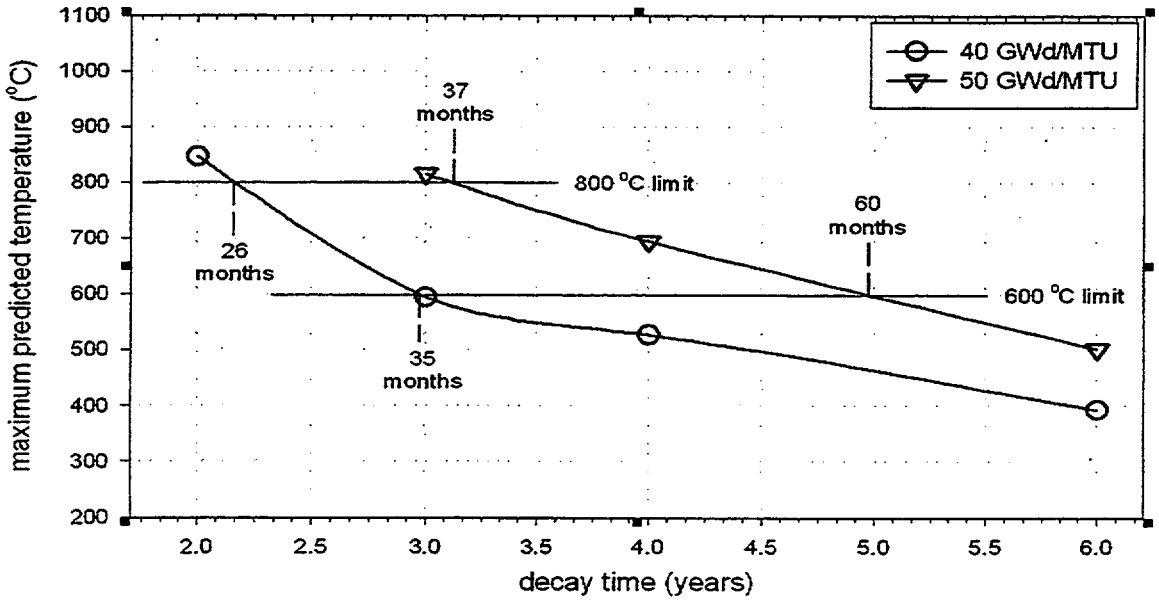

Figure 17. Best-Estimate Results for Maximum Temperature vs. Decay Time

SUMMARY

In support of the NRC rulemaking activity related to decommissioning, the Office of Research is using the FLUENT CFD code to study the air cooling phenomena of a spent fuel storage pool after a complete pool drainage. This study provides insights into the natural circulation cooling phenomena for a BWR spent fuel pool configuration. A series of sensitivity studies are completed to show the significance of some of the assumptions and parameters used to complete the predictions. This study focuses on convective cooling which is a limitation of previous spent fuel heatup predictions which rely on simplified flowfield models. This three-dimensional CFD treatment avoids the need for many flowfield assumptions in the fuel and rack region. These results give significant insights into the spent fuel pool cooling issue. The natural circulation flows predicted are the most significant factor in removing heat from the fuel under these conditions. These results help reduce the uncertainty associated with this most significant aspect of spent fuel pool cooling. The model does not include terms for the radiation and exothermic cladding reactions. These terms are significant at elevated temperatures. The present predictions form one piece of an overall solution to this issue. When using these predictions, the assumptions and limitations should be considered.

The series of predictions completed form a set of results which help define the natural circulation flows associated with this spent fuel cooling scenario. These results provide a basis for determining the applicability of the simplified flowfield assumptions used in previous models. Significant findings include the variations in pressure and temperature both above and below the fuel racks. Other relevant results include the downcomer flows. Part of the downcomer is essentially blocked by the rising hot plume of air. Another section of the downcomer flow is enhanced by the momentum of the cold plume falling from the main containment building down through the pool. Simplified constant temperature and pressure boundary conditions used in previous studies do not predict this behavior. The basis for the boundary temperatures and pressures applied in prior models can be re-considered in light of the results obtained here.

A similar global flow pattern is predicted for most of the solutions. The primary flow travels down around the fuel racks and then up through the hot fuel. A hot plume rises from the pool to the containment ceiling and exits through the outlet vent. Temperatures, pressures, velocities, and mass flow rates are recorded for a series of cases designed to quantify the effect of important input parameters.

The primary sensitivity study focused on the critical decay time. The maximum predicted temperature drops with decay time along a curve similar to a decay curve. Using the best-estimate ventilation rate and wall heat transfer coefficient on the containment walls and ceiling, the critical decay times for the 800 and 600 °C temperature limits are 26 and 35 months, respectively, for the 40 Gwd/MTU burnup. At a burnup of 50 Gwd/MTU, the critical decay times are 37 and 60 for the 800 and 600 °C limits respectively. The applicability of these critical temperature limits is beyond the scope of this report.

Containment ventilation can significantly affects the predictions. Increasing ventilation rates beyond the baseline of 2 building volumes per hour has a small effect. Decreasing the ventilation rate to 1 building volume per hour increases the predicted peak temperature by over 400 °C. For a given fuel decay and burnup, the ventilation rate is the most significant parameter in this study. These results are completed with adiabatic containment walls.

The overall heat transfer coefficient for the containment wall is varied from 0 to 4 W/m^2-K. A value of 2 W/m^2-K is used for best-estimate predictions. The variations in the heat transfer coefficient at 48 months decay time cause the peak predicted temperature to drop by 60 °C as the overall heat transfer coefficient is increased from 0 to 4 W/m^2-K. A larger temperature change is predicted at shorter decay times, where the containment temperatures are higher.

Porous resistance and thermal conductivity are parameters computed separately for use in the model. These parameters are varied to quantify the effect of their uncertainties on the final predictions. Varying the flow resistance in the racks up and down by 20% resulted in temperature changes of 49 and -18 °C, respectively. Reducing the expected thermal conduction parameter in the fuel racks by 50% increased the peak predicted temperature by 33 °C. These variations are minor compared to the effect of other input parameters in the model.

Most predictions in this study assumed an average fuel burnup of 40 GWd/MTU. A sensitivity study completed with 50 GWd/MTU at 4 years decay time increased the peak temperature by 175 °C. The increased burnup significantly increases fuel power. The increase in temperature associated with the higher burnup fuel is consistent with the increased fuel heat load. Fuel burnup is a significant parameter in these predictions.

REFERENCES

1. Nourbakhsh, H.P., et al, "Analysis of Spent Fuel Heatup Following Loss of Water in a Spent Fuel Pool, A Users Manual for the Computer Code SHARP," NUREG/CR-6441, May 1998.

2. Benjamin, A.S., et al., "Spent Fuel Heatup Following Loss of Water During Storage," NUREG/CR-0649, March 1979.

3. Sailor, V.L., et al., "Severe Accidents in Spent Fuel Pools in Support of Generic Safety Issue 82," NUREG/CR-4982, July 1987.

4. Fluent Inc., "Fluent 5 Users Guide," Canterra Resource Park, 10 Cavendish Ct, Lebanon, NH 03766, 1998.

5. Anderson, J.D., *Computational Fluid Dynamics: The Basics with Applications*, McGraw-Hill Series in Mechanical Engineering, McGraw Hill, 1995.

6. ASHRAE, "*Handbook of Fundamentals*", 1981.

7. White, F.M., *Viscous Fluid Flow*, Mc Graw Hill, 1991.

8. Boyd, C.F., "Predictions of Spent Fuel Heatup After a Complete Loss of Spent Fuel Pool Coolant," NUREG-1726, June 2000.

9. Todreas, N.E., Kazimi, M.S., *Nuclear Systems I: Thermal Hydraulic Fundamentals*, Hemisphere Publishing Corporation, 1990.

USNRC Thermal-Hydraulics Program

Jennifer Uhle
Chester Gingrich
U.S. Nuclear Regulatory Commission
Washington, DC 20555
jxu1@nrc.gov

ABSTRACT

USNRC Office of Nuclear Regulatory Research has established an integrated approach to advance its capability to perform thermal-hydraulic reactor system analysis to audit vendor or licensee analyses of new or existing designs, to establish and revise regulatory requirements, to study operating events and to anticipate problems of potential significance. This approach is focused around the development of a modernized code that can be used for all transients of current designs. The existence of one code with an extensible architecture allows improvements to be made efficiently and will prevent the fragmentation of resources as well as the knowledge-base. Experimental programs are in progress with the specific an aim of developing models to alleviate identified code deficiencies. USNRC staff in conjunction with external researchers will work jointly on this integrated program to provide the technological bases for regulatory decisions involving thermal-hydraulics.

The previous approach to maintaining a thermal-hydraulics system analysis capability relied on the existence of four separate codes, each with a dedicated purpose. However, the distinct differences in functionality have eroded over the years and presently, these codes are redundant in capability. The four codes were developed in the 1970's, so memory limitations and limited features of the available computer languages forced the use of cryptic programming styles. Because ingenuity was focused on overcoming these limitations, less was focused on code architecture. As a result, the codes are limited in their readability, extensibility, and ultimately maintainability. Code deficiencies and conservatism have been identified and require improvement but due to the architecture and budget reductions, making improvements to each of these codes is an inefficient prospect. To advance its current capability, USNRC is adopting a different approach by consolidating the capabilities of the suite of codes into one code to prevent the fragmentation of resources that occurs with four codes.

The base code for the consolidation is TRAC-P. The architecture of the code has been completely revamped to conform to the concept to modularity using Fortran90 language. This code is now referred to as TRAC-M to reflect the modernized architecture. The functionality of the predecessor codes are being incorporated into TRAC-M. To date, that of TRAC-B and RAMONA have been recovered and the consolidation of RELAP5 is in progress. Once completed, TRAC-M will have the ability to read both RELAP5 and TRAC-B input decks as well as legacy TRAC-P decks. At this stage, developmental assessment will be performed to select a set of constitutive relations that will allow TRAC-M to simulate the applications of the predecessor code with equivalent fidelity.

Capitalizing on the code architecture's enhanced extensibility, some work is being performed in parallel with the consolidation effort that focuses on making user requested improvements. A graphical user interface, SNAP (Symbolic Nuclear Analysis Package), will increase the ease of use of the code and help to minimize the user effect. The analysts will be provided with a graphically based input model generator as well as both two-dimensional (2-D) and three-dimensional (3-D) views onto which the data can be mapped and animated. SNAP will also provide runtime intervention so that the code can be run in a simulator-like mode. Other improvements include coupling to a 2-D and 3-D kinetics model, incorporation of an alternate matrix solver for use with large 3-D matrices will several 1-D connections, enabling an alternate less diffusive numerical scheme, and development of an Exterior Communications Interface (ECI), which facilitates coupling to processes or codes running outside of TRAC-M. The ECI is used to run the code in parallel, achieving high parallel efficiencies and a reduction in runtime.

Since the predecessor codes were known to have deficiencies in modeling some phenomena, experimental programs are underway to supplement the existing database with more detailed data using advances made in instrumentation. These models will be incorporated into the code when completed, which is estimated to range from the year 2001 to 2003. The programs include: Rod Bundle Heat Transfer Program to develop a mechanistic reflood model; Interfacial Area Transport to replace the static flow regime maps with a transport equation for interfacial area; Phase Separation at Tees to develop models over all flow regimes with data that is prototypic of reactor designs; and Subcooled Boiling at Low Pressure which will produce a model that is valid at low pressure.

USNRC staff in conjunction with external researchers will work jointly on this integrated program to provide the technological bases for regulatory decisions involving thermal-hydraulics.

1. Introduction

The USNRC currently relies on four different thermal-hydraulic system analysis codes to audit vendor or licensee analyses of new or existing reactor designs, to establish and revise regulatory requirements, to study operating events, to anticipate problems of potential safety significance and to support risk-informed regulation by determining thermal-hydraulic success criteria. The codes have similar but not identical capabilities.

For PWRs, the RELAP5 code is primarily used for simulations of SBLOCAs and plant transients and provides a 1-D representation of the flow-field. Generally, RELAP5 was developed as a fast-running, more simplistic code for long-term transients. In contrast, TRAC-P was utilized for faster transients, such as LBLOCAs, and provided a more detailed description of the flow-field with a 3-D representation of the vessel. In recent years, this distinct separation of functionality has been eroded and the present capabilities of the two codes overlap. However, the codes often model the same phenomena with different constitutive packages and also employ different numerical schemes. Until recently, the reactor physics capabilities of the two codes were limited to point kinetics. As will be explained in detail in Section 4.3, a 3-D kinetics capability has been provided to both RELAP5 and the consolidated code (TRAC-M) with tight parallel coupling to an advanced three-dimensional kinetics package using Parallel Virtual Machine (PVM).

For BWRs, the situation is comparable. The RAMONA code treats the flow field as 1-D but incorporates a 3-D kinetics package. A 3-D representation of the flow field is provided by the TRAC-B code, but the neutronics model is limited to either point or 1-D. The TRAC-B code stemmed from the TRAC-P code

and was developed in parallel specifically for BWRs. It incorporates BWR specific models, such as the jet pump and feedwater heater and also utilizes a different constitutive package and numerical scheme. The development of both TRAC codes proceeded independently.

The USNRC system analysis codes were developed in the 1970s and do not take advantage of today's abundant supply of inexpensive, fast memory. In addition, older programming languages did not readily provide a means for dynamic memory allocation. As a result, creative programming styles such as "bit packing" and "container arrays" were invoked to overcome these limitations. Unfortunately, these techniques produced cryptic coding and compromised readability (the ability to read the code), maintainability (the ability to fix errors in the code), extendibility (the ability to add new capabilities) and portability (the ability to run on different platforms). Presently, a great deal of effort is vested in deciphering these codes in order to fix bugs or improve the physical models or numerics. Since when the codes were first developed, less than optimal architecture was chosen in order to conserve memory, architecture modifications are now necessary to ameliorate these development difficulties.

Other issues exist in which code architecture is a secondary concern. Assessment studies have identified physical models that require improvement. Physical models requiring further development include those pertaining to the phenomena of phase separation at tees, subcooled boiling at low pressure, and reflood heat transfer. By initiating separate effects test programs, USNRC is in the process of supplementing the existing database in order to improve these models. More detailed or prototypic data are being generated for assessment as well as model development. These test programs are further described in Section 5. If such codes are to be used to support risk-informed regulation, then in addition to improvements in physical models, numerical methods should be upgraded to enhance the speed and robustness of the code and to minimize numerical diffusion to preserve property gradients, which can be important in 3-D kinetics calculations. A well designed architecture makes revision or replacement of physical models and numerical methods much easier.

User convenience was not the highest priority when the codes were developed. The older technology relied on command line input, which did not provide the analyst a means of easily determining the configuration of the modeled system or which code options were used in the simulation. In addition to not being user-friendly, the codes had limited ability to minimize the user effect, aside from generating a text output summarizing user options. Therefore, development of a graphical user interface (GUI), which will facilitate use of the code and help minimize user effect, is necessary for each of the four codes.

Since each code requires modernization and would benefit from an improved user-interface and an upgrade in physical models and numerics, USNRC is consolidating the suite of codes into one, with an aim of minimizing the dilution of resources that occurs with the development of four separate codes. As a result, user needs will be accommodated more expediently, since effort will not be distributed amongst the four codes. Additionally and perhaps most importantly, the consolidation will enhance analysis capabilities, as the USNRC and user community can focus its attention on one code thereby developing collective expertise far more efficiently than is possible when four codes are utilized. Input deck construction will not be duplicative, as all transients for a plant would be performed with one code instead of two.

2. Consolidation Plan

When the USNRC set the general goals for the consolidated code, a choice was required for the starting point of the effort. The options were to write the consolidated code from scratch, or to evolve an existing code to the final desired state. The evolutionary approach was suggested by a panel of code development experts that was convened in 1997 by USNRC, and was adopted for the following reasons:

1) Ability to have a functional code at all stages of the development process;
2) Existence of a large set of input decks for code testing;
3) Ability to design a sequence of code changes so that most test problems match results to the last bit (null testing); and
4) Automatic reuse of subprograms or code segments that already meet new requirements.

TRAC-P was selected as the base version of the consolidation because its structure was more modular and object-oriented, making it more closely aligned with final design goals for the consolidated code. It has 3-D flow modeling capabilities not available in RELAP5, and was a better target for installation of special purpose BWR component models developed for the TRAC-B code series. Through the use of the Graphical User Interface (SNAP), currently under development, the consolidated code will have the ability to process all archival RELAP5, TRAC-P, TRAC-B input decks. Simply, SNAP was chosen to process input, and TRAC-P was selected as the starting point for the computational engine of the consolidated code.

Our experience thus far with the evolutionary approach has been very positive. The null testing capabilities have speeded development and increased our confidence in the resulting code. BWR capabilities have merged very smoothly into the original PWR code. The underlying architecture has evolved into a new, much more "developer friendly" environment. We have significantly enhanced extensibility, readability and in turn, maintainability over the predecessor codes. Optimization of the architecture to enhance these attributes continues to be the prime design goal, as future development and maintenance efforts will be accelerated and developer expertise gained more rapidly. The end result will be a code that can be adapted new user needs with far less effort than the current generation of safety analysis codes.

2.1. Consolidation Stages

Consolidation consists of three major stages. The first is creation of a modern architecture under which desired features can be implemented and maintained with minimal effort. The second is installation of the general modeling capabilities (mesh topology, system components, and physical processes) of the four predecessor codes. The third is assessment during which the best model or correlation from the predecessor codes will be installed, so that the consolidated code will generate results as good as the predecessor codes for the targeted applications. The first stage was completed as described in Section 3. Stage 2 has been completed for the TRAC-B and RAMONA applications and RELAP5 is in progress. Some effort has begun with respect to the fourth stage but the majority of the work will be done once Stage 3 is completed. Figure 1 depicts a timeline of the consolidation activities and is described in Section 4.

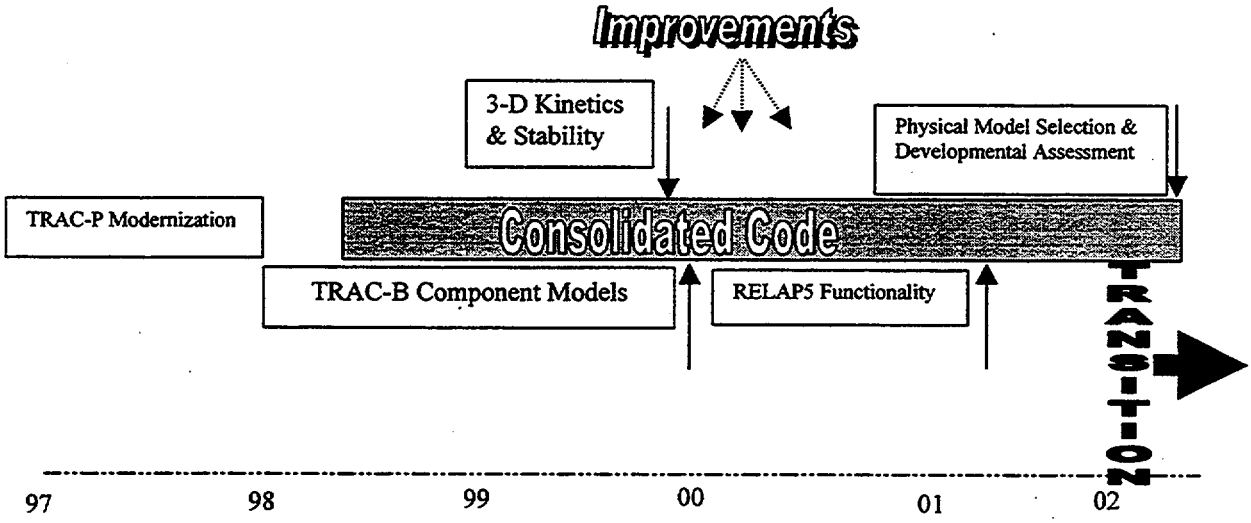

Figure 1: Consolidation Plan Timeline

2.2. Code Configuration and Software Quality Assurance

The plan of the consolidation stresses the importance of documentation and version control. To manage the versions created during the consolidation, USNRC has developed a configuration control system utilizing Concurrent Versions System (CVS) [http://www.sourcegear.com/CVS] and a development website. The development history is evident by perusing the "Build Page" of the website. The Build number, which is a hypertext link to download the code; 2) links to the directory containing the modified files, test files and documentation; 3) a brief description of the modification; 4) the developer's name. By perusing the Build Page, a developer can quickly determine what changes have been made to the code. Future versions are also listed to enable developers working on potentially conflicting changes to resolve any problems. The website contains other pages, such as the Test Page, which provides links to download various test sets and describes what each test set covers, and a Troubles page which provides links into the Trouble Report Database, so that users can upload bug reports or developers can enter the resolution. When a report is filed, the user and developer are automatically E-mailed that the report has been assigned to a developer and the uploaded input deck has been received. When the bug fix is incorporated into the code, the user is E-mailed the resolution report and informed which code version, accessible from the Build Page, contains the fix. If a version on the Build Page was developed as a bug fix, then the Build Page entry describing the modification will contain a link to the Trouble Report Database.

The documentation uploaded depends on the type of code modification. If a bug fix is submitted, then an error correction report is filed and is accessible from the Build Page. The Trouble Report Database also contains this resolution description. If a more expansive change, such as a BWR component is uploaded, then full Software Quality Assurance (SQA) documentation is submitted. This documentation includes:

- Software Requirements Document- what does this component have to do?
- Software Design and Implementation Document- how is the functionality achieved in the code?

- Test Plan- what tests must be run to prove the requirements have been met?
- Completion Report- summary and results of the test plan

A summary document is also submitted. It is accessible from the Build Page by the links into the directory containing the uploaded files. The summary document describes the main points of the SQA documents, so that the full reports do not have to be read if another developer wants to get an overview of the change. When new functionality is added to the code, uploaded tests are run to ensure the requirements are satisfied, and then made accessible from the Test Page. An automated developmental assessment script allows the tests to be run for each version created, and stores the results by version number. Therefore, changes in code results are easily traced.

The CVS code repository, development website, automated testing, and Trouble Report database have resulted in an organized and efficient development process. The modifications made to the code during the development are described in following sections.

3. Architectural Improvements to TRAC-P

As depicted in Figure 1, the first stage in the consolidation is the creation of a modern architecture under which desired features can be implemented and maintained with minimal effort. The following sections summarize the new architecture and the modifications made to the TRAC-P code in its evolution to TRAC-M.

3.1. Code Language and Database Design

The base TRAC-P code was written in Fortran77 (F77) and utilized a container array and integer pointers as its form of home-spun dynamic memory allocation as well as common blocks to provide communication of the global data. The associated coding was difficult to decipher. Fortran restrictions that drove the original TRAC-P data structures, have been eliminated with the introduction of derived types, dynamically allocatable arrays, pointers, and modules in Fortran 90 (F90). Features new to F90 also eliminated portability issues common in F77 codes. As a first step in the evolution of the consolidated code, TRAC-PF1/MOD2 version 5.4.25 was converted into F90 and designated TRAC-M.

By utilizing F90 features, TRAC-M data integrity is preserved by limiting the use of common blocks and eradicating the container array. Subroutines only have access to data either passed through argument lists or through the use of modules. A module is a F90 program unit, which allows other program units to access variables, derived type definitions, and subprograms declared within it by the F90 USE association. The general use of F90 modules helps to protect data, compartmentalize functionality and data, and ensures data type consistency. F90 derived types serve as the primary mode of storage. A derived type allows the storage of several data types in one array. Therefore, integers, characters, reals and logicals can be contained in one data structure. As an example, general scalar variables associated with a system component (pipe, tee, etc.) are organized in the following derived type:

```
TYPE genTabT
        INTEGER(sik) :: num
        INTEGER(sik) :: ncell
        CHARACTER*8 :: type
        ...
END TYPE genTabT .
```

The derived type, containing the component number, the number of cells, and the component type (PIPE, TEE, ROD, etc...), is denoted genTab in reference to the fact that this information is common to all components and is "generic". Array data can also stored in derived types. Therefore, state information, such as phasic temperatures and velocities, void fraction, and pressure can also be stored in derived types. Each state variable is an element of the derived type and is an array with length equal to the number of cells in the component. These derived types are implemented as arrays with lengths equal to the total number of components. This makes location of information within a calculation very simple. As an example, the user specified ID for the fifth component in the input deck is stored in genTab(5)%num. The volume of the 3rd cell in this component would be obtained from g1DAr(5)%vol(3). g1DAr refers to the fact that this array data is generic to all 1-D components.

These derived types provide great flexibility in database design and allow the storage to be designed based on how the information will be used rather than by data type. The database restructuring capitalized on features of F90 such as dynamic memory allocation, module data protection, and derived types to meet the design goals of enhanced readability, portability, extensibility and maintainability.

3.2. Code Modularity

Originally TRAC-P was designed to contain component and functional modularity. Both the data and program structure were organized around modules in the physical system (e.g. pipes, pumps, vessels). Once the F90 conversion was completed, effort was expended to enhance the code modularity. Modularity was and continues to be a prime design goal, as it reduces conflicts between simultaneous development efforts, and also allows development expertise to be efficiently gained and utilized. For example, a developer working on the control system does not need to know the details of the heat structure coding. All that is necessary is an understanding of the communication service between the control system and heat structure database. Modularity also facilitates code re-use. If isolated tasks are performed by isolated program units, then in each instance the code only needs to call this particular function or subroutine instead of repeating the same logic in a variety of locations. Code repetition produces multiple maintenance points and adds complexity. Therefore, the goal of the modularization work was to provide a code structure with the minimum number of maintenance points, clean interaction points between component-types, separation of functionality at both a high and low level and also preservation of data integrity. In general, there are four basic forms of modularity in TRAC-M, including high and low level functional modularity and both interior and exterior component based modularity.

Functional modularity means that a subroutine or a set of subroutines collectively performs one function. TRAC-M is comprised of four general tasks: input processing, initialization, equation solution and output. These tasks are isolated by specific driver routines so that the code is structured to be functionally modular at a high level. This has been enhanced by improvements in data communication and isolation of equation solutions. In TRAC-P, the solution of linear systems was mixed with coding setting up terms

in the flow equations, inhibiting the ability to adapt improved linear solvers to the code and parallelism. In TRAC-M terms in the finite volume equations are now evaluated and the matrix set up in a set of subroutines that are distinct from the subroutine that solves the matrix. This facilitated the incorporation of a new sparse matrix solver that reduces the run-time of the AP600 LBLOCA deck by 25%, while also enhancing parallelism. The new component data structure makes access to information adjacent to any given component very simple. However, direct access of one component's information by another component can disable parallelism within the code. As a result a system service was developed to manage the data communication between components. The service supports communication of information between fluid components, communication of fluid properties to heat structures, communication of heat flux information from heat structures to fluid components, and communication of information from any component to signal variables used by the control system. Most coding and computational effort associated with this service is contained in the initialization stage of a calculation. Timing tests on a 1-D model of LOFT produced identical results using 5% less time immediately after this transfer service was installed, while also enhancing code modularity.

High level modularity has also been impacted by the isolation of ASCII input deck processing into a separate program. This separation began by simply isolating old subroutines used to process native TRAC-P and TRAC-B input decks. The only input activities remaining in the consolidated code are associated with reading a binary restart file. Communication between input processor and the computational engine is via a platform independent binary (PIB) dump file, which contains all necessary initial conditions for the solution of the flow and conduction equations. This file enables the new graphical user interface, SNAP, to serve as the primary source of input for the consolidated code. SNAP will have the ability to generate PIB dump files for either RELAP5 or the new consolidated code. In normal mode the PIB files will be generated from user interaction with the GUI and a library of typical system configurations. To summarize, SNAP will have the ability to accept archival ASCII input decks for RELAP5, TRAC-P, or TRAC-B, permit user modifications via the GUI, and generate a PIB file to start the consolidated code.

Low level modularity enhances readability and facilitates bug fixes, as the functions of subroutines are clearly understood and simple enough for a developer to grasp and retain. Due to the obvious benefits of low-level functional modularity, some effort has been expended to enhance it. For example, the original TRAC-P code evaluated interfacial drag coefficients, developed terms in the 1-D momentum equations, and took steps to solve the equations in a single subroutine. This complicated any modifications to terms in the momentum equation or interfacial drag models, hindered replacement of the solver and hampered readability. This routine was streamlined and now one driver routine calls one subroutine for each physical model. Another driver routine calls the subroutine to set up terms in the momentum equation and calls another subroutine to handle the solution. This work facilitated the consolidation of the TRAC-B BWR components, as special terms were needed in the momentum equations to model the turbine and jet pump components. In our final stage of consolidation, isolation of the physical model evaluation will also expedite incorporating BWR component specific physical models, or generic RELAP5 correlations found to be superior to those in the current consolidated code.

4. General Modeling Capabilities

As depicted in Figure 1, the consolidation will recover all capabilities of the current suite of codes. It is paramount that the following point be understood: USNRC is not simply lumping all of the code together and renaming it TRAC-M, since the consolidated code would be the same size as the current suite of

codes, and it would still be necessary to know each of the four codes in order to use, maintain and develop it. In contrast, the consolidation involves using TRAC-B philosophy to develop BWR components out of TRAC-M components. The same approach is being used to recover the RELAP5 capabilities.

4.1. TRAC-B

BWR components/features that have been incorporated into TRAC-M to model BWRs include:

- Jet Pump
- Turbine
- Level Tracking (1-D and 3-D)
- CHAN (BWR fuel channel)
- Feedwater Heater
- Containment
- Separator/Dryer
- BWR Control Systems
- BWR Input Processing

Using the jet pump as an example, the consolidation method will be described. In TRAC-B the jet pump was based on a tee component. In order to accurately predict the pressure rise due to mixing of suction and drive line flows, TRAC-B applied a negative K-loss (derived from a properly formulated momentum source term) at the cell that models the mixing region of the jet pump. This was necessary in order to make this prediction consistent with an analytical result (obtained by assuming no pressure drop at the suction line flow) because the tee component momentum equation neglected the side leg momentum flux contribution. In contrast, TRAC-M uses a properly formulated momentum source term for tees, so that it was not necessary to add a negative loss coefficient for the jet pump in TRAC-M. It should be noted that the negative K-loss term was incorporated explicitly into the momentum equations, potentially limiting the maximum achievable time step size to avoid numerical instabilities, whereas the tee momentum source term in TRAC-M is implicit, imposing no limit on time step size.

Additionally, consistent with the TRAC-B modeling approach, the irreversible losses due to incomplete mixing of the high-velocity drive flow and the low-velocity suction flow and the unique geometry of the drive nozzle must be accounted for. The irreversible loss coefficients are based on the $1/6^{th}$ scale INEL jet pump test. So in summary, a user will specify a jet pump component and will input the geometry information for the jet pump but interior to TRAC-M standard tee routines will be used to calculate the terms in the finite volume equations with additional terms for the jet pump-specific irreversible losses. In addition to the output generated for a tee, the jet pump specific parameters are calculated and printed out, such as jet pump efficiencies (M and N ratios).

This example demonstrates that the tee-specific coding was not simply copied from TRAC-B and merged with TRAC-M, since TRAC-M already can model a tee. Instead, only the additional features required to model a jet pump were incorporated into TRAC-M. This same approach was used for all the TRAC-B components although more discussion is necessary to explain the CHAN component.

In TRAC-B, the CHAN component represents the BWR fuel channels. In a TRAC-B BWR plant model, this component provides a 1-D flow path over the fuel rods and a leak path that allows some fluid flow from the fuel channel to the bypass volume between the channels in the vessel. In TRAC-B, the CHAN

component is based on a pipe, a standard 1-D component, which can only be connected to other components at its ends. TRAC-B developers could have used a tee component to model the CHAN- the primary flow path through the core in the channel box would have been the tee primary leg, and the tee side leg would have allowed the primary leg to be connected to the vessel. They did not use a tee because the side leg would have had at least one cell volume, which is not an exact representation of the geometry of the leak path in a BWR core. Instead, a pipe was used and the source terms of mass, energy and momentum coming from the CHAN and flowing into the vessel (or vice versa) were modeled explicitly, i.e. explicit leak path model. Therefore, these terms were added to the right hand side (the known quantities) of the vessel and subtracted from the right hand side of the pipe.

During the consolidation, a decision was made to improve the hydraulic model of the CHAN component when it was incorporated into TRAC-M. An implicit rather than explicit leak path is provided in TRAC-M, to prevent instabilities that had been caused by TRAC-B's explicit connection of the CHAN to the vessel bypass. This improvement could be accomplished only by developing a new component, called a single junction. This junction has no volume and allows the cell of the CHAN pipe to be connected to a cell in the vessel implicitly (at new time). Additional work was needed in the code to allow this new type of connection, which modifies the structure of the matrices (the left-hand side quantities, evaluated at new time).

Using a single junction component will also aid RELAP5 input deck conversion, since in RELAP5 1-D components do not have end junctions built into the components, and single junctions must be used to connect them. The single junction component will also help alleviate differences in the way valves are modeled in the codes.

In order to preserve TRAC-B input decks, TRAC-M has been modified to process TRAC-B input decks. Due to the input separation task previously described in Section 3.2, this was done cleanly and did not hamper the readability of the code. Currently, SNAP is being used to process RELAP5 input decks, so that the investment in legacy input decks will be recovered.

4.2. Stability

Semi-Implicit numerics scheme was added to TRAC-M, so that an alternative technique could be used in place of the standard TRAC-M SETS method (Mahaffy, 1982) in situations where it is necessary to limit numerical diffusion, such as stability analysis. This work was made more efficient because of the numerical solution modularization effort, previously described in Section 3.2.

4.3. 3-D Kinetics

3-D kinetics and 1-D kinetics have been consolidated by coupling TRAC-M to a neutronics package through PVM (Parallel Virtual Machine). The benefit of this coupling methodology is that the codes remain isolated and communicate across a well-defined interface. Essentially, each code runs as a separate process. The neutronics package receives thermal-hydraulic data from TRAC-M, such as void fraction, phasic densities, temperatures, boron concentration, and fuel temperatures and returns the power back to TRAC-M. Therefore, a developer in TRAC-M is not required to have knowledge of the details of the neutronics package when trying to either debug a problem or add a capability. Only the knowledge of what needs to be passed and what is returned during the solution procedure is necessary. This methodology also allows upgrades to the neutronics package to take place without hindrance from TRAC-M development.

4.4. RELAP5 Capabilities

Currently, the capabilities of RELAP5 are being consolidated into TRAC-M. The main difference between RELAP5 and TRAC-M is the connectivity of hydraulic components. The single junction component added to TRAC-M in support of the TRAC-B CHAN component consolidation has facilitated the mapping of RELAP5 components to those of TRAC-M. TRAC-M also uses different independent state variables than RELAP5. Therefore, initial conditions specified in a RELAP5 input deck must be converted to those of TRAC-M via a call to the equation of state. Details like this are being handled inside the GUI. Recently work has begun to replace the equation of state in RELAP5 to minimize the mass error. Due to the modularity of TRAC-M, minimal effort was required to implement the new steam tables into TRAC-M. TRAC-M is also being modified to output the same information as RELAP5 so that users will be familiar with the code results. Since the semi-implicit numerical scheme was enabled during the recovery of RAMONA, no numerics work is required to consolidate RELAP5. The GUI will provide TRAC-M to process RELAP5 input decks. During the consolidation, USNRC will continue to maintain RELAP5 and make user-requested improvements, such as the minimization of mass error, flow oscillations, and time-step/platform dependency. USNRC will ensure that user needs are accommodated and will provide a transition period during which the codes are maintained until the user community has acclimated to the consolidated code.

4.5. Developmental Assessment and Physical Model Selection

As depicted in Figure 1, the final stage in the consolidation process is developmental assessment. The TRAC-B, TRAC-M, RAMONA, and RELAP5 functionality will be tested using a consolidated developmental assessment matrix that is based on existing PIRTS, CSNI test matrices and each of the codes' developmental assessment matrices. To be more systematic, scaled test data and code simulations were used to generate the ranges of conditions over which the ranked phenomena operate during the transients the consolidated code is tasked to simulate. These tests will be run to ensure that the consolidated code simulation fidelity is acceptable for all applications.

For example, the current constitutive relationships in TRAC-M may not be suited well for simulating the flow conditions common in BWRs. Whenever necessary, the TRAC-B specific constitutive relations will be incorporated into TRAC-M. For example, currently in TRAC-M the CHAN component uses interfacial drag for a pipe, since it is based on a TRAC-M pipe. Therefore, the TRAC-B interfacial drag model for rod bundles will have to be incorporated for use only when the PIPE component represents a rod bundle. Otherwise, the PIPE component will continue to use the original TRAC-M model for the pipe. The improvements to the code architecture, such as component based modularity, has facilitated this effort.

Some preliminary work has begun on assessing the differences between TRAC-B and TRAC-M against BWR specific data and in preparing input decks. In some cases TRAC-M has shown better predictive capability than TRAC-B for integral effects tests. However, further assessment and model selection must be done to ensure that the consolidated code fidelity is acceptable for all applications.

5. Code Improvements

Throughout the consolidation, improvements have been made to the TRAC-M code and merged whenever logistically feasible (Figure 1). The following section describes these modifications.

5.1. Graphical User Interface

As alluded to in Section 3.2, work is in process to extend the graphical user interface, SNAP, to TRAC-M in an effort to enhance the user friendliness of the code. The SNAP front end will replace current text-based input deck preparation and will assist the analyst in executing the model. Expert systems will provide default nodalization and other user conveniences. Component templates will be available to simplify the construction of plant models. Analysts will only have to make plant specific modifications to system loss coefficients or other geometric details. Furthermore, the user effect will be minimized, as SNAP will report any modeling practices that are not recommended. The SNAP back end will serve as the visualization tool. The back end capabilities will include a 3-D representation of the piping system and components, a simulator-like mask of the system with animation (colors represent temperatures, trips enunciated, strip charts depicting time traces of system parameters, etc...), and run-time control system linkage. The latter feature will allow the user to interact with the model/execution of the code as is common with simulators, thereby having the capability to change things such as positions of valves, pump speeds, and trip settings during run-time. The back-end will also have multiple masks, allowing the analyst to run and display different models simultaneously with the ability to pause and resume each calculation.

5.2. Exterior Communication Interface

As the user community requests additional code capabilities in response to increases in available computing power, the danger exists to complicate the code and its architecture, hindering further development and maintenance. To prevent this, USNRC has adopted the design strategy of coupling the code across a well-defined interface. This strategy was utilized in providing the code with a 3-D kinetics capability. To allow this logic to be extended to other functional models and to make its implementation consistent in each case, an exterior communication interface has been developed. As a proof of principle, a RELAP5 accumulator model has been coupled to TRAC-M utilizing this interface. Currently in TRAC-M, an accumulator is simply an option in a pipe that has a very low interfacial drag at the interface to provide phasic stratification. Since an accumulator is more physically modeled by simple perfect gas expansion and does not require full two-fluid model solution, the RELAP5 accumulator model can replace the current TRAC-M approach. The exterior communication interface will also be utilized to allow the GUI back-end to communicate with the TRAC-M control system, so that TRAC-M can be run in "simulator-like" mode. The exterior communication interface will also facilitate coupling to other codes, such as CFD codes, sub-channel analysis codes or more detailed containment codes. Effort is underway to couple the CONTAIN (Washington, 1991) code to TRAC-M to allow a more detailed containment analysis and the REMIX code (Iyer, 1981) to TRAC-M for PTS analysis using the ECI.

5.3. Parallel Simulations

As part of the modularization effort, the computational and data flows of the consolidated code were revised to fully enable component-based parallelism. Computational stages have been restructured so that any component in a given stage only requires boundary data generated by adjacent components at a previous stage. Data is transferred at synchronization points between the stages of the calculation.

Within a given stage, computations in any given component are independent of results generated for any other component in that stage. In fact the parallelism carries to a deeper level. Within a given stage calculations performed in any computational mesh cell are independent of results from any other computational cell obtained in that stage. This permits consideration of fine grain parallelism as well as the coarse grain component-based parallelism already achieved.

Our first emphasis in development has been coarse granularity, both as a source of speed enhancement and as an organizational strategy to facilitate future code extensions. Examples given in Section 5.2 further explain the concept of extendibility. By utilizing the ECI in a mode where copies of the code are running on separate processors and are communicating via the ECI, the code is executing in parallel. Timing studies were run to determine the parallel efficiencies of a perfectly load balanced model. Simple flow loops were constructed with a fixed number of volumes spread evenly over 2, 3, and 4 pipes. Single phase liquid flow was modeled to ensure equal work loads in evaluating fluid state information in each mesh cell. With a well balanced computational load, we were able to examine the basic overhead associated with parallel data communications.

Parallel efficiencies achieved by the code are given in Table 1. The cases run included 2 to 4 pipes containing an equal number of cells. The column labeled "300 cells" describes runs with two 150 cell pipe components, three 100 cell pipes, and four 75 cell pipes. The column labeled "600 cells" describes runs with two 300 cell pipes, three 200 cell pipes, and four 150 cell pipes. In the parallel cases, each pipe was distributed to one processor. Typical plant models use more than 600 computational volumes. Results in Table 1, indicate that a well load balanced plant model could produce results nearly twice as fast on a dual processor computer, and at least 3.5 times faster using 4 processors. Dual processor PC's are now fairly common and affordable, and relatively inexpensive four processor PC's are not too far away. Practical benefits can be obtained from the ECI without a major investment in computer hardware.

CPUS	300 cells	600 cells
2	95%	97%
3	87%	93%
4	79%	87%

Table1: Parallel Efficiencies

5.4. Model Development

Since code deficiencies have been identified, USNRC has initiated work to ameliorate these limitations. These new features will be merged with the consolidated code when available and when logistically feasible. This approach was adopted, since it was necessary to supplement the currently available database before some models could be developed. Therefore, four separate effects tests are being run in an attempt to minimize the time required before these deficiencies can be improved.

5.4.1. Subcooled Boiling at Low Pressure

In two-fluid codes, only one temperature is specified for each phase in a cell. Therefore, in order to predict boiling on the heated surface when the volume averaged temperature is subcooled, a special model is required to predict vaporization in the superheated near wall region. RELAP5 uses the Saha-Zuber (Saha, 1974) criteria for the onset of significant void to determine if subcooled boiling can occur and then a modified form of the Lahey subcooled boiling model (Lahey, 1978) to determine the fraction of the wall heat flux that results in vapor generation. This model utilizes a liquid to vapor density ratio to account for buoyancy induced "pumping" that mixes the near wall region and suppresses nucleation. At low pressures, the density ratio is huge (0.2 MPa, the ratio is 1300 vs. a ratio of 6 at 15 MPa) and the net vapor generation is dramatically under-predicted. The AP600 analysis proved that the subcooled boiling model at low pressure requires improvement.

5.4.2. Interfacial Area Transport

TRAC-M and most two-fluid codes use interfacial area to determine the total force between phases for heat transfer and drag. Currently the codes use static flow regime maps and deduce the representative interfacial area. As mass flux and void fraction change, the flow regimes change instantaneously with no regard of the physical time and length scale of flow regime development. This approach causes instabilities and limits code accuracy. An alternative approach is to use a transport equation for interfacial area with source and sink terms representing the actual processes that govern the change in interfacial area. A preliminary model has been incorporated a test version of the code to predict the development of interfacial area in a vertical pipe. Good agreement with data was achieved.

5.4.3. Phase Separation at Tees

During depressurization, phase separation at tees can dominate the course of a transient, since the effluent quality determines how fast the system depressurizes and the liquid inventory. Perfect separation will maximize depressurization while minimizing the loss of inventory, resulting in a non-conservative result. Underprediction of separation may be conservative but may limit design in cases of low inventory, such as beyond design base accident scenarios. During AP600 analysis, the phase separation at tee model in RELAP5 was proven to be of limited applicability, since data only covered a limited range of conditions. USNRC is currently supplementing this database and reviewing existing models with an aim of either developing or identifying applicable models over all ranges of conditions prototypic of nuclear reactor operation.

5.4.4. Rod Bundle Heat Transfer Program

The goal of this effort is to develop a more mechanistic model for reflood heat transfer. The test facility will generate data in a manner that will help isolate each of the many phenomena that affect reflood. For example, data on convection heat transfer alone will be taken, as well as the effects of drops (induced turbulence, distributed heat sink, etc...) and radiation only. The facility will also measure detailed data on drop size distribution, drop velocity, vapor superheat, void distribution in froth region to help identify the effect of void fraction on heat transfer, and will have instrumented spacer grids to measure rewetting and droplet break-up. The current database lacks this information, which is expected to help minimize the uncertainty in current reflood models.

6. Conclusions

The goal of the consolidation is to recover the functionality of the current suite of codes, while reducing the maintenance and development burden so that the capabilities can be extended more efficiently and the knowledge-based developed more rapidly. The first stage of the effort was improving the architecture of TRAC-P to serve as the basis of consolidated code. The architecture was revamped and the language migrated to FORTRAN90 to produce a more modular, readable, extendable and developer-friendly code. TRAC-B and RAMONA capabilities have been incorporated into the code while adhering to the new modular architecture concepts. Therefore, the TRAC-B and TRAC-P finite volume equations were compared and only those additional terms required to model the BWR components were consolidated. The RELAP5 functionality consolidation is underway using this same approach. During the TRAC-B consolidation code modifications were made to TRAC-M that has reduced the work involved in the RELAP5 consolidation. These modifications include enabling a semi-implicit numerical scheme, development of a single junction component and a RELAP5 accumulator model. To enhance modularity, 1-D and 3-D kinetics were coupled to the code across a well-defined interface. This coupling strategy has been extended into an exterior communication interface, which will facilitate coupling other codes in the future. The RELAP5 accumulator model was coupled in this manner to prove the feasibility of the approach. The graphical user interface, SNAP, has also been extended to provide the input processing for the consolidated code. SNAP will also allow the consolidated code to process RELAP5 input decks, so that the code will be able to read TRAC-B, TRAC-P and RELAP5 decks.

The final stage of the work involves assessing TRAC-M against the other codes and data for the targeted applications and modifying the constitutive models so that TRAC-M will have equal or better simulation fidelity than the predecessor codes.

Throughout the consolidation effort, improvements have been and will continue to be made to the code. These include: a semi-implicit numerics scheme to be used as an alternative to SETS in order to reduce numerical diffusion; an exterior communication interface, which facilitates the coupling of TRAC-M to processes running outside of the TRAC-M code, such as a simplified accumulator model; a faster sparse matrix solver to be used as an alternative for large 3-D matrices; development of a graphical user interface and post-processor; and a coarse grain parallel simulation capability to increase the speed of the code. Model improvements will be merged with the code when completed.

Once completed, the consolidation effort will produce a code that recovers the functionality of the current suite of codes. Throughout the effort, RELAP5 will be developed and maintained to accommodate user needs. A transition period will also be provided to allow the user community to acclimate to the consolidated code. With one code, the knowledge-base will be enhanced as the user and developer community can focus on one code instead of four and code improvements will be made more efficiently.

7. References

K. Iyer et al., REMIX: A Computer Program for Temperature Transition duet o High Pressure Injection After the Interruption of Natural Circulation, NUREG/CR-3701, 1986.

R.T. Lahey, "A Mechanistic Subcooled Boiling Model," *Proceedings of the Sixth International Heat Transfer Conference*, Toronto, Canada, 1978, Volume 1, pp. 293-297.

J. Mahaffy, A stability-enhancing two-step method for fluid flow calculations, J. Comput. Phys. **46**, 1982, pp. 329-341.

J. Mahaffy, J. Uhle, J. Dearing, T. Downar, R. Johns, C. Murray, "Architecture of the USNRC Consolidated Code", *Proceedings of ICONE 8, 8th International Conference on Nuclear Engineering*, April 2-6, 2000, Baltimore, MD.

RELAP5/MOD3 Code Manual, Vols. 1-6, Idaho National Engineering Laboratory Report, INEL-95/0174, US Nuclear Regulatory Commission Report, NUREG/CR-5535, 1995.

P. Saha and N. Zuber, "Point of Net Vapor Generation and Vapor Void Fraction in Subcooled Boiling," *Proceeding of the Fifth International Heat Transfer Conference*, 1974, Volume 4, pp 175-179.

TRAC-BF1/MOD1: An Advanced Best-Estimate Computer Program for BWR Accident Analyis, Vols. 1-3, Idaho National Engineering Laboratory Report, EGG-2626, US Nuclear Regulatory Commission Report, NUREG/CR-4356, 1992.

TRAC-PF1/MOD1: An advanced best-estimate computer program for pressurized water reactor thermal-hydraulic analysis, Los Alamos National Laboratory Report, LA-10157-MS, US Nuclear Regulatory Commission Report, NUREG/CR-3858, 1986.

K. Washington et al., Reference Manual for the CONTAIN 1.1 Code for Containment Severe Accident Analysis, NUREG/CR-5715, 1991.

Wulff, W., Cheng, H. S., Diamond, D. J., and Khatib-Rahbar, M., Description and Assessment of Ramona-3B MOD.O Cycle 4: A Computer Code with Three-Dimensional Neutron Kinetics for BWR System Transients, Brookhaven National Laboratory Report, BNL-NUREG-51746, NUREG/CR-3664, 1984.